Historical aerial photographs and digital photogrammetry for landslide assessment

This item was submitted to Loughborough University's Institutional Repository by the/an author.

Additional Information:

- Submitted in partial fulfilment of the requirements for the award of the degree of Doctor of Philosophy of Loughborough University.

Historical Aerial Photographs and Digital Photogrammetry for Landslide Assessment

by

Jan Walstra

A Doctoral Thesis

Submitted in partial fulfilment of the requirements

for the award of

Doctor of Philosophy of Loughborough University

November 2006

Abstract

Key words: Digital photogrammetry, Historical aerial photographs, Landslide monitoring, Landform change, Digital Elevation Model (DEM), Orthophoto, Displacement vector, Data quality.

This study demonstrates the value of historical aerial photographs as a source for monitoring long-term landslide evolution, which can be unlocked by using appropriate photogrammetric methods.

The understanding of landslide mechanisms requires extensive data records; a literature review identified quantitative data on surface movements as a key element for their analysis. It is generally acknowledged that, owing to the flexibility and high degree of automation of modern digital photogrammetric techniques, it is possible to derive detailed quantitative data from aerial photographs. In spite of the relative ease of such techniques, there is only scarce research available on data quality that can be achieved using commonly available material, hence the motivation of this study.

In two landslide case-studies (the Mam Tor and East Pentwyn landslides) the different types of products were explored, that can be derived from historical aerial photographs. These products comprised geomorphological maps, automatically derived elevation models (DEMs) and displacement vectors. They proved to be useful and sufficiently accurate for monitoring landslide evolution. Comparison with independent survey data showed good consistency, hence validating the techniques used.

A wide range of imagery was used in terms of quality, media and format. Analysis of the combined datasets resulted in improvements to the stochastic model and establishment of a relationship between image ground resolution and data accuracy. Undetected systematic effects provided a limiting constraint to the accuracy of the derived data, but the datasets proved insufficient to quantify each factor individually.

An important advancement in digital photogrammetry is image matching, which allows automation of various stages of the working chain. However, it appeared that the radiometric quality of historical images may not always assure good results, both for extracting DEMs and vectors using automatic methods.

It can be concluded that the photographic archive can provide invaluable data for landslide studies, when modern photogrammetric techniques are being used. As ever, independent and appropriate checks should always be included in any photogrammetric design.

Acknowledgements

This thesis is the reward of three years of research at Loughborough University. Although I have enjoyed these years very much, completion would not have been possible without the support of so many people.

First of all, I am very grateful to my supervisors, Jim Chandler and Neil Dixon, for their endless patience, constant encouragement and valuable advice throughout my research. Also, I would like to thank Tom Dijkstra for sharing some of his enthusiasm about landslides. I also appreciated the help by Alan Forster, Kevin Northmore (both of BGS) and Howard Siddle (Halcrow), who provided me with useful advice and reports on the landslides in South Wales. Special thanks go to 'ze dzjermans', Uli and René (in chronological order), not only for their company in and outside the office, but especially for resisting the 'lovely' British weather during the field surveys. For the latter I also owe thanks to Patricia, although she actually enjoyed it.

However, my time in Loughborough would have never been quite so enjoyable without the special crews from 'residence 114' and 'Middleton Place' (no need for names) – and the many, many great friends from every corner of the world that I met in this little town (too many names). Sometimes I cannot help wondering if I should say 'in spite of' them I managed to accomplish this work. Anyway, thanks for the unforgettable time!

My final thanks are to my parents; without their undisputable support and consideration I would not have got this far.

Loughborough, May/November 2006

Contents

List of figures

List of tables

Chapter One

1 Introduction

1.1 Background

Landslides represent a widespread geologic hazard. Yearly, extreme landslide disasters kill hundreds of people worldwide. Less extreme events pose threats to infrastructure and cause significant economical losses. Growth of urban areas and expanded land use have increased the vulnerability to landslides. Moreover, the impact of climate change may result in higher frequency of such events in future. For responsible planning, it is not only important to recognise the causal factors that initialise landslide failures, but also understand their long-term development in relation to changing environmental factors. The response of landforms to climate change is complex and difficult to model, requiring extensive data records. Whereas usually long climate data records are available, obtaining accurate historical data about landslide movements is more challenging.

There are sophisticated tools available for monitoring geomorphological change and landslide movements. Traditional instruments include inclinometers, tiltmeters, extensometers and land surveying devices (Franklin 1984). Modern tools include global positioning systems (GPS) (Gili *et al.* 2000; Mora *et al.* 2003; Mills *et al.* 2005; Squarzoni *et al.* 2005) and remote sensing methods such as satellite (Hervás *et al.* 2003; Delacourt *et al.* 2004) and aerial imagery (see review

in Section 3.7), synthetic aperture radar (SAR) (Buckley *et al.* 2002; Squarzoni *et al.* 2003; Tarchi *et al.* 2003), and light detection and ranging (LIDAR) (Adams & Chandler 2002; Ager *et al.* 2004). However, most of these methods are usually not capable of revealing quantitative data about past movements, and the length of their records are restricted. Systematic aerial surveys started after the Second World War, providing potential data coverage of more than 50 years.

Recent advances in information technology have led to the development of automated digital photogrammetry techniques, allowing for rapid and cost-effective data collection. Hence, the aerial photographic archive offers great potential for studying landslide evolution. A sequence of photographs captures morphological change, which can be unlocked by using appropriate photogrammetric methods.

1.2 Aim and objectives

Although modern digital photogrammetric techniques allow vast amounts of data to be acquired easily, caution should be taken during their interpretation. Limited quality of available archival imagery affects the accuracy of derived data. This study focused on using automated photogrammetric techniques to acquire accurate and relevant data from historical aerial imagery, for quantifying landslide movements. The project aim was formulated as *"to evaluate the use of historical aerial photographs and the latest digital photogrammetric techniques for investigating past landslide dynamics"*. This aim was accomplished through achieving four main objectives:

- *Review state-of-the-art photogrammetric techniques, with particular attention to applications in landslide studies and related topics.*

This objective was achieved through carrying out an extensive literature review on landslides to identify the key elements required for investigation of their mechanism and development. Also the main photogrammetric techniques were studied in order to reveal what data can potentially be obtained, and their application to landslide studies.

- *Extract morphological data from historical aerial photographs and identify the main controls on data quality.*

Two landslide case-studies explored the photogrammetric techniques to extract high-resolution data from historical aerial photographs. A variety of available material was used, to identify the key controls on quality of derived data.

- *Use extracted data to quantify and visualise landslide dynamics.*

This objective comprised the acquisition of diverse spatial products from the extracted data; showing their potential value to quantify and visualise landslide dynamics.

- *Identify the role of historical image sequences in understanding and modelling of landslide mechanisms.*

The different products that were acquired from historical imagery were evaluated regarding their accuracy and relevance to monitoring of long-term landslide dynamics.

1.3 Contribution to knowledge

The contribution of this research to knowledge is to demonstrate the value of historical aerial photographs to the long-term monitoring of landslides, and the wide range of relevant data that can be recovered relatively easily, using modern digital photogrammetric techniques. This study explores the various types of data that can be acquired by these means, and recognises their potential relevance to landslide studies. It is demonstrated that multi-temporal elevation models are especially useful for quantifying terrain changes associated with displacement of relatively large ground masses; displacement vectors can be measured where the integrity of the displaced terrain surface has remained; qualitative interpreted information is essential during analysis of these quantitative data. Additionally, the constraints on data quality, inherent to using historical photographs and the application of automated digital photogrammetric techniques, are identified in this study and, to some extent, quantified.

1.4 Structure of thesis

The structure of this thesis broadly corresponds to the chronological order that was adopted throughout the research, which also relates to the objectives listed previously.

- Chapter 1 places this study in its wider context, states the aims and objectives and presents the structure of the thesis.

- Chapter 2 provides a literature review on landslides; their description, causes, and mechanisms. Particular attention is focussed on the use of aerial

photographs in the recognition of landslide features and associated mechanisms.

- Chapter 3 presents an extensive literature review on digital photogrammetric processing. The main principles are explained, such as aerial triangulation, digital image matching, automated DEM extraction and orthophoto generation. Issues about data quality are discussed and finally, applications of photogrammetry in landform change research are reviewed.

- Chapter 4 explains the strategies that were followed to fulfil the aims and objectives of this research – i.e. the problems that arose in the course of work and the decisions that were taken to overcome them. The process of identifying these issues and their satisfactory solution led to the identification of key issues and recommendations in Chapter 7.

- Chapter 5 describes the case study on the Mam Tor landslide. This site was used to develop and test the various techniques described in Chapter 4. The site has been subject to frequent investigations in the past, and hence offered the potential to compare the results from this study with other data sets. The extensive range of historical photography made it possible to evaluate the results in the context of varied photo quality, as discussed in Chapter 7.

- Chapter 6 describes the case study on the East Pentwyn landslide. This site was used to validate the techniques developed in the Mam Tor case study. The landslide was initiated recently and its development is well documented. Of particular interest is that the entire development of the landslide is recorded by historical aerial photographs.

- Chapter 7 combines the findings from the two case-studies and discusses their implications for landslide research. The variety of photo quality that was used, allowed the identification of the main controls on data quality, and an attempt to formulate a relation between these. Also some weaknesses of this study are identified leading to recommendations for further research. Finally, a short overview is given of the different data types acquired in this study and guidance on their relevance to landslide investigations.

- Chapter 8 summarises the main conclusions and recommendations culminating from this study.

Chapter Two

2 Landslides

An important step in landslide investigation is to collect adequate data for their description by mapping, historical archive analysis and pro-forma preparation. Natural conditions need to be described properly and measured to avoid mistakes in classification, monitoring, laboratory determinations and slope stability analyses.

This chapter describes the landslide phenomenon, its description, causes, and mechanisms. Particular attention will be focussed on the use of aerial photographs in the recognition of landslide features and associated mechanisms.

2.1 Definitions and terminology

Landslides include a wide range of ground movements, such as rock fall, deep failure of slopes, and shallow debris flows. Due to this great diversity, many different definitions have been formulated, and various attempts have been made to create unambiguous classification schemes, according to many different criteria. Which particular criteria and definitions are being used depends on the objective of the project.

The natural landscape is very complex and possible preparatory, triggering and sustaining mechanisms of landslides are so varied that their description and classification is an eminent problem (Brunsden 1993). In general, the term

landslide is used for a whole range of ground movements. Often cited is the following definition, originally by Varnes (1958):

> "*The term landslide denotes downward and outward movement of slope-forming materials composed of natural rock, soils, artificial fills, or combination of these materials*".

However, later Varnes (1978) indicates that the broader heading slope movement would be a better comprehensive term to capture the full range of movements, since landslide infers a particular process and therefore should be used in stricter sense only. For the same reason, Brunsden (1984) prefers the term mass movement for all processes which do not require a transporting medium such as water, air or ice (as opposed to mass transport).

A stricter definition for landslides would therefore refer to the particular process of sliding that is involved in the movement. Varnes (1978):

> "*In true slides, the movement consists of shear strain and displacement along one or several surfaces that are visible or may reasonably be inferred, or within a relatively narrow zone*".

The International Geotechnical Societies' UNESCO Working Party for World Landslide Inventory (WP/WLI 1993) produced a multilingual landslide glossary. The clearly defined terminology is recommended for use in communication (Table 2.1).

2.2 Landslide classification

There are many criteria to distinguish between different types of slope movement in classification schemes. An extensive overview is given by Hansen (1984b). Since this research focuses on the use of (multi-temporal) aerial photographs for landslide assessment, the only relevant criteria in this context are those that can be obtained by interpretation of aerial photographs. Morphology, and to a certain extent material type, can directly be examined on (stereo-pairs of) air photos. In general, there is a clear relation between landslide mechanism and its resulting morphological features. Moreover, patterns and rates of movement can be determined from multi-temporal images (see Sections 3.7.2 and 3.7.3), which are obviously related to the mechanisms as well. Therefore, mechanism is another relevant criterion.

Table 2.1. Definitions of landslide features (WP/WLI 1993).

undisturbed ground — — — · original ground level ⣿ extent of displaced material
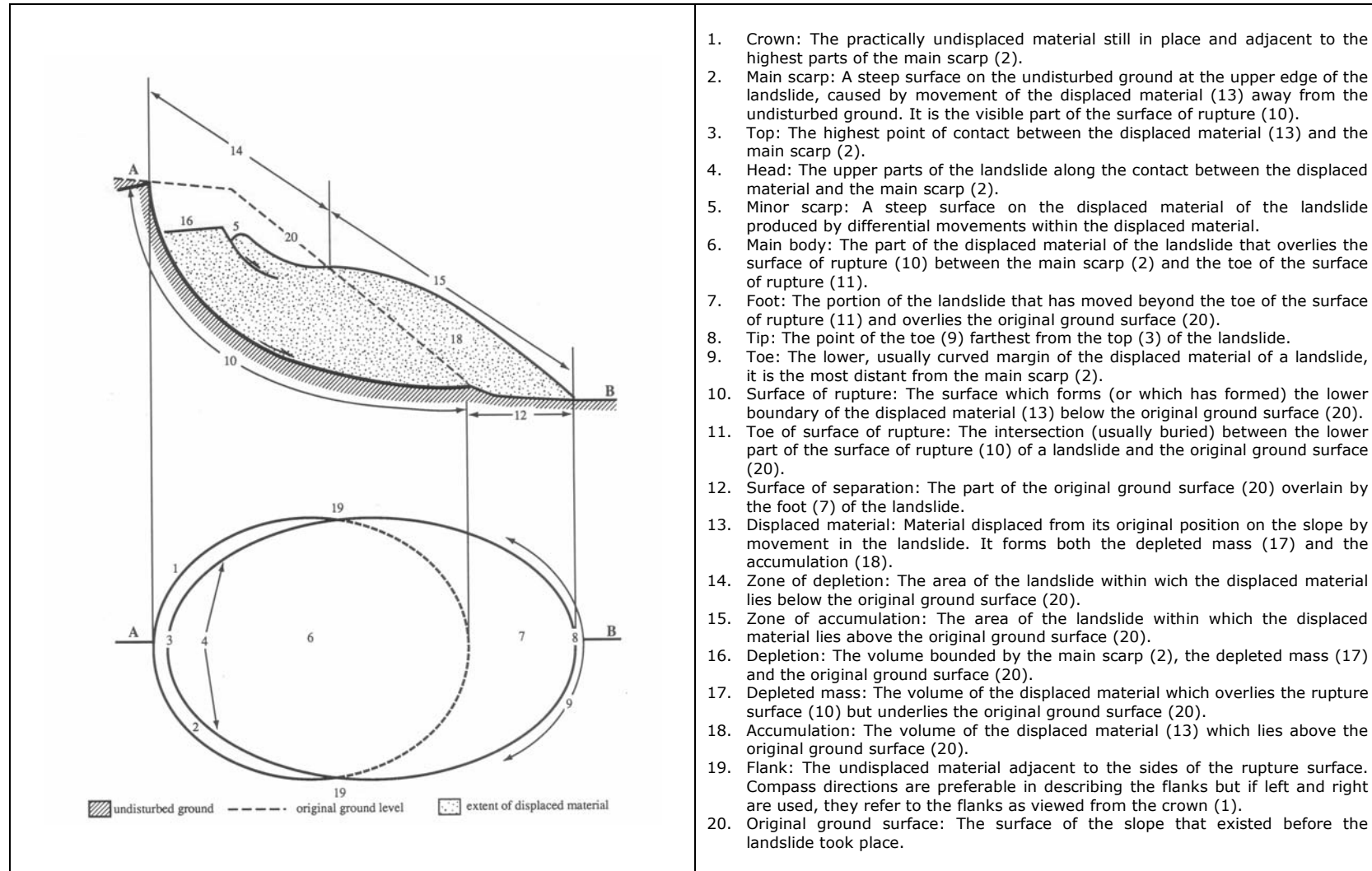
1. Crown: The practically undisplaced material still in place and adjacent to the highest parts of the main scarp (2).
2. Main scarp: A steep surface on the undisturbed ground at the upper edge of the landslide, caused by movement of the displaced material (13) away from the undisturbed ground. It is the visible part of the surface of rupture (10).
3. Top: The highest point of contact between the displaced material (13) and the main scarp (2).
4. Head: The upper parts of the landslide along the contact between the displaced material and the main scarp (2).
5. Minor scarp: A steep surface on the displaced material of the landslide produced by differential movements within the displaced material.
6. Main body: The part of the displaced material of the landslide that overlies the surface of rupture (10) between the main scarp (2) and the toe of the surface of rupture (11).
7. Foot: The portion of the landslide that has moved beyond the toe of the surface of rupture (11) and overlies the original ground surface (20).
8. Tip: The point of the toe (9) farthest from the top (3) of the landslide.
9. Toe: The lower, usually curved margin of the displaced material of a landslide, it is the most distant from the main scarp (2).
10. Surface of rupture: The surface which forms (or which has formed) the lower boundary of the displaced material (13) below the original ground surface (20).
11. Toe of surface of rupture: The intersection (usually buried) between the lower part of the surface of rupture (10) of a landslide and the original ground surface (20).
12. Surface of separation: The part of the original ground surface (20) overlain by the foot (7) of the landslide.
13. Displaced material: Material displaced from its original position on the slope by movement in the landslide. It forms both the depleted mass (17) and the accumulation (18).
14. Zone of depletion: The area of the landslide within wich the displaced material lies below the original ground surface (20).
15. Zone of accumulation: The area of the landslide within which the displaced material lies above the original ground surface (20).
16. Depletion: The volume bounded by the main scarp (2), the depleted mass (17) and the original ground surface (20).
17. Depleted mass: The volume of the displaced material which overlies the rupture surface (10) but underlies the original ground surface (20).
18. Accumulation: The volume of the displaced material (13) which lies above the original ground surface (20).
19. Flank: The undisplaced material adjacent to the sides of the rupture surface. Compass directions are preferable in describing the flanks but if left and right are used, they refer to the flanks as viewed from the crown (1).
20. Original ground surface: The surface of the slope that existed before the landslide took place.

The most widely used classification scheme was formulated by Varnes (1978), and is based on mechanism and type of material involved. The scheme is set up according to features that may be observed at once or with minimum investigation, and without any reference to the causes of the landslide. It classifies slope movements into falls, topples, slides, lateral spreads, and flows. Wherever two or more types of movement are involved, the slides are termed complex. The material of the moving mass is divided into two classes, rock and soil; the latter split further into debris (predominantly coarse material) and earth (predominantly fine). The classification is summarised in Table 2.2.

Table 2.2. Classification of mass movements (Varnes 1978).

TYPE OF MOVEMENT		TYPE OF MATERIAL		
		BEDROCK	ENGINEERING SOILS	
			Predominantly coarse	Predominantly fine
FALLS		Rock fall	Debris fall	Earth fall
TOPPLES		Rock topple	Debris topple	Earth topple
SLIDES	ROTATIONAL	Rock slide	Debris slide	Earth slide
	TRANSLATIONAL			
LATERAL SPREADS		Rock spread	Debris spread	Earth spread
FLOWS		Rock flow	Debris flow	Earth flow
		(deep creep)	(soil creep)	
COMPLEX		Combination of two or more principal types of movement		

The following is a brief description of the main types of movements that are distinguished by Varnes' classification (see Figure 2.1 for illustrations):

1. Falls – Very rapid movements of slope material that separates from steep slopes or cliffs. Most of the movements occur due to free fall or by rolling and bouncing.

2. Topples – Blocks of rock that tilt or rotate forward on a pivot, then separate from the main mass, fall on the slope, and subsequently bounce and roll further downslope.

3. Slides – Movements that are characterised by a shear failure along one or more discrete surfaces of rupture. Vectors of relative motion are parallel to the surface of rupture. The two principal types of slide are rotational and translational.

a. Rotational failures have a curved surface of rupture, concavely upward; the movements are more or less rotational on an axis parallel to the contour of the slope; the characteristic scarp at the head may be nearly vertical. The surface of each moving unit typically tilts backward toward the slope. At the toe, upward thrusting occurs. Rotational failures generally occur on slopes of homogeneous clay, shale, weathered rocks, and soil. They may be single rotational, multiple rotational, or successive rotational types.

b. Translational failures involve slides on more or less planar surfaces. The movement of a translational slide is strongly controlled by weak surfaces such as beddings, joints, foliations, faults, and shear zones. In many translational slides the mass is deformed or breaks up into many independent units while moving downslope.

4. Spreads – Movements that involve liquefaction whereby saturated, cohesionless sediments are transformed into a liquid state.

5. Flows – Rapid movements of material as a viscous mass where inter-granular movements predominate over shear surface movements. This category includes creep, the slow, spatially continuous deformations in rock and soils. There is a gradual transition from debris slides to debris flows, depending on the water content, mobility, and the character of movement. Debris flows may develop from slumps, when the ground mass breaks up while advancing downslope.

6. Complex – Failures that involve a combination of the basic types of movements, within various parts of the slope or at different times in its development.

The classification developed by the European EPOCH project (Casale *et al.* 1994), is based on Varnes' scheme with some differences in nomenclature (Dikau *et al.* 1996). The most comprehensive scheme is the one proposed by Hutchinson (1988), which is primarily based on morphology, with some consideration given to mechanism, material and rate of movement (Table 2.3). Whereas the original classifications by Hutchinson (1968) and Varnes (1958) showed some major distinctions (e.g. Hutchinson did not recognise flow as a primary failure mechanism), they have converged in the course of time. Varnes' scheme may be easier to apply and requires less expertise, while Hutchinson's has particular appeal to engineers contemplating stability analysis (Crozier 1986).
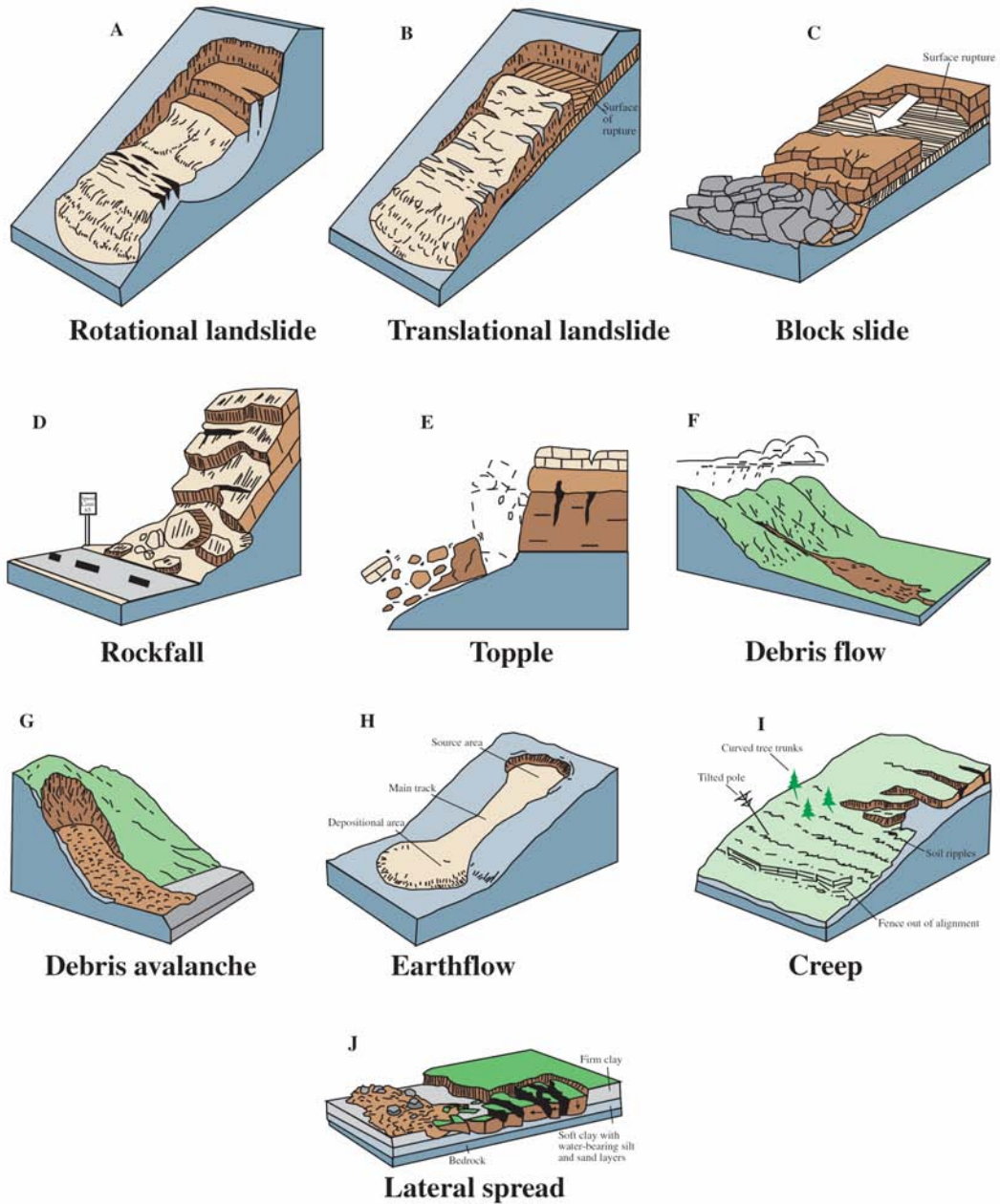
Figure 2.1. Schematic illustrations of the main types of mass movements (USGS 2004).

Table 2.3. Hutchinson's classification of mass movements (Hutchinson 1988).

A. REBOUND
Movements associated with:
1. Man-made excavations
2. Naturally eroded valleys

B. CREEP
1. Superficial, predominantly seasonal creep; mantle creep:
   a. soil creep, talus creep (non-periglacial)
   b. frost creep and gelifluction of granular debris (periglacial)
2. Deep-seated, continuous creep; mass creep
3. Pre-failure creep; progressive creep
4. Post-failure creep

C. SAGGING OF MOUNTAIN SLOPES
1. Single-sided sagging associated with the initial stages of landsliding:
   a. of rotational (essentially circular) type (R-sagging)
   b. of compound (markedly non-circular) type (C-sagging); (i) listric (CL), (ii) bi-planar (CB)
2. Double-sided sagging associated with the initial stages of double landsliding, leading to ridge spreading:
   a. of rotational (essentially circular) type (DR-sagging)
   b. of compound (markedly non-circular) type (DC); (i) listric (DCL), (ii) bi-planar (DCB)
3. Sagging associated with multiple toppling (T-sagging)

D. LANDSLIDES
1. Confined failures:
   a. in natural slopes
   b. in man-made slopes
2. Rotational slips:
   a. Single rotational slips
   b. successive rotational slips
   c. multiple rotational slips
3. Compound slides (markedly non-circular, with listric or bi-planar slip surfaces):
   a. released by internal shearing towards rear; (i) in slide mass of low to moderate brittleness, (ii) in slide mass of high brittleness
   b. progressive compound slides, involving rotational slip at rear and fronted by subsequent translational slide
4. Translational slides
   a. sheet slides
   b. slab slides, flake slides
   c. peat slides
   d. rock slides; (i) planar slides, block slides, (ii) stepped slides, (iii) wedge failures
   e. slides of debris; (i) debris-slides, debris avalanches (non-periglacial), (ii) active layer slides (periglacial)
   f. sudden spreading failures

E. DEBRIS MOVEMENTS OF FLOW-LIKE FORM
1. Mudslides (non-periglacial)
   a. sheets
   b. lobes (lobate or elongate)
2. Periglacial mudslides (gelifluction of clays):
   a. sheets
   b. lobes (lobate or elongate, active and relict)
3. Flow slides
   a. in loose, cohesionless materials
   b. in lightly cemented, high porosity silts
   c. in high porosity, weak rocks
4. Debris flows, very extremely rapid flows of wet debris:
   a. involving weathered rock debris (except on volcanoes); (i) hillslope debris flows, (ii) channelised debris flows, mud flows, mud-rock flows
   b. involving peat; bog flows, bog bursts
   c. associated with volcanoes; lahars; (i) hot lahars, (ii) cold lahars
5. Sturzstroms, extremely rapid flows of dry debris

F. TOPPLES
1. Topples bounded by pre-existing discontinuities:
   a. single topples
   b. multiple topples
2. Topples released by tension failure at rear of mass

G. FALLS
1. Primary, involving fresh detachment of material; rock and soil falls
2. Secondary, involving loose material, detached earlier; stone falls

H. COMPLEX OF MOVEMENTS
1. Cambering and valley bulging
2. Block-type slope movements
3. Abandoned clay cliffs
4. Landslides breaking down into mudslides or flows at the toe:
   a. slump-earthflows
   b. multiple rotational quick-clay slides
   c. thaw slumps
5. Slides caused by seepage erosion
6. Multi-tiered slides
7. Multi-storied slides

2.3 Landslide mechanisms

Even though a simple classification of the mechanisms, causes and forms of landslides is easy, an understanding of more detail of causes and failure mechanisms is needed for improving slope stability modelling. The ability to measure landslide deformation at high precision has revealed extremely variable patterns (Brunsden 1993).

2.3.1 Failure

The development of landslides is influenced by many factors, and the triggering mechanism may be just the final factor that set in motion a mass which was already on the edge of failure. A failure occurs when the disturbing forces that create movement exceed the resisting forces of the material. Hence, factors contributing towards movement can be divided in factors that increase the driving

Table 2.4. Factors contributing to slope failure (Varnes 1978; Selby 1993).

Factors contributing to high shear stress:

- **Removal of lateral support**
  o Stream, water or glacial erosion
  o Subaerial weathering, wetting, drying, and frost action
  o Slope steepness increased by mass movement
  o Quarries and pits, or removal of toe slopes by human activity
- **Increase of loading**
  o Weight of rain, snow talus
  o Fills, waste piles, structures
  o Vegetation
  o Seepage pressure of percolating water
- **Transitory stresses**
  o Earthquakes – ground motions and tilt
  o Vibrations from human activity – blasting, traffic, machinery
- **Removal of underlying support**
  o Undercutting by running water
  o Subaerial weathering, wetting, drying, and frost action
  o Subterranean erosion (eluviation of fines or solution of salts), squeezing out of underlying plastic soils
  o Mining activities, creation of lakes, reservoirs
- **Lateral pressure**
  o Water in interstices
  o Freezing of water
  o Swelling by hydration of clay
  o Mobilization of residual stress
- **Increase of slope angle**
  o Tectonic tilting
  o Volcanic processes

Factors contributing to low shear strength:

- **Physical properties of soil material**
  o Weak materials such as volcanic tuff and sedimentary clays
  o Loosely packed materials
  o Smooth grain shape
  o Uniform grain sizes
- **Weathering effects**
  o Softening of fissured clays
  o Physical disintegration of granular rocks
  o Cation exchange in clays
  o Hydration of clay minerals
  o Drying of clays and shales, creating cracks
  o Solution of cements
- **Effects of pore water**
  o Buoyancy effects
  o Reduction of capillary tension
  o Viscous drag of moving water on soil grains, piping
- **Changes in structure**
  o Spontaneous liquefaction
  o Progressive creep with reorientation of clays
  o Reactivation of earlier shear planes
- **Vegetation**
  o Action of tree roots
  o Removal of trees: reducing normal loads, removing apparent cohesion of tree roots, raising of water tables, increased cracking
- **Geological structure**
  o Discontinuities such as joints, faults, bedding planes, and other planes of weakness
  o Beds of plastic and impermeable soils
  o Layers inclined toward free slope face
  o Slope orientation

forces, and factors that decrease the shear strength of the slope material. An overview of contributing factors is summarised in Table 2.4. The most significant factors are discussed in detail below.

2.3.1.1 Material

The stability behaviour of slopes depends largely on the type of material they consist of. There is a range of different definitions for the terms *rock* and *soil*, dependent upon the interest of the user. For engineering purposes, rock can be defined as a hard, elastic substance which does not significantly soften in water. Its strength is mainly controlled by discontinuities rather than the strength of the grains or crystals. Soft rocks are distinct since their strength is reduced in water and they do not develop continuous joints. A soil is a loose deposit formed from weathering of harder rock. The shear strength of soil material is derived from the contact between particles which transmit the normal and shear forces. These interparticle contacts are primarily due to friction and cohesion (Selby 1993).

2.3.1.2 Geology

As said above, the rock slope stability is largely controlled by discontinuities. They not only reduce the shear strength of the rock, but also control the movement of ground water through the mass. Discontinuities in rock or soil comprise tectonic joints, faults, lithological boundaries and bedding planes (Selby 1993). The main contributing factors to shear strength of persistent joints according to Hencher (1987) are:

- Adhesion;
- Interlocking and ploughing (surface texture);
- Overriding;
- Cohesion.

A particular geologic process is bulging of slopes after stress release, resulting in the development of shear planes. In tectonic active areas, increase of relief influences the orientation of layers and the creation of joints is relevant (Selby 1993).

2.3.1.3 Water

Water is by far the most important contributor to slope failures in soil material and influences slope stability in many ways: capillary tension, buoyancy effects,

aggregation of soil particles, viscous drag on soil grains by seepage, hydration of clay, undercutting of slopes, weight of rain, as an agent in weathering, as soil ice, in spontaneous liquefaction, etc (Selby 1993).

In dry soils the shear strength is entirely supported on the contacts of particles, and hence controlled by cohesion and friction (Equation 2.1).

$$\tau_f = c + \sigma_n \tan\phi$$

(2.1)

Where τ_f is the shear strength, c is the cohesion, σ_n is the normal stress, and φ is the angle of friction.

In moist soils suction due to capillary stresses provides an apparent cohesion, increasing soil strength. In a fully-saturated soil this apparent cohesion is lost and part of the normal stress of the overburden is transferred onto the pore-water, resulting in a decreased effective stress, and hence a decreased soil strength (Equation 2.2). Figure 2.2 shows a graphical representation of a typical relation between pore-water content and associated shear strength.

$$\tau_f = c' + \sigma'_n \tan\phi'$$

(2.2)

Where τ_f is shear strength, c' is the effective cohesion, σ'_n is the effective normal stress (σ_n-u; u is pore-water pressure), and φ' is the effective angle of friction.

In clays, electrostatic bonding between the particles may contribute up to 80 percent of the shear strength, which will decrease extremely when hydrated. In this context the composition of pore-water is also of great importance. Another adverse effect of saturation is the falling apart of aggregations of soil particles, thereby decreasing the internal friction of the soil (Selby 1993).

Seepage is the drag of moving water on soil particles. Seepage changes the pore water pressure, thereby changing the effective stress and hence the shear strength. Where seepage pressure gradients are steep, these may trigger landslides (Selby 1993).

Macropore flow and piping may cause weakening of the soil by detachment of soil particles, and cause a sudden drop in pore pressure through rapid escape of subsurface water (Selby 1993).
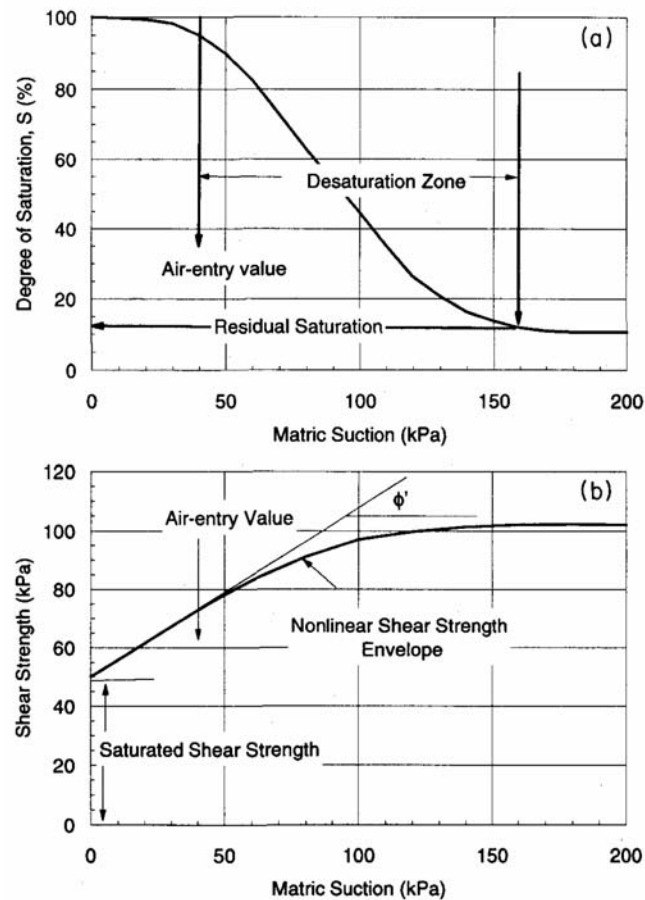
Figure 2.2. A typical soil water retention curve and shear strength behaviour of a soil related to soil water content (Vanapalli et al. 1996).

2.3.1.4 Vegetation

The mechanisms through which vegetation influences slope stability may be broadly classified as either hydrological or mechanical in nature. Mechanical factors arise from the physical interactions of the foliage and root system with the slope material. Hydrological mechanisms involve vegetation as part in the hydrological cycle. The controls of vegetation on slope stability are complex, often interrelated, and therefore difficult to quantify. In general, the hydrological mechanisms that lower pore-water pressure are beneficial, while those that yield increased pore pressures are adverse. Mechanical mechanisms that increase shear resistance in the slope are beneficial; those that increase shear stress are adverse (Figure 2.3). An extensive overview of vegetation and slope stability can be found in Greenway (1987).
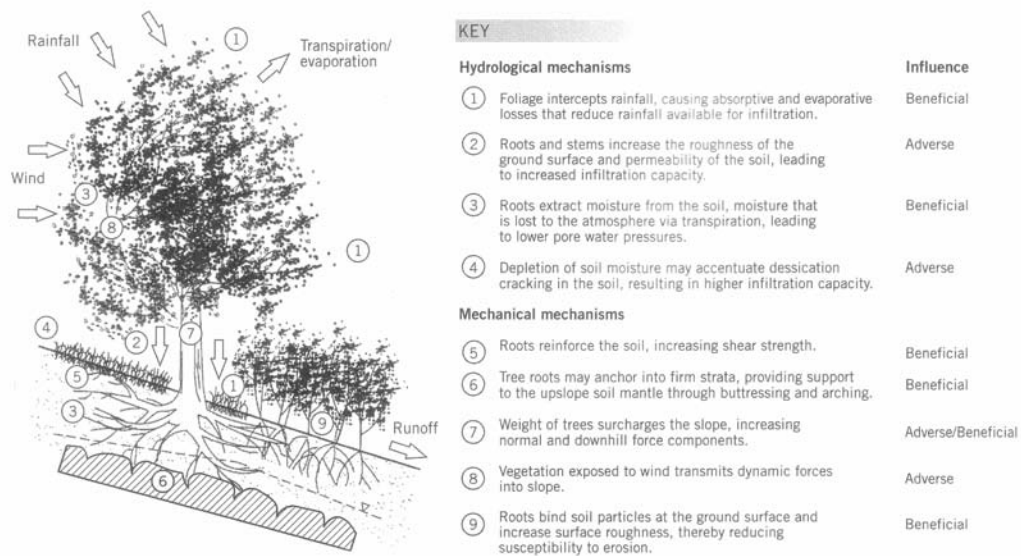
Figure 2.3. Effects of vegetation on slope stability (Greenway 1987).

2.3.1.5 Time

Besides the long-term effects of tectonics, weathering and erosion, the shear behaviour of soils can also be strongly influenced by stress history:

- An overconsolidated soil is caused by larger stresses in the past than at present, with as a result in general stronger and less compressible material (Nash 1984);

- In clays with a low permeability, the movement of water is hindered when the volume changes. It may take years after a change of surface loading for excess pore pressures to dissipate and for effective stresses to reach equilibrium (Nash 1984);

- After the initial failure, the shear strength of material along the slip surface is reduced to its residual value, so that subsequent movement can take place at a lower level of stress (Bell 2003).

2.3.2 Movement

After the initial failure, further movement of the ground mass will take place according to one of the different mechanisms, depending on material characteristics and the amount of energy released. In case of true slide movement, the ground will largely remain intact while moving along a well-defined shear plane. The shear strength along the slip surface is reduced to its residual value, so that subsequent movement can take place at lower levels of stress. In flow-type of movements,

there is not a discrete slip surface present, velocity of the movement varies with depth, and the material is internally disrupted (Varnes 1978). Some characteristic movement types are described in more detail below.

2.3.2.1 Translational slides

A translational slide involves translational motion on a shear plane parallel to the ground surface (see Figure 2.1). The movement is largely controlled by surfaces of weakness within the slope forming material. Translational slides in soil and debris are normally shallow, and therefore susceptible to seasonal changes in groundwater level (Ibsen *et al.* 1996).

In general, the displacement and velocity of translational slides tend to reach higher values than rotational slides, because the movement does not reach a new equilibrium until the bottom of the slope is reached (Sorriso-Valvo & Gullà 1996). As deformation and water-content of the sliding mass frequently increase while moving downslope, slides may progressively develop into flow-type movements (Varnes 1978). Under conditions of low friction, the movement may accelerate rapidly. Processes involved may be fluidisation, cohesionless grain flow, air lubrication, heat generation, steam production, rock fusion and rate of shear effects, leading to devastating velocities up to 350 km/h ($\simeq$100 m/s) and large run-out distances (Sorriso-Valvo & Gullà 1996; Crozier 2004).

2.3.2.2 Rotational slides

In the case of rotational slides, transverse cracks develop and slide mass may disintegrate into several blocks. In the head area, these blocks tilt backwards while sliding downhill. Sliding along the flanks causes longitudinal and diagonal shear stresses, resulting in 'en echelon' cracks in the main body. The lower part of the mass moves over the toe of the failure surface thereby bulging, cambering, overriding and producing transverse tension cracks. Due to a lack of horizontal support, the toe area may develop into a flow or lateral spreading, forming lobes with patterns of radial tension cracks. Movement rates of rotational slides can vary between a few centimetres per year up to several meters per second (Buma & Van Asch 1996). The typical features of rotational slides are illustrated in Figure 2.4.
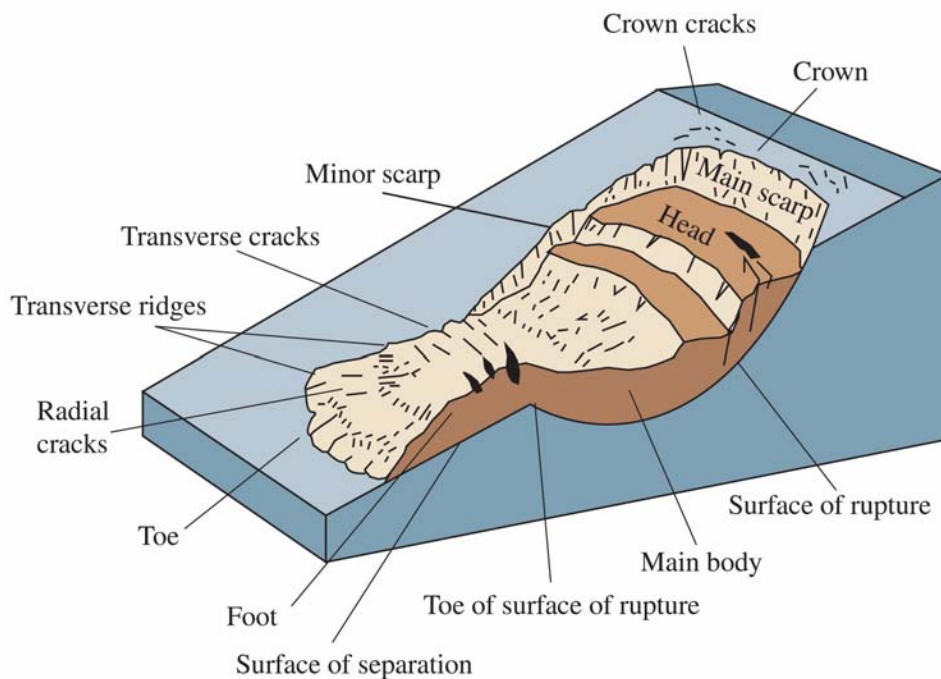
Figure 2.4. Typical features of a rotational landslide (USGS 2004).

Multiple rotational slides involve two or more sliding units, each with a sliding surface intersecting a common basal sliding surface. Usually the removal of horizontal support against the main scarp of the original failure causes the gradual downward movement of the next slice, leaving a new bare scar. The different slices are involved in a complex series of adjustments in the stress pattern, affecting each other by both their downward thrust and removal of underlying support. Consequently, the slices move at different times and rates (Buma & Van Asch 1996).

2.3.2.3 Mudslides

Mudslides are regarded as complex movements, involving rotational failures at the head, subsequent transportation of the debris downslope along a discrete shear surface, and a lobate or elongate accumulation zone (Figure 2.5). Mudslides often display complex crack patterns, with at the head tension cracks and open shears between blocks; in the track complex shear zones, tension cracks or compression ridges; in the lobe radial shears, push ridges and domes appear. Movement rates are generally slow (1-25 m/yr) and seasonal, although extreme events have been recorded at hundreds of meters a day (Brunsden & Ibsen 1996).
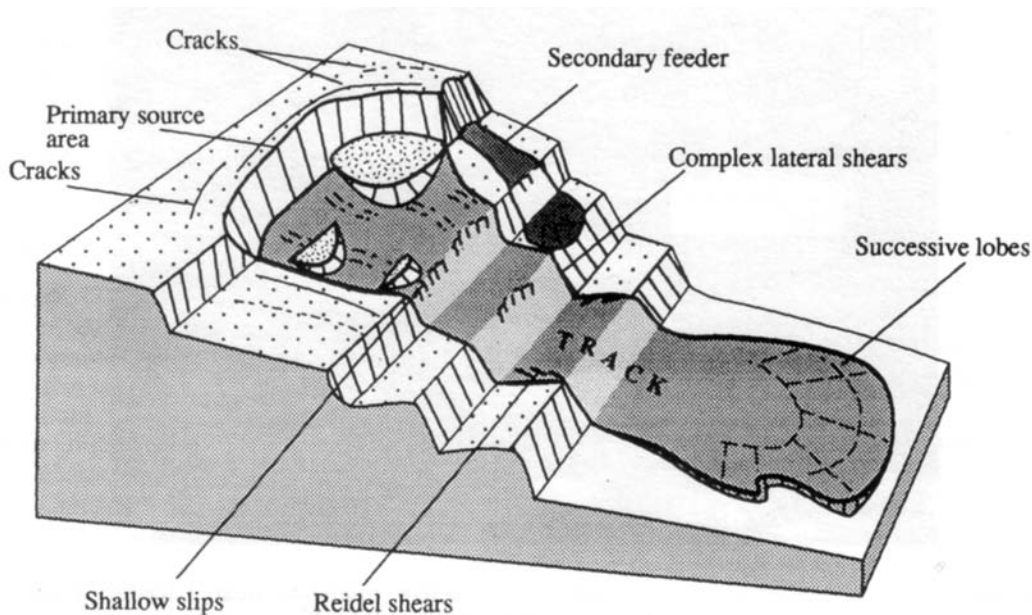
Figure 2.5. Schematic block diagram of a typical mudslide (Brunsden & Ibsen 1996).

The term slump-earthflow essentially represents a shortened mudslide with the same three distinct morphological sections: at the head, down-slipped blocks with surfaces tilted into slope; in the central part a disrupted area with wide transverse fissures; and in the lower part, anticlinal ridges (Brunsden & Ibsen 1996).

2.4 Aerial photographs in landslide studies

Aerial photographs are a generally accepted resource used in landslide studies. They not only provide a metric model from which quantitative measurements can be obtained, but also give a qualitative description of the earth surface. These two capabilities are irrefutably related to each other, as *"one must know what one is measuring"* (Lo 1976).

The application of aerial photographs to landslide investigations provides a number of distinct advantages. Reconnaissance of the study area can greatly benefit from the three-dimensional representation that is provided by stereoscopic viewing, thereby showing relationships between the various landscape elements more obviously than from a ground perspective. Furthermore, photographically based derivatives provide a suitable base on which boundaries can be delineated accurately. In addition, photographs support the efficient planning of field investigations and sampling schemes, without the need for visiting the site physically, which is especially useful in remote and inaccessible areas (Crozier

1984; Van Zuidam 1985). A final and important advantage is the quantitative topographic information contained, that can be unlocked by appropriate photogrammetric techniques. Quantitative use of aerial photographs creates some difficulties, such as the requirement of experienced analysts and appropriate equipment, combined with sufficient knowledge of the site under investigation (Lo 1976).

Air photos can be used in various stages of landslide investigations (Mantovani *et al.* 1996):

- Detection and classification of landslides; when properly interpreted air photos allow the identification of diagnostic surface features, such as morphology, vegetation cover, soil moisture, and drainage pattern.

- Monitoring the activity of existing landslides; recent photographs can be compared with historical imagery to assess landslide conditions over different periods of time and allow the progressive development to be examined.

- Landslide hazard mapping; air photos can be used to delimit terrain units and map the controlling factors affecting slope stability.

Aerial photo-interpretation (API) and geomorphological mapping are important techniques for obtaining qualitative data from aerial photographs, and therefore described in the following sections. The photogrammetric techniques needed for extraction of quantitative data are described in Chapter 3.

2.4.1 Aerial Photograph Interpretation (API)

The value of API for analysing slope stability has been reported by many investigators (e.g. Rib & Liang 1978; Brunsden & Prior 1984; Soeters & Van Westen 1996). The interpretation of photographs for any purpose relies on several basic characteristics of the surface. These are tone, texture, pattern, shape, context and scale, all qualitative attributes, and their use very much a matter of experience and personal bias (Drury 1987):

- Tone refers to colour or relative brightness of the surface making up the scene, expressed as different grey-levels in black-and-white photographs. It is related to reflectance properties of the surface material, illumination conditions (therefore absolute tone is of less use than relative tonal difference between different objects), but also affected by image processing and printing.

- Texture is a combination of the magnitude and frequency of tonal change in an image. Scale and resolution determine which features dominate texture.

- Pattern is the result from the spatial arrangement of different tones and textures which make up the image, originated by the arrangement of vegetation, topographic features, drainage channels or geological structure.

- Interpretation of particular tones, textures, patterns and shapes, always depends on their context, i.e. location relative to known terrain attributes, and scale.

Obviously, tone, texture, pattern and shape may change depending on the time of day and year of the image acquisition, due to illumination conditions, vegetation cover, and soil moisture content.

The quality of API is affected by a number of factors, which can be separated in four categories: photographic parameters, natural factors, equipment and analysis techniques, and the qualification of the interpreter. These factors are further described below.

2.4.1.1   Photographic parameters

Natural colour and panchromatic (black-and-white) films are the most widely available film types. Colour film is especially valuable for outlining differences in soil conditions, drainage and vegetation. Colour infrared films are most suitable for detecting landslides, mainly due to the capability of identifying the presence of water and consequently show the vigour of vegetation cover (Norman *et al.* 1975). Panchromatic films, on the other hand, provide a better image resolution (Lo 1976) and are generally less expensive. Most historical imagery is of this form, although resolution tends to degrade with increasing photo age due to developments in photographic emulsion that have subsequently occurred.

A typically available format is 9 x 9 inch (23 x 23 cm) vertical photography, taken with an aerial mapping camera. Successive photographs in a flight strip usually have an overlap of 60 percent to provide stereoscopic coverage. Oblique photographs can provide a better view on steep slopes and cliffs (Rib & Liang 1978), and provide a more familiar perspective for the less experienced interpreter (Chandler 1989).

Landslide features are most frequently recognised by a combination of morphology and tone or pattern, which confirms the importance of using stereoscopic viewing (Norman *et al.* 1975). Vertical exaggeration, when viewing stereoscopically, can be enhanced if a super wide angle lens is used during photo acquisition. The lower flying height increases the base/distance ratio. However, this may create problems of 'dead ground' on far side of hills and in narrow valleys (Norman *et al.* 1975).

The ability to identify landslide features improves with larger scales. For classification purposes, larger scale is required than for detection, as individual elements within the landslide body should be recognisable (Mantovani *et al.* 1996). Small-scale photographs are useful in determining regional spatial distribution of variables affecting landsliding, whereas large-scale photographs support landslide inventory and analysis activities (Soeters & Van Westen 1996). Soeters & Van Westen (1996) suggest 1/15,000 as the optimum scale for analysing landslides, and consider 1/25,000 as the smallest useful scale. Norman *et al.* (1975) quote 1/5,000 as an optimum scale.

The time of the day when photographs are taken determines the length of shadows. In general, photographs taken when the sun is high are best for interpretation. However, in areas of low topography, the relief will be enhanced by long shadows (Norman *et al.* 1975). The time of the year is of importance regarding drainage and vegetation conditions (Norman *et al.* 1975; Soeters & Van Westen 1996).

The quality of photographs depends on the various processes the images go through. (Norman *et al.* 1975) use the following (subjective) criteria for assessing photo quality: sharpness, over or under exposure, cloud cover, shadow and print quality.

Recently, rapid developments have taken place in the field of airborne digital sensors (e.g. Fricker *et al*. 2000; Hinz & Heier 2000), but a common way of obtaining digital imagery remains through scanning the original film (see Section 3.6.1). Modern software packages allow digital images to be easily adjusted to the needs of the user, for example zooming in on particular areas or enhancing the contrast.

2.4.1.2   Natural factors

Brardinoni *et al.* (2003) compared the results of a landslide inventory in a forested area, by API and field surveying. Their study gave evidence that a significant proportion of the landslides was not identified on photographs. Factors affecting landslide visibility appeared to be, in order of importance: land use, gully relation (deposited material is likely to be washed away when directly connected to drainage network), slope gradient, valley width, slope position and stream connection.

Optimal conditions for detecting anomalies in vegetation may be expected in either the very early or very late stages of the growing season. Differences in drainage conditions are most pronounced shortly after the start of the wet season or shortly after the snowmelt period in spring (Soeters & Van Westen 1996).

It is obvious that weather conditions will have an important influence on the photo quality: clouds and snow cover may obscure the ground surface, haze decreases contrast, and solar angle influences shadowing (see previous section, Rib & Liang 1978).

2.4.1.3   Experience of the interpreter & analysis techniques

The quality of API is also influenced by the human interpreter, and his/her knowledge of the phenomena and processes that are being studied. A higher 'reference level' (Tait 1970) will lead to a larger number of features that will be recognised. Various authors have shown the large subjective element in photo-interpretation by comparing maps of the same landslide area, but created by different persons. Identifying the exact positions of a landslide feature can be difficult, especially delineating the boundaries (Chandler 1989). Moreover, different classes can be assigned to a specific feature, due to different interpretation. Obviously, different mapping systems and legends can lead to very different maps (Van Westen *et al.* 1999).

Van Westen (1993) demonstrated the subjectivity in API by comparing geomorphological maps of a landslide-affected area in Colombia, created by four different teams. Only 10% of the area was similarly mapped by all groups, hence the overall mapping uncertainty was as much as 90%. The author concluded that experience of the interpreter and the amount of time available for ground-checking are fundamental for producing reliable geomorphological maps. Such a view is supported by Carrara *et al.* (1995) who described five case-studies in California and

Italy, revealing discrepancies ranging from 53-78% in mapping landslides from aerial photographs.

2.4.2 Geomorphological mapping

A useful tool in landslide studies is geomorphological mapping. Geomorphological maps are transmitters of information about the form, origin, age and distribution of landforms together with their formative processes, rock type and surface materials (Brunsden *et al.* 1975). They are not only a way of presenting data, but also the result of a method of research, revealing associations of landforms, which is essential for understanding of both individual landforms and landscapes (De Graaff *et al.* 1987). Geomorphological studies can recognize past landslide activity, assess slope stability conditions and identify potentially unstable areas (Al-Dabbagh & Cripps 1987; Van Westen & Getahun 2003). The great value of geomorphological maps in hazard assessment, particularly at the reconnaissance and site investigation stages of engineering projects, has been demonstrated by various authors (e.g. Brunsden *et al.* 1975; Hansen 1984a; Cooke & Doornkamp 1990; Soeters & Van Westen 1996). Small scale geomorphological surveys are rapid and inexpensive techniques for reconnaissance of large areas. Large scale geomorphological plans, at the site investigation stage, provide detailed information on stability conditions, slope steepness, bedrock characteristics, drainage conditions and vegetation cover (Brunsden *et al.* 1975).

The first step in a comprehensive geomorphological survey is identification and mapping of geomorphic units by API. Most of the morphology can be identified and many questions of morphogenesis answered, slope angles estimated and classified, relative relief determined, etc. During the second step, a field work is carried out to check the accuracy of the photo-interpretation and map small features (Hayden 1986).

A general geomorphological map can emphasize different aspects (Van Zuidam 1985):

- Morphology – describing the general relief, either qualitatively (in terms as plains, hills, mountains, plateaus, etc) or quantitatively (e.g. slope steepness, height, exposure, ruggedness, etc);

- Morphogenesis – describing the origin and development of landforms and processes acting on them;

- Morphochronology – relative and absolute dating of the landforms;

- Morphoarrangement – describing the spatial arrangements and interrelationships of various landforms and processes.

These different aspects can be depicted in the map by coloured area symbols, patterns, and line symbols, depending on the importance that is assigned to each aspect.

An example of a purely morphological legend was developed by Savigear (1965). Plane and curved elements of a slope are separated by discontinuities, either slope breaks or more gentle inflections. The nature of the change of slope is shown on the map by standard symbols, and the elements themselves can be classified by their slope gradient (Figure 2.6).

The geomorphological survey system developed by Van Zuidam (1985) distinguishes the highest level (coloured areas) on the basis of morphogenesis. Morphology is displayed as line and letter symbols in grey and brown; morphochronology indicated by letters and numbers in black; certain important morphometric and typical geological features can be represented by black line symbols; and coloured line symbols are used for morphodynamics. The system was designed for multipurpose (hence, applied maps can be produced, highlighting specific aspects) and applicable on all scales (hierarchical structure allows generalisation).

De Graaff *et al.* (1987) developed a mapping system, designed for large-scale (1/10,000) mapping of high-mountain terrain (Figure 2.7). Their maps contain three major sources of information: form and relief (line symbols), materials (screen-like symbols) and processes (colour of line symbols).
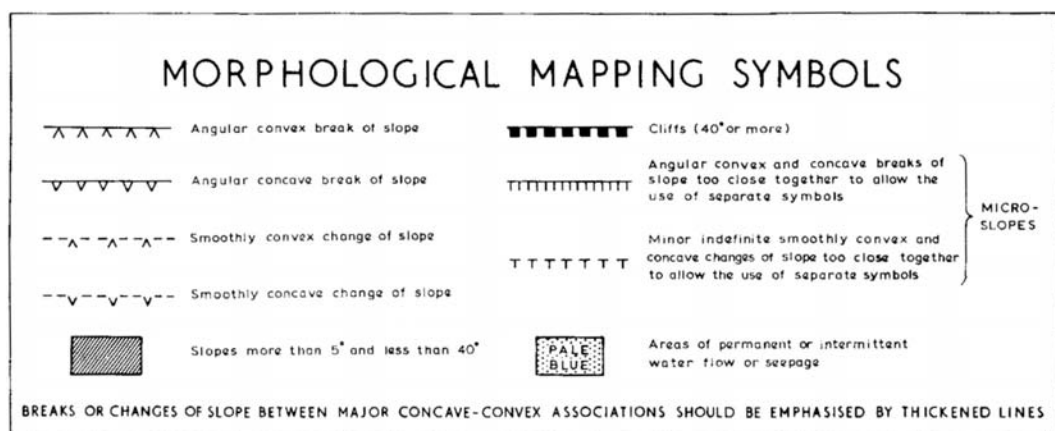
Figure 2.6. Example of a purely morphometric mapping legend (Savigear 1965).

Figure 2.7. Example of a geomorphological legend containing morphometric elements, material, and genesis (De Graaff et al. 1987).

2.4.3 Recognition of landslides

Recognition of landslides and identification of the type and causes of movement are important in the development of procedures for their prevention and correction (Rib & Liang 1978). The nature of surface features and their positions and orientation, are indicative of different kinds of deformation. Their mapping may help in understanding of the behaviour of the landslide (Parise 2003). Based on diagnostic features, statements can be made on the type of movement, degree of activity and depth of movement (Mantovani *et al.* 1996). It is possible to discriminate between direct and indirect indicators of deformation. Direct indicators are features directly connected to structural discontinuities affecting the landslide material, such as bulging, minor failures in embankments, disturbed infrastructure, cracks, and minor scarps. Indirect indicators include changes in the hydrography or vegetation cover at the landslide surface (Parise 2003).

The interpretation of landslides from aerial photographs is based mainly on characteristic morphology, vegetation and drainage conditions of the slope. Because the information from aerial photographs is not as detailed as can be obtained from field evidence, a simplified classification has to be used; local adaptations can be justified to prevent ambiguities (Soeters & Van Westen 1996). Soeters & Van Westen (1996) provide an overview of terrain features associated with landslides and their characterisation on aerial photographs (see Table 2.5). The landslide types that can be distinguished according to these characteristics are summarised in Table 2.6. Figure 2.8 and Figure 2.9 illustrate some distinctive landslide features visible on aerial photographs (see also Figure 5.32).

2.4.4 *Monitoring of landslides*

The importance of large-scale geomorphological mapping and especially its repetition in time, in the study of active mass movements is stressed by Parise (2003): a combination of detailed multi-temporal mapping of surface features, indirect indicators of deformation and displacements may result in better understanding of the landslide and its zonation in different elements, characterised by different styles of deformation.

Several studies demonstrated the value of monitoring surface displacements for investigating the landslide mechanisms. Petley (2004) demonstrated that failures are preceded by accelerating deformation patterns in the slope, which permit prediction of future behaviour of unstable slopes. It was also shown that the processes occurring in the basal region of a landslide can be assessed from surface movement patterns. Petley *et al.* (2005) used detailed records of surface displacement to distinguish different movement patterns in the Tessina landslide. The movement patterns appeared to be in close correspondence with independently defined morphological assessments of the landslide complex. Surface movement patterns have also been used to analyse strains in the landslide body (e.g. Baum *et al.* 1998; Rutter *et al.* 2003). In these studies, zones of compression were associated with a downslope decrease of movement rates whereas zones of extension exhibited increasing rates.

When the sliding ground mass moves as a rigid body, the movement at the surface can be considered parallel to the shear surface. Hence, when surface movement directions on the landslide and the positions of the toe and backscar are known, the position of the slip surface may be estimated. Carter & Bentley (1985)

Figure 2.8. Aerial photograph of the Ruamahanga slump (New Zealand) showing some distinctive features (Crozier 1984).

Figure 2.9. Aerial photograph of the Black Ven landslide (UK) showing distinct features of a mudslide system (Ordnance Survey: © Crown copyright).

Table 2.5. Morphologic, vegetation and drainage features characteristic of landslide processes and their photographic characteristics (Soeters & Van Westen 1996).

Terrain features	Relation to slope instability	Photographic characteristics
Morphology		
Concave/convex slope features	Landslide niche and associated deposit	Concave/convex anomalies in stereo model
Steplike morphology	Retrogressive sliding	Steplike appearance of slope
Semicircular backscarp and steps	Head part of slide with outcrop of failure plane	Light-toned scarp, associated with small, slightly curved lineaments
Back-tilting of slope facets	Rotational movement of slide blocks	Oval or elongated depressions with imperfect drainage conditions
Hummocky and irregular slope morphology	Microrelief associated with shallow movements or small retrogressive slide blocks	Coarse surface texture, contrasting with smooth surroundings
Infilled valleys with slight convex bottom, where V-shaped valleys are normal	Mass movement deposit of flow-type form	Anomaly in valley morphology, often with lobate form and flow pattern on body
Vegetation		
Vegetational clearances on steep scarps, coinciding with morphological steps	Absence of vegetation on headscarp or on steps in slide body	Light-toned elongated areas at crown of mass movement or on body
Irregular linear clearances along slope	Slip surface of translational slides and track of flows and avalanches	Denuded areas showing light tones, often with linear pattern in direction of movement
Disrupted, disordered, and partly dead vegetation	Slide blocks and differential movements in body	Irregular, sometimes mottled grey tones
Differential vegetation associated with changing drainage conditions	Stagnated drainage on back-tilting blocks, seepage at frontal lobe, and differential conditions on body	Tonal differences displayed in pattern associated with morphological anomalies in stereo model
Drainage		
Areas with stagnated drainage	Landslide niche, back-tilted landslide blocks, and hummocky internal relief on landslide body	Tonal differences with darker tones associated with wetter areas
Excessively drained areas	Outbulging landslide body (with differential vegetation and some soil erosion)	Light-toned zones in association with convex relief forms
Seepage and spring levels	Springs along frontal lobe and at places where failure plane outcrops	Dark patches sometimes in slightly curved pattern and enhanced by differential vegetation
Interruption of drainage lines	Drainage anomaly caused by headscarp	Drainage line abruptly broken off on slope by steeper relief
Anomalous drainage pattern	Streams curving around frontal lobe or streams on both sides of body	Curved drainage pattern upstream with sedimentation or meandering in (asymmetric) valley

Table 2.6. Characteristic features of different types of mass movements visible on aerial photographs (Soeters & Van Westen 1996).

Type of movement	Characterisation based on morphological, vegetation and drainage aspects visible on stereo images	
Fall and topple	Morphology:	Distinct rock wall or free face in association with scree slopes (20 to 30 degrees) and dejection cones; jointed rock wall (>50 degrees) with fall chutes
	Vegetation:	Linear scars in vegetation along frequent rock-fall paths; vegetation density low on active scree slopes
	Drainage:	No specific characteristics
Sturtzstrom	Morphology:	Extremely large (concave) scars on mountain, with downslid blocks of almost geological dimensions; rough, hummocky depositional forms, sometimes with lobate front
	Vegetation:	Highly irregular/chaotic vegetational conditions on accumulative part, absent on sturtzstrom scar
	Drainage:	Irregular disordered surface drainage, frequent damming of valley and lake formed behind body
Rotational slide	Morphology:	Abrupt changes in slope morphology characterised by concave (niche) and convex (runout lobe) forms; often steplike slopes; semilunar crown and lobate frontal part; back-tilting slope facets, scarps, hummocky morphology on depositional part; D/L ration 0.3 to 0.1; slope 20 to 40 degrees
	Vegetation:	Clear vegetational contrast with surroundings, absence of land use indicative for activity; differential vegetation according to drainage conditions
	Drainage:	Contrast with nonfailed slopes; bad surface drainage or ponding in niches or back-tilting areas; seepage in frontal part of runout lobe
Compound slide	Morphology:	Concave and convex slope morphology; concavity often associated with linear grabenlike depression; no clear runout but gentle convex or bulging frontal part; back-tilting facets associated with (small) antithetic faults; D/L ratio 0.3 to 0.1, relatively broad in size
	Vegetation:	As with rotational slides, although slide mass will be less disturbed
	Drainage:	Imperfect or disturbed surface drainage, ponding in depressions and in rear part of slide
Translational slide	Morphology:	Joint controlled crown in rock slides, smooth planar slip surface; relatively shallow, certainly in surface material over bedrock; D/L <0.1 and large width; runout hummocky, rather chaotic relief, with block size decreasing with larger distance
	Vegetation:	Source area and transportational path denuded, often with lineations in transportation directions; differential vegetation on body in rock slides; no landuse on body
	Drainage:	Absence of ponding below crown, disordered or absent surface drainage on body; streams deflected or blocked by frontal lobe

Table 2.6 (continued).

Lateral spread	Morphology:	Irregular arrangement of large blocks tilting in various directions; block size decreases with distance and morphology becomes more chaotic; large cracks and linear depressions separating blocks; movement can originate on very gentle slopes (<10 degrees)
	Vegetation:	Differential vegetation enhancing separation of blocks; considerable contrast with unaffected areas
	Drainage:	Disrupted surface drainage; frontal part of movement is closing off valley, causing obstruction and asymmetric valley profile
Mudslide	Morphology:	Shallow concave niche with flat lobate accumulative part, clearly wider than transportation path; irregular morphology contrasting with surrounding areas; D/L ratio 0.05 to 0.01; slope 15 to 25 degrees
	Vegetation:	Clear vegetational contrast when fresh; otherwise differential vegetation enhances morphological features
	Drainage:	No major drainage anomalies beside local problems with surface drainage
Earth flow	Morphology:	One large or several smaller concavities, with hummocky relief in source area; main scars and several small scars resemble slide type of failure; path following stream channel and body is infilling valley, contrasting with V-shaped valleys; lobate convex frontal part; irregular micromorphology with pattern related to flow structures; slope >25 degrees; D/L ration very small
	Vegetation:	Vegetation on scar and body strongly contrasting with surroundings, land use absent if active; linear pattern in direction of flow
	Drainage:	Ponding frequent in concave upper part of flow; parallel drainage channels on both sides of body in valley; deflected or blocked drainage by frontal lobe
Flowslide	Morphology:	Large bowl-shaped source area with steplike or hummocky internal relief; relatively great width; body displays clear flow structures with lobate convex frontal part (as earth flow); frequently associated with cliffs (weak rock) or terrace edges
	Vegetation:	Vegetational pattern enhancing morphology of scarps and blocks in source area; highly disturbed and differential vegetation on body
	Drainage:	As with earth flows, ponding or disturbed drainage at rear part and deflected or blocked drainage by frontal toe
Debris avalanche	Morphology:	Relatively small, shallow niches on steep slopes (>35 degrees) with clear linear path; body frequently absent (eroded away by stream)
	Vegetation:	Niche and path are denuded or covered by secondary vegetation
	Drainage:	Shallow linear gully can originate on path of debris avalanche
Debris flow	Morphology:	Large amount of small concavities (associated with drainage system) or one major scar characterising source area; almost complete destruction along path, sometimes marked by depositional levees; flattish desolate plain, exhibiting vague flow structures in body
	Vegetation:	Absence of vegetation everywhere; recovery will take many years
	Drainage:	Disturbed by main body; original streams blocked or deflected by body

presented a technique to graphically reconstruct the shear surface, based on movement data from a number of monitoring survey stations. Tests on three landslips in South Wales, in which the reconstructed position of the slip surface was compared with evidence from site investigations, showed the technique is reasonable accurate, depending on the accuracy of the survey data.

Monitoring requires accurate quantitative data and therefore rigorous photogrammetric techniques need to be applied (Chandler & Cooper 1989). Advantages of using photogrammetry instead of field instrumentation for monitoring displacements are the complete field of view covered, rather than a set of pre-located targets; inaccessible slope faces can be surveyed (Franklin 1984; Brunsden 1993); and historical photographs can be used to measure past movements (e.g. Crozier 1986; Chandler 1989; Hapke 2005). The photogrammetric techniques are extensively described in Chapter 3.

2.4.5 Landslide hazard mapping

The term hazard is defined by Varnes (1984) as "*the probability of occurrence within a specified period of time and within a given area of a potentially damaging phenomenon*". Landslide hazard zonation requires a detailed knowledge of the active processes in an area, and the factors leading to the occurrence of the potential phenomenon (Soeters & Van Westen 1996). Ideally, a map of slope instability hazard should provide information on the spatial probability, temporal probability, type, magnitude, velocity, run-out distance, and regression limit of the mass movements predicted in a certain area (Hartlen & Viberg 1988). The probability of occurrence requires an analysis on the recurrence of triggering factors, and their relation to landslides. Usually hazard maps rather express the susceptibility to the phenomenon on the basis of local terrain conditions (Soeters & Van Westen 1996). Varnes (1984) warns estimation of the degree of potential hazard in areas often involves simple and subjective evaluation of the terrain, and the overall accuracy of their mapping remains unevaluated.

Different approaches can be applied in landslide hazard mapping. These are based on three fundamental assumptions (Varnes 1984):

- The past and present are keys to the future – natural slope failures will most likely be in geological, geomorphological, and hydrological situation that have led to past and present failures;

- The main conditions that cause landsliding can be identified – the basic factors controlling slope stability should be mapped and correlated with past failures;

- Degrees of hazard can be estimated – estimation of the relative contribution of conditions that cause slope instability, providing a summery of potential hazard.

Slope stability is commonly related to landforms and relief patterns, hence geomorphological and geological mapping techniques are very useful for determining the distribution of relevant parameters.
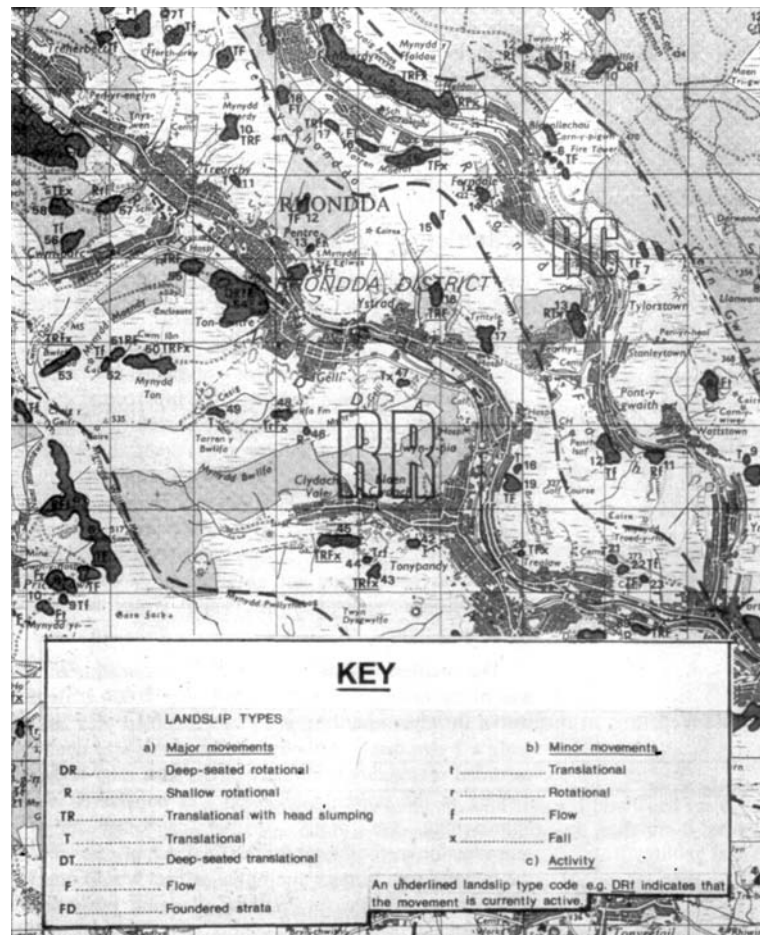
Figure 2.10. Example of a landslide distribution map (Conway et al. 1980).

The various methodological approaches differ in the way of estimating the degree of landslide hazard (Soeters & Van Westen 1996):

- Landslide inventory – providing a spatial distribution of mass movements (Figure 2.10);

- Heuristic approach – classification of the hazard, based on expert knowledge on the causal factors of slope instability. Problem is the reproducibility of the maps;

- Statistical approach – the combination of factors that have led to landslides in the past are determined statistically and used to predict future activity (Figure 2.11). This approach provides a higher degree of objectivity;

- Deterministic approach – the most sophisticated methodology, based on slope stability modelling. These models require reliable input data, hence only applicable when the geomorphological and geological conditions are fairly homogeneous over the entire study area, and the landslides typically simple.
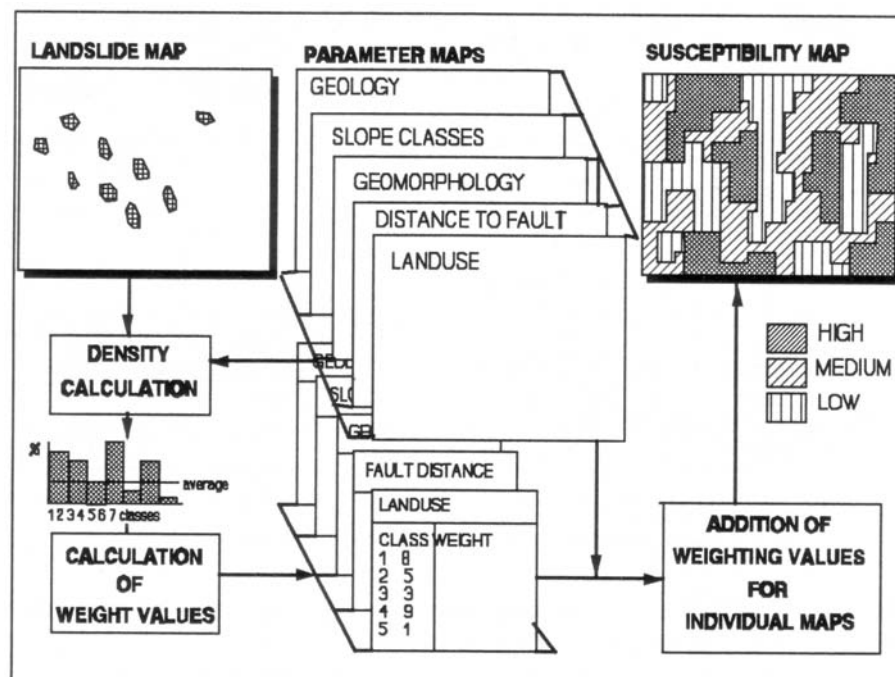
Figure 2.11. Schematic representation of using statistical analysis for landslide hazard mapping, resulting in a map differentiating between three degrees of potential hazard (Van Westen 1993).

API is a powerful tool in landslide hazard mapping. Landslide inventories and geomorphological units can be easily delineated from aerial photographs, and large areas can be mapped in an efficient way. Soeters and Van Westen (1996) show that many of the input data for landslide hazard analysis can be readily derived from aerial photographs.

2.5 Summary

This chapter started with a summary of the various definitions and terminologies of landslides commonly in use. The main mechanisms of landslides were briefly discussed and the many factors controlling failure and movement.

It was shown that aerial photography is useful at various stages of landslide management: detection and classification of landslides, monitoring of their progressive development, and landslide hazard mapping. Detection of landslide features and mapping their controlling factors involves qualitative interpretation of aerial photographs (API). The reliability of these interpretations depends not only on the quality of the photographs and the characteristics of the terrain, but also largely on the experience of the interpreter, as it is a highly subjective technique.

Monitoring of landslide movements requires quantitative data. Patterns of surface movement provide important information on the mechanisms. Photogrammetry has the advantage that inaccessible terrain can be measured without contact. Another important and unique aspect of distinct value to understanding landslide dynamics, is that past movements can be measured from archival imagery, as will be described in the next chapter.

Chapter Three

3 Digital photogrammetric techniques

Photogrammetry is an effective tool in geomorphological studies (Lane *et al.* 1993; Chandler 1999). Surface morphology can be accurately measured in three dimensions from stereo-photographs. Multi-temporal images can be used to measure surface changes, and hence quantify the morphological effects of underlying processes. The photographic archive provides an extensive source of historical data allowing long-term analysis, an important advantage over other monitoring systems. Recent developments in digital photogrammetry have resulted in increased appreciation of photogrammetric techniques (Lane *et al.* 1994).

In this chapter, first some background information concerning the development of photogrammetry will be provided. Then, the main principles in digital photogrammetric processing will be explained: aerial triangulation, digital image matching, automated DEM extraction and orthophoto generation. Issues concerning data quality will be discussed and finally, applications of photogrammetry in landform change research will be reviewed.

3.1 Development of photogrammetry

The development of photogrammetry started soon after the invention of photography in the 19th century. The developments can be separated into four

phases, each following a critical stage of technological development (Konecny 1985):

1. Plane table photogrammetry (1850-1900) – Soon after invention of the camera, Colonel Laussedat, of the French army, utilised photographic images to derive topographic information. Soon, the techniques proved useful in many other applications such as architecture, archaeology, and glacial surveys

2. Analogue photogrammetry (1900-1960) – The use of stereoscopy and the invention of the airplane formed the basis for analogue photogrammetry. Mechanical-optical instruments made accurate surveys more practicable, while aerial survey cameras allowed taking vertical photographs with regular overlap. Due to these developments 'mapping' was established as the main application of photogrammetry.

3. Analytical photogrammetry (1960-1985) – Although the principles of analytical restitution were already developed by Sebastian Finsterwalder in 1899, the process only became practicable after development and mass-production of the computer. The first analytical plotter was introduced in 1957 by Helava.

4. Digital photogrammetry (1985-present) – increased computational power allows automated digital processing of photographs.

Recent developments in computer technology have had a significant impact upon photogrammetry. Use of analytical photogrammetric methods remain expensive, complex and require a significant amount of experience (Lo 1976; Brunsden 1993; Chandler 2001). Advances in automated digital photogrammetry now allow high-resolution quantitative data to be extracted automatically (Walker & Petrie 1996; Brunsden & Chandler 1996). It has been shown that digital systems outperform analytical systems both in terms of data collection time and overall accuracy (Baily *et al.* 2003). Additional advantages include (Chandler 1999):

• Applicable at any scale;

• Allowing creation of high-density DEMs of consistent precision;

• Commercial software available at competitive rates;

• Software runs on relatively cheap UNIX workstations and PCs;

- User-friendly interface of software makes the techniques available to non-specialists. However, Baily *et al*. (2003) state that a high level of expertise is still required to avoid simple errors.

3.2 Analytical restitution

Restitution is the procedure of establishing appropriate functional and stochastic models for describing the relationship between ground and photo coordinates. In many software systems analytical photogrammetry is the basis for the restitution. Analytical photogrammetry entails the formulation of the mathematical relationship between measured ground and photo coordinates, and camera parameters.

3.2.1 *The collinearity condition*

The main principle of analytical photogrammetry is the concept of collinearity, in which an object, the projection centre and its corresponding point appearing on the focal plane of the camera, all lie along a straight line (Figure 3.1). Based on this principle, three-dimensional object space coordinates can be extracted from a stereo-pair of photographs, provided that the interior and exterior orientation of the camera at the moment of exposure are known. However, a bundle of light rays will never pass from object through the camera lens system and onto the imaging device in a perfectly straight line. Therefore, for accurate photogrammetric work corrections have to be made for lens distortion, atmospheric refraction and earth curvature (Wolf & Dewitt 2000).

3.2.1.1 Interior orientation

The internal geometry of a camera is defined by the elements of interior orientation, or camera constants. For aerial mapping cameras, calibration certificates are usually provided by the camera manufacturer and include the location of the principal point, focal length, photo coordinates of the fiducial marks, and measures of lens distortion (Wolf & Dewitt 2000). The focal length is the distance from the principal point to the perspective centre. The principal point is defined as the point where a line from the rear nodal point of the camera lens and perpendicular to the focal plane intersects the focal plane (Wolf & Dewitt 2000). More simply, it is the point where the camera axis intersects the focal plane. Realisation of the principal point is assisted by fiducial marks which are superimposed on the image and have a known position relative to the principal

point. When using scanned imagery, a transformation is needed to define the relation between image (pixel) and photo coordinates (Figure 3.2). An affine transformation is normally used and is also able to compensate for film shrinkage due to aging, and variable with direction (Equation 3.1, Leica Geosystems 2003).
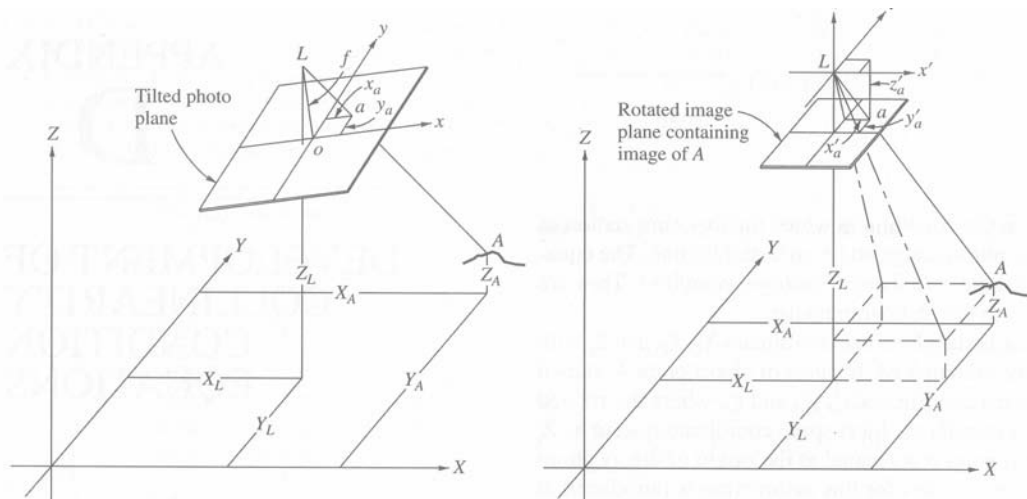
Figure 3.1. The collinearity condition (left); photo coordinate system rotated parallel to object space coordinate system (right) (Wolf & Dewitt 2000).
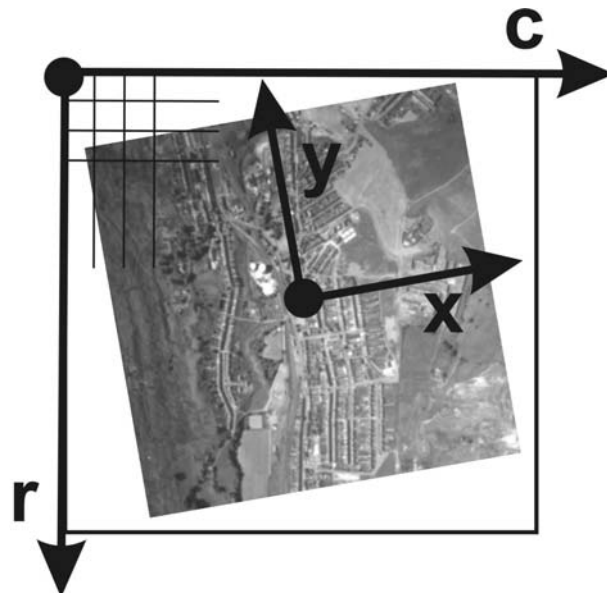
Figure 3.2. Image coordinates (column, row) versus photo coordinates (x, y).

$$x = a_1 + a_2 c + a_3 r$$
$$y = b_1 + b_2 c + b_3 r$$

$$(3.1)$$

Where x and y are photo coordinates associated with the calibrated fiducial marks; c and r are the image coordinates (column, row) of the measured fiducial marks; a_1, a_2, a_3, b_1, b_2, and b_3 are the six coefficients of the affine transformation.

3.2.1.2 Exterior orientation

The elements of exterior orientation define the position and angular orientation of the camera during image capture. Positional elements X_0, Y_0 and Z_0 define the position of the perspective centre in ground space coordinates; the rotational elements (ω, φ and κ) define the relationship between the ground coordinate and the photo coordinate system. The rotation parameters are derived by applying sequentially a rotation of ω about the x-axis, φ about the y-axis and κ about the z-axis. After applying these rotations (Equation 3.2), the photo coordinates are parallel to the ground coordinate system and can be entered into the collinearity equations.

$$x' = m_{11} x + m_{12} y + m_{13} z$$
$$y' = m_{21} x + m_{22} y + m_{23} z$$
$$z' = m_{31} x + m_{32} y + m_{33} z$$

$$(3.2)$$

Where x, y, z are the original photo coordinates; x', y', z' are rotated photo coordinates, parallel to the ground coordinate system (see figure 3.1); m's are the rotational parameters, all function of the rotation angles ω, φ and κ (see Wolf & Dewitt 2000 for details).

3.2.1.3 Collinearity equations

The basic collinearity equations are simply based on similar triangles, illustrated in Figure 3.1 and Equation 3.3.

$$\frac{x'_a}{X_A - X_0} = \frac{y'_a}{Y_A - Y_0} = \frac{f}{Z_A - Z_0}$$

$$(3.3)$$

Where x'_a and y'_a are rotated photo coordinates of point a (from equation 3.2); f is the focal length; X_A, Y_A, and Z_A are ground space coordinates of object A; X_0, Y_0, and Z_0 are ground space coordinates of the perspective centre.

Combination and rearrangement of Equations 3.2 and 3.3 gives the collinearity equations (Equation 3.4). Details about the derivation of these equations can be found in standard textbooks (e.g. Wolf & Dewitt 2000).

$$x_a - x_0 = -f\left[\frac{m_{11}(X_A - X_0) + m_{12}(Y_A - Y_0) + m_{13}(Z_A - Z_0)}{m_{31}(X_A - X_0) + m_{32}(Y_A - Y_0) + m_{33}(Z_A - Z_0)}\right]$$
$$y_a - y_0 = -f\left[\frac{m_{21}(X_A - X_0) + m_{22}(Y_A - Y_0) + m_{23}(Z_A - Z_0)}{m_{31}(X_A - X_0) + m_{32}(Y_A - Y_0) + m_{33}(Z_A - Z_0)}\right]$$

(3.4)

Where x_a and y_a are the photo coordinates of point a; X_A, Y_A, and Z_A are object coordinates of point A; X_0, Y_0, and Z_0 are object coordinates of the perspective centre; f is the camera focal length; x_0 and y_0 are corrections for the principal point offset; m's are the rotational parameters.

These collinearity equations are only valid in ideal conditions. In practice, light rays never project in perfectly straight lines from object to image, and corrections need to be made for various systematic effects which create small but significant distortions. Most important are the principal point offset from the centre of the lens (incorporated in Equation 3.4), lens distortion, and the effects caused by atmospheric refraction and earth curvature.

   Lens distortion occurs when light rays are bent whilst passing through the lens. Radial lens distortion is caused by imperfections in the camera lens, distorting the image points along radial lines from the principal point. The effects of radial lens distortions can be approximated by a polynomial curve (Equation 3.5). Decentring or tangential distortion is caused by imperfect alignment of the lens elements. Because decentring distortion is usually an order of magnitude less than radial distortion and to a large extent compensated by the principal point offset, its effects are negligible (Brown 1971; Remondino & Fraser 2006).

$$\Delta r = k_0 r + k_1 r^3 + k_2 r^5$$ *(3.5)*

Where Δr is the radial distortion along radial distance r from the principal point; k_0, k_1 and k_2 are the radial distortion parameters.

Due to atmospheric refraction, light rays do not travel in straight lines through the atmosphere. Refraction causes imaged points to be displaced outward from their

correct positions. The magnitude of refraction distortion increases with increasing flying height and angle. Corrections need to be applied to the photo coordinates to compensate. Usually, the angular distortion is expressed as a function of angle, flying height, and assuming a standard atmosphere (Equation 3.6). Angular distortion can simply be converted to radial distortion values using simple trigonometry, and then used to compute corrected photo coordinates (Wolf & Dewitt 2000).

$$\Delta\alpha = K \tan\alpha \qquad (3.6)$$

Where $\Delta\alpha$ is angular distortion; K is a value depending upon flying height above sea level and elevation of object point; α is angle between vertical and ray of light.

Traditionally, corrections for the effects of earth curvature are applied also. The need for these can be avoided by using a three-dimensional orthogonal object space coordinate system (Wolf & Dewitt 2000).

Even when the main distortions have been accounted for, the mathematical model remains an approximation. Several effects cause unknown systematic image errors (Jacobsen 2005): not strictly planar image, influence of air temperature on the focal length, deformation of the bundle of rays through air in front of the camera, and deformation of the photos during the developing process. The scanning process may introduce another source for systematic errors. Common systematic errors associated with low-cost digital video cameras are differential scale and non-orthogonality of the image axes (Patias & Streilein 1996). Additional parameters in a self-calibrating bundle block adjustment (Section 3.2.2) can be used to estimate and compensate for these errors.

3.2.2 Photogrammetric solutions

Solution of the non-linear collinearity equations requires linearisation and hence an iterative procedure. Generally, a least-squares solution is adopted to provide the best estimates for the unknown parameters (Wolf & Dewitt 2000). Additional measurements provide redundancy, thereby increasing the precision of the solution.

Traditionally, a stereomodel can be formed in a relative orientation procedure, in which the position and orientation of one camera relative to another is determined. This approach is generally based on co-planarity. The computational

procedure is based on the measurement of tie points identifiable on both images and requires no control for a solution. Once a stereomodel has been created, it can be referenced to the object coordinate system through absolute orientation. This procedure involves a three-dimensional conformal coordinate transformation, and requires a minimum of two horizontal and three vertical control points (Wolf & Dewitt 2000).

Space resection is an alternative procedure to determine the exterior orientation of the frames. Using at least three ground control points with known *XYZ* object coordinates, the collinearity equations can be solved for the unknown exterior orientation parameters (Wolf & Dewitt 2000). Subsequently, object coordinates of features appearing in the overlapping area of the images can be determined through measurement of the photo-coordinates and intersection (Wolf & Dewitt 2000).

A more flexible alternative to the space resection technique is the bundle adjustment in which all photographs in the block are simultaneously adjusted to ground control, in one single solution. Tie points connect adjacent photographs, while control points fix the solution into the object coordinate system. The unknowns associated with a bundle adjustment are the object coordinates of the tie points and the exterior orientation parameters of all the photographs. The measurements include photo coordinates of the object points and ground coordinates of the control points, weighted according to their assumed precision. Advantages of the procedure are the limited ground control required (Figure 3.2), and minimising and distribution of the errors among the frames. Recent developments, such as airborne GPS and inertial navigation systems, have led to the capability to directly measure the exterior parameters, and include these observations in the bundle adjustment (Wolf & Dewitt 2000).

When the interior parameters of the camera are unknown (for example, when using archival photographs or a non-metric camera) these can also be incorporated in the least-squares estimation. This procedure is known as a self-calibrating bundle adjustment (Brown 1956; Kenefick *et al.* 1972; Granshaw 1980; Chandler & Cooper 1989). Additional terms may be included in the adjustment to account for systematic errors (as described in section 3.2.1). Inclusion of extra unknowns requires more measurements. Groups of parameters can be left out or others included, which makes the self-calibrating bundle adjustment a flexible technique. However, simply including additional parameters does not guarantee

△ Horizontal control point
⊙ Vertical control point
⨂ Horizontal and vertical control point
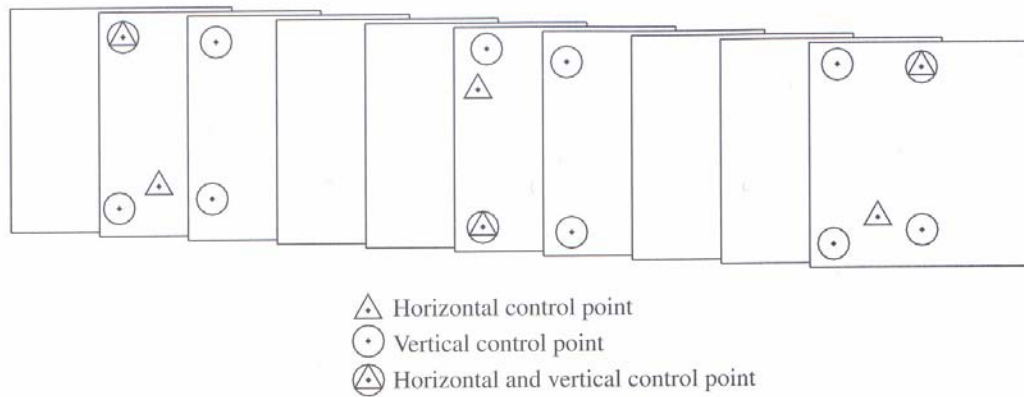
Figure 3.3. Limited ground control required in a bundle adjustment (Wolf & Dewitt 2000).

their solution. Strong correlation between parameters may lead to unsatisfactory results. According to Granshaw (1980) one should guard against estimating too many parameters by *a priori* weighting of additional parameters, statistically testing their values, and eliminating those that are insignificant. Granshaw (1980) also states that in aerial triangulation the interior orientation elements cannot be recovered accurately, because of their high correlation with the exterior orientation. This rarely creates a problem, because any residual errors will have little effect through the process of projective compensation. This means that exterior orientation parameters will be adjusted correspondingly, so that the final accuracy of derived data is not significantly reduced.

3.2.3 Stochastic models

Measurements can be regarded as random variables (see also Section 3.6.1). By eradicating gross and minimising the effects of systematic errors it can be assumed that only random errors remain. These can be described by the variances of the measurements, the so-called stochastic model. In a bundle adjustment, the measurements are weighted according to their variances, which are subsequently propagated through the functional model, thereby providing estimates of the variances of the derived data (Cooper & Cross 1988).

3.3 Image matching

Another fundamental principle in the digital automation of photogrammetry is known as image matching. Image matching involves the identification of conjugate

points in overlapping images, i.e. image points appearing on multiple images corresponding to an identical object feature. The technique forms the basis for automatic tie point generation used for intensifying the triangulation in the bundle adjustment, as well as automated DEM extraction (Leica Geosystems 2003).

The three best known matching methods are area-based, feature-based and symbolic (Schenk 1997). Area-based matching is associated with matching the grey-level distribution between two image patches. The matching entities in feature-based matching are usually interest points or edges. Symbolic or relational matching uses topological properties as criteria for matching (Schenk 1997). The similarity measures include cross-correlation and least-squares for area-based matching. Feature-based and relational matching rely on cost functions based on differences in their attributes (Heipke 1997).

3.3.1 Cross-correlation matching

A commonly applied area-based matching strategy is using cross-correlation. In this procedure a template window is chosen in the first image, and a search performed for its corresponding match within the second image. Using a moving window approach, the correlation coefficient is determined for each candidate match, according to their grey level distributions. In normalised cross-correlation the radiometric differences between the two images are eliminated through correcting each pixel value according to the mean value of the image patch (Equation 3.7) (Wolf & Dewitt 2000); this accounts for slight differences in exposure arising from automated metering of aerial cameras.

$$c = \frac{\sum_{i=1}^{m} \sum_{j=1}^{n} \left[\left(A_{ij} - \overline{A} \right) \left(B_{ij} - \overline{B} \right) \right]}{\sqrt{\left[\sum_{i=1}^{m} \sum_{j=1}^{n} \left(A_{ij} - \overline{A} \right)^2 \right] \left[\sum_{i=1}^{m} \sum_{j=1}^{n} \left(B_{ij} - \overline{B} \right)^2 \right]}} \qquad (3.7)$$

Where c is the correlation coefficient; m and n are row and column numbers; A_{ij} and B_{ij} are the digital numbers, at row i, column j of respectively image patches A and B; $\overline{A}$ and $\overline{B}$ are the average digital numbers in the respective image patches.

The normalised correlation coefficient can range from −1 to +1, whereby a value of +1 indicates a perfect match. Normalised cross-correlation is essentially the same operation as linear regression: a set of ordered pairs is statistically analysed to

determine the correspondence to a straight-line relationship, and a best-fit line through the data established. The candidate window exhibiting the largest correlation value is considered to be the best match. Important parameters for the success of image matching are the size of the template and search window, the interest operator used to select suitable feature points, and acceptance criteria. Perfect matches will never occur in reality due to noise, differences in illumination, and geometric distortion (Wolf & Dewitt 2000; Leica Geosystems 2003).

3.3.2 *Least-squares matching*

Cross-correlation techniques work fast and well only when the images contain enough signal and when geometrical and radiometric distortions are minimal. Perspective and relief distortion in stereo images require the use of additional corrections regarding the geometry of image patches. Basic equations to account for both the radiometric and geometrical differences are set up in the context of a least squares estimation. Such a least-squares procedure also allows an assessment of the quality of the match in terms of precision and reliability (Gruen 1985). A commonly used form is implementing the following equations (Equation 3.8; Wolf & Dewitt 2000). The first equation corrects for radiometric differences between the two images, while the other two define the geometric relationship between the conjugate pixels using an affine transformation (Equation 3.1).

$$A(x, y) = h_0 + h_1 B(x', y')$$
$$x' = a_0 + a_1 x + a_2 y \qquad\qquad (3.8)$$
$$y' = b_0 + b_1 x + b_2 y$$

Where $A(x,y)$ is the digital number from image patch of image A, at location x, y; $B(x',y')$ is the digital number from search area of image B, at location x', y'; h_0 and h_1 are radiometric corrections (offset and scale factor); a_0, a_1, a_2, b_0, b_1, and b_2 are parameters specifying an affine relationship between coordinates of conjugate pixels in both photos.

A good initial estimation of the corresponding pixel in the second image is essential for an efficient algorithm. This can be achieved through use of image pyramids, by first matching at an upper level of the pyramid and progressively matching down to the bottom level (Wolf & Dewitt 2000). Further improvements can be made by performing epipolar resampling on the images, so that rows of the images line up with epipolar lines (i.e. the intersection line of the plane defined by the object and

the camera centres with the image planes). In this way the transformation equations can be simplified (Equation 3.9) and the search region can constrained along a single line (Wolf & Dewitt 2000).

$$x' = a_0 + a_1 x$$
$$y' = b_0$$
$$(3.9)$$

Where x is the location of the pixel in image A; x', y' are the coordinates of the conjugate pixel in image B; a_0, a_1, and b_0 specify the relationship between coordinates of conjugate pixels.

3.4 Automated DEM extraction

A Digital Elevation Model (DEM) can be defined as *"a quantitative model of a part of the earth's surface in digital form"* (Burrough & McDonnel 1998). DEMs are a valuable basis for terrain representation and subsequent extraction of terrain-related attributes. Information can be extracted through visualisation or quantitative analysis (Weibel & Heller 1991). DEMs are usually modelled by rectangular grids or Triangular Irregular Networks (TINs). Handling of grids is relatively simple, since their data structure corresponds to the matrix structure used in computers, and modelling algorithms are straightforward (Weibel & Heller 1991). TIN structures are typically based on a Delaunay triangulation, with vertices at the sample points. Structural features can easily be incorporated and point density can be adjusted to the complexity of the terrain (Weibel & Heller 1991).

The process of automatic DEM extraction from a stereomodel comprises three tasks: image matching, surface fitting (or interpolation) and quality control (Schenk 1996). Image matching was described in the previous section. The three-dimensional ground coordinates of the successfully matched points are calculated by using space forward intersection. The resulting points can be used to create either a TIN or a grid DEM.

In order to obtain a regular grid, interpolation must be applied from the original sampling points. Various interpolation methods exist, differing in the degree to which structural features can be taken into account and the interpolation function can be adapted to the varying terrain character (Weibel & Heller 1991). In nearest neighbour interpolation the pixel value is determined by the nearest single data point. Unless there are many observations, this method is not appropriate for gradually varying phenomena. Inverse distance interpolation is a more commonly

used approach and computes an average value from neighbouring data points, weighted according to their distance. The simplest form is a linear interpolator, in which the weights are linearly related to the distance to data points. In spline methods a polynomial function is fitted through the point data, resulting in a smooth representation of the surface whilst retaining small-scale features (Burrough & McDonnel 1998).

Procedures for detection and correction of errors are also important. Some automated procedures to remove blunders have been presented (e.g. Hannah 1981) and are used in many commercial algorithms (Leica Geosystems 2003). Quality control and evaluation are further discussed in Section 3.6.

Visualisation of elevation data is an important tool for the researcher to explore the terrain, and to communicate results and concepts. The usefulness of visualisation products depends on their communicational effectiveness and their ability to support interpretation. Conventional forms of depiction of relief are contour lines and hillshading. An important limitation of contours is that they give no immediate impression of landforms. Shaded relief is a more convenient way to perceive landforms, although it gives no information about absolute elevation. Contour and hillshade displays can be overlaid with other elements, such as other terrain attributes, maps, or orthophotos. Perspective displays provide much more convincing visualisation results, although certain areas may be hidden from display. Perspective views can be overlaid with hillshading, maps, or orthophotos. Sequences of scene renderings can be used to create animations, such as flight simulations (Weibel & Heller 1991).

3.5 Orthophoto generation

Orthophotographs combine the image characteristics of a photograph with the geometric qualities of a map (Wolf & Dewitt 2000). Orthophotos are created through differential rectification, which eliminates image displacements due to photographic tilt and terrain relief so that all ground features are displayed in their true ground position. This allows direct measurement of distances, areas, angles, and positions. Orthophotos are often used as base maps in GIS because of their accuracy and visual characteristics (Wolf & Dewitt 2000).

The rectification procedure requires a photograph with known orientation parameters and a DEM. First, for each ortho-image pixel its corresponding elevation

value is extracted from the DEM. The acquired 3D ground point is projected into the photograph using the collinearity equations in the direct form (Equation 3.4). The image grey value at the specified location is obtained by interpolation, and assigned to the pixel of the ortho-image (Krupnik 2003).

3.6 Data quality – controls and evaluation

As pointed out by Fryer *et al.* (1994) and Lane *et al.* (2000), the ease with which terrain data may be generated using digital photogrammetric techniques has focused attention more on analysis and interpretation of the acquired results, than on issues of data quality. In addition to the conventional controls on photogrammetric data, the automated algorithms in digital processing have important influence on the quality of the results.

As defined by Cooper & Cross (1988), the quality of derived data is a function of the precision, accuracy and reliability of the measurements and the functional model used. Precision can be related to random errors inherent in any measurement procedure. Accuracy can be associated with systematic errors in the model. Reliability refers to the presence of gross errors.

3.6.1 Precision

The bundle adjustment procedure is capable of propagating stochastic properties of the estimated parameters and measurements through the functional model, thereby providing an estimation of the precision (Butler *et al.* 1998); see also Section 3.2.3.

The precision of image measurements is inherent to the source data, and a function of the resolving power or sharpness of the lens and film used. The resolving power of an image can be described by its spatial frequency (lines/mm) and the contrast. The resolving power of a typical photogrammetric camera is usually limited by the film rather than the lens or image motion during exposure. Other factors are the atmospheric conditions, target contrast, and film processing (Slama 1980). The grain size of the silver crystals in film emulsions provides a much better resolving power than can be achieved using paper prints. In general, colour films are grainier than black-and-white film, and grains tend to be larger in older material due to lower quality of the emulsions (Lo 1976). In the case of digital imagery, the pixel resolution of the sensor or scanner is an important control on the

resolving power. Graham (Graham 1998) recommends 3 pixels = 1 line-pair for conversion to traditional lines/mm units.

The effects of the different components in a photographic imaging system on the sharpness of an image can be characterised by a Modulation Transfer Function (MTF) (Graham 1998). The MTF is a measure of how much contrast is lost, as a function of the spatial frequency (Nikon 2006).

The measurement precision that can be achieved using digital imagery is often to sub-pixel, depending on the object and contrast. Values in the literature vary greatly, ranging from to 0.02-0.4 of a pixel, using centre of gravity operators (Dare *et al.* 2002; Robson & Shortis 1998).

The effects of photo-scale and image resolution can be combined in terms of ground resolution distance, which determines the level of horizontal detail in object space that is visible on the photographs (Equation 3.10, Lillesand & Kiefer 1994). The vertical resolution can be obtained by multiplying the horizontal resolution with the inverse base/height ratio (Equation 3.10).

$$HR = \frac{scalenumber}{imageresolution}$$

$$VR = \frac{scalenumber}{imageresolution} \cdot \frac{H}{B}$$

(3.10)

Where HR and VR are respectively horizontal and vertical ground resolution distance; and H/B is the inverse base/height ratio.

From Equation 3.10 follows that a strong convergence (large base/height ratio), and consequently large relief displacement gives rise to highly precise vertical object coordinates (Wolf & Dewitt 2000). According to Fryer *et al.* (1994) the optimum precision that can be expected using standard mapping configurations is about 1-3 parts per 10,000 of the flying height.

In spite of recent developments in the field of airborne digital sensors (e.g. Fricker *et al*. 2000; Hinz & Heier 2000), the most common way of obtaining digital imagery remains scanning of the original film exposed in a metric aerial camera. Scan resolution and geometric and radiometric quality of the scanner provide important controls (Wolf & Dewitt 2000). Radiometric resolution of a scanner is an indication of the number of differences in image density that can be distinguished. The geometric quality of a scanner can be expressed by its spatial resolution and

the positional accuracy of pixels. In order to preserve an original film resolution of 30-60 lines per mm, a scanned pixel size of 6-12 μm would be needed. For many practical applications, such as DEM generation, good results can be achieved with 25-30 μm resolution (Baltsavias 1999).

DEM resolution is typically lower than the original source, since it involves interpolation. The image matching procedure for automated DEM extraction needs a certain template size for correlation (typically 5 times the object space pixel dimensions). An associated increase in grid spacing will smooth the topography and hence degrade the precision of the data (Lane *et al.* 2000). A study by Saleh & Scarpace (2000) showed that within limits, the influence of scanning resolution on DEM surface height precision is rather low.

3.6.2 Accuracy

The accuracy can be related to the presence of uncorrected systematic errors, which may be difficult to isolate, and generally provide a limiting constraint on the quality of the derived data. Systematic errors can be instigated during the measurement process or due to deficiencies in the functional model.

Systematic errors in a stereo-model arise from a variety of sources including lens distortion, atmospheric effects, film deformation, scan distortions, and inaccurate or poorly distributed control points (Buckley 2003; Chandler 1989). Accounting for all systematic effects in a self-calibrating bundle adjustment is difficult, because many cannot be modelled explicitly, and there is usually high correlation between the modelling parameters (see Section 3.2.2). Control points should be evenly distributed over the images to gain a strong geometry. Ideal locations tie frames together and surround the volume of interest. A minimum of two planimetric and three height points is needed to define a datum, but more control points are desirable as redundancy provides appropriate checks (Wolf & Dewitt 2000). The only way to quantify the accuracy of a photogrammetric solution is to compare estimated coordinates with accepted values. Traditionally, accuracy is evaluated by computing the RMS error of independent checkpoints.

Concerning DEM accuracy, accuracy of the interpolated surface depends not only on the accuracy of the measured points, but also on their density. Automated image matching is influenced by variations in surface texture and geometric distortion caused by different viewing angle. The controls upon automated generation of elevation data are of special relevance to complex terrain surfaces

(Lane *et al.* 2000). If there is insufficient texture, the software is unable to match two points successfully and an interpolated estimate may be created. Surface roughness has a positive effect on texture, and consequently on matching. However, this effect may be countered by the increasing differences in the viewing of areas, thereby reducing the level of correlation between the images. In addition, interpolated estimates will be least effective in areas of great roughness. DEM collection parameters can be optimized, but these control individual matches rather than affecting the resulting surface accuracy (Lane *et al.* 2000).

RMS error of checkpoints is the most widely used measure to assess DEM accuracy. However, according to Li (1988) the combination of mean and standard deviation of error are more appropriate in a statistical sense. Although such statistics are an accepted strategy for determining DEM accuracy, its limitation is the subjectivity in selecting checkpoints, which may therefore not be representative for the entire DEM (Florinsky 1998).

3.6.3 Reliability

Reliability can be related to gross errors, and the ease with which they may be detected (Cooper & Cross 1988). Gross errors are genuine mistakes or blunders that arise during photogrammetric measurement, for example caused by mismatching in the process of automatic tie-point generation. Fortunately, most gross errors are normally easy to detect and eradicate because of their size. They can be detected and eliminated by increasing the redundancy of measurements (Hoittier 1976), giving rise to datasets that are "internally reliable" (Cooper & Cross 1988).

Gross error sources that commonly affect the determination of exterior orientation include misidentified or mistyped control points. Fortunately, these errors give rise to large residuals at the bundle block adjustment stage and, if data redundancy is high, are normally readily identifiable.

Cooper & Cross (1988) distinguish between internal and external reliability. Internal reliability is a measure of the size of the marginally detectable error. External reliability refers to the effect of an undetected gross error on data derived from the measurements. Butler *et al.* (1998) compared DEMs extracted from different stereo-pairs in the same block, as a measure of internal reliability.

3.7 Review of photogrammetry in landform change studies

Aerial photographs can be used for accurate modelling of terrain surfaces. Recent photographs can be compared with historical imagery to measure the progressive development of landslides and other dynamic landforms. Quantitative data can only be obtained when rigorous photogrammetric techniques are applied (Chandler & Cooper 1989). Approaches to quantitative landslide monitoring can be divided into three categories: those based on APIs, DEMs, and displacement vectors.

3.7.1 *API-based monitoring*

The value of API for mapping landslide features was already outlined in Section 2.4. Chandler & Brunsden (1995) stated that an accurate definition and coding of geomorphological boundaries by photogrammetric techniques allows quantitative comparison between photo-interpreted maps from different periods.

Analyses of multi-temporal APIs have been used in several geomorphological studies. Welch & Howarth (1968) used photogrammetric measurements in the interpretation of rapidly changing glacial landforms. Accurate graphical plots of the main landforms were plotted from sequential aerial photographs, and proved to be beneficial in examining the formation and destruction of glacial landforms.

Chandler & Cooper (1989) and Chandler & Brunsden (1995) used analytical photogrammetric techniques to map the main geomorphological features of a coastal mudslide, Black Ven, UK, from sequential aerial photographs. These multi-temporal maps, in combination with extracted surface profiles and DEMs, allowed them to develop an evolutionary model of the landslide system.

Van Westen & Getahun (2003) documented the evolution of the Tessina landslide, Italy, by using multi-temporal landslide maps produced through interpretation of sequential aerial photographs. The photo-interpretations were converted to large-scale multi-temporal topographic maps and digitised, resulting in detailed landslide activity maps.

Also, series of oblique and terrestrial photographs have been used in determining geomorphological activity. Kalaugher *et al.* (1987) applied high-oblique aerial photographs to identify geomorphological processes on coastal cliffs in East Devon, UK. Schuster & Smith (1996) compared new, terrestrial photos with archival ones to observe changes in main-scarp geometry of the Slumgullion landslide, US.

3.7.2 DEM methods

Subtracting two DEMs of different epochs from each other, creates a grid surface representing the change of form over that period. This surface of change, or 'DEM of difference', quantifies the effects of geomorphological processes. Areas experiencing removal of material will be indicated by depressions, while areas receiving material are indicated by peaks. Caution should be taken, as areas exhibiting no change are not necessarily inactive regions; they can represent areas where input of material has equalled output (Chandler & Cooper 1989; Chandler & Brunsden, 1995). Additional DEM products that can be used to study geomorphological processes include (Chandler & Brunsden 1995):

- Perspective views, displaying the site morphology in 3D, thereby giving the possibility to view it from different angles for interpretation;

- Profiles, enabling quantitative morphogenetic comparison if repeated along the same plane at different epochs;

- Slope maps and histograms.

A challenge in the use of archival photographs for analysing long-term geomorphological evolution is the lack of ground control and camera calibration data, resulting in systematic errors in the DEMs. Chandler & Brunsden (1995) and Hapke (2005) minimised these effects by means of a self-calibrating bundle adjustment. Mills *et al.* (2005) used surface matching techniques, based on a least-squares approach, to orientate DEMs from different sources relatively to each other, thereby reducing systematic errors. Betts *et al.* (2003), in their study on gully erosion, countered the problem *a posteriori*, by measuring and correcting for residual systematic errors in stable control areas. Apparent elevation differences in these control areas were interpolated to an error surface and subtracted from the whole 'DEM of difference' image.

Further developments of digital photogrammetry have led to an increased effectiveness of the techniques. In recent years, multi-temporal DEMs have proven their value in many more landslide studies (e.g. Cheng 2000; Adams & Chandler 2002; Kerle 2002; Gentili *et al.* 2002; Van Westen & Getahun 2003; Ager *et al.* 2004; Baldi *et al.* 2005; Bitelli *et al.* 2004; Hapke 2005) and other geomorphological applications such as fluvial sediment transport (Stojic *et al.* 1998), river bank erosion (Pyle *et al.* 1997; Lane 2000), gully erosion (Betts & DeRose 1999; Betts *et al.* 2003), coastal monitoring (Hapke & Richmond 2000;

Mills *et al.* 2005), coastal dunes (Brown & Arbogast 1999), rock glaciers (e.g. Kääb & Vollmer 2000; Kaufmann & Ladstädter 2000), and glaciers (Fox & Nuttall 1997). A summary of these studies is given in Table 3.1.

An important recent development is airborne laser scanning (LIDAR), which offers a competitive alternative for rapid and accurate acquisition of terrain elevation data. Various studies have demonstrated the high potential of this method in measuring landform change and also showed the ease of integration with photogrammetrically derived data (e.g. Adams & Chandler 2002; Ager *et al.* 2004; Mills *et al.* 2005). Evidently, LIDAR is only an alternative source for obtaining current elevation data and does not provide extensive past records.

3.7.3 Displacement vectors

Displacement vectors can be obtained by measuring the position of objects from sequential pairs of photographs. These positions can either be measured directly from the original images in a stereo model (3D), or from orthophotos (2D).

The value of using multi-temporal photographs to measure slow morphological changes to the earth surface was recognised in the early days of analytical photogrammetry. In 1931, Richard Finsterwalder developed a method for measuring movement parallax from terrestrial images in order to determine the movement of glaciers; Hofmann later modified this method for aerial images (see Barsch & Hell 1975, p.120). However, the technique for directly measuring movement parallax requires images of comparable scale and quality and similar flight directions. In their study on rock glaciers, Barsch & Hell (1975) avoided this problem by orientating each stereomodel individually, and subsequently determining the coordinates of objects in each model. This approach was applied successfully by many other authors on glaciers (Konecny 1964), rock glaciers (Evin & Assier 1982; Gorbunov *et al.* 1992; Kääb *et al.* 1997; Kaufmann 1996), and landslides (Baum *et al.* 1998; Smith 1996).

Developments in digital photogrammetry have led to the general availability of orthophotos. Orthophotos provide a very straightforward means of measuring horizontal positions of objects. Powers *et al.* (1996) analysed morphological change of a landslide, by comparing orthophotos from different epochs in a GIS. Identification of surface objects was done manually.

Digital techniques allow the potential of automatic measurement of objects on images. Scambos *et al.* (1992) used an area-based image matching algorithm to

Table 3.1. Summary of landform change studies using multi-temporal DEMs; it should be noted that the information provided on accuracy is very variable among different authors (and sometimes measures of precision rather than accuracy, as described in this study), and therefore not allowing direct comparison.

Author	Location	Date (epochs)	Source*	Media	Resolution	Scale	DEM res	Max. diff.	DEM acc.
Chandler (1989) Chandler & Brunsden (1995)	Black Ven landslide (UK)	1946-1988 (5)	AP (B&W, O+V)	Diapos.	A**	1/4,000-1/40,000	5m	45 m	
Brunsden & Chandler (1996)	Black Ven landslide (UK)	1988-1995 (2)	AP (B&W+C)	Scanned diapos.	40 µm	1/4,200	5 m	30 m	>0.03 m
Fox & Nuttall (1997)	Finsterwalderbreen (Svalbard)	1970-1990 (2)	AP (FC) Topomap			1/50,000	25 m	50 m	3 m
Kääb et al. (1997)	Gruben rock glacier (Swi)	1970-1995 (6)	AP		A	1/6,000-1/14,000	25 m	15 m	0.4 m
Pyle et al. (1997)	River bank erosion, Haut Glacier d'Arolla (Swi)	1995 (3)	Close range	Scanned B&W negatives	20 µm	1/180	20 mm	0.6 m	12 mm
Kääb et al. (1998)	Murtèl rock glacier (Swi)	1987-1996 (2)	AP		A		5 m	2 m	0.2 m
Stojic et al. (1998)	Small-scale river model		Close-range	Scanned neg.	12.5 µm	1/70	7.5 mm	2.4 mm	>1.7 mm
Brown & Arbogast (1999)	Coastal dunes Michigan (US)	1965-1987 (2)	AP (B&W+IR)	Scanned prints	42 µm	1/16,000-1/20,000	3 m		15 m
Betts & DeRose (1999)	Gullies, Waipaoa catchment (NZ)	1939-1992 (3)	AP		25-63.5 µm	1/12,000-1/26,000	5 m	66 m	2.4-5.8 m
Kääb & Vollmer (2000)	Muragl rock glacier (Swi)	1981-1999 (6)	AP		A & 30 µm	1/6,000-1/7,000	10 m	6.5 m	0.2 m
Kaufmann & Ladstädter (2000)	Hochebenkar rock glacier (Aus)	1953-1997 (8)	AP (B&W)		10 µm	1/12,000-1/38,000	2.5 m	24 m	0.5 m
Cheng (2000)	Tsau-Lin landslide (Tai)	1980-1995 (2)	AP (C)	Scanned neg.	20 µm	1/5,000-/10,000	10 m		
Adams & Chandler (2002)	Black Ven landslide (UK)	1976-1998 (2)	AP (B&W) & lidar	Scanned diapos.	20 µm	1/7,500	2 m	45 m	0.43 m
Gentili et al. (2002)	Corniglio landslide (Ita)	1994-1996 (6)	AP (B&W)		28 µm	1/12,000	5 m	28 m	>0.42 m
Kerle (2002)	Casita volcano (Nic)	1996-2000 (2)	AP, TS, Topomap		14 µm	1/40,000	5 m		1.11-7.76 m
Kaufmann (2002)	Blaubach landslide (Aus)	1953-1999 (11)	AP			1/9,300-1/45,800	1 m	15 m	
Betts et al. (2003)	Gullies, Mangawhairiki catchment (NZ)	1999-2000 (2)	AP	Scanned B&W diapos.	7-10.6 µm	1/8,000-1,10,000	0.5 m	6 m	0.02 m
Ager et al. (2004)	Holly Hill landslide (UK)	1989-2003 (3)	AP & lidar					1 m	0.3 m
Bitelli et al. (2004)	Cà di Malta landslide (Ita)	2000-2004 (3)	AP & TLS		25 µm	1/4,400	2 m	4 m	0.42 m
Baldi et al. (2005)	Sciara del Fuoco landslide, Stromboli (Ita)	2001-2003 (15)	AP (B&W + C)		25 µm	1/5,000-1/17,000	5 m	70 m	1.7-3.3 m
Hapke (2005)	Big Sur landslides (US)	1942-1994 (2)	AP		25 µm	1/24,000-1/30,000	15 m	40m	9-11 m
Mills et al. (2005)	Filey Bay coast (UK)	2000-2002 (3)	AP, GPS	Digital	6 Mpix	1/22,000		1.36 m	0.414 m

* AP= aerial photographs; B&W= black-and-white; C= colour; IR= infrared; FC= false-colour infrared; O+V = oblique + vertical imagery; TS= terrestrial survey; TLS= terrestrial laser scanning; Topomap= topographical maps
** A= analogue imagery
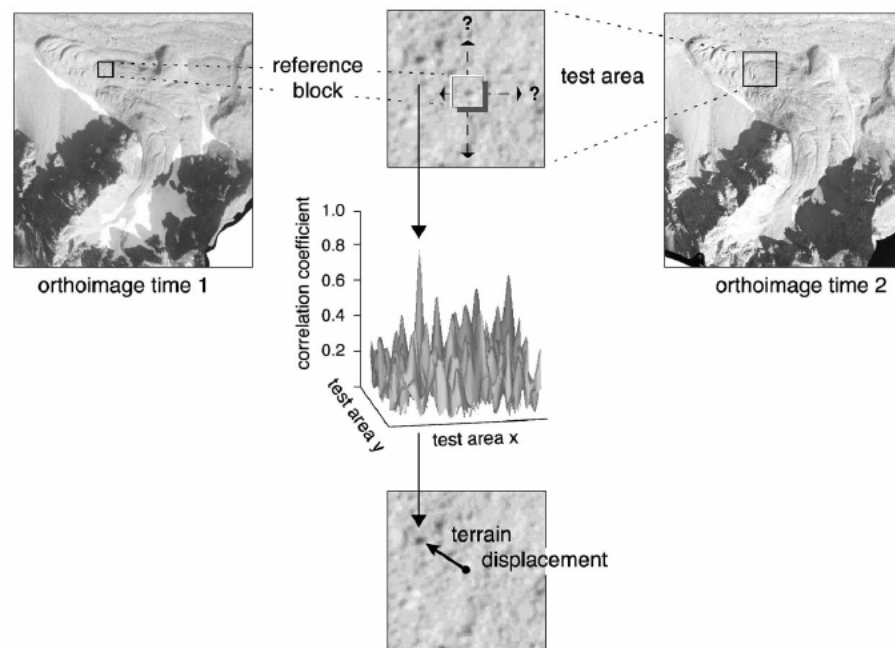
Figure 3.4. Schematic representation of measuring surface displacements from repeated digital orthophotos by area-based image matching techniques (Kääb & Vollmer 2000).

map the velocity field of moving ice from pairs of satellite images. Kääb & Vollmer (2000) were the first to apply this methodology on orthophotos, created from scanned aerial photographs (Figure 3.4). Their fully digital chain of image processing and analysis was successfully applied in studies on different types of surface movements, such as glaciers, rock glaciers and landslides. The high density and accuracy of the velocity data provided by the technique make it possible to extract meaningful strain-rate information (Kääb 2002).

Some authors found the accuracy of the displacement vectors from orthophotos overly limited by the quality of the DEMs used in the orthorectification procedure. Casson *et al.* (2003) tackled this issue by proposing alternative algorithms for creating better DEMs. Kaufmann & Ladstädter (2002) developed a concept based on the automatic matching of pseudo-orthophotos. Pseudo-orthophotos in combination with the rough DEM still contain the same stereo-information as the original photos, which enable strict 3D reconstruction (see Figure 3.5).
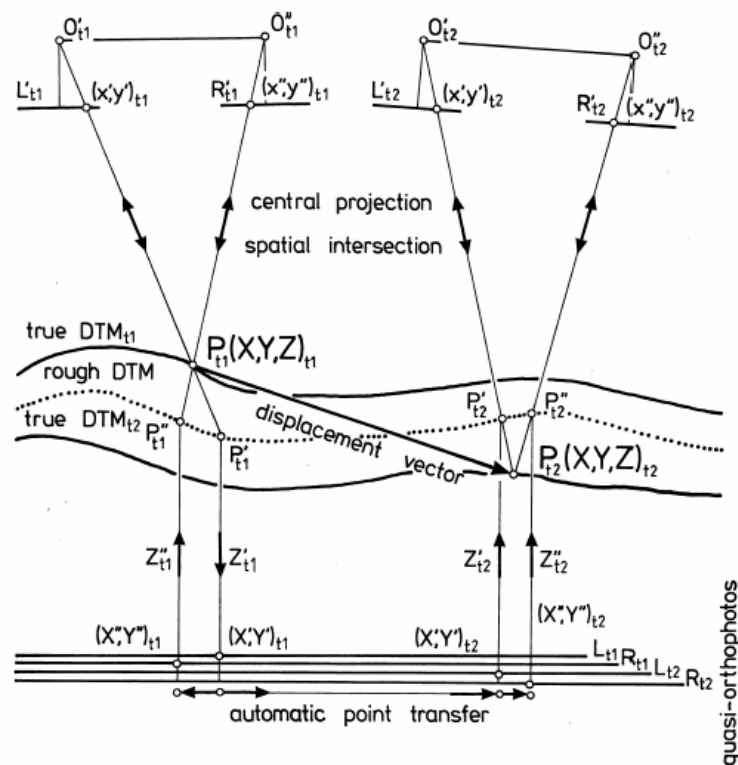
Figure 3.5. Computation of 3D displacement vectors from pseudo-orthophotos (Kaufmann & Ladstädter 2002).

Using pseudo-orthophotos for matching has several advantages (Kaufmann & Ladstädter 2004):

- Perspective distortions have been removed to a great extent;
- Increased accuracy and robustness of the area-based matching algorithm;
- Processing may be restricted to the area of interest, hence less storage space is needed;
- 3D perception of motion parallaxes in multi-temporal pseudo-orthophotos provides a visual impression of surface changes.

A summary of studies using displacement vectors from aerial photography is given in Table 3.2.

3.8 Summary

Literature revealed that recent developments in digital photogrammetry have greatly increased the application of photogrammetry to landform studies, and more

Table 3.2. Summary of landform change studies using photogrammetrically derived displacement vectors. As in Table 3.1, the accuracy measures are not directly comparable, but for indication only.

Author	Location	Date (epochs)	Photo scale	Media* & resolution	A/D**	Meas. density	Max displ. (hor/vert)	Accuracy (hor/vert)
Von Barsch & Hell (1975)	Murtèl rock glacier (Swi)	1932-1971 (3)	1/13,000-1/23,000	Diapos.	A	50-70 pts	5.2 / 0.4 m	0.7 / 0.5 m
Evin & Assier (1982)	Asti rock glacier (Fra)	1948-1980 (2)			A	15 pts	6.6 / 3.9 m	< 1 m
Gorbunov *et al.* (1992)	6 rock glaciers in Tien Shan (Kaz)	1969-1984 (2-3)	1/20,000-1/40,000		A	4-15 pts	70 m	25 m
Powers *et al.* (1996)	Slumgullion earthflow (US)	1985-1990 (2)	1/6,000-1/12,000	Scanned diapos. (63.5 µm)	D	800 pts	29 m	2 m
Smith (1996)	Slumgullion earthflow (US)	1985-1990 (2)	1/6,000-1/12,000		A	310 pts	25 m	0.44 / >0.5 m
Kääb *et al.* (1997)	Gruben rock glacier, (Swi)	1970-1995 (6)	1/6,000-1/14,000		A	25 m	25 m	0.4 m
Baum *et al.* (1998)	2 landslides in Honolulu (US)	1969-1989 (3)	1/8,000-1/13,000		A		4.3 / 1.1 m	0.4 / 0.6 m
Kääb *et al.* (1998)	Murtèl rock glacier (Swi)	1987-1996 (2)			A	10m res.	1.4 m	0.2 m
Kaufmann (1996)	Dösen rock glacier (Aus)	1954-1993 (5)	1/8.000-1/35,000	B&W + CIR	A	150 pts	6.6 m	0.2 m
Kääb & Volmer (2000)	Muragl rock glacier (Swi)	1981-1999 (6)	1/6,000-1/7,000	10 µm	A & D	10 m	6.5 m	0.4 m
Kaufmann & Ladstädter (2000)	Hochebenkar rock glacier (Aus)	1953-1997 (8)	1/12,000-1/38,000	30 µm	D	>10.000 pts	23 m	0.3 m
Kääb (2002)	Aletsch rockslide (Swi)	1976-1995 (2)	1/10,000		D	0.3 m	2 m	
Kaufmann (2002)	Blaubach landslide (Aus)	1953-1999 (11)	1/9,300-1/45,800	Scanned diapos.	D	39,900 pts	53.9 m	
Casson *et al.* (2003)	La Clapière landslide (Fra)	1983-1999 (3)	1/17,000-1/30,000		D	14 pts	104 m	20 m
Delacourt *et al.* (2004)	La Clapière landslide (Fra)	1995-2003 (3)		AP & Sat.	D	1 m	60 m	2 m
Kaufmann & Ladstädter (2004)	Hinteres Langtalkar rock glacier (Aus)	1954-1999(11)		10 µm	D		29.7 m	
Chadwick *et al.* (2005)	Salmon Falls landslide (US)	1990-2002 (3)	1/40,000	AP & Sat. (25 µm)	D	20 pts	16.4 m	2.8 m

* B&W= black-and-white; CIR= colour-infrared images; AP= aerial photographs; Sat.= satellite imagery
** A= analogue; D= digital imagery

specifically in landslide monitoring. It was shown that the techniques are highly automated which makes them increasingly available to non-specialists.

The main mathematical principles used in photogrammetry are based on the collinearity condition, which allows three-dimensional coordinates to be extracted from stereo photographs. Camera parameters and ground control points are required for obtaining a photogrammetric solution. In a bundle adjustment the collinearity conditions for all photographs in a block are solved simultaneously using least-squares estimation. This procedure requires only limited ground control, minimises errors, and offers the flexibility of incorporating additional parameters for estimating unknown camera parameters (self-calibration) and other systematic distortions. The inclusion of a stochastic model allows measurements of differing quality to be combined in a rigorous way.

An important advancement in digital photogrammetry is image matching, which allows automation of various stages in the photogrammetric working chain, such as tie point generation in the triangulation process, and DEM extraction. Under favourable conditions image matching can be employed with multi-temporal photographs for extracting displacement vectors. Most common products of digital photogrammetry are DEMs and orthophotos, valuable both for visualisation and quantitative analyses.

There are numerous examples of studies involving the application of multi-temporal aerial photographs to measure progressive development of landform change. The approaches can generally be divided into three categories: based on APIs, DEMs, and displacement vectors. API-based monitoring involves comparison of photo-interpreted maps. 'DEMs of difference' can be created from DEMs of different epochs, to quantify elevation changes. Displacement vectors can either be measured directly in the stereo-model or from orthophotos. It was shown that such velocity data allow to extract meaningful strain-rate information.

Although often ignored, it is essential to evaluate the quality of the acquired data. Precision is mainly dependent on the source data and can be estimated through propagation of the stochastic properties through the bundle adjustment. Undetected systematic errors provide a limiting constraint on the accuracy of the derived data. The most common measure of accuracy is the RMSE error of checkpoints, but mean and standard deviation of error yield more useful information. Reliability can be related to gross errors, which are usually easy to detect and eliminate.

Owing to the flexibility and high degree of automation of digital photogrammetric techniques, it is possible to derive accurate quantitative data from archival photography. In this way, the photographic archive can provide a source for long-term monitoring of landslides. Scarce research has been done up to now on the value of commonly available, archival material in such studies. Key elements of using these sources and the implications for data quality need further study and provided the motivations for this research project.

Chapter Four

4 Methodology

This chapter has been drafted to explain the strategies that were followed to fulfil the aims and objectives of this research – i.e. the problems that arose in the course of work and the decisions that were taken to overcome them. The process of identifying these issues and their satisfactory solution led to the identification of key issues and recommendations for the potential end-user in Chapter 7.

The chapter is structured according to the aims and objectives outlined in Chapter 1, and the individual steps taken during their accomplishment, as described in the following two case-studies (Chapters 5 and 6).

4.1 Selection of field sites

The first stage in this research comprised the selection of appropriate field sites. One site was used to develop the methodologies, while a second site was used to validate the application of these methods. Especially in the development stage it was considered important to have alternative data sources to compare the results with. It is evident that the sites should involve mass movements that are suitable for measurement from aerial photographs. This leads to the following criteria used for selection of the sites:

- Type/processes involved – The landslide should be deep-seated and its movement mainly controlled by climatic conditions, as this would assure more or less continuous activity on a prolonged time-scale.

- Present/recent activity – The landslide should be subject to movements in the last 50 years, in order to be able to use historical aerial photography for their investigation.

- Size – Not only should the size of the landslide be large enough for identification on aerial photographs, but also the magnitude of its movements should be significant in order to be detected and measured by using photogrammetric techniques. Although this also depends on the quality of the photographs, it was believed that the movements should be at least several meters during the time interval between two successive photographic epochs.

- Aerial photography – It is evident that there should be aerial photography available of good quality and suitable scale of the site. The photographs should be from different age and their succession should cover a period during which significant movements took place.

- Other data – The availability of historical records about the landslides activity would be helpful for validation of the photogrammetrically derived data.

- Damage – Damage to infrastructural works would be useful in the sense that it very likely provides additional information sources, such as site investigations and reports about repairs. Another aspect is that the occurrence of economic losses underlines the benefits of this research for the society.

The original aim of this project was to incorporate the extracted data in climate-landslide modelling for prediction of future landslide movements. For this reason the search was initially restricted to inland landslides that are controlled by climatic variables, rather than influences of sea, complex geological structures or mining activities. Also the field sites were searched for in different parts of the UK to reflect different climatic regimes. However, as the project progressed the climatic aspect was dropped and the focus directed towards the use of historical aerial photographs in any landslide study. For this reason it was not a problem that one of the selected

landslides was in fact triggered by mining activities, with the succeeding movements influenced by climatic variables.

The choice for the Mam Tor landslide (Derbyshire, UK) as the subject for the first case study was straightforward, since its movement history has been extensively recorded and the relation between movements and rainfall characteristics investigated in various studies (e.g. Waltham & Dixon 2000). The slide is well-known owing to the main road between Manchester and Sheffield that was constructed across the slide, but abandoned in the late 1970s as a result of continuing damage. Detailed monitoring data from ground surveys in the 1990s was available.

The second case study focused on the East Pentwyn landslide (Ebbw Vale, South Wales, UK). This location was selected after consulting landslide experts from the British Geological Society (Alan Forster & Kevin Northmore, 9 May 2003), who hold an extensive database of recorded landslides in the UK, and Halcrow (Howard Siddle, 28 June 2005), with much expertise on landslides in South Wales. Initial failure of the East Pentwyn landslip took place in 1954 as a result of mining activities. Subsequent movements have been related to rainfall (Halcrow 1983). An advantage of this site is the young age of its initial failure, allowing analysis of preceding imagery. Site investigation reports include monitoring data from the 1980s. The location of the two field sites is displayed in Figure 4.1.
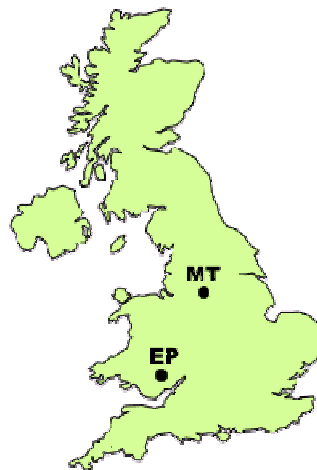
Figure 4.1. Location of the Mam Tor (MT) and East Pentwyn (EP) landslides.

4.2 Extracting morphological data from images

Accomplishment of this objective was most time-consuming. It includes the search for and acquisition of aerial photographs, collecting ground control, photogrammetric processing, and assessment of the quality of the extracted data.

4.2.1 Acquiring photographs

Acquiring historical aerial photographs is a time-consuming procedure. In the UK, imagery is distributed over numerous archives and libraries, held by a range of institutions, among them the National Monuments Record, the collection of Cambridge University, commercial mapping companies and various local authorities. Some of these organisations have standardised their search and request systems, which makes the archives easily accessible to public. However, in some cases this standardisation makes it more difficult to deal with specialist demands, for example high resolution scans of photogrammetric quality. Sometimes there is no access to the original negatives or access to a photogrammetric scanner lacking. The main sources for historical photographs in England and Wales are shortly described below; their contact details can be found in Appendix 2.

4.2.1.1   National Monuments Record (NMR)

The NMR is English Heritage's public archive. The NMR holds a collection of around 2.7 million aerial photographs, covering the whole of England from the 1940s to the present day. The collection includes vertical and oblique photographs, flown by the RAF, Ordnance Survey (from before 1980), and also significant additions by Meridian Airmaps Limited and the Environment Agency (Hall *et al.* 2003).

Aerial photo searches are performed free of charge. Unfortunately, the NMR provided no access to the original diapositives of the images, neither appeared in possession of a photogrammetric-quality scanner. Hence, the acquired scans have a low resolution (600 dpi/42 μm) with uncertain geometric quality. Interesting is the comment by Mills (2006), stating that NMR in fact do store diapositives. It seems that either diapositives are only available for part of the collection, or their accessibility is very much restricted.

Often prints are the only media available, since the storage of film is expensive, and many companies destroyed the original negatives for silver recovery

(Chandler 1989). For this reason it was important to include this media format in this study, and assess the data quality that can be achieved from such material.

4.2.1.2   Central Register of Air Photography for Wales (CRAPW)

The Central Register indexes all aerial survey coverage flown over Wales by the RAF, OS and commercial companies and holds an extensive collection of aerial photographs of Wales since the 1940s (Wales on the Web 2006). The collection comprises many of the original films and photogrammetric-quality scans can be supplied.

4.2.1.3   Cambridge University Collection of Aerial Photographs (CUCAP)

The CUCAP is the result of annual airborne survey campaigns conducted by the university since 1947. The collection contains some 500,000 images of which approximately half are obliques (Unit for Landscape Modelling 2001). A cover search can be performed in their online catalogue. Scanned images of photogrammetric quality can be provided as the archive has retained the original negatives.

4.2.1.4   Ordnance Survey (OS)

The OS revises its maps by using aerial photography. In former times this revision process comprised 30.000 maps a year; nowadays these are integrated in digital products such as Mastermap. As a result OS has a comprehensive collection of vertical photographs available. Searches can be performed through any of the OS outlets (Ordnance Survey 2006a). OS photography from before 1980 is available through the NMR for England and the Central Register for Air Photography for Wales (NAPLIB 1999).

4.2.1.5   Agricultural Development and Advisory Service (ADAS)

Originally part of the Ministry of Agriculture, Fisheries and Food, ADAS now is a privatised company. Available cover is widely distributed, including entire counties and national parks, and held in negative form (NAPLIB 1999). However, photogrammetric scans can not be produced in-house.

4.2.1.6   Local authorities

Archives of local authorities such as county councils and national park authorities usually hold aerial photographs of their area. They usually do not posses the original films, but can normally provide contact information of the original sources.

4.2.1.7 Commercial sector

Sources in the commercial sector can provide recent imagery and may hold historical photographs in their archives. Of particular interest is the image library of Simmons Aerofilms, comprising over two million oblique and vertical photographs dating back to 1919 (Simmons Aerofilms Ltd. 2006). The library offers a free online search service. Other companies that produce aerial photography are for example Bluesky, Infoterra and BKS. In general, commercial companies can supply high-quality photogrammetric scans.

It was important to visually inspect the photographs before purchase to assure the coverage and quality. Either photocopies of the frames were requested, or the archive personally visited. The final selection of aerial photographs for purchase was based on the following considerations (in order of importance):

- Ground coverage – The area of interest should be completely covered by stereoscopic overlap of the images.

- Scale – The scale of the photograph determines with what precision photo-coordinates can be measured and what feature sizes can be discerned.

- Geometry – The parallax and hence heighting precision is affected by flying height, airbase, and focal length of the camera.

- Format – Best results are obtained when using high-resolution scans (15-20 µm) of contact diapositives from the original negatives, using a photogrammetric quality scanner. However, as these are not always available, use of scans from contact prints was considered.

- Time – The sequential epochs should be chosen such that they cover periods of significant ground movements.

Costs for aerial photography were variable. In all cases cover searches were conducted free of charge. Sometimes small charges applied to requests for photocopies, or travel expenses were involved in case the institution needed to be visited personally for inspection of the photographs. In general, non-profit organisations supplied photographs at lower prices than the commercial sector. To give an indication, the price for one stereopair of digitally scanned images acquired during this project ranged from £15 (poor-quality scanned contact prints from NMR) up to £75 (high-quality colour scans from Infoterra).

4.2.2 Collecting ground control

Once the imagery was acquired, ground control points were identified and measured. The use of differential GPS is recommended for photoscales of 1/4,000-1/50,000 (Chandler 1999). For the principles of GPS surveying, reference can be made to standard text books (e.g. Leick 1990; Uren & Price 2006); in this section only the practical considerations relevant for this study are discussed.

High-precision geodetic GPS receivers were available for the ground control surveys. Initially, a combination of Leica system 200 and 300 single frequency receivers was used for surveying. During the second case-study a set of two Leica system 500 dual frequency receivers became available. A radio link between the receivers enabled real-time processing, which speeded up the survey and gave the opportunity to check the data immediately. The data was also stored to facilitate post-processing.

The two GPS receivers were used in the 'stop-and-go' mode of surveying (Uren & Price 2006). One of the receivers was fixed on a tripod and served as a base station, while the other (rover) was mounted on a pole and rapidly moved around the area to record the positions of control points relatively to the base station (Figure 4.2). At the start of each session, the rover had to perform an initialisation procedure, requiring about 15 minutes, during which unknown integer

Figure 4.2. Leica System 500 receivers: base station on tripod (left) and rover antenna mounted on pole (right).

ambiguities could be resolved. These ambiguities refer to the differences in phase range between radio signals from different satellites, providing a more precise position estimate than achievable when using only the code information carried by the signals (Uren & Price 2006). As long lock was maintained with the satellites, the rover only needed to collect data over very short time intervals (10-15 sec) at each surveyed point.

The precision of this type of surveying, using phase comparison, is typically 10-20 mm +1 ppm horizontally and 20-30 mm +1 ppm vertically (Uren & Price 2006), but depends on the observing conditions. An important control on precision is the number of satellites available and the geometry of their positions. For this reason it was important to be aware of the changing satellite configuration throughout the day. A satellite availability plot (see example in Figure 4.3) showed the number of satellites available and GDOP values for the selected location and time. GDOP (Geometric Dilution Of Precision) indicates the uncertainty in GPS position as a result of the satellite configuration, and should not be too high during measurements (a GDOP value of 5 and below was considered acceptable). Signals from satellites at angles lower than 15° above the horizon were excluded from processing as these experience excessive systematic effects arising from the atmosphere. It was also recognised that at this latitude (i.e. in the UK) most satellites are in the southern section of the sky, as can be seen in the 'sky plot' below (Figure 4.4). This had implications for the position of nearby mountains or buildings that might obstruct the satellite signals.

Post-processing of the data was performed by using Leica's SKI-Pro software (Version 2.5), revealing the relative positions of the control points to a precision of less than 0.01 m. The National GPS Network enabled the positions to be referenced in ETRS89 coordinates (European Terrestrial Reference System 1989). This network was established by the Ordnance Survey and consists of 30 active stations distributed over Great Britain, with a quoted precision of better than 0.008 m in plan and 0.020 m in height (Ordnance Survey 2006b). From the website (Ordnance Survey 2006b) GPS data of the nearest active station were downloaded. The long continuous observation time of the base station allowed high-precision coordinates to be determined with respect to this active station, and consequently of all surveyed control points. The observation time is a function of distance to the active station, typically in the order of hours (see Figure 4.5).
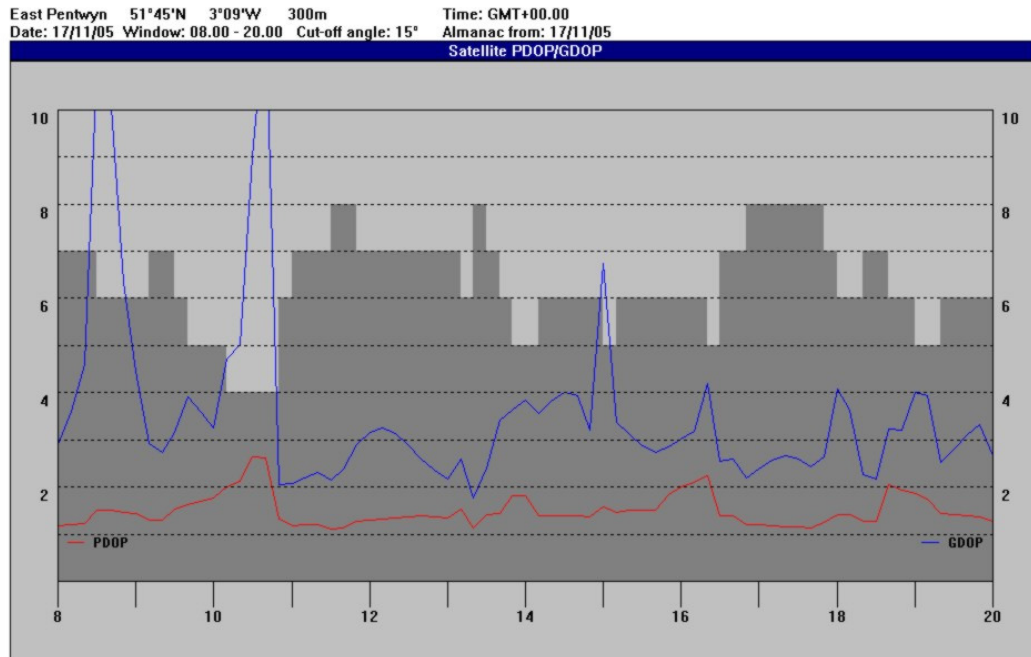
Figure 4.3. A typical plot of satellite availability throughout a day; note the high peaks in GDOP value during the morning which should be avoided for observations. This plot was created using SKI-Pro sofware.
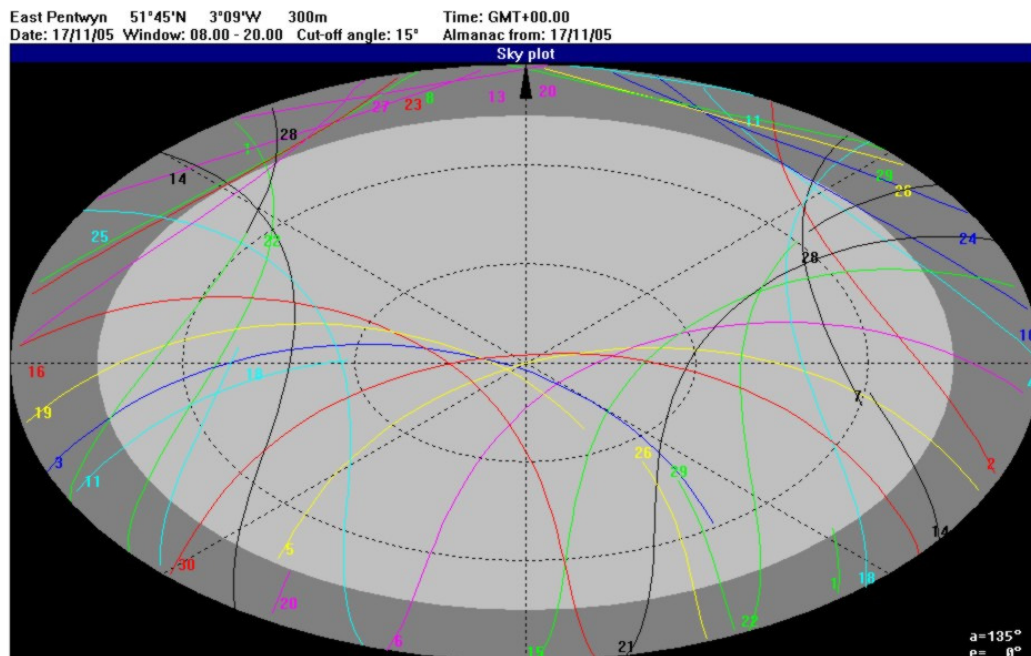
Figure 4.4. A typical sky plot, showing the tracks of satellites throughout a day; note that most satellites are in the southern part of the sky. This plot was created using SKI-Pro software.
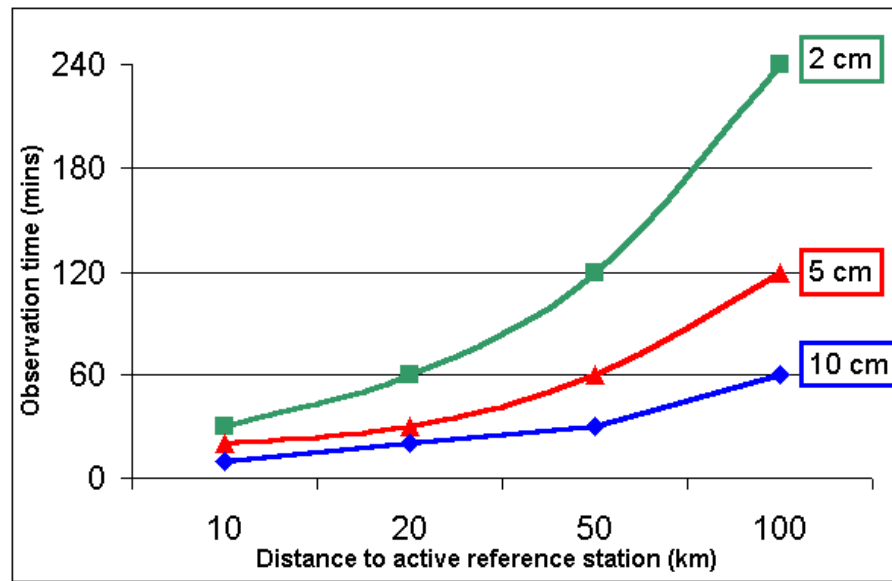
Figure 4.5. Typical GPS observation time as a function of distance to the active reference station (Ordnance Survey 2006b).

The ETRS89 coordinates were transformed into national grid coordinates (OSGB36 datum) by using the online software provided by the Ordnance Survey, Grid InQuest (Version 6.0). Referencing of the data to the National Grid was not essential, but important for comparing with other data sources and possible future use of the data.

Suitable control points were well-defined natural features, easily accessible in the field and clearly identifiable on the photographs. Typically, these points were selected from the photographs prior to the survey, to make sure they were visible on the images.

A minimum of two planimetric and three height points were needed to define a datum, but more control points were desirable as redundancy would provide appropriate checks (Section 3.2.2). Control points were identified evenly over the area to ensure a strong geometry in the photogrammetric models. Because the various image epochs did not cover equal areas and due to logistic matters, the obtained control was not ideally distributed for every epoch. As a consequence of the geographical setting of the landslides, it was also difficult to surround the volume of interest; control was readily accessible in the valleys, but it was more challenging to find suitable targets along the hill ridges. An additional issue associated with using historical photographs is that the measured features must have been stable since the moment of image capture. Typical targets for

ground control were therefore corners of older buildings, stonewalls and gravestones (see for example Figure 5.7 and Figure 6.7).

4.2.3 Photogrammetric processing

During photogrammetric processing the relationship between photo and ground coordinates was established through determination of the interior and exterior orientation of the camera. Most of the photogrammetric work was done using the Leica Photogrammetric Suite (Version 8.7).

4.2.3.1 Restitution

A photo coordinate system is defined by the fiducial marks on each frame (3.2.1). LPS uses a 2D affine transformation to convert the image coordinates of these fiducials to their known photo coordinates. Usually calibrated coordinate values for each fiducial mark were available in the calibration certificate. Sometimes the distances between fiducials were provided rather than their coordinates and these first needed to be converted.

When there was no calibration data available, the fiducials were measured manually. Although definition of the photo coordinate system is often ambiguous, the guidelines by LPS were adopted, with the origin at the centre of the image and the x-axis in the flying direction. Clear reference marks were present at each side or corner of the photographs, and the principal point was simply defined at the intersection of opposite marks. In the case where only three marks were clearly visible, the origin of the system was defined midway between the two opposite marks. The exact choice of the origin is arbitrary as long as it is consistent between the different frames, since any offset from the true principal point would be accounted for in the self-calibration. A similarity transformation was used to correct for translation and rotation during the scanning procedure (Equation 4.1). The photo coordinates of the fiducials were measured in all frames to detect any anomalies; their mean values were used in further processing.

$$x = a_0 + m(x'' \cos\alpha - y'' \sin\alpha)$$
$$y = b_0 + m(x'' \sin\alpha + y'' \cos\alpha)$$

$$(4.1)$$

Where x and y are the photo coordinates; x'' and y'' are the digital image coordinates; a_0 and b_0 are offset of the origin; α is the angle between the two systems; and m is a scale factor.

The interior orientation of the images is further defined by the camera parameters which were available from the calibration certificate or needed to be estimated in a self-calibrating bundle adjustment. Although most of the photogrammetric processing was done in LPS, the self-calibration was performed by using the external program GAP (General Adjustment Program) developed by Clarke and Chandler (1992).

Image coordinates of the control points and an additional amount of tie points were measured in the Point Measurement tool of LPS. The performance of the automatic tie point generator was very dependent on the image quality, but generally it was possible to generate a few hundreds of extra tie points. The coordinates were transformed into film coordinates and together with initial estimates of the orientation parameters exported to GAP. After successful recovery of the interior orientation, these parameters were transferred back into LPS and the processing continued. Transfer of the calibrated values of focal length and principal point offsets is straightforward, but the parameters for radial distortion differ from those used in LPS. Therefore, the polynomial function that models the distortion was used to compute distortion values for a range of radial distances and these were then transferred into the LPS blockfile.

During the bundle adjustment the measurements were constrained by a stochastic model (Section 3.2.3) according to the assumed precision of each measurement. The precision of the ground control and image point measurements was specified in a standard deviation value. Standard deviations for the ground control points were set to 0.01 m, which correspond with the precision of the GPS measurements. For the image points a standard deviation of 0.2 pixels was adopted. This last value was increased in case of poor image quality.

4.2.3.2   DEM extraction

After recovering the photogrammetric model, DEMs could be extracted automatically. The grid spacing of a DEM is limited by the object space pixel dimension and the size of the correlation window used during image matching, default 7x7 pixels in LPS. The success of the matching process could be influenced by a number of strategy parameters; among these were the search window size, correlation window size and correlation coefficient limit. The optimal search window size along the epipolar line (x-direction) was estimated according to a formula given in the LPS User's Guide (Leica Geosystems 2003), reflecting the variation of

ground elevations in that window. As for aerial images the epipolar line usually can be computed accurately, three pixels in cross-direction (y) were sufficient. Generally, the default values for DEM-extraction parameters were used; in images with low contrast the correlation coefficient was lowered in order to increase the number of mass points collected.

4.2.3.3   Orthophoto generation

The original images and the extracted DEM were used to generate orthophotos. Nearest neighbour resampling was applied, and a ground pixel size selected depending on the resolution of the original images. Since ground resolution varies within an image due to elevation differences, the ground resolution at the centre of the landslide was chosen to be an optimal pixel size.

4.2.4 Data quality assessment

The quality of the photogrammetric solution and resulting products can be evaluated in a number of ways.

The bundle adjustment provides residuals of the control points, which reflect the difference between measured coordinates and newly estimated values (based on the estimated exterior orientation parameters and measured image coordinate values). Relatively large residual values are indicative of errors in the photogrammetric network of observations (attributed to faulty measured control points, data entry errors, poor quality of control points, or poor camera calibration; see Sections 3.6.2 and 3.6.3). Control points with large residuals were corrected or removed until a optimum solution was achieved. This is a highly interactive and subjective procedure. In general, residuals greater than the pre-defined standard deviation of the measurement were considered suspicious. However, removal of too many control points would weaken the reliability of the photogrammetric model, especially if many parameters were to be estimated. In case there were obvious causes for errors, such as poor camera calibration, it was justified to accept larger residuals (e.g. a size of two or three standard deviations).

A crude but useful global measure of the solution effectiveness was provided by the standard deviation of the residuals of control points. As mentioned in Section 3.6.2, only the mean and standard deviations of the residuals of checkpoints provide a truly independent measure of accuracy. These statistics were all available from the triangulation reports in LPS.

There are also a number of ways to assess DEM quality. Visual inspection of the mass point distribution indicates areas where automatic image matching failed, mainly in areas of steep relief (due to relief displacement) or low reflective contrast (Section 3.6.2). LPS provides an option to create a DEM point status image, based on the correlation value of an image match, and neighbouring DEM points. Points classified as 'isolated' and 'suspicious' correspond to areas lacking mass points. However, it was experienced that these point status images can be misleading, as they show the status of the mass points, not of the DEM pixels. Hence, in areas lacking mass points the pixels values may exhibit a "good" status, when this area is merely surrounded by "good" mass points. This disguises that these pixels were in fact interpolated from surrounding points, sometimes at great distance.

An independent measure of DEM accuracy was provided by the statistics of check points, available from the DEM extraction report in LPS. However, some limitations of these measures for accuracy assessment were explained in Section 3.6.2.

A semi-independent but more inclusive way of evaluating DEM quality was achieved by comparing DEM elevations from different stereopairs within the same epoch. Statistical analysis of the errors revealed the magnitude of systematic (mean) and random errors (standard deviation). This analysis should only be applied if the data is free of gross errors in the DEM, which was rarely the case in the entire overlap region.

Ideally, a DEM of higher accuracy from a different source should be used for rigorous accuracy assessment. Unfortunately there were no alternative DEM sources available for this study. Alternatively, DEMs derived from different image epochs could be compared, on condition that only stable terrain was involved in the analysis. This approach was applied in the analyses of 'DEMs of difference' for removing systematic errors between different DEMs (see Section 4.3.2).

The positional accuracy of orthophotos was evaluated through measuring the positions of checkpoints and computing their mean and standard error.

4.3 Quantify and visualise landslide dynamics

The use of sequential photography and their products offered various ways of visualising and analysing the geomorphological change occurring on landslides, and

the responsible mechanics. Usefulness of these methods depended on the type of mechanisms under investigation and the data quality. The following products were evaluated to their value to landslide studies:

- Geomorphological maps

- 'DEMs of difference'

- Displacement vectors

- Animations

4.3.1 *Geomorphological maps*

Sequential geomorphological maps were produced to show the progressive development and displacement of surface features. For this research it was decided to emphasize morphogenetic aspects in the geomorphological legend, since the aim is to gain a better understanding of landslide mechanisms. The primary aim was to identify different morphological elements in the landslide body that may correspond to specific movement styles. Geomorphological boundaries were identified through three-dimensional viewing of the photographs in ERDAS Imagine's Stereo Analyst. The geomorphological features were mapped onto an orthophoto to assure geometric accuracy, and the possibility for quantitative comparison of the maps obtained from different epochs.

Figure 4.6. Legend used for geomorphological mapping.

4.3.2 *'DEMs of difference'*

'DEMs of difference' were created by subtracting a DEM of one epoch from another, depicting vertical displacements of the terrain surface (Section 3.7.2). The 'DEMs of
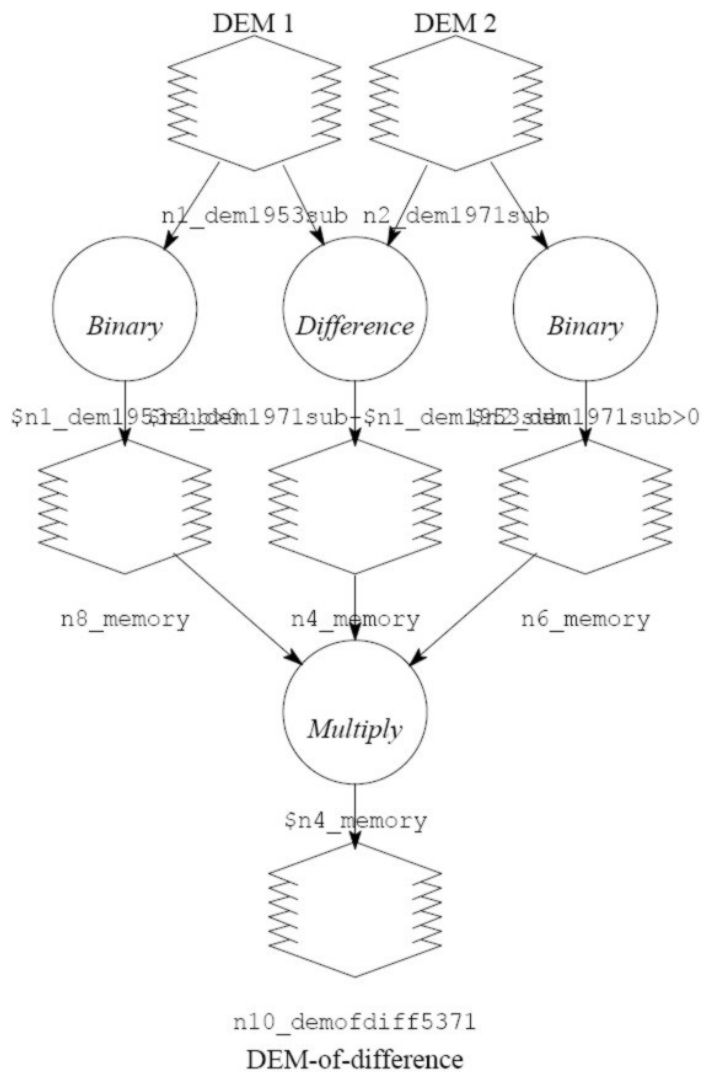
Figure 4.7. Graphical model for generating a 'DEM of difference'. The result was
multiplied by binary maps to avoid erroneous values in case of no-data values in any
of the DEMs.

difference' could be generated using a simple graphical model in ERDAS Imagine
(Figure 4.7).

Although systematic errors in the DEMs were minimised during the bundle
adjustment procedure, unresolved errors may still be present in the 'DEM of
difference'. These remaining systematic errors could be quantified in stable 'control
areas', interpolated to an error surface (using the 3D surfacing tool in Erdas
Imagine) and then subtracted from the original 'DEM of difference', analogous to
the method by Betts *et al.* (2003) described in Section 3.7.2. However, this simple

approach did not account for the gross errors due to mismatches and poor interpolation in areas of low contrast and steep relief (Sections 5.5.2 and 6.5.2).

4.3.3 Displacement vectors

The measurement of displacement vectors required identification of identical features on different sets of photographs. The ERDAS' Stereo Analyst tool was used for 3D viewing of the stereopairs, and manual measurement of features. Alternatively, points could be measured in LPS and processed as tie-points in the bundle adjustment, thereby providing estimates for the ground coordinates, but this latter approach was more laborious. It was recognised that the vertical precision of the data was rather limited in relation to expected elevation change so that only horizontal displacement vectors were achievable (Sections 5.5.3 and 6.5.3).

The significance of the vectors was assessed by evaluating measurements in stable areas. The magnitude of apparent displacements of control points, which were reasonably assumed to be stable during that period, gave an indication of the error arising from the measurement approach. Covariance matrixes were created, based on the differences in coordinates of these points between the epochs. Based on these covariance matrices, error ellipses were created and plotted over the initial points, so that vectors piercing the ellipse depict significant displacements at the specified confidence level (Cooper 1987). A script was written in Matlab for plotting the vectors and error ellipses.

The point measurements could be interpolated to a continuous grid surface or a contour plot of displacement, using an 'Inverse Distance Weighted' interpolation function in ArcView. However, such an interpolation would only be meaningful if the point distribution was sufficiently dense.

As part of this study automation of the procedure was explored. An image matching algorithm was developed in Matlab that was able to match features in orthophotos from different epochs, and determine their displacements.

The image matching procedure basically involved two stages. Firstly, suitable features were identified in one image. Because image matching requires sufficient image contrast (Section 3.3), the selection of appropriate points was based on image texture. Image texture was characterised through applying a filter operation to the image. The simplest form is a Laplacian filter, which calculates the

2nd spatial derivative of an image, highlighting regions of rapid intensity change and is therefore often used for edge detection. This filter operation results in zero values for uniform regions, while contrast-rich areas give large values. Since Laplacian filters are sensitive to noise they are often applied in combination with a smoothing filter (e.g. using a Gaussian filter) to reduce noise (Matthys 2001). The Laplacian of Gaussian (LoG) operator can be described by Equation 4.2 and is shown in Figure 4.8.

$$LoG(x, y) = -\frac{1}{\pi\sigma^4}\left[1 - \frac{x^2 + y^2}{2\sigma^2}\right]e^{-\frac{x^2+y^2}{2\sigma^2}} \qquad (4.2)$$

Where x and y are pixel coordinates and σ is a specified standard deviation.
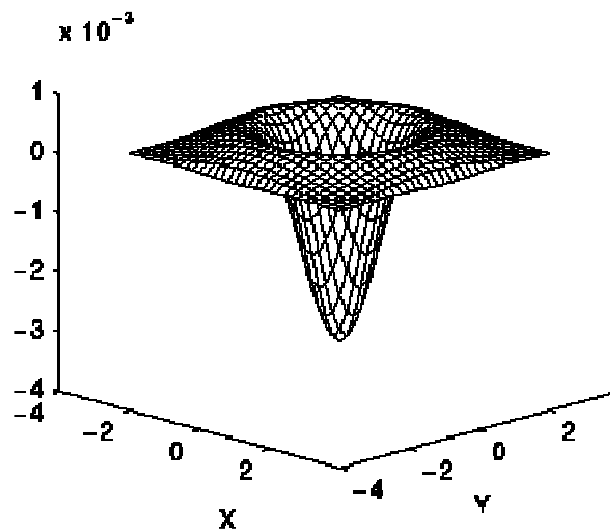
Figure 4.8. The 2D Laplacian of Gaussian (LoG) function; the x and y axes are marked in standard deviations σ (Fisher et al. 2003).

After applying a 7x7 LoG filter, points with maximum texture were selected. These points were searched within a predefined window size, and subject to a specified threshold. Pixel locations of selected points were stored in a binary image.

In the second stage, a search in the other image was performed for each selected point using a correlation technique, as described in Section 3.3. Since geometrical differences were already removed through orthorectification, a simple normalised cross-correlation algorithm was considered to be appropriate. Another advantage of using this technique was that it is a standard function in Matlab, and therefore easy applicable. A match was accepted if the correlation coefficient exceeded a predefined threshold value. The location of the match was determined

to sub-pixel precision by using a centre of gravity (or centroid) operator. The centre of gravity was found through taking into account the neighbouring pixels, weighted according to their correlation values (Equation 4.3, Russ 2002). Only pixel values larger than an arbitrary threshold of 90% of the matched pixel were incorporated.

$$CG_x = \frac{\sum_i c_i x_i}{\sum_i c_i}$$

$$CG_y = \frac{\sum_i c_i y_i}{\sum_i c_i}$$

$$(4.3)$$

Where CG is the centre of gravity location; c is the pixel correlation value; x and y are coordinates of the pixel.

After a successful match was established and its position determined, the displacement of the point was simply calculated through subtracting the second pair of coordinates from the first one. Results were written to a data file and plotted on one of the orthophotos. Error ellipses were plotted around each vector, using the script described above.

The success of the matching procedure depended on the arbitrary values for the various window sizes and thresholds used, and on the quality of the images. During the first phase, the LoG filter size was chosen according to the size of features in the image, such that their edges could be detected while image noise was ignored. A suitable texture threshold value was dependent on the image contrast, but in general a value of 220 (when values scaled between 0-255) was satisfying. The window size for searching points of maximum texture merely controls the number of points to be selected and associated processing time. The parameters in the second stage are more crucial. Template size is very important and was selected according to the size of features in the image; small templates reduce the chances on a unique match, but large templates increase the processing time. Search window size was based on the maximum displacement that could be expected between the images; a larger size would lead to unnecessary processing time. The minimum correlation value to accept a match was also important; a low value would result in many mismatches, but due to different image qualities high values may be difficult to achieve.

The algorithm was successfully tested on an orthophoto of Loughborough University Campus, in which part of the image was manually shifted. The results of this experiment are displayed in Figure 4.9 and Table 4.1. Statistical analysis of the measured vectors correctly show insignificant displacements of the stable image points, while the shifted points show movements of a magnitude reasonably close to their real values (average values of 5.91 (x) and 7.64 (y) m, compared to real displacements of respectively 5 and 10 m).

The Matlab scripts are included in Appendix 3.

4.3.4 Animations

Sequential images were combined in animations to illustrate the progressive development of the terrain surface. These image sequences could for example consist of orthophotos, 'DEMs of difference', or displacement fields. Shareware software was readily available and had the ability to rapidly generate animations in different format, such as animated GIF or video files.

Erdas Imagine's Virtual Viewer has a tool for creating 'fly-throughs'. A fly-through over a 3D-model of an orthophoto draped over a DEM provided a very realistic impression of the study area. This proved a very useful product for exploring the site without the need of actually visiting it. Fly-throughs can be stored in common media formats and are therefore easy accessible for a wide public.

Such powerful visualisations can exclusively be acquired by using photogrammetric techniques, adding a big advantage of photogrammetry over other surveying methods. Some examples of animations were published on a website (Walstra 2006).

4.4 Use data for landslide mechanisms

This objective involved interpretation of the acquired data in such a way as to lead to a better understanding of landslide mechanisms. Also, the results were compared with independent data from other studies. This part of the study should prove the value of photogrammetrically derived data for landslide investigations.

4.4.1 Landslide mechanisms

The photogrammetrically extracted data was used in various ways to quantify landslide dynamics. 'DEMs of difference' were used to identify areas experiencing
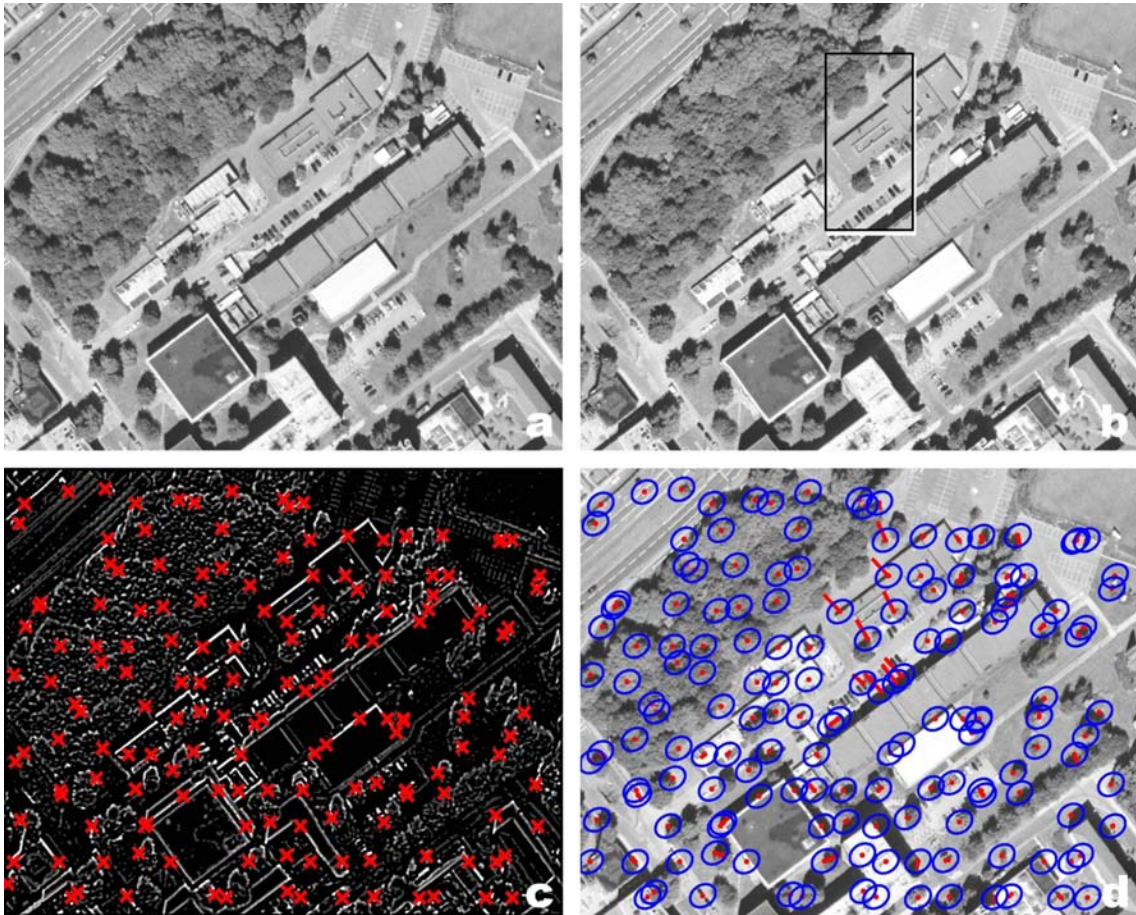
Figure 4.9. Testing the Matlab script on two orthophotos of LU campus (a & b). In one of the images (b) a small sub-area has been shifted (10 pixels vertically, 5 pixels horizontally. Image (c) was created through applying a 7x7 LoG filter; red crosses mark the selected points (based on maximum texture within an 80x80 window, scaled value > 240). Image (d) shows the successfully matched points (using a search window size of 25, template size of 7x7 pixels and a correlation threshold of 0.90), their displacement (5x image scale), and error ellipses (at 95% confidence level).

Table 4.1. Statistics of measured displacements of stable and manually shifted image points, using the Matlab script.

	Number of measurements	Displacement (x)	Displacement (y)
Stable points	146	0.17 ±1.08	0.10 ±1.20
Shifted points	9	5.91 ±1.51	7.64 ±1.48

removal or accumulation of material, manifested as respectively negative and positive changes in elevation (Section 3.7.2).

The spatial pattern of surface displacements provided information on the type of movement. Visual inspection of contour plots of displacements revealed zones of lateral extension or compression, coinciding with areas that show respectively increasing and decreasing movement downslope (3.7.3). A more rigorous approach for strain analysis was described in Section 2.4.4, but this was beyond the scope of this study. It was also shown that shape and depth of the slip surface could be estimated based on surface displacements (Section 2.4.4). However, this required accurate data in both horizontal and vertical directions, something that could not be achieved in the described case-studies (Sections 5.5.3 and 6.5.3).

Geomorphological maps of the study areas provided a qualitative interpretation of the landslide processes, which proved very helpful in analysing the quantitative data.

Interpretation of the extracted data would only be meaningful if the accuracy was taken into account. For this reason assessment of the data quality (Section 4.2.4) was critical.

4.4.2 Compare with other work

The availability of alternative data sources such as site investigation and monitoring reports gave the opportunity to compare the results with independent data. In order to be meaningful, the compared monitoring data should be restricted to similar entities in time and space. Therefore, survey data referenced in different coordinate systems had to be transformed into OSGB coordinates. A 3D similarity transformation was applied to the monitoring data, using a simple executable file. Three points with known coordinates in both systems were required in order to define the transformation. The positions of these three monitoring points could only be approximately identified on the photographs. But absolute positioning of the surveyed points was not essential; only the accurate, relative position of points through time was important. Suitable features in the image that were used for the comparison were identified within a distance of a few meters. It was considered reasonable to assume that movements within that area were uniform.

Another issue to be addressed was the difference in measurement frequency between different sources. Often ground survey monitoring schemes included

yearly or even more frequent measurements, while the time span between the image epochs was much larger, usually in the order of 5-10 years. Direct comparison would be possible if absolute displacements were averaged to yearly rates, but the yearly variation would still be undetected by the photogrammetrically acquired data.

4.5 Summary

This chapter explained in detail the strategies for fulfilling the aims and objectives of this study. Firstly, the procedure of selecting two suitable field sites was described: Mam Tor for developing techniques and East Pentwyn for validation. The selection criteria for these sites were identified and fully discussed.

The second section dealt with the most exhaustive part of this study, namely the extraction of morphological data from aerial photographs. This included the search for suitable imagery in archives and their acquisition, collection of ground control by using differential GPS systems, digital photogrammetric processing, and assessment of data quality. Important issues were identified regarding the use of historical photographs, which inevitably would have implications for the data accuracy that could be achieved. It was considered of great importance to evaluate the effects of different photographic parameters on the resulting data quality.

Following, methods were described to create a range of products that could potentially be used for visualising and quantifying landslide dynamics, including geomorphological maps, 'DEMs of difference', displacement vectors and animations. Special attention was paid to extraction of displacement vectors using automated image processing.

The final stage comprised interpretation of the extracted data in terms of landslide mechanisms. It also described how results were compared to independent data. The findings from these analyses in the following two case-studies feed into the discussion in Chapter 7, which evaluates the value of the described methods.

Chapter Five

5 Case study Mam Tor

This chapter describes a case study on the Mam Tor landslide. This site was used to develop and test the various techniques, as described in the previous chapter. The site has been subject to frequent investigations in the past, and hence offers the potential to compare the results from this study with other data sets. There is an extensive range of historical photography available, which makes it possible to evaluate the results in the context of varied photo quality.

Firstly, a brief description of the landslide is given, including a summary of previous work. Then, the acquired photographs are presented and the procedures for necessary fieldwork and photogrammetric restitution are explained. In the last part of this chapter, the extracted data are visualised, analysed regarding the landslide dynamics, and compared with other data sets. A fuller discussion of the implications of these results will follow in Chapter 7.

5.1 Site description

The landslide is situated on the eastern flank of Mam Tor, a 517m high hill, at the head of Hope Valley, Derbyshire, UK (Ordnance Survey coordinates SK135835, Figure 5.1). The former main road between Sheffield and Manchester, the A625, was constructed across the slide, but abandoned in 1979 as a consequence of

continual damage due to the moving ground mass. The primary failure was a rotational landslide, which broke into a complex of blocks and slices while advancing downhill. Continuing disintegration of the front slices created a debris mass, flowing further down. There is evidence that present movements are not continuous but accelerate during wet winters, when rain-fall exceeds certain limits (Waltham & Dixon 2000). According to Varnes' scheme (Section 2.2) this landslide can be classified as a slump-earthflow type.

Figure 5.1. The Mam Tor landslide: head scarp on the right, debris slide on the left side, and the abandoned road crossing the slide area in the central area.

5.1.1 Geology

The upper slopes of Mam Tor consist of predominantly sandstone sequences, belonging to the Mam Tor Beds. They overlie the dark shales and mudstones, known as the Edale shales. Both stratigraphic units are of Namurian age, and dip roughly to the north at 5-15°. The underlying limestones outcrop just south of Mam Tor, forming a plateau. A mineral vein crosses the northern tip of the limestone outcrop and has been worked for about 700 years until mining ceased in 1869 (Ford & Rieuwerts 1976); remnants of the Odin mine are still visible just south of the landslide. A minor fault cuts through the landslide zone, but dies out before reaching the north boundary of the landslide. Evidence from boreholes shows that the bedrock beneath the landslide has not been shifted (Skempton *et al.* 1989).

A few scattered traces of till are evidence of early glaciations, which might have contributed to oversteepening of the face of Mam Tor. During the last glaciation, Hope Valley was ice-free and periglacial activity produced solifluction

sheets, which are still covering the valley floor. These head deposits are up to 2.7 m thick and consist of clay material containing fragments of sandstone (Skempton *et al.* 1989).

5.1.2 Morphology

The landslide is large, measuring 1,000 m from head scarp to toe, while elevation drops from 510 to 230 m O.D. From borehole data it can be concluded that the maximum depth of the failure surface is at 30-40 m (Skempton *et al.* 1989). Volume of the slipped mass is estimated at 3.2 Mm^3. The slope of the original hillside would have been 30-35°, whereas the mean slope of the landslide mass is about 12° (Skempton *et al.* 1989). A plan and cross-sections of the site are shown in Figure 5.2 and Figure 5.3.

The scarp face stands at an average slope of 45° to a height of 80 m in the Mam Tor Beds. At its foot, scree extends down onto the slide mass. According to Waltham and Dixon (2000), the landslide mass can be divided in three distinct zones, typical for rotational failures (see Section 2.3.2):

1. The upper part consists of a series of rock slices produced by a non-circular rotational failure in the original slope, exhibiting little movement at present. The back-tilted strata dip at angles from 30-50°. In boreholes two closely spaced slip surfaces have been recognised, immediately above unweathered mudstone. Blocks of sandstone in the debris demonstrate a displacement along the slip surface of approximately 160 m (Skempton *et al.* 1989).

2. The transition zone is composed of an unstable complex of blocks and slices overlying the steepest part of the landslide's basal shear surface. In this zone, the foot of the slump is transformed into the head of the earthflow. The shear zone is at relatively shallow depth, on top of the weathered mudstone (Skempton *et al.* 1989). At present, this is the most active part of the slide, moving on average 0.35 m/yr (Rutter *et al.* 2003).

3. A debris flow with an average slope of 8°, formed by disintegration of the lower part of the slide mass. This part has moved in translation over the original ground surface. The surface is hummocky, with transverse ridges in the upper part. Due to high groundwater levels there are marshy vegetation and ponds present (Skempton *et al.* 1989).
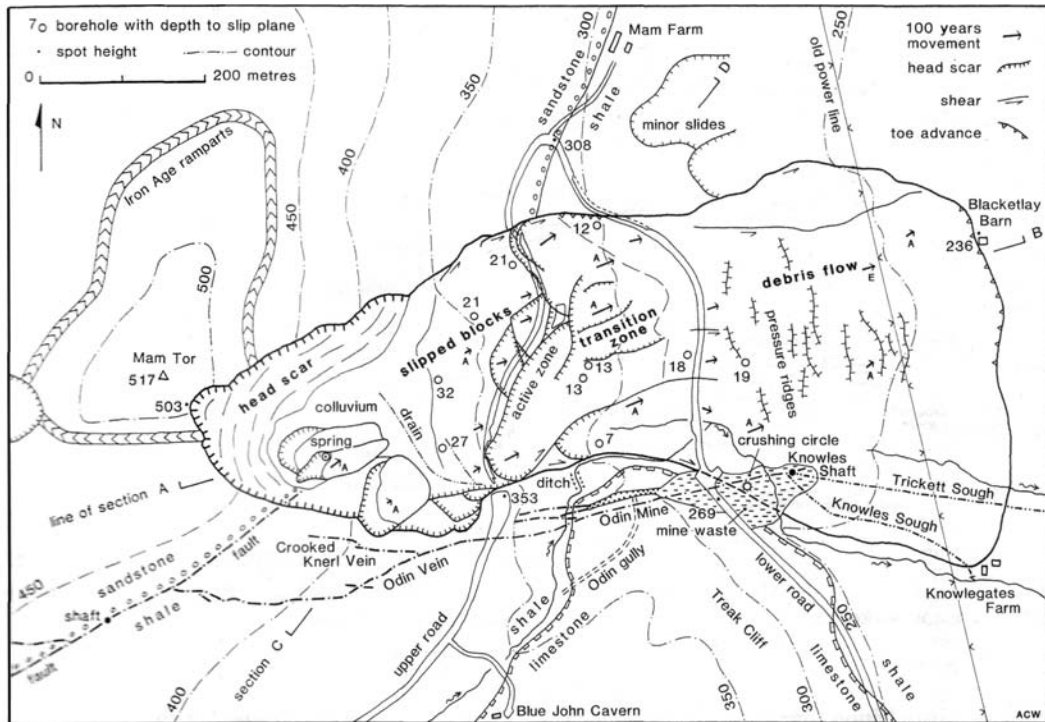
Figure 5.2. Plan of the Mam Tor landslide (Waltham & Dixon 2000).
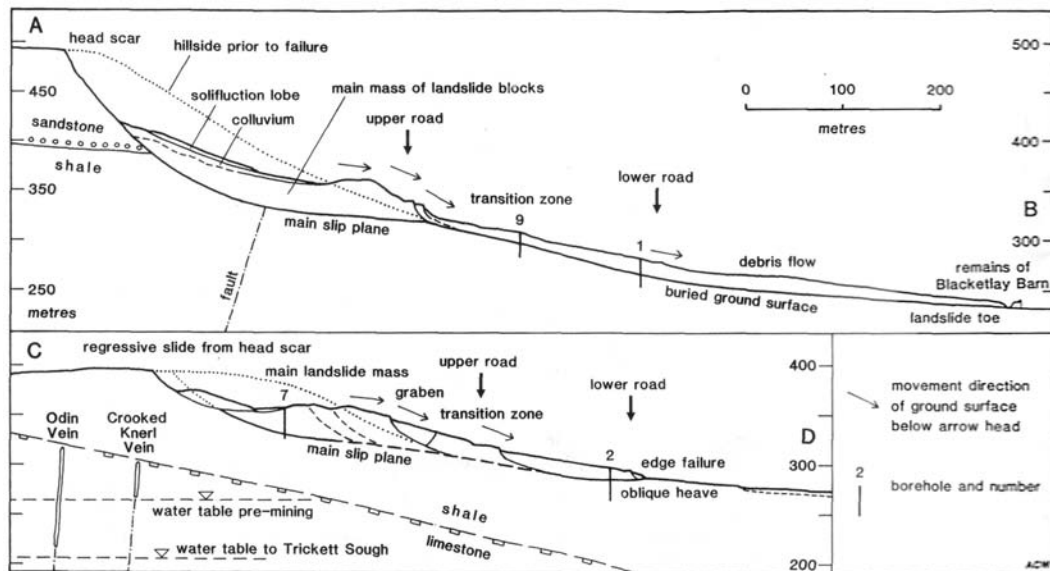
Figure 5.3. Cross-sections through he Mam Tor landslide along lines indicated in Figure 5.2 (Waltham & Dixon 2000).

Based on its surface geomorphology the landslide can be further divided in 16 component elements (Waltham & Dixon 2000), see Figure 5.4).

5.1.3 Movement history

Evidence for the age of the landslide is provided by a tree root found in a borehole in an old soil, overridden by the toe debris. Radiocarbon dating of the root (3200 ±200 years BP) and extrapolating the landslide movement back in time reveals an estimated age of 3600 years (Skempton *et al.* 1989).

key	landslide element	movement mm/year	dip of basal shear
A	Head scar in Mam Tor Sandstone, north of fault	0	~50
B	Head scar in Edale Shale, south of fault	0	~35
C	Scree, colluvium and fans below head scar; partly covering upper end of slide complex H	-	-
D	Solifluction lobe within scree and fans	?	~25
E	Subsidiary solifluction lobe within D	high	~25
F	Regressive slide block from shale head scar	low	~30
G	Group of four minor regressive slides	very low	?
H	Main complex of multiple slide blocks; component sections not currently definable	107	6
J	Graben block descending between H and K	154	23
K	Subsidiary block active on front of H	177	20
L	Main active frontal block	234	29
M	Northern active frontal block	248	21
N	Central zone of active multiple blocks; individual boundaries not clearly definable	high	10
P	Southern edge degenerated into active debris flow; boundary to T not clearly definable	93	8
R	Main active toe debris flow; boundary to T not clearly definable	149	~5
T	Less active southern part of toe debris flow	very low	~4

Figure 5.4. Main elements of the Mam Tor landslide. Movement rates of each element are averaged values and obtained from ground surveyed monitoring data (Waltham & Dixon 2000).

The road across the landslide was constructed at the beginning of the 19th century, replacing the steeper route through the nearby Winnats Pass. The road became the main connection between Sheffield and Manchester, but difficulties arising from ground movement were soon experienced. Notes about regular disturbance and repairs of the road, from 1907 until the final closure in 1979, are kept by the Derbyshire County Council. After major movements in 1977, a survey and stability analysis was carried out. The findings of this site investigation were published in a paper by Skempton *et al.* (1989). Historical records of movement and rainfall data were analysed, groundwater levels monitored, boreholes drilled, soil strength parameters measured, and a stability analysis executed. The study showed a clear tendency of instability during wet winter seasons with rising ground water table. Stability analyses of possible slip surfaces showed that various parts of the slide are delicately balanced in a state close to limiting equilibrium with groundwater level at about the normal winter maximum.

The County Surveyor recommended drainage of the landslide and road repairs in accordance with Skemptons report (Derbyshire County Council 1978). However, replacement of the route was favoured. Decisions were delayed by budget constraints, and eventually the idea was abandoned when it was realized that traffic patterns had successfully adapted to the loss of the Mam Tor road (Waltham & Dixon 2000). The road has to date not been reopened.

The displaced and tilted road sections provide a spectacular example of the destructive impact that landsliding can have on man-made structures. Evidence of continual resurfacing of the road is clearly visible by the thick layers of tarmac that are exposed (Figure 5.5). Blacketlay Barn, at the north-western margin of landslide, was reported to be destroyed in 1983, when the slide toe advanced into it (Waltham & Dixon 2000). Remnants of a power line placed across the toe in the 1940s are now 6 m out of line (Waltham & Dixon 2000).

After final closure of the road, monitoring schemes were set up by various institutes: 1981-83 by Sheffield University, 1990-98 by students from Nottingham Trent University and since 1996 by Manchester University.

Researchers from Sheffield University monitored the movement of 21 survey points across the whole landslip area through repeated Electromagnetic Distance Measurement (EDM) surveys. The monitoring period spanned only a short time (Oct

Figure 5.5. Thick layers of tarmac, exposed in the upper road section.

1981- May 1983), but was sufficient to detect increased movement rates during wet periods and variability between different parts of the landslide (Al-Dabbagh 1985).

Nottingham Trent University started regular monitoring by repeated surveys in 1990. A chain of 46 monitoring points was established along the upper road section and from 1994 another 20 stations along the lower road. The points were surveyed each year by final year students, using theodolites and total stations. These surveys provided a vast amount of data, which have been summarised in Waltham & Dixon (2000). Movement rates for seven representative points across the landslide are displayed in Table 5.1. The recorded movement patterns are consistent with the distinguished landslide elements in Figure 5.4.

Since 1996 researchers from Manchester University have carried out annual monitoring by EDM of a network of about 30 stations on the landslide (Rutter *et al.* 2003). Some of Nottingham Trent University's stations were reoccupied and additional stations established off-road. Recent movement rates were found to be up to 50 cm/yr. Comparison with an old topographic map surveyed in 1880, gave an impression of longer-term movements: the lower road section was transported 40 m eastwards (35 cm/yr), while the displacement of the upper section was only about 5 m (4 cm/yr). These values are much higher than the long-term estimates in Skemptons report (Skempton *et al.* 1989).

Table 5.1. Summary of absolute displacements of different elements within the Mam Tor landslide (Waltham & Dixon 2000).

Monitored points	Landslide element	Annual movement (mm)		
		Mean	Wet Year	Dry year
Main complex of multiple slide blocks				
06	H	118	324	30
13	J	154	424	35
18	K	177	454	49
Active frontal blocks				
03	L	234	567	37
36	M	248	658	56
Toe debris flow				
B7	R	149	324	90
G2	P	93	200	62

The ratio of horizontal to vertical movements varies over the landslip, with larger vertical displacements occurring in the upper part. To some extent this pattern reflects the slope of the basal slip surface, but the effect of lateral variations in shear should also be considered. Rutter *et al.* (2003) used their network of measurement station for strain analysis within the slide mass. After correcting for the effects of strain, the ratio of vertical to horizontal displacements proved a good estimator of the basal slip surface, consistent with the dips defined from boreholes by Skempton *et al.* (1989).

These ground surveyed data are valuable because they provide independent field data to compare the photogrammetrically acquired movement data to (see 5.5.4).

5.1.4 Correlation with rainfall data

Skempton *et al.* (1989) suggested deceleration of movement towards an ultimately stable situation, analogous to other landslides in the region. However, the measurements by Waltham & Dixon (2000) and Rutter et al. (2003) indicate that at present, and for the past 120 years, movement rates were significantly higher than the long-term average. According to Rutter *et al.* (2003) loading of the ground mass with the construction of the road since 1810 is unlikely to be of significant influence. The authors suggest that higher groundwater levels associated with higher winter rainfall during the past 500 years is more likely to have had an effect.

Studies on Mam Tor all imply a relationship between wet winters and accelerated movement (Waltham & Dixon 2000). In the central part the movement is only about 60 mm in dry years, while about 500 mm in wet years. Correlation of movement records with rainfall data shows that the rate of movement does not rise in direct proportion to rainfall, but sharply increases once critical thresholds have been exceeded. The movements appear to be most closely correlated with the preceding 1 and 6 months of rainfall: increased movement occurs when rainfall exceeds 210 mm in one calendar month in winter (which is >50% above mean), when following a 6-month period with more than 750 mm (which corresponds to an average amount). The return period of accelerated movements is close to four years. Little data is available about the response of the earth flow to rainfall, but it is suggested that the movement is more readily being maintained during drier winters.

5.2 Acquired photographs

A search for aerial photography of Mam Tor revealed a large number of images available from 1947 until present. The criteria that were used for selecting suitable epochs have been described in Section 4.2.1. It is obvious that all acquired images should cover the landslide area. From a geotechnical perspective it was desirable to have an extensive sequence, separated at regular intervals, to obtain a complete record of the development of the landslide. From a photogrammetric perspective it was of interest not just to acquire the best-quality photographs, but a variety in format (i.e. size, type of film, etc), scale, media and quality, as this would provide an indication for the potential of the applied techniques to commonly available material.

From the NMR two epochs, RAF imagery from 1953 and Ordnance Survey images from 1971 were acquired. Although an easily accessible archive, the quality of the provided data was rather limited. Lacking possession of the original diapositives and a photogrammetric scanner, only poor-quality scans of contact prints could be provided. Also, there was no camera calibration data available for these epochs. These limitations gave rather low expectations in terms of data accuracy that could be achieved.

The CUCAP proved a very fruitful source from which four different epochs were acquired. The combination of a set of vertical images and a series of obliques,

both acquired at the same time (1973), provided an excellent opportunity to compare results that can be achieved from using oblique and vertical imagery. The other epochs were dated 1990 and 1995, the latter adding another variable in the image sequence, namely colour as opposed to black-and-white. Camera calibration data of the verticals were available and high-resolution (15 μm) photogrammetric-quality scanned diapositives could be provided, hence the requirements for quantitative analysis were met.

The image sequence was complemented by 1984 photographs from ADAS. This epoch consists of rather small-scale black-and-white images. Lacking a photogrammetric scanner, hardcopy diapositives were obtained and scanned by the staff from the CUCAP library.

Finally, the sequence was completed with a recent set of colour images, dated 1999, acquired from Infoterra. This addition was of particular interest regarding the comparison between photogrammetrically derived data and the ground surveys from the 1990s.

Summarising, a total of eight image epochs were acquired, forming a complete time series of 46 years in length and representing a very wide variety of images, with different scale, scan quality, black-and-white or colour, contact print or diapositive, vertical or oblique (see Table 5.2).

Table 5.2. Characteristics of the acquired photographic epochs.

Date	Source	Scale	Focal length	Scan resolution	Ground resolution	Image type**	Format	Original media
1953	NMR	1/10,700	547 mm*	42 μm	0.45 m	B/W Vertical	18x21 cm	Contact prints
1971	NMR	1/6,400	304 mm*	42 μm	0.27 m	B/W Vertical	23x23 cm	Contact prints
1973	CUCAP	1/4,300	153 mm	15 μm	0.065 m	B/W Vertical	23x23 cm	Diapos.
1973	CUCAP	Oblique	207 mm*	15 μm	-	B/W Oblique	12x13 cm	Diapos.
1984	ADAS	1/27,200	152 mm	15 μm	0.41 m	B/W Vertical	23x23 cm	Diapos.
1990	CUCAP	1/12,000	153 mm	15 μm	0.18 m	B/W Vertical	23x23 cm	Diapos.
1995	CUCAP	1/16,400	152 mm	15 μm	0.25 m	Colour Vertical	23x23 cm	Negatives
1999	Infoterra	1/12,200	153 mm	21 μm	0.26 m	Colour Vertical	23x23 cm	Negatives

* estimated values from self-calibration.
** B/W = black-and-white.

5.3 Ground control collection

Ground control was collected through a differential GPS survey using two geodetic GPS receivers (Leica System 200 and 300), as described in Section 4.2.2. The base-station was located on the grounds of the Hollowford Centre in Castleton. Clusters of points were distributed evenly over the entire area and in particular, closely located around the periphery of the landslide. Typical control points were corners of buildings and stonewalls that appeared to have remained unchanged for the past 50 years (Figure 5.7). The danger of using buildings for control was that they obstruct part of the sky, thereby reducing the amount of 'visible' satellites. But, as was explained in Section 4.2.2, the satellite geometry for these latitudes usually allows good measurements of the south-facing sides of buildings.

GPS data from the active station in Leeds (nearest, at 50 km distance) were downloaded from the National GPS Network website, and used for the post-processing (see Section 4.2.2). The data from 27 control points were successfully processed to a precision of less than 0.01 m. As a check, the position of the base station was also processed relative to active data from Nottingham (at 59 km distance). The coordinates showed a difference of about 0.5 m in plan, which was much larger than the accuracy quoted by Ordnance Survey. In a later stage, it was recognised that this discrepancy was most likely caused by the inability of the software to model tropospheric/ionospheric effects for such long baselines. IGS precise orbit data are available on the worldwide web and should be used in conjunction with the active station data to correct for these effects during post-processing and achieve optimal accuracy.

Although the referencing of this survey to the global coordinate system had a lower accuracy than was initially expected, this did not affect the relative accuracy of the control points as the base line distances within the survey network were only few kilometres. Eventually, the ETRS89 coordinates were converted to National Grid, ready to be used as control and check points in the photogrammetric processing. The distribution of the control and checkpoints is conveyed in Figure 5.6.
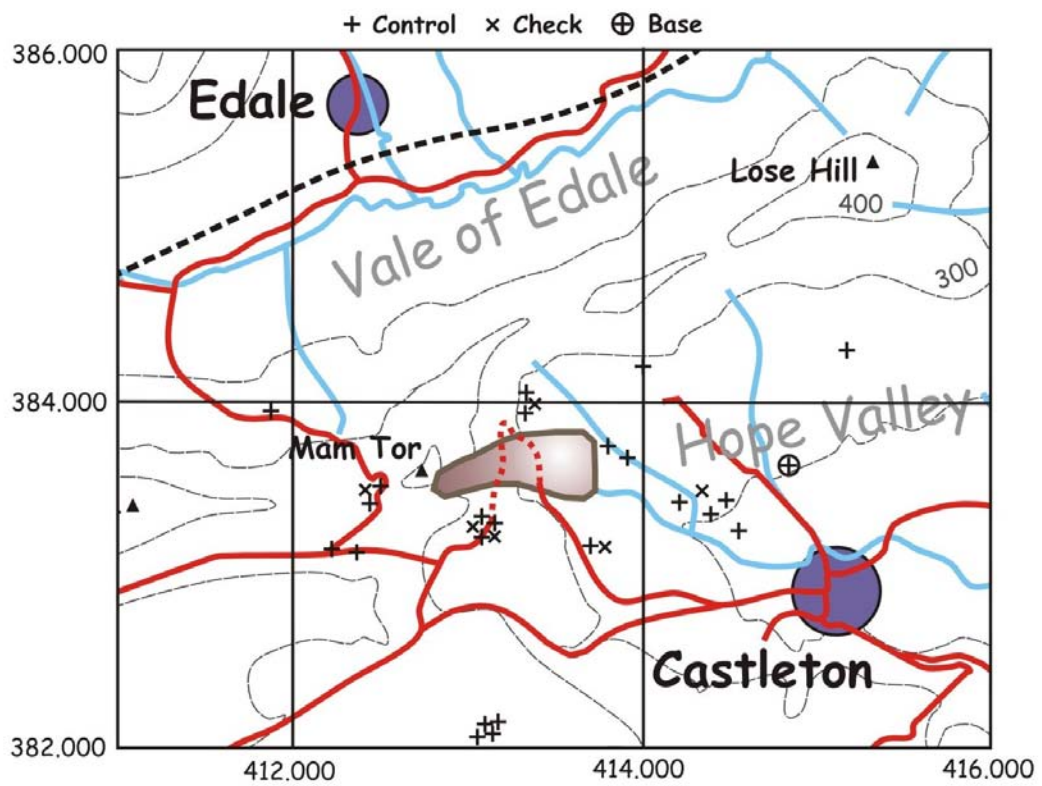
Figure 5.6. Distribution of GPS surveyed ground control and check points.

Figure 5.7. Typical targets for ground control: corner of a building and stonewall.

5.4 Photogrammetric processing

5.4.1 Restitution

As previously stated (Section 5.2), the 1953 images were derived from contact prints scanned at only 42 µm resolution. Characteristics of this epoch are presented in Table 5.3 and clearly show the poor ground resolution (0.45 m) and base/height ratio (1/8), which were unfavourable for the precision of the extracted data. There were no calibration data available, so the interior orientation needed to be estimated in an off-line self-calibrating bundle adjustment. Marks on each side of the frames (Figure 5.8) were used as reference marks to define a photo-coordinate system; their positions were manually measured and transformed using a similarity transformation (as described in 4.2.3). Initial estimates for focal length (20 inch) and flying height (16,666 ft) could be read from the data strips on the frames. Due to the haziness of the photos, the LPS software had difficulty in automatic tie point generation. Nevertheless, 200 tie points were used in addition to 16 control points, to achieve an acceptable photogrammetric solution. As expected, the interior orientation parameters found to be significant in the self-calibration were focal length, offset of the principle point, and two radial distortion parameters (Table 5.4).

Four checkpoints provided an independent measure for the accuracy of the model. Both image and object residuals are comparatively large (see Table 5.5) but acceptable when considering the many limitations of these images. The residuals indicate an object accuracy of 0.55 and 1.40 m in respectively x and y direction. The particularly poor accuracy in height (4.21 m) can be attributed to the low base/height ratio of the frames.

The 1971 images were also poor-quality scanned contact prints, though the contrast of these images was much better than the previous epoch (Figure 5.11). Its larger photo scale and base/height ratio supported higher precision data extraction to be achieved.

No calibration data were available, but again reference marks could be identified on the frames (Figure 5.11) and used to define the photo coordinate system. Estimates for the focal length (12 inch) and flying height (7,100 ft) were provided on the data strips. The photogrammetric model was set up using 13 control points and 400 automatically generated tie points (Table 5.8). A self-

calibrating bundle adjustment successfully recovered the interior orientation of the camera (Table 5.7) and resulted in acceptable object accuracies, considering the residuals of check points: circa 0.45 m in plane and 1.16 m in height (Table 5.8).

The 1973 epoch comprised photogrammetric-quality scanned diapositives, supplied with the camera calibration certificate. The large photo-scale of 1/4,300 (Table 5.9) allowed high precision measurements. On the other hand, the frames covered a relatively small ground area and only a limited amount of ground control could be used (6 control points, Figure 5.15). The long shadows in the photographs may be helpful for qualitative interpretation because details of the relief are very pronounced; however, large areas were obscured by the shadows (Figure 5.14), which was unfavourable for automatic matching techniques. A good solution was obtained for the triangulation, with very low residuals of check points in object space: 0.11 and 0.23 m in plane and 0.43 m in vertical (Table 5.10).

Some oblique photographs had been obtained during the same aerial sortie for the verticals. This series consisted of six images focussed specifically on the landslide, taken with a handheld Hasselblad camera. The photographs were of good quality, though shadows obscured part of the images (Figure 5.16).

Since no calibration data was available for this camera, an estimate for the interior orientation was gained through self-calibration. Reference marks on the frames were measured and used as uncalibrated fiducials. Only a few control points could be identified on the images and initial estimates of interior and exterior orientation proved to be of vital importance to achieve convergence of the solution. According to the CUCAP staff the camera would have been a Hasselblad ELM500 with a lens of either 100 or 150 mm and 70 mm film (Desmond 2004). However, this information was from memory and not recorded anywhere. Through trial and error an estimate of 200 mm proved much better, and the self-calibration eventually revealed a value of 207 mm (Table 5.12). The camera positions were achieved through outlining the viewing area of the photographs on a topographical map, and back-estimating the position of their capture.

One frame (BPD069) could not be incorporated in a converging solution of the bundle adjustment; because of its limited coverage of the actual landslide area it was decide to exclude this frame from the adjustment, with the cause of the problem remaining unidentified. Two pairs of photographs (070/071 and 073/074)

provided good stereo viewing and allowed automatic matching for tie point generation and DEM extraction. The automatic procedures failed on the other pairs, due to their large base to distance ratio (up to 1/1.3) resulting in very different viewing angles.

The large base to distance ratio of the frames provided a very strong geometry, and the residuals of the solution show that a good accuracy can be achieved from the obliques. The object residuals in plane (0.29 and 0.10 m) are of comparable size to the vertical images, while vertical residuals (0.21 m) are even smaller (Table 5.13). However, it should be noted that these values are based on only two checkpoints.

The 1984 epoch comprised diapositives, high-quality scanned at 15 µm resolution (Figure 5.19). Camera calibration data was available and due to its large coverage (Figure 5.20) as many as 16 control points could be used in the bundle adjustment. The small photo scale and associated low ground resolution, resulted in a somewhat reduced accuracy in the object space: 0.45 and 0.40 m horizontally and 1.67 m vertically (Table 5.15).

The 1990 photographs were taken with the same camera as the 1973 verticals. Hence difference in accuracy of the photogrammetric models can be mainly attributed to differences in scale and base/height ratio. Image residuals of both epochs are of comparable size, whereas as expected object residuals of the 1990 epoch are larger in plan: 0.26 and 0.34 m (Table 5.17). Interestingly, the vertical residuals are slightly smaller than in the 1973 epoch (0.41 m compared to 0.54 m); a possible explanation is the larger amount of control points that was used, although their distribution is far from ideal in relation to the configuration of the photographs, with lack of control on both ends of the strip (Figure 5.22). The radiometric contrast in the 1990 is also better, with not as many shaded areas as in the 1973 images (Figure 5.21).

The last two epochs (1995 and 1999) comprised colour images (Figure 5.23 and Figure 5.25). The photo scale of the 1995 images is smaller than 1999 (respectively 1/16,400 and 1/12,200), but as a result of higher scan resolution (15 and 21 µ) the effective ground resolution is almost identical (Table 5.18 and Table 5.20). Also the camera focal length and base/height ratio are very similar, and in both cases the

control points are well-distributed over the frames. Overall, the residuals in the 1995 images perform slightly better (compare Table 5.19 and Table 5.21); remarkable is the significant lower value of the vertical residuals in object space compared to the 1999 images (respectively 0.47 and 0.74 m). There were no issues regarding the use of colour imagery instead of black-and-white, other than the extra amount of disk storage space needed.

Figure 5.8. Frame 0432 of the 1953 epoch (RAF); the enlargement shows one of the reference marks that were manually measured and used as uncalibrated fiducials.

Table 5.3. Details of the 1953 epoch.

Source	NMR
Media	Scanned B&W contact prints
Sortie number	RAF/58/1094
Frame numbers	0431-0433
Date	21 April 1953
Scale	1/10,700
Resolution	42 µm
Ground resolution	0.45 m
Flying height	6,100 m
B/H ratio	1/8.0
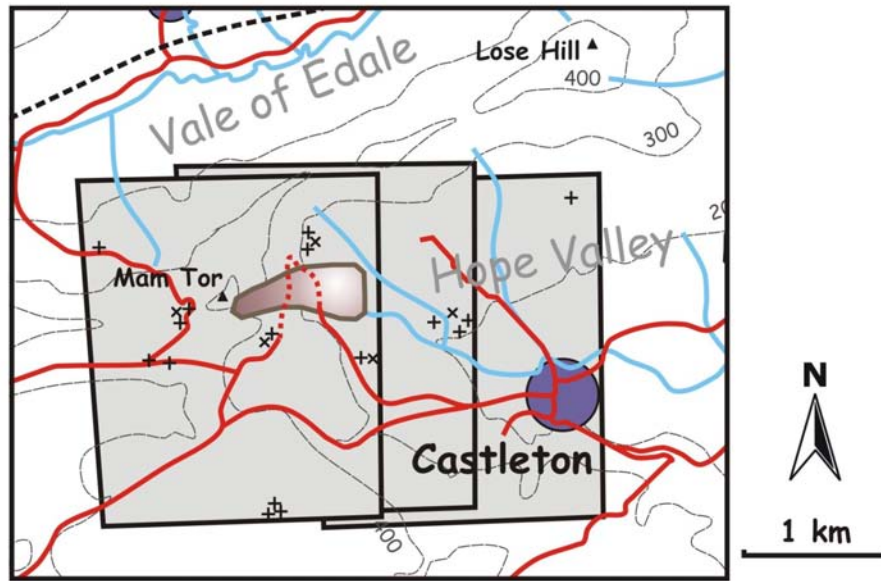
Figure 5.9. Coverage of the 1953 epoch and distribution of control and check points.

Table 5.4. Estimated interior orientation parameters from the self-calibrating bundle adjustment, 1953 epoch.

Focal length (mm)	547.42 ± 2.44
x_0 (mm)	1.19 ± 0.32
y_0 (mm)	0.63 ± 0.70
k_1	-0.15 ± 0.02
k_2	6.4 ± 0.9
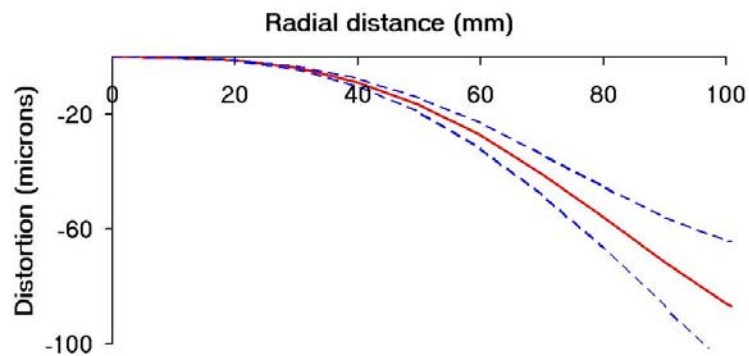
Figure 5.10. Radial distortion curve for the 1953 images (based on estimated k_1, k_2).

Table 5.5. Results from the bundle block adjustment, 1953 epoch.

			x	y	z
Control points	16				
Tie points	474	Image residuals control (μm)	81.12	44.53	
Checkpoints	4	Image residuals check (μm)	27.20	35.79	
Std. photo (pixels)	0.20	Ground residuals control (m)	0.015	0.009	0.002
Std. ground (m)	0.01	Ground residuals check (m)	0.55	1.40	4.21
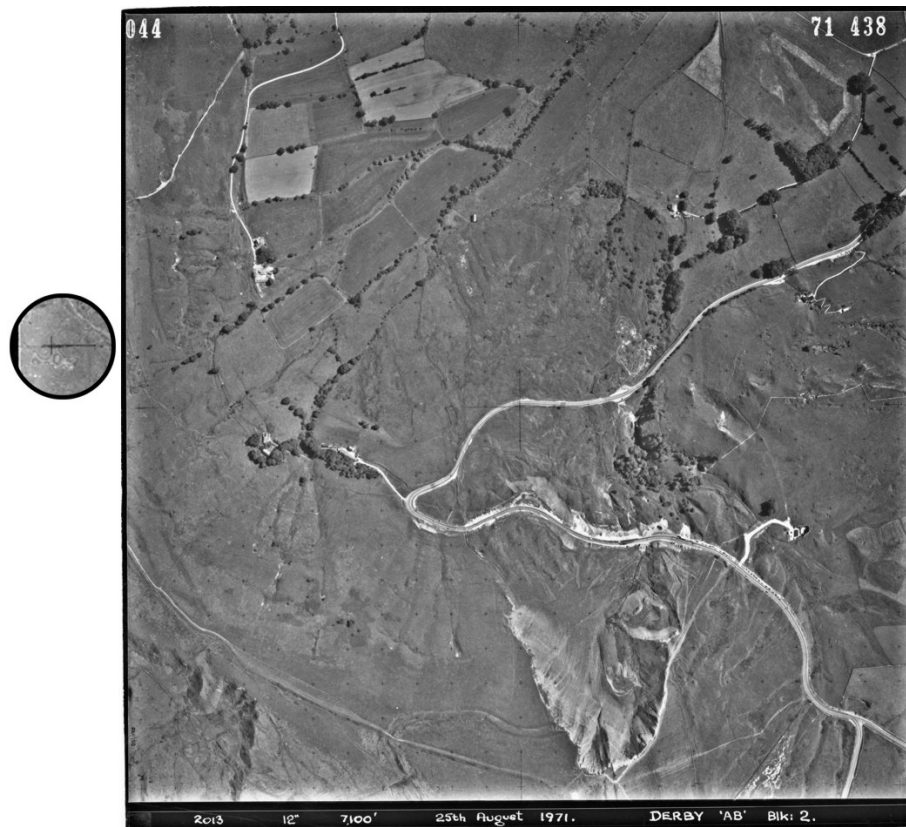
Figure 5.11. Frame 044 of the 1971 epoch (Ordnance Survey: © Crown copyright);
enlargement shows one of the reference marks.
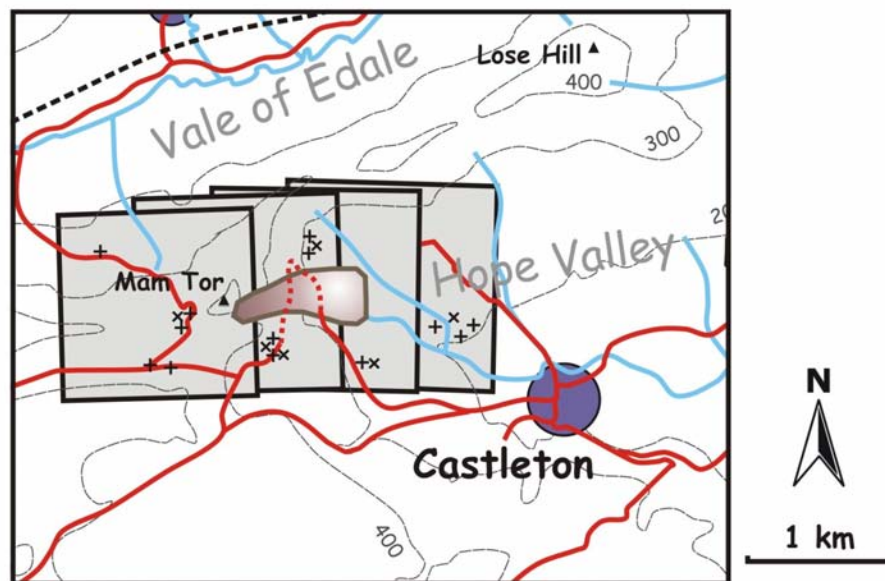
Figure 5.12. Coverage of the 1971 epoch and distribution of control and check points.

Table 5.6. Details of the 1971 epoch.

Source	NMR
Media	Scanned B&W contact prints
Sortie number	OS/71438
Frame numbers	042-045
Date	25 August 1971
Scale	1/6,400
Resolution	42 µm
Ground resolution	0.27 m
Flying height	2,200 m
B/H ratio	1/3.4

Table 5.7. Estimated interior orientation parameters from the self-calibrating bundle adjustment, 1971 images.

Focal length (mm)	303.54 ± 0.95
x_0 (mm)	0.31 ± 0.21
y_0 (mm)	0.27 ± 0.24
k_1	0.05 ± 0.01
k_2	-1.0 ± 0.4
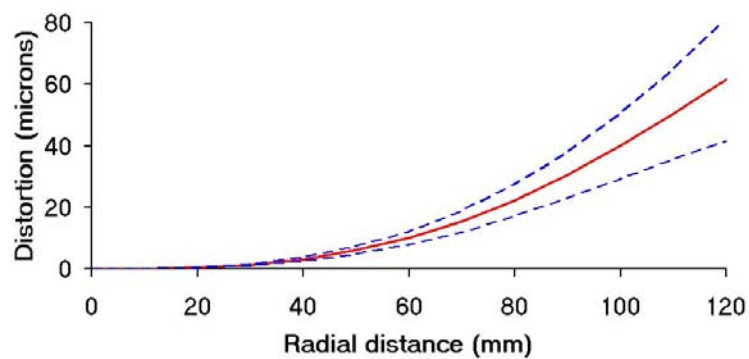
Figure 5.13. Radial distortion curve for the 1971 images.

Table 5.8. Results from the bundle block adjustment, 1971 epoch.

			x	y	z
Control points	13				
Tie points	400	Image residuals control (µm)	65.57	64.91	
Checkpoints	5	Image residuals check (µm)	28.17	50.19	
Std. photo (pixels)	0.20	Ground residuals control (m)	0.021	0.026	0.002
Std. ground (m)	0.01	Ground residuals check (m)	0.46	0.42	1.16
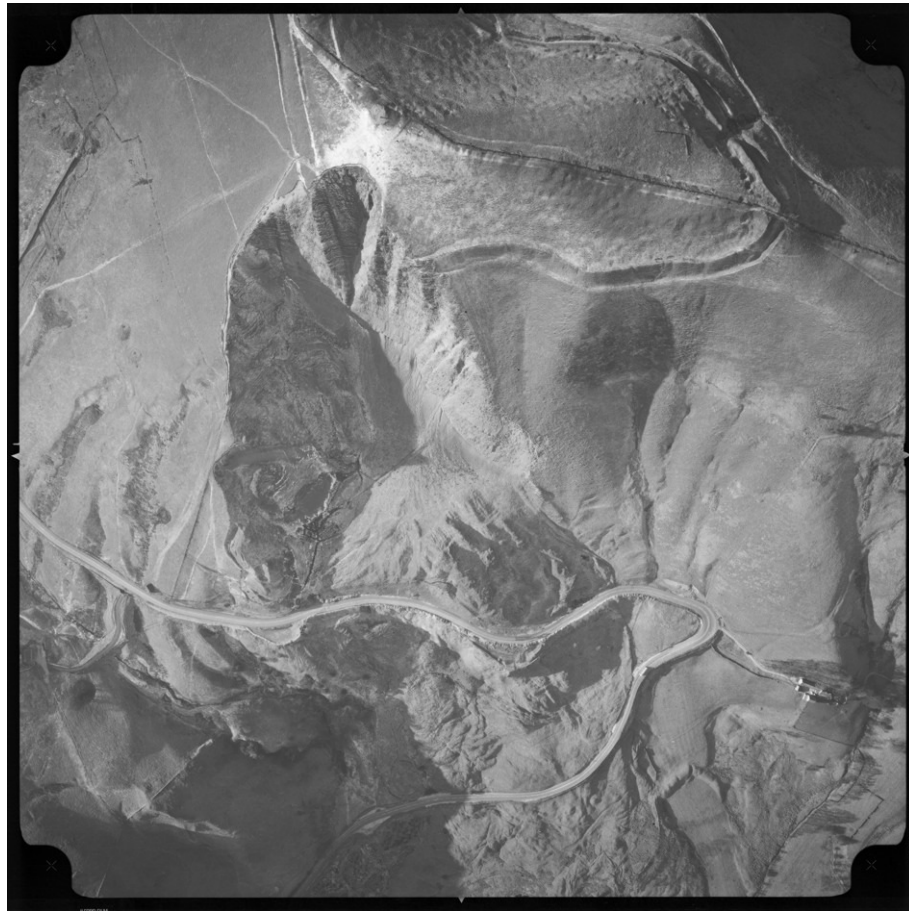
Figure 5.14. Frame RC8-AN005 of the 1973 epoch (© copyright CUCAP).
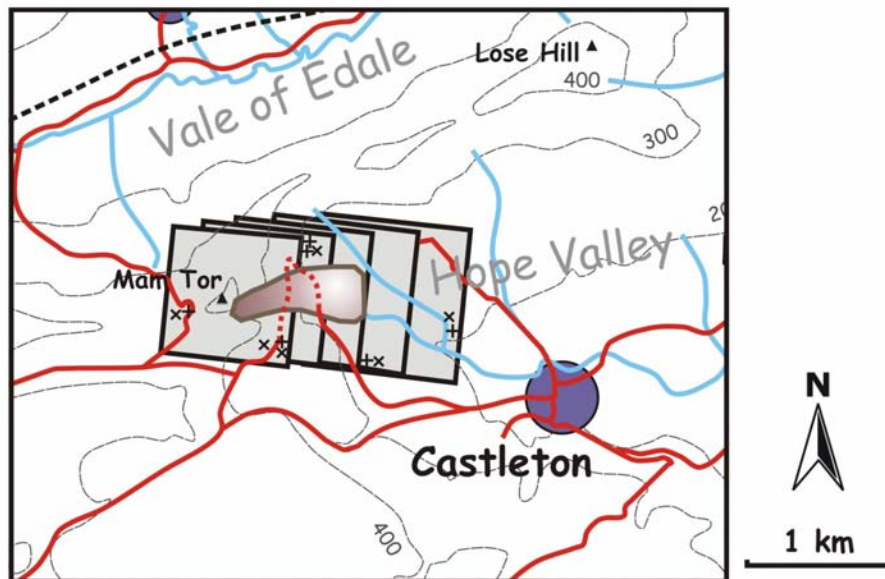
Figure 5.15. Coverage of the 1973 epoch.

Table 5.9. Details of the 1973 epoch.

Source	CUCAP
Media	Scanned B&W diapositives
Frame numbers	RC8-AN002 – RC8-AN006
Date	27 November 1973
Scale	1/4,300
Resolution	15 µm
Ground resolution	0.065 m
Flying height	950 m
B/H ratio	1/2.5
Focal length	152.7320 mm
x_0	0.0140 mm
y_0	0.0030 mm

Table 5.10. Results from the bundle block adjustment, 1973 epoch.

				x	y	z
Control points	6					
Tie points	295	Image residuals control (µm)		40.80	25.17	
Checkpoints	6	Image residuals check (µm)		20.80	7.47	
Std. photo (pixels)	0.20	Ground residuals control (m)		0.084	0.049	0.29
Std. ground (m)	0.01	Ground residuals check (m)		0.11	0.23	0.43
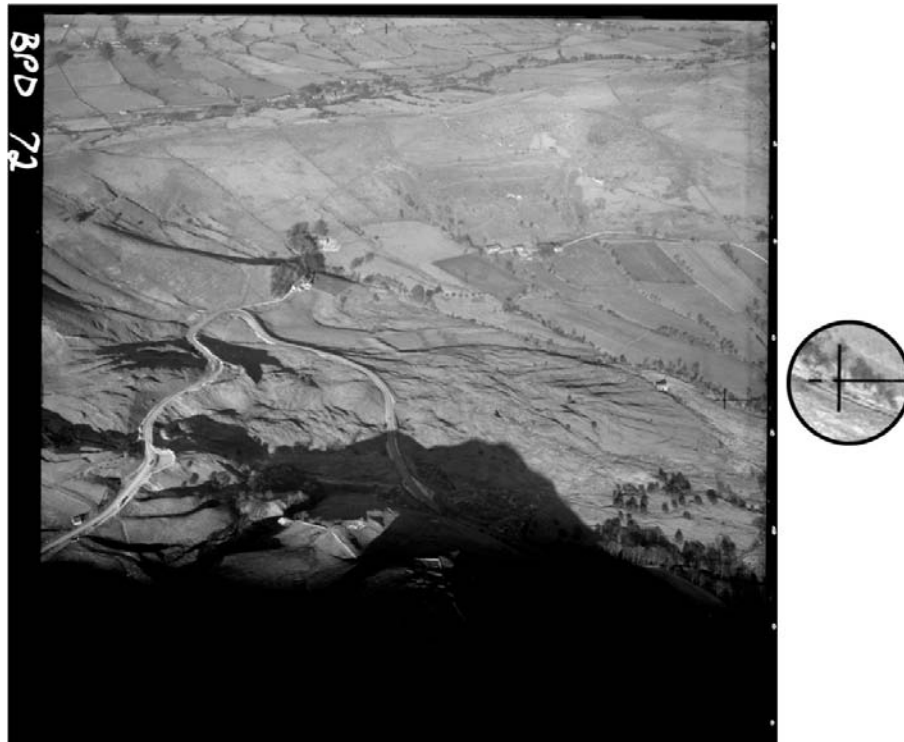
Figure 5.16. Frame BPD072 of the 1973 obliques (© copyright CUCAP); enlargement shows one of the manually measured reference marks.
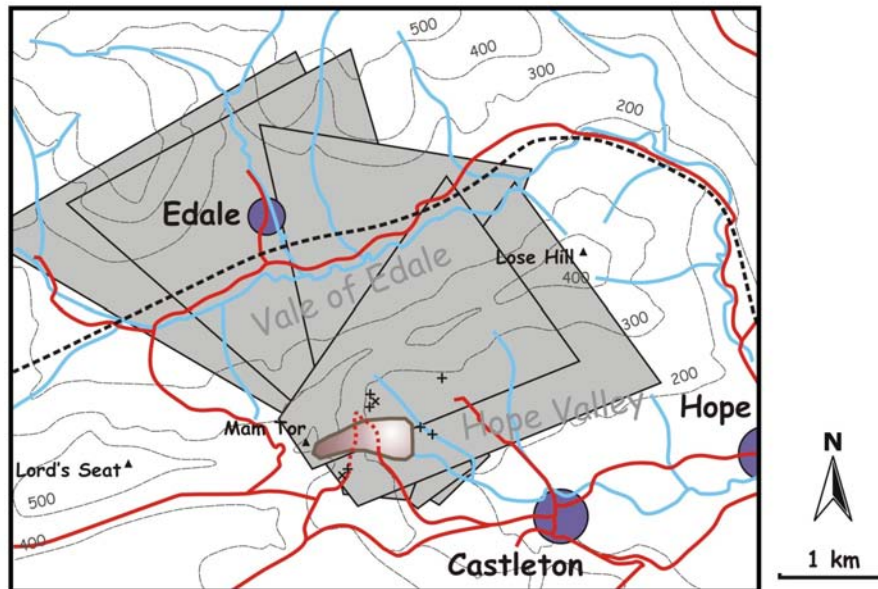
Figure 5.17. Coverage of the oblique images.

Table 5.11. Details of the obliques.

Source	CUCAP
Media	Scanned B&W diapositives
Frame numbers	BPD069-BPD074
Date	27 November 1973
Scale	Oblique
Resolution	15 µm
B/H ratio	1/1.3 – 1/5.6 (variable)
Flying height	950 m

Table 5.12. Estimated interior orientation parameters from the self-calibrating bundle adjustment, obliques.

Focal length (mm)	207.17 ±0.18
x_0 (mm)	-0.20 ±0.052
y_0 (mm)	3.89 ±0.28
k_1	-0.34 ±0.05
k_2	88.6 ±6.2
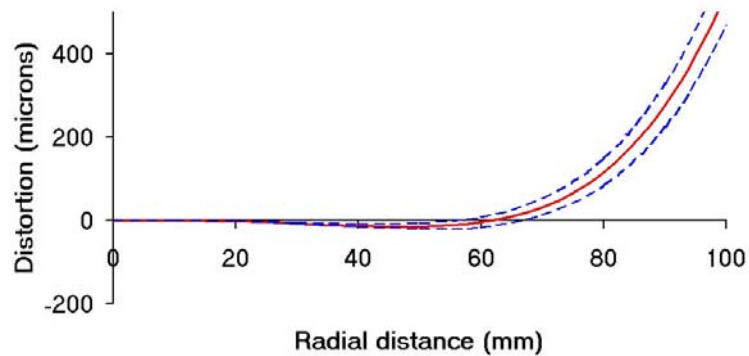
Figure 5.18. Radial distortion curve for the oblique images.

Table 5.13. Results from the bundle block adjustment, obliques.

			x	*y*	*z*
Control points	6				
Tie points	163	Image residuals control (µm)	14.60	14.35	
Checkpoints	2	Image residuals check (µm)	19.49	14.68	
Std. photo (pixels)	0.20	Ground residuals control (m)	0.12	0.60	0.23
Std. ground (m)	0.01/0.1	Ground residuals check (m)	0.29	0.10	0.21

Figure 5.19. Frame 209 of the 1984 epoch (ADAS: © Crown copyright).
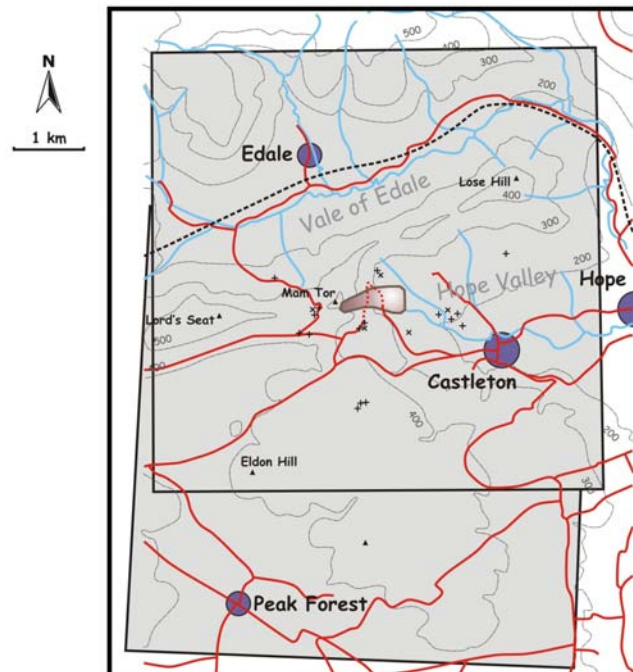
Figure 5.20. Coverage of the 1984 epoch.

Table 5.14. Details of the 1984 epoch.

Source	ADAS
Media	Scanned B&W diapositives
Frame numbers	208 & 209
Date	26 April 1984
Scale	1/27,200
Resolution	15 µm
Ground resolution	0.41 m
Flying height	4,400
B/H ratio	1/1.7
Focal length	152.0400
x_0	0.0250
y_0	-0.0100

Table 5.15. Results from the bundle block adjustment, 1984 epoch.

			x	y	z
Control points	16				
Tie points	288	Image residuals control (µm)	14.14	19.48	
Checkpoints	5	Image residuals check (µm)	13.85	0.41	
Std. photo (pixels)	0.20	Ground residuals control (m)	0.009	0.013	0.003
Std. ground (m)	0.01	Ground residuals check (m)	0.45	0.40	1.67

Table 5.16. Details of the 1990 epoch.

Source	CUCAP
Media	Scanned B&W diapositives
Frame numbers	RC8-LW258 – RC8-LW260
Date	9 April 1990
Scale	1/12,000
Resolution	15 µm
Ground resolution	0.18 m
Flying height	2,100
B/H ratio	1/1.8
Focal length	152.7320
x_0	0.0140
y_0	0.0030

Table 5.17. Results from the bundle block adjustment, 1990 epoch.

			x	y	z
Control points	11				
Tie points	240	Image residuals control (µm)	15.42	15.73	
Checkpoints	6	Image residuals check (µm)	17.99	2.86	
Std. photo (pixels)	0.20	Ground residuals control (m)	0.024	0.021	0.015
Std. ground (m)	0.01	Ground residuals check (m)	0.26	0.34	0.41

Figure 5.21. Frame RC8-LW259 of the 1990 epoch (© copyright CUCAP).
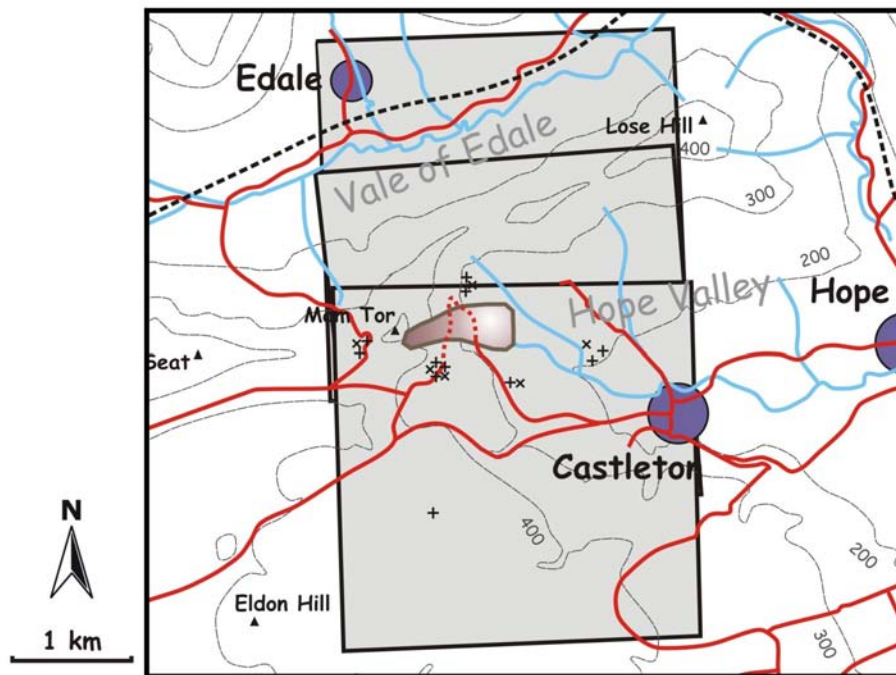
Figure 5.22. Coverage of the 1990 epoch.

Figure 5.23. Frame Zkn-eq094 of the 1995 epoch (© copyright CUCAP).
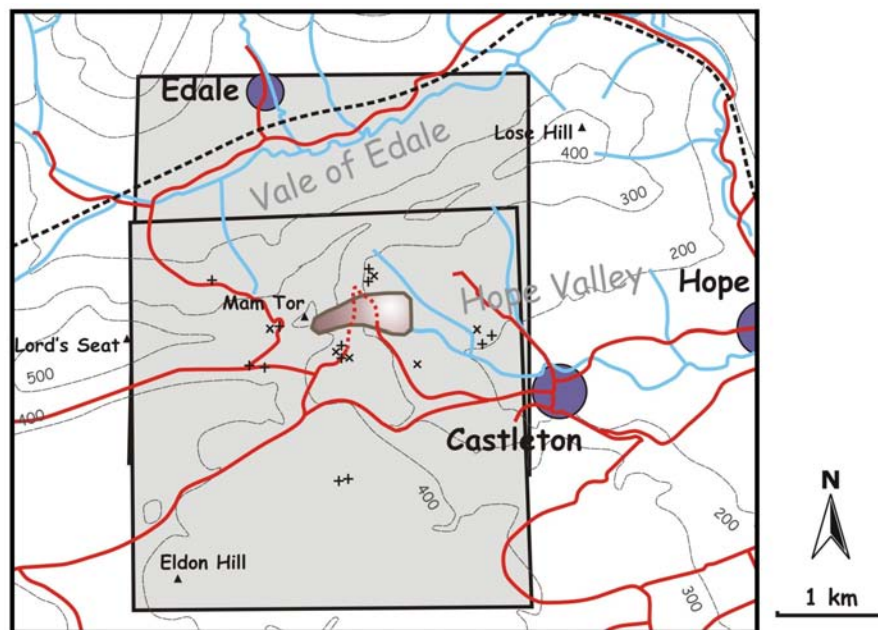
Figure 5.24. Coverage of the 1995 epoch.

Table 5.18. Details of the 1995 epoch.

Source	CUCAP
Media	Scanned colour negatives
Frame numbers	Zkn-eq094 & Zkn-eq095
Date	27 June 1995
Scale	1/16,400
Resolution	15 µm
Ground resolution	0.25 m
Flying height	2,700
B/H ratio	1/1.9
Focal length	152.2330
x_0	-0.0090
y_0	-0.0020

Table 5.19. Results from the bundle block adjustment, 1995 epoch.

			x	y	z
Control points	12				
Tie points	219	Image residuals control (µm)	12.03	12.31	
Checkpoints	6	Image residuals check (µm)	0.24	11.90	
Std. photo (pixels)	0.20	Ground residuals control (m)	0.011	0.014	0.003
Std. ground (m)	0.01	Ground residuals check (m)	0.35	0.24	0.47

Table 5.20. Details of the 1999 epoch.

Source	Infoterra
Media	Scanned colour negatives
Frame numbers	P255.99.085 & P255.99.086
Date	5 September 1999
Scale	1/12,200
Resolution	21 µm
Ground resolution	0.26m
Flying height	2,100
B/H ratio	1/1.9
Focal length	152.8960
x_0	0.0020
y_0	0.0010

Table 5.21. Results from the bundle block adjustment, 1999 images.

			x	y	z
Control points	11				
Tie points	254	Image residuals control (µm)	16.53	12.68	
Checkpoints	5	Image residuals check (µm)	3.24	13.61	
Std. photo (pixels)	0.20	Ground residuals control (m)	0.011	0.010	0.004
Std. ground (m)	0.01	Ground residuals check (m)	0.26	0.30	0.74
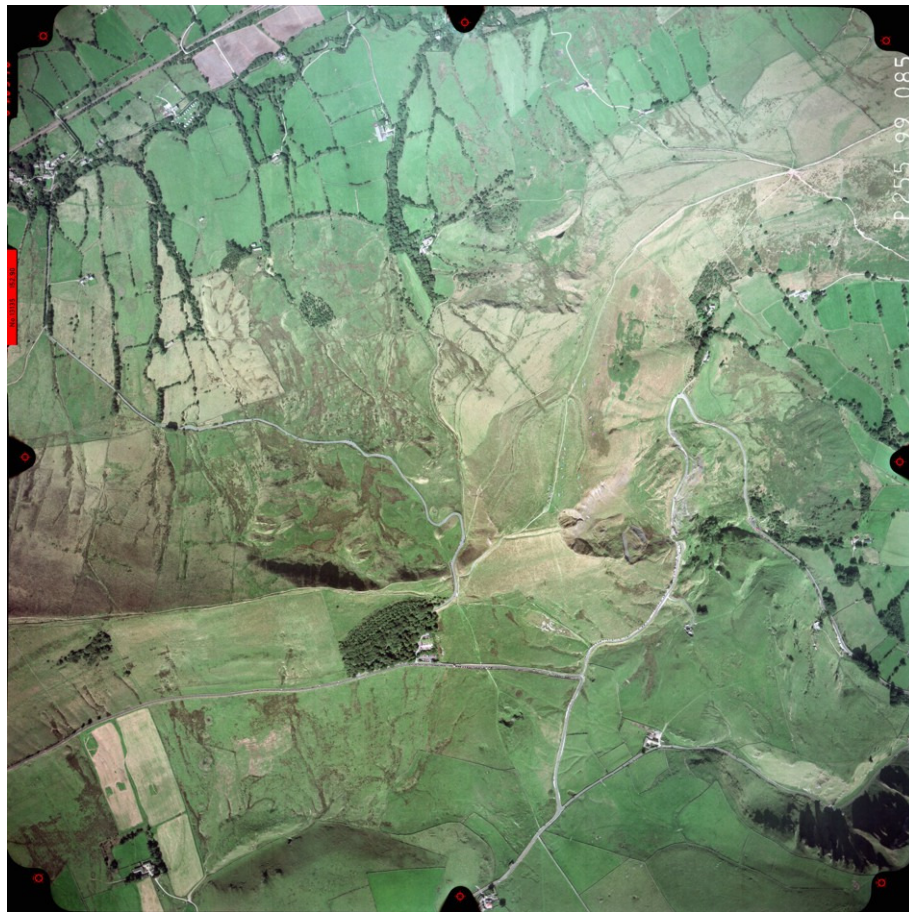
Figure 5.25.Frame P255.99.085 of the 1999 epoch (© copyright Infoterra).
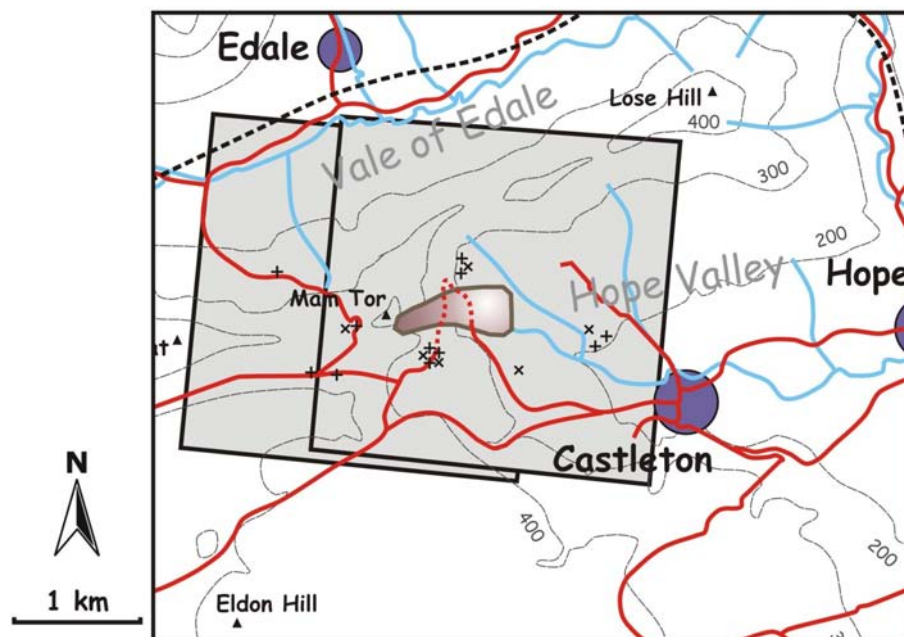
Figure 5.26. Coverage of the 1999 epoch.

5.4.2 DEM extraction

DEMs were automatically extracted from all epochs. Normally, a grid spacing of 1 m was used, except for the 1953 and 1984 epochs, which required a larger cell size, due to their lower ground resolution. The search window for image matching was optimised according to the guidelines by ERDAS (see Section 4.2.3); in the case of the poor-quality 1953 and 1971 images, a distance of five pixels in the direction across the epipolar line was adopted. In all cases the default correlation size of 7x7 pixels gave satisfying results. The correlation coefficient was set to 0.75 for all epochs, except for the 1953 and 1999 images, in which case this value was lowered to 0.70 to increase the number of achieved matches. The values for all the strategy parameters are presented in Table 5.22. This table also displays the amount of successfully matched points in each epoch – in order to be able to compare the different epochs, this was constrained to a subset of the area, and converted to points per hectare since not all epochs fully covered this sub-area. In addition, checkpoints provided an indication for the accuracy of the extracted elevation models.

As was mentioned before (p. 98), only two pairs of oblique photographs allowed automatic matching and hence DEM extraction. The other pairs resulted in useless data. Because of their very different viewing angle and area, the two DEMs were analysed separately, and therefore two values are presented in Table 5.22, the first one referring to pair 070/071 and the second one to pair 073/074.

5.4.3 DEM quality

As discussed in Section 4.2.4, there are a number of ways to assess the quality of a DEM. Analysis of the statistics of errors of checkpoints indicated the size of systematic and random errors in the DEM, respectively by their mean and standard deviation (Section 4.2.4). The values in Table 5.22 suggest that systematic errors were small in comparison to random errors. Furthermore it was observed that the accuracy compares very well to the object residuals of check points in the photogrammetric model, which confirms a reasonable overall performance of the DEM extraction. Only in the case of the oblique photographs are these values considerably worse (standard errors of 2.52 and 0.60 m, whereas object residual was only 0.21 m); this suggests that their oblique geometry is less suitable for automated DEM extraction.

Table 5.22.Values for strategy parameters used in DEM extraction, amount of matched mass points, and RMSE of checkpoints.

	1953	1971	1973	1973o	1984	1990	1995	1999
Search Size	15x5	27x5	33x3	27x3	15x3	21x3	17x3	25x3
Correlation Size	7x7	7x7	7x7	7x7	7x7	7x7	7x7	7x7
Coefficient Limit	0.70	0.75	0.80	0.75	0.75	0.75	0.75	0.70
Topographic Type	RH*	M**	M	M	RH	M	RH	M
Object Type	OA†	OA	OA	OA	OA	OA	OA	OA
DTM Filtering	high	mod	mod	mod	mod	mod	mod	mod
Cell Size (m)	2	1	1	1	2	1	1	1
Mass points (per ha)	751	5,921	5,108	512 3,652	470	2,424	1,029	1,031
Number of checkpoints	11	14	8	4/6	21	13	16	12
Checkpoints, Mean error (m)	1.57	-0.42	0.50	2.07 0.60	-0.24	0.06	-0.05	-0.22
Checkpoints, Standard error (m)	5.22	1.34	0.76	2.52 0.96	1.58	0.83	0.76	1.13

* RH = Rolling Hills; ** M = Mountains; † OA = Open Area

It should be noted that these error values should be interpreted with care. On one hand they could be regarded as a rather conservative measure of DEM accuracy, since the checkpoints were usually at terrain edges (corners of buildings, stonewalls), which are smoothed out in a DEM of 1 m resolution. This effect will be less in open areas, such as the landslide. On the other hand, some image patches would be considerably less suited for automated DEM extraction, resulting in mismatches or interpolated elevations, which were not reflected in these global errors.

It was therefore also important to inspect the number and distribution of mass points that were used for interpolation of the DEM. A low density of mass points indicated areas where image matching failed, and consequently DEM values were interpolated. Dense and evenly distributed mass points suggest a higher accuracy could be achieved. Overall densities of mass points for the different epochs are included in Table 5.22. Figure 5.27 conveys the spatial distribution of mass points extracted from the 1953 and 1990 images. The 1953 epoch clearly shows the difficulties of matching in areas of low contrast and steep relief (e.g. grassland, shadows, backscar of the landslide). In contrast, the mass points extracted from the 1990 images are much denser and uniformly distributed. It is

remarkable that in both epochs the mass points are most dense on the landslide surface.

The same pattern appears from the DEM point status images: many 'excellent' and 'good' points in the 1990 DEM, while the 1953 DEM shows extensive 'isolated' and 'suspicious' areas (Figure 5.28).
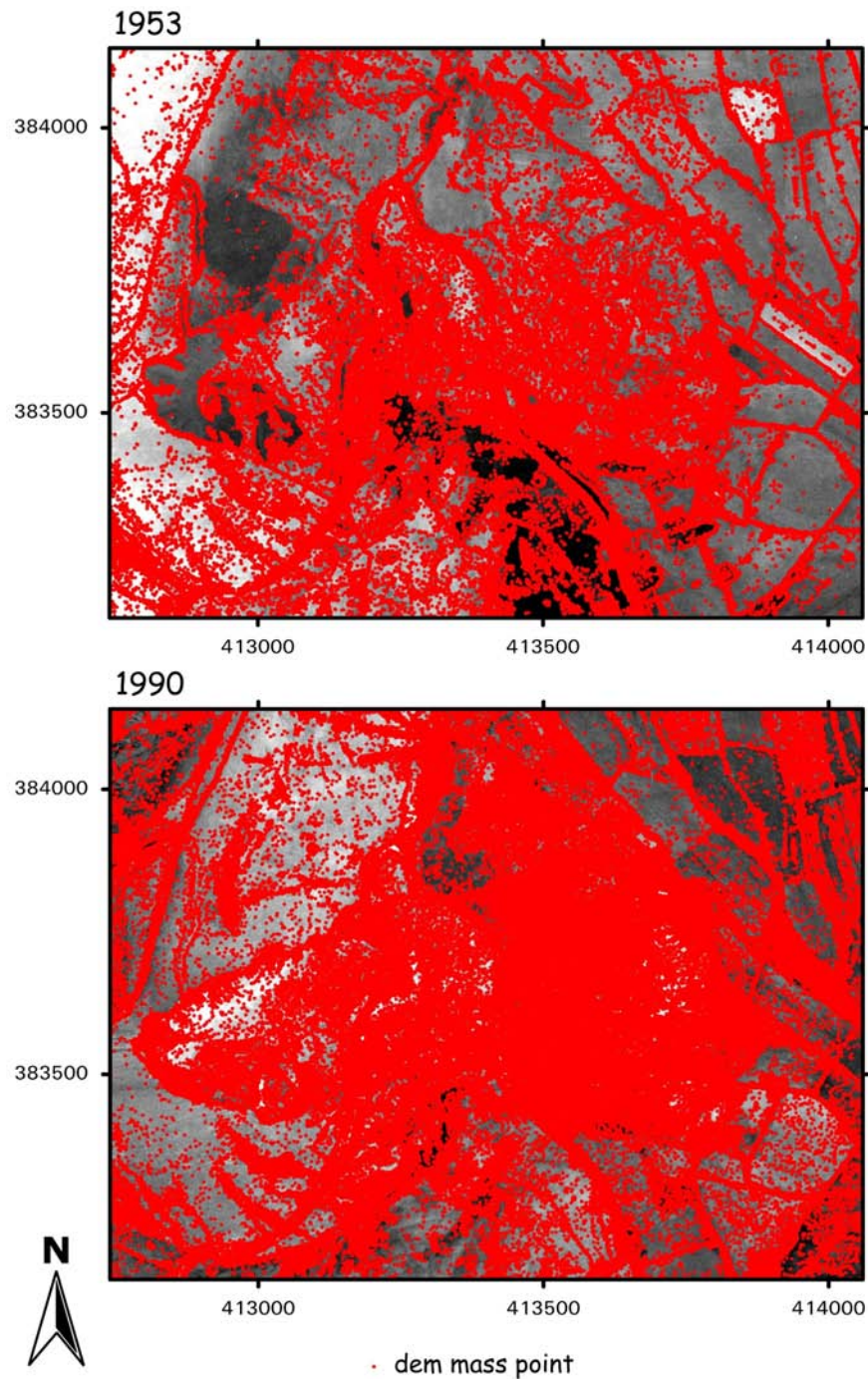
Figure 5.27. Mass point distribution for DEM extraction: 1953 and 1990 epochs.
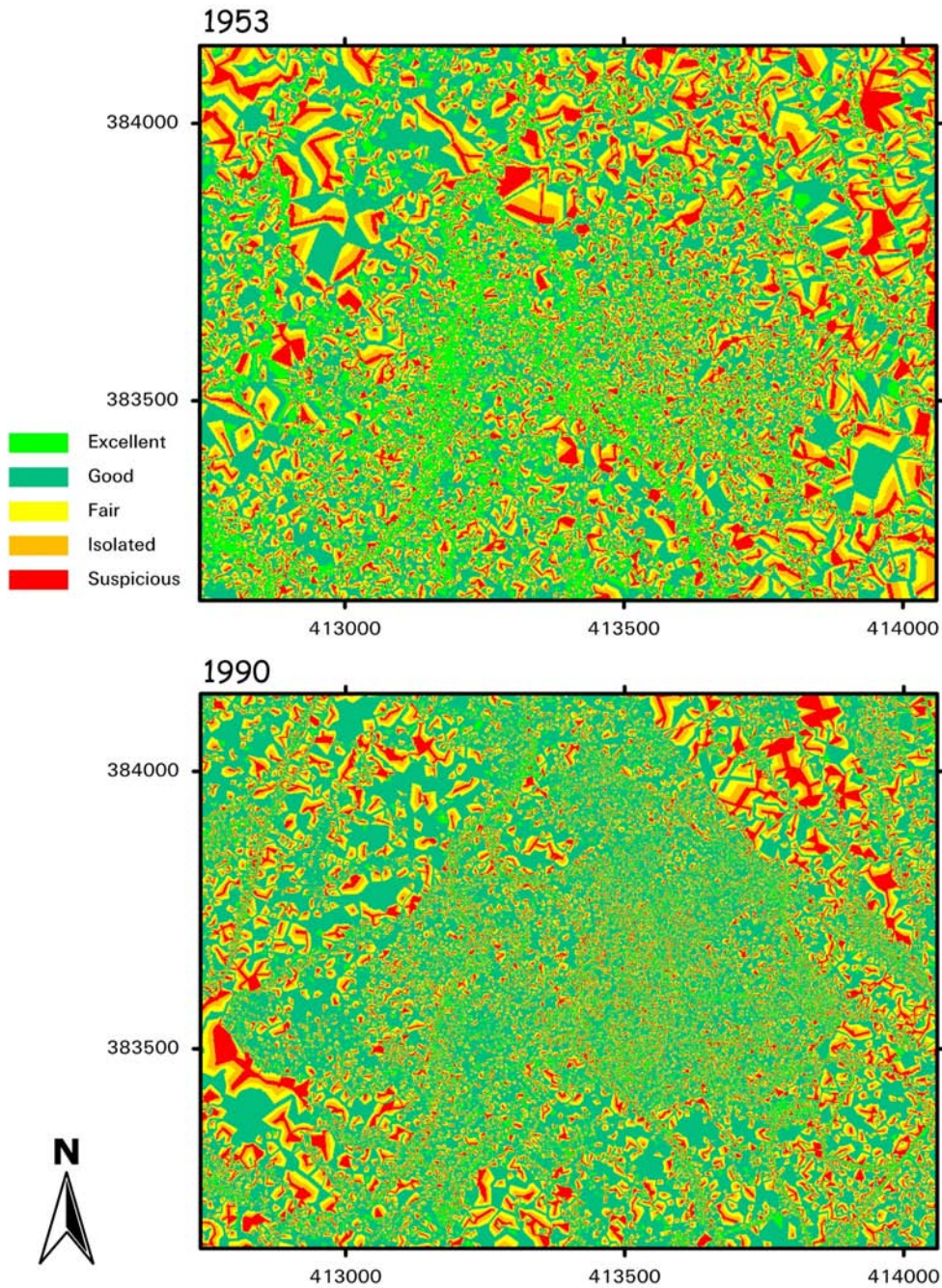
Figure 5.28. DEM point status images, 1953 and 1990 epochs.

Epochs that consisted of multiple stereopairs, offered the opportunity to compare DEMs extracted from the different stereopairs. Mean and standard deviation of errors from these analyses are shown in Table 5.23. Figure 5.29 displays a 'DEM of difference' image created from the different 1973 stereopairs. The image clearly shows some large errors within the shadowed and steep areas, in respectively the southern and western part of the images. These gross errors account for a large

part of the errors presented in the table. When only a subset of the DEMs is used for the analysis, excluding these unreliable areas, the accuracy is much improved: mean errors close to zero and standard error of less than 0.5 m.

Table 5.23. Error analysis 'DEMs of difference' from different stereopairs: mean and standard deviation of errors. Values within brackets refer to the sub-area, excluding gross errors.

Epoch	DEMs	Mean error	Std. error
1953	0431/0432 vs. 0432/0433	-0.78	8.01
1971	042/043 vs. 043/044	0.65	6.30
	043/044 vs. 044/045	0.16	1.70
1973	002/003 vs. 003/004	-9.53 (0.15)	23.74 (0.36)
	003/004 vs. 004/005	-1.06 (0.09)	1.94 (0.44)
	004/005 vs. 005/006	-3.79 (0.00)	11.18 (0.49)
1973o	070/071 vs. 073/074	-2.81 (-2.24)	11.40 (8.77)
	070/071 vs. vertical	-3.02 (-1.91)	11.08 (6.43)
	073/074 vs. vertical	3.59 (0.23)	21.50 (7.45)
1990	258/259 vs. 259/260	-0.36	7.69
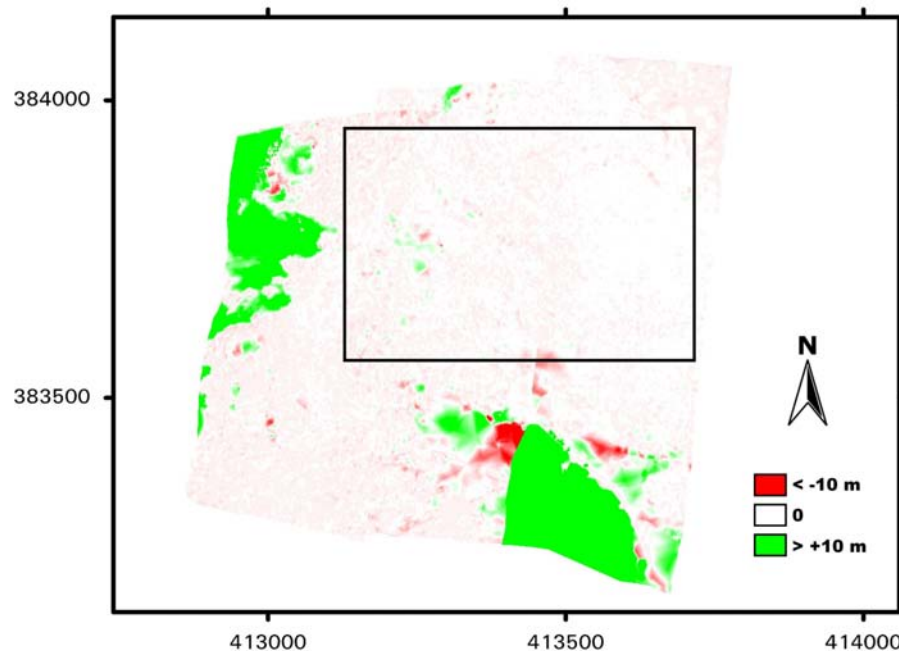
Figure 5.29. 'DEMs of difference' obtained through subtracting the DEMs from different stereopairs of the 1973 epoch (three 'DEMs of difference' are merged together for display; the box shows location of the sub-area used during the analysis).

Particularly interesting was to compare the DEMs from the oblique and vertical 1973 images. Differences between these DEMs are relatively large (standard errors of respectively 6 and 7 m in the subset; see Table 5.23), indicating that the geometry of these obliques is less suitable for DEM extraction than vertical images. This issue is further discussed in Section 7.5 (p. 191).

5.4.4 Orthophoto generation

The last stage in the photogrammetric processing involved the generation of orthophotographs. The minimum resolution for each epoch was adopted, corresponding to the ground resolution of the original images. Measurement of coordinates of four checkpoints, stable features around the landslide area, provided a measure of orthophoto accuracy (Table 5.24). The errors of these checkpoints are generally larger than the horizontal errors in the bundle adjustment (compare with the values in Section 5.4.1), and can be attributed to the effect of errors in the DEMs (see also Section 7.3).

For the purpose of automated extraction of displacement vectors, orthophotos were required at an identical resolution. Therefore, from each epoch, additional orthophotos of a sub-area were extracted, at an equal resolution of 0.5 m. Figure 5.30 shows an orthophoto created from the 1990 images.

Table 5.24. Accuracy of orthophotos.

Epoch	Resolution	Mean error checkpoints	Std. error checkpoints
1953	0.45 m	1.59	0.50
1971	0.27 m	0.80	0.36
1973	0.065 m	0.72	0.61
1984	0.41 m	1.14	0.90
1990	0.18 m	0.26	0.24
1995	0.25 m	0.67	0.15
1999	0.26 m	0.34	0.06

5.5 Visualisation and analysis

5.5.1 Geomorphological map

A detailed geomorphological map of the landslide area was created through photo-interpretation of the 1990 images based on the legend from Figure 4.6. Figure 5.31 displays an anaglyph of the landslide area created with Leica Stereo Analyst,
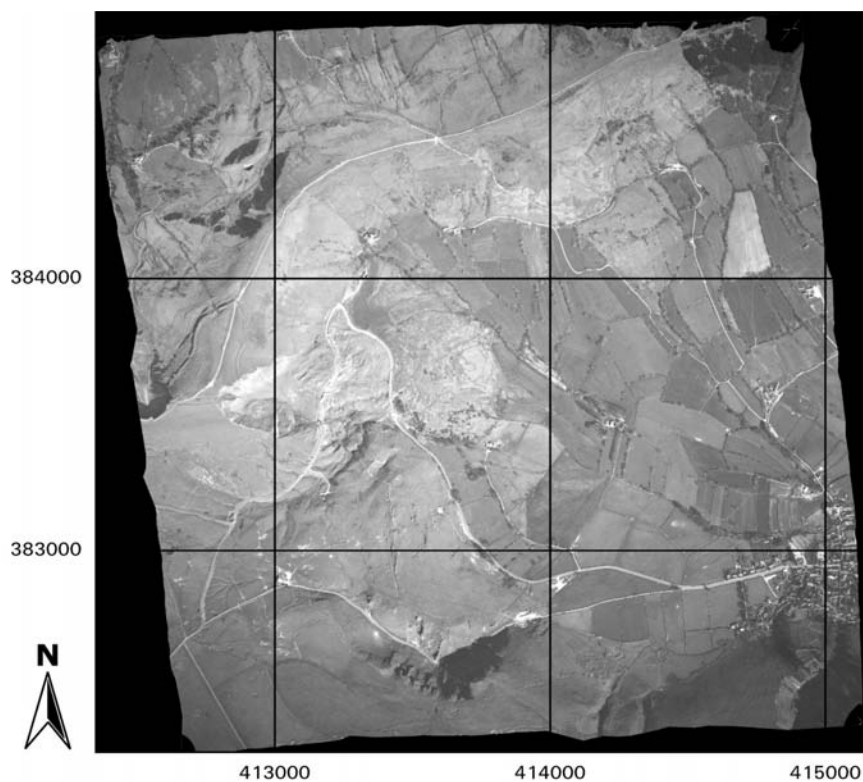
Figure 5.30. Orthophoto, created from the 1990 epoch.
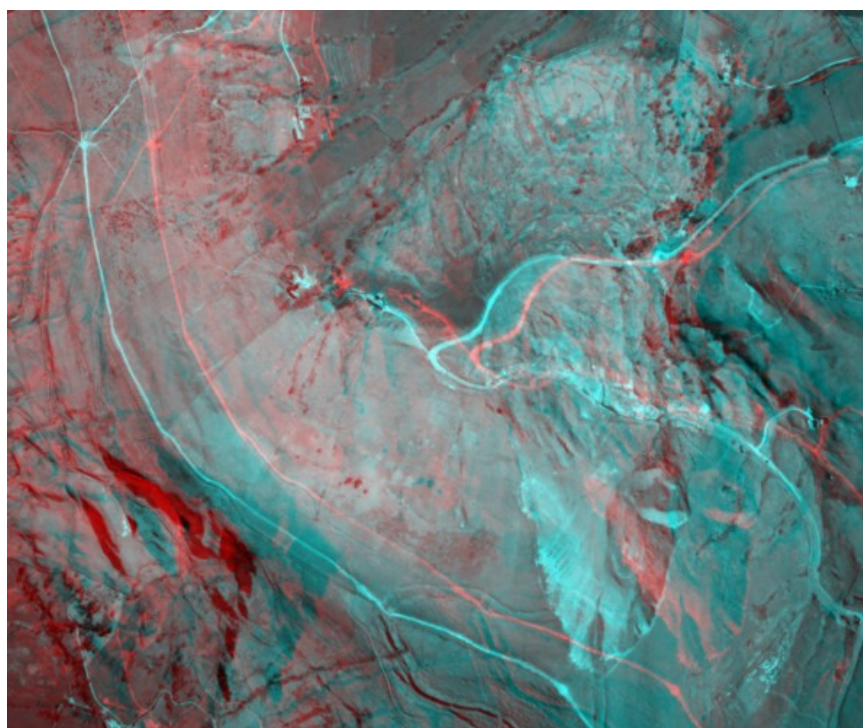
Figure 5.31. Anaglyph from 1990 images, used for stereo viewing (colour print must be viewed in conjunction with appropriate red/blue anaglyph glasses).

enabling 3D viewing and used for the photo-interpretation. The features were mapped on an overlay on top of an orthophoto to assure geometric exactness. During a field survey the map was checked and further details added.

Figure 5.32 illustrates some characteristic features of the landslide observed on aerial photographs and from a ground perspective. Without doubt the most striking feature of the landslide is the head scar standing up to an impressive height of 80 m in sandstone (A). Active rockfall supplies the colluvium underneath with fresh scree, further washing down the slope and forming fans. Regressive failures occurred in the southern part of the head scar and in the colluvium material (B). The upper part of the slide mass consists of largely intact blocks forming an irregular topography (C). At the front of this zone, individual blocks are breaking up thereby developing large steps in the upper road section. This zone is bound by a scarp (D), marking the steeper inclined slip surface. The material from this cliff breaks up into a debris flow, extending further downhill. The plastic behaviour of the debris flow is demonstrated by the distortion of the lower road section which is badly twisted but not broken up. The earthflow lobe forms an undulating topography, badly drained as is reflected in the presence of several ponds and bracken (E). The presence of more developed vegetation cover along the southern margins suggests little movement in this part. The northern part of the toe is steeper inclined and its progression led to the destruction of Blacketlay Barn (F).

The geomorphological map that was eventually created is presented in Figure 5.33. The location of major geomorphological units remained unchanged during the image sequence, and therefore it was not justified to map these from the different epochs. Even so, this single geomorphological map proved to have great value for identifying the different elements in the landslide body and help interpreting the quantitative data that were extracted from the photographs in later stages.

5.5.2 'DEMs of difference'

Considering the relatively small vertical displacements (maximum of 0.8 m during the period 1990-1998 according to Waltham & Dixon 2000) compared to the vertical accuracy that can be achieved from the images, a 'DEM of difference' seems not to have much value for this site. A combination of any two epochs would lead to an uncertainty of at least 1.8 m.
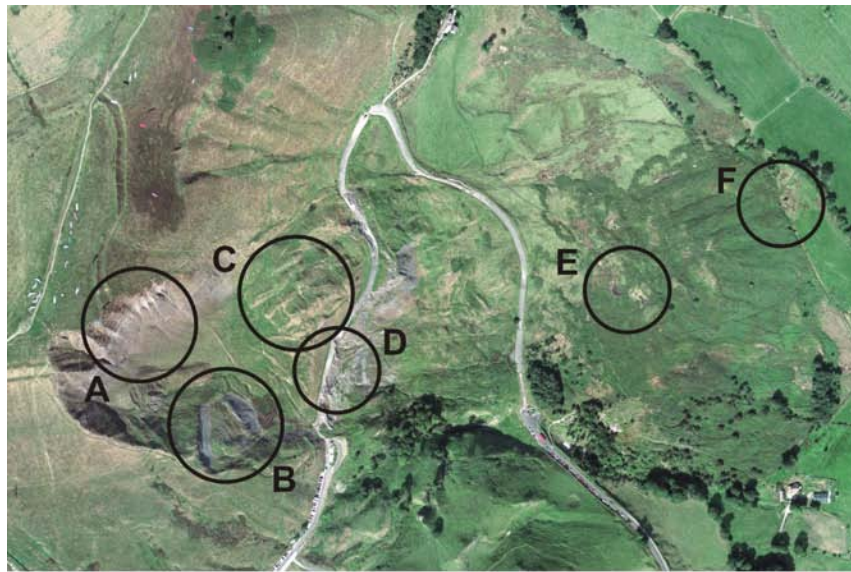
Figure 5.32. Some typical features of the Mam Tor landslide, observed on aerial photographs (1999 epoch) and in the field: (A) head scar in sandstone, (B) regressive landslip in shales. Continued on next page: (C) Slipped blocks, largely intact, (D) breaking up of upper road section, (E) ponds, (F) Blacketlay Barn, destroyed by advancing toe.

Figure 5.32 (continued).

LEGEND

Mass movements

∪ rotational slip
∼ earth flow
⌄̣ᵥ rock fall
\\ slope wash

Landforms

◤ scarp
▷ earthflow toe
⊤⊤ ridge
- - - slope break
200 contour line

Hydrology

≃ stream (intermittent/perennial)
● pond

Vegetation

⊛• tree/bush
    bracken

Infrastructure

◣ building
    road
...... footpath
- \ - stonewall
⋙ iron age ramparts

N

0   100   200 m
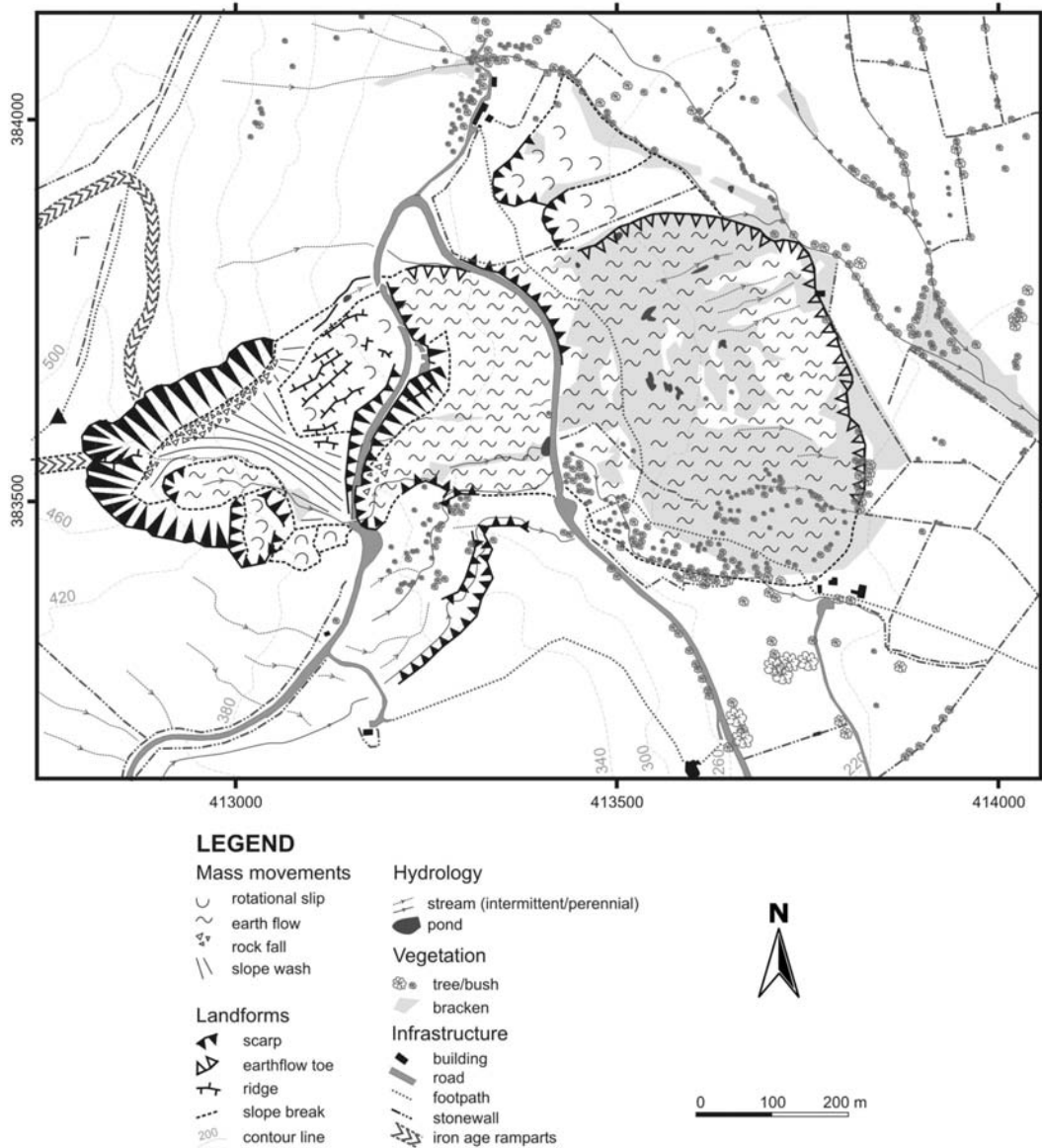
Figure 5.33. Geomorphological map of the Mam Tor landslide.

The 'DEM of difference' from 1973 and 1990 epochs was used to apply the approach described by Betts *et al.* (2003; see Section 3.7.2), to reduce systematic errors between DEMs. These two epochs were chosen because high vertical accuracy had been achieved and an extensive period had elapsed between the epochs, as to increase the chance of detecting significant vertical change. An 'error surface' was created based on the mean errors of five selected stable sub-areas outside the active landslide, and subtracted from the 'DEM of difference'. The statistics of the 100x100 m sized areas are tabulated below (Table 5.25). The 'DEMs of difference' before and after correction are displayed in Figure 5.34.

Table 5.25. Statistics of the 'DEM of difference' image 1999-1973 in five sub-areas.

	Mean error	Std. error
Area A	-0.16	0.53
Area B	-0.50	0.35
Area C	-0.93	0.78
Area D	-0.38	0.43
Area E	-0.39	0.73
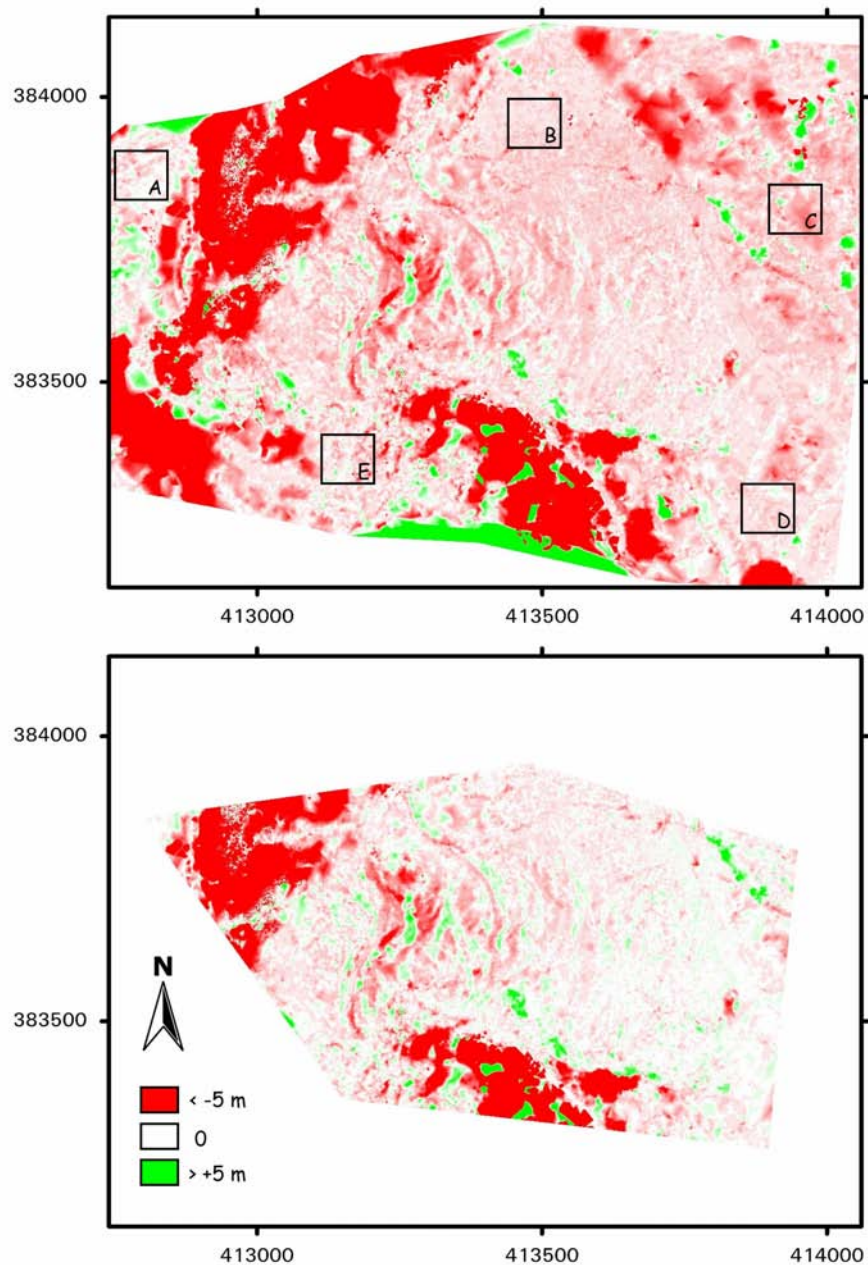
Figure 5.34. 'DEMs of difference' 1999-1973, before (top) and after (bottom) correction for systematic errors. The boxes indicate the sub-areas in Table 5.25.

Since the systematic errors were minor, the improvement to the 'DEM of difference' was only limited. The corrected 'DEM of difference' should therefore be interpreted with caution, as the vertical differences may be either attributed to genuine surface changes or to remaining gross errors in the DEMs. The latter is for example the case for areas that proved difficult for automated DEM extraction, such as the shadowed patches in the 1973 images. Figure 5.35 shows a 'DEM of difference' of the central part of the landslide, draped over a normal DEM for better interpretation. Red areas represent a lowering of elevation, while green areas depict an increase in height. In spite of the limited quantitative value, this 'DEM of difference' certainly demonstrates evidence of morphological change that is consistent with the geomorphological processes operating. It is striking that the transverse pressure ridges show up clearly, with positive height difference downslope and negative values upslope, consistent with their downhill displacement.
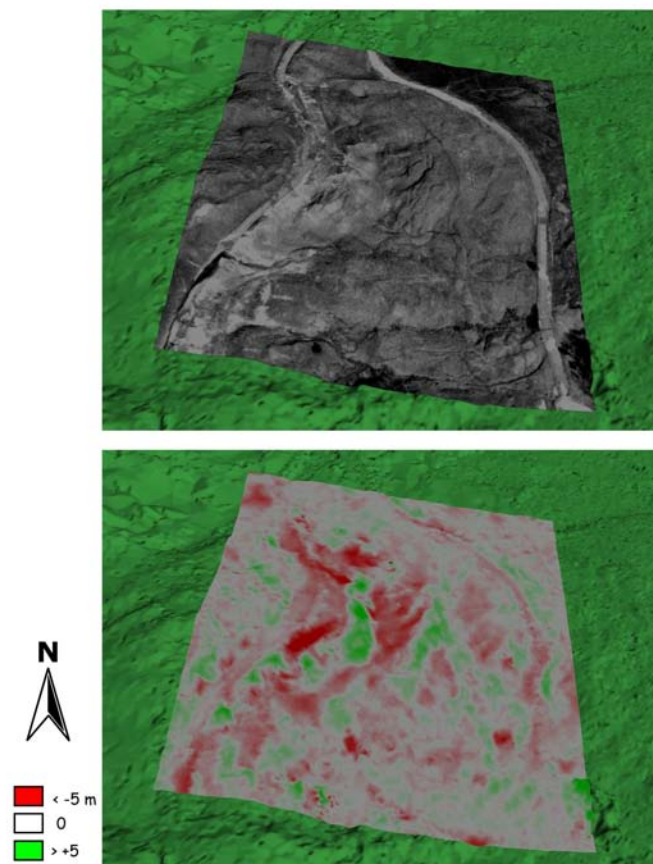
Figure 5.35. 'DEM of difference' of central part of the landslide, draped over normal DEM (bottom). The upper image displays an orthophoto of the same area.

5.5.3 Displacement vectors

Surface deformations of the landslide are rather slow, therefore it was expected that surface features could easily be identified throughout the image sequence, and their displacements measured. However, a significant problem was that the terrain is largely covered with vegetation, and their seasonal change is masking long-term changes of the ground surface. In the pre-1979 epochs, the road could not provide suitable targets, since its surface was constantly distorted and repaired. Eventually, a total of 50 features were identified in most of the epochs. These features include shrubs and trees, ponds, stonewalls, distinct ground marks, and (only in the recent epochs) features on the road surface.

Additional measurements of stable points outside the landslide area provided information on the effects of systematic errors between different epochs, and hence an independent measure of accuracy of the vectors (see Table 5.26). Based on the covariance matrices of these control data, error ellipses were created around each displacement vector, assuming uniformity of error across the whole area (as described in Section 4.3.3, p. 78). A plot presenting error ellipses for the various time intervals is displayed in Figure 5.36.

Table 5.27 shows the measured coordinates of four selected points from the 1973 and 1999 images, with their computed horizontal and vertical displacements. The displacements were visualised in vector plots, showing the spatial variation in magnitude and orientation of landslide movements during a particular period of time. Figure 5.37 shows horizontal displacement vectors of the period 1973-1999 (the four selected points from Table 5.27 are indicated in Figure 5.37). Vectors piercing the error ellipse represent significant displacements at the specified confidence level.

Table 5.26. Error assessment of the 'stable' control points.

Time interval	Var x	Var y	Var z	Covar xy	Covar xz	Covar yz
1953-1971	0.70	2.71	8.11	-0.21	-1.10	-2.34
1971-1973	0.41	0.39	3.26	-0.20	-0.84	0.40
1973-1984	0.57	0.38	1.77	0.25	0.15	-0.22
1984-1990	0.52	0.34	2.99	0.19	0.65	0.48
1990-1995	0.16	0.32	0.57	0.10	0.05	0.10
1995-1999	0.19	0.82	1.41	0.15	-0.14	0.24
1953-1999	2.36	3.57	9.64	-1.06	1.65	-4.83
1973-1999	0.16	0.47	1.37	0.14	-0.24	-0.14
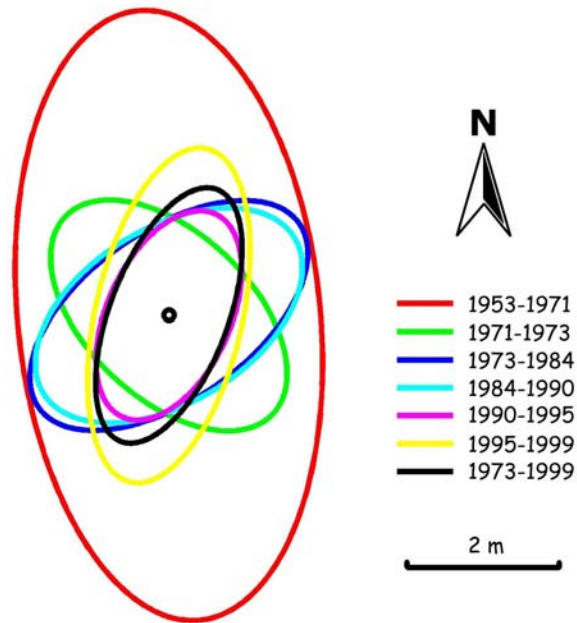
Figure 5.36. Error ellipses for the different time intervals based on statistics of the control points, at 95% confidence level.

Table 5.27. Measured coordinates and displacements of four selected points, from 1973 and 1999 images; the standard errors of the displacements are based on the variance data of control points in Table 5.26.

	1973			1999			Change	
Point	*x*	*y*	*z*	*x*	*y*	*z*	*dxy (±0.79)*	*dz (±1.17)*
10	413252.43	383706.63	324.24	413257.42	383708.66	323.17	5.39	-1.07
15	413195.01	383498.95	344.27	413207.98	383508.94	338.58	16.37	-5.69
27	413723.22	383666.25	244.60	413727.58	383665.38	244.55	4.46	-0.05
33	413532.42	383508.28	262.47	413537.68	383507.09	263.53	5.39	1.05

By measuring targets throughout all images a time series of displacements can be obtained. Figure 5.38 shows the progressive horizontal displacement of the four selected monitoring points. It can be seen that whether or not the displacement is significant depends on its magnitude in relation to data accuracy. Magnitude of a vector in turn depends on movement rate and time interval between two image epochs. Hence, when displacements between successive epochs are small, they may still be significant in the longer term.
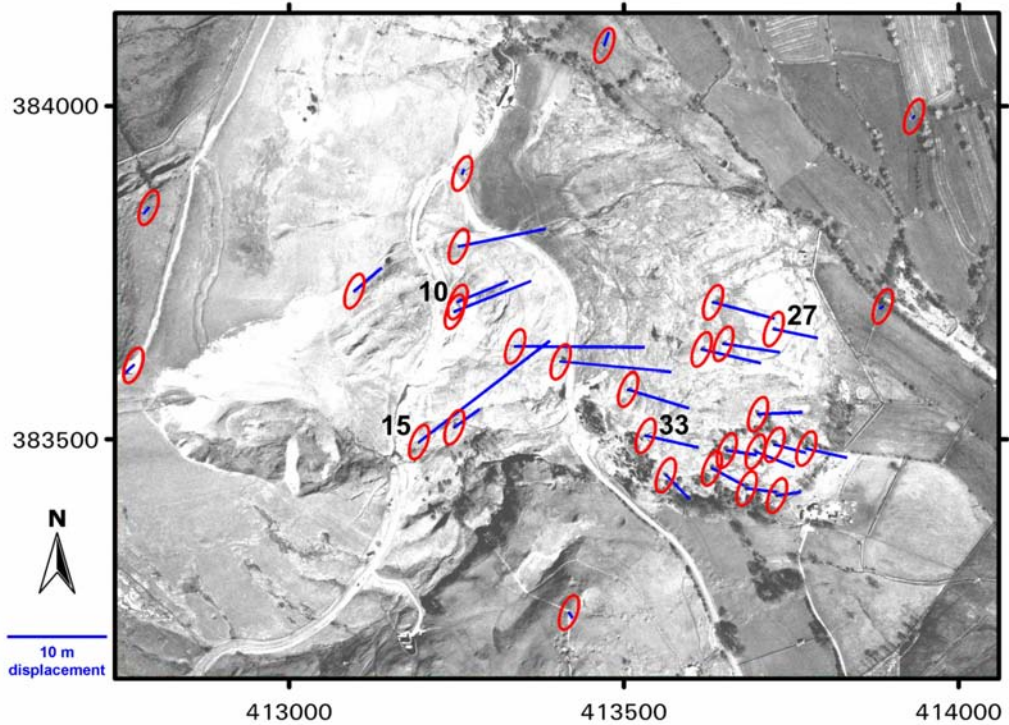
Figure 5.37. Horizontal displacements between 1973 and 1999, represented by displacement vectors. Error ellipses correspond to initial positions (1973), whilst vectors piercing through the ellipses depict significant movements. Background image is an orthophoto created from 1990 images. The scale of vectors is 15x scale of background image. Error ellipses are based on 95% confidence level. The numbers refer to the four selected points in the text.
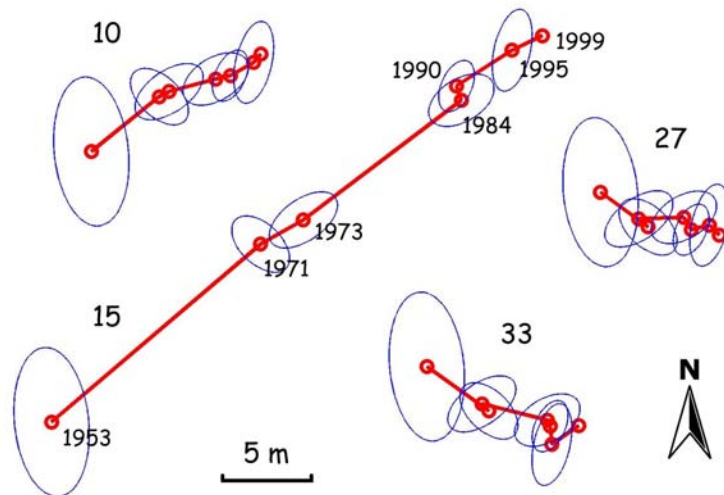
Figure 5.38. Horizontal displacement of monitoring points 10, 15, 27 and 33. Error ellipses are based on 95% confidence level.

Average movement rates were also calculated (in m/yr), and used to analyse the variability of landslide activity through time. Table 5.28 and Figure 5.39 show the horizontal displacements and movement rates for the four selected points. A consistent pattern of high movement rates during the 1970s and 1990s is apparent, while activity decreased during the 1980s. Table 5.29 and Figure 5.40 show the vertical displacements of the same points. It is again evident that the vertical accuracy of the data is rather limited.

Table 5.28. Absolute horizontal displacements and average movement rates of four selected points.

	1953-71	**1971-73**	**1973-84**	**1984-90**	**1990-95**	**1995-99**	**1953-99**
Displ. (m)	*±1.85*	*±0.89*	*±0.98*	*±0.93*	*±0.69*	*±1.01*	*±2.50*
10	4.75	0.59	2.63	0.82	1.46	0.59	10.61
15	14.90	2.67	10.76	0.81	3.59	1.81	33.90
27	3.20	0.66	2.45	0.78	1.04	0.75	6.86
33	4.14	0.54	3.67	0.36	1.00	1.77	8.85
Rate (m/yr)	*±0.10*	*±0.45*	*±0.09*	*±0.15*	*±0.14*	*±0.25*	*±0.05*
10	0.26	0.29	0.24	0.14	0.29	0.15	0.23
15	0.83	1.33	0.98	0.14	0.72	0.45	0.74
27	0.18	0.33	0.22	0.13	0.21	0.19	0.15
33	0.23	0.27	0.33	0.06	0.20	0.44	0.19
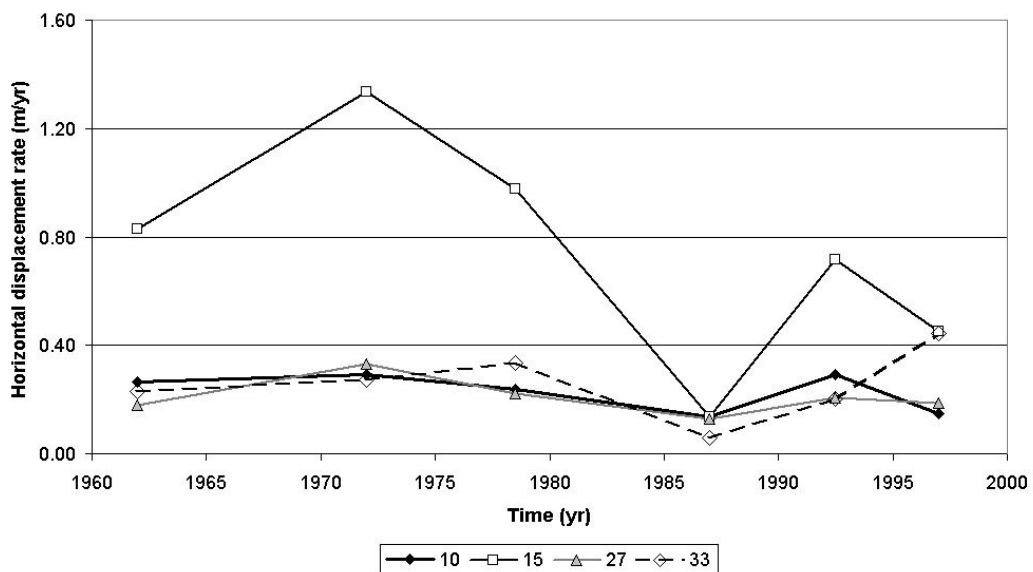
Figure 5.39. Movement rate of the four selected points.

Table 5.29. Vertical displacements of the four points.

	1953-71	1971-73	1973-84	1984-90	1990-95	1995-99	1953-99
	±2.85	±1.81	±1.33	±1.73	±0.75	±1.19	±3.12
10	-4.20	-0.76	1.18	-2.31	-2.33	2.38	-6.03
15	-1.07	0.07	-1.32	-2.81	-0.46	-1.10	-6.69
27	6.72	0.37	-1.00	-0.18	0.05	1.08	7.03
33	6.50	-0.07	-0.25	0.86	-0.83	1.28	7.48
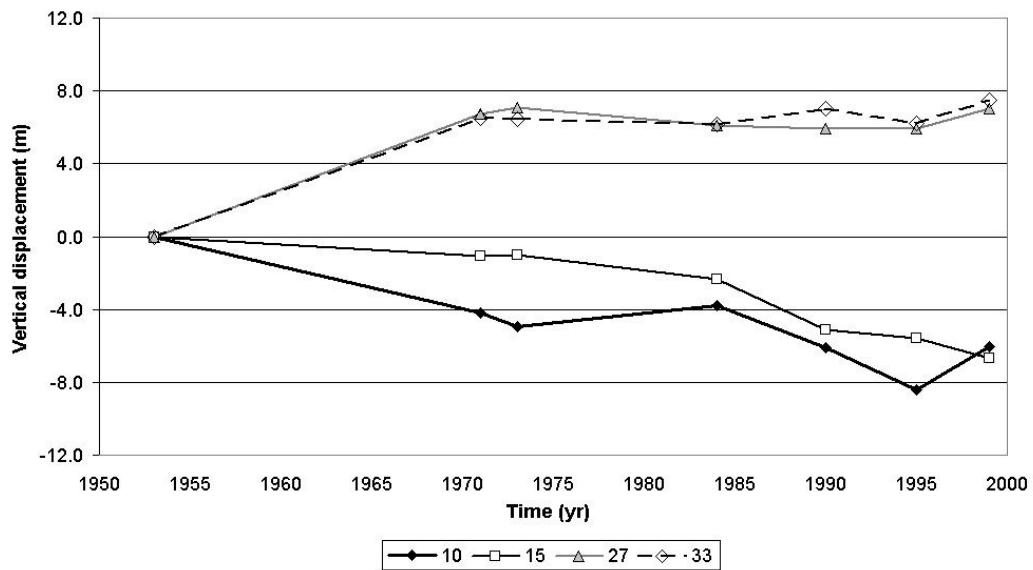
Figure 5.40. Vertical displacement of the four points.

Attempts to apply image matching techniques to the sequence of orthophotos for automatic measurements of displacement vectors were ultimately unsuccessful. Orthophotos from the 1995 and 1999 epochs were used for testing the specially developed Matlab script (4.3.3). These epochs were selected because of their similar lighting and vegetation conditions (both sorties were flown during summer), and comparable ground resolution (respectively 0.25 and 0.26 m). From both orthophotos, a sub-area of the central part of the landslide was converted to greyscale and resampled to 0.25 m resolution. The different parameters in the script were adjusted, in order to get optimal results. A search window size of 15x15 pixels was used, exceeding the maximum displacement of about 1.81 m that was observed during this period (Table 5.28). Different values for template size and correlation threshold were used, but none of the attempts led to gaining satisfactory results. Figure 5.41 illustrates some typical outputs from the script. The first result was obtained using a template of 9x9 pixels and a correlation threshold

of only 0.75; the second one was achieved using a template of 7x7 pixels and a correlation threshold of 0.85. In both cases the vectors seem rather randomly orientated, on as well as off the landslide. Only the roadside seems to provide distinct features for successful image matching.

The technique failed, probably because surface features were too indistinct; especially the 1995 images which suffered because of limited image contrast. Also, the lighting conditions may have been too different (e.g. the shadows of trees in lower part of the images), and vegetation obscured the ground surface. In fact, it was experienced that even manual identification of features between the epochs was already challenging.
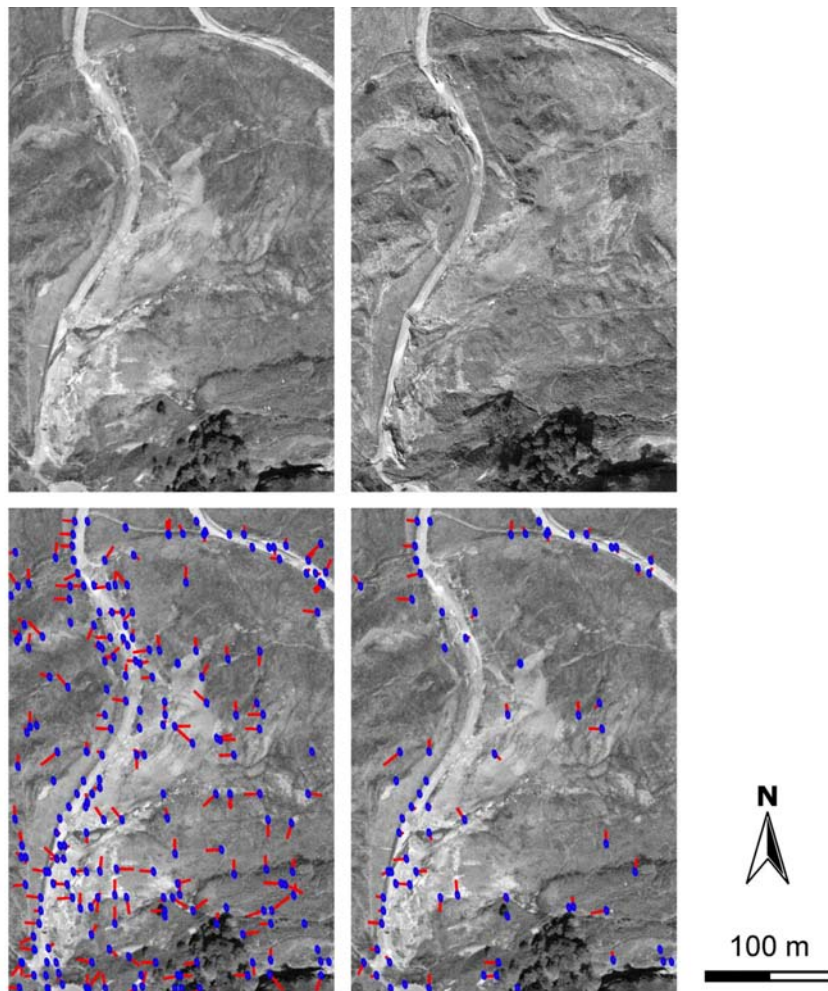
Figure 5.41. Orthophotos from 1995 and 1999 (upper), and two attempts to automatic image matching (bottom).

5.5.4 Comparing with ground survey data

Ground surveyed monitoring data provided a good opportunity to validate the photogrammetrically derived data. The data sets cover the periods of 1981-83 (Al-Dabbagh 1985), 1990-98 (Waltham & Dixon 2000) and 1996-2002 (Rutter *et al.* 2003). Because the ground surveys were oriented within a local coordinate system, they first needed to be transformed into OSGB coordinates. This was done through measuring the locations of three ground surveyed points in the photogrammetric model, and deriving the parameters of a 3D similarity transformation (Section 4.3.3). The accuracy of the transformation that could be achieved was only about 0.5 m, which was considered adequate for this purpose. The positions of the ground survey points could not be exactly identified on the photographs, but it was assumed that movement was uniform within each landslide unit.

Figure 5.42 shows a plot in which displacement vectors from all datasets and the photogrammetric derived vectors are combined. The displacements from the different periods were scaled to averaged yearly rates, in order to make a direct comparison possible. The magnitude, orientation and spatial variation of the photogrammetric acquired vectors are consistent with the ground-surveyed data: greatest movement rates occur in the central part of the landslide while slower movements take place in the toe.
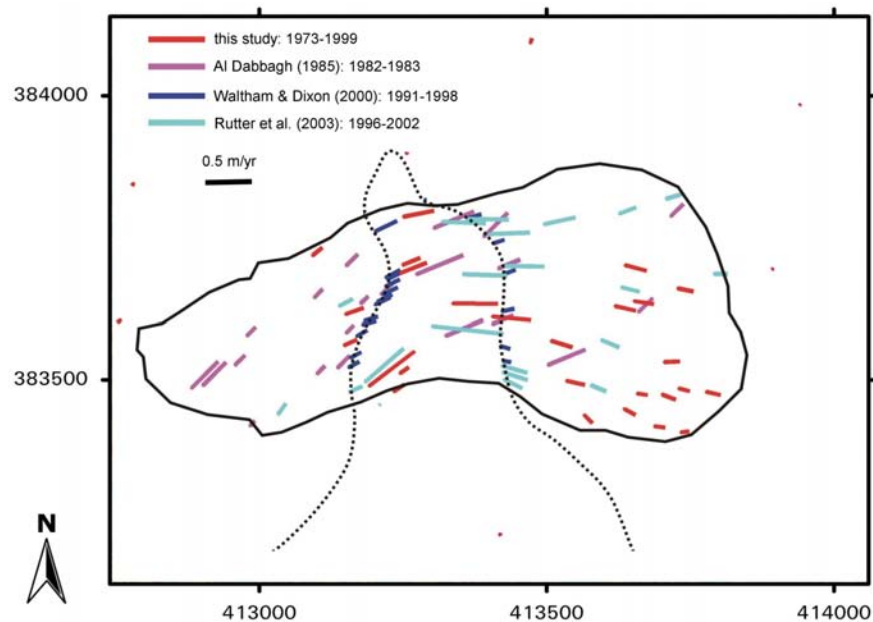
Figure 5.42. Displacement vectors from different datasets, all scaled to yearly rates.
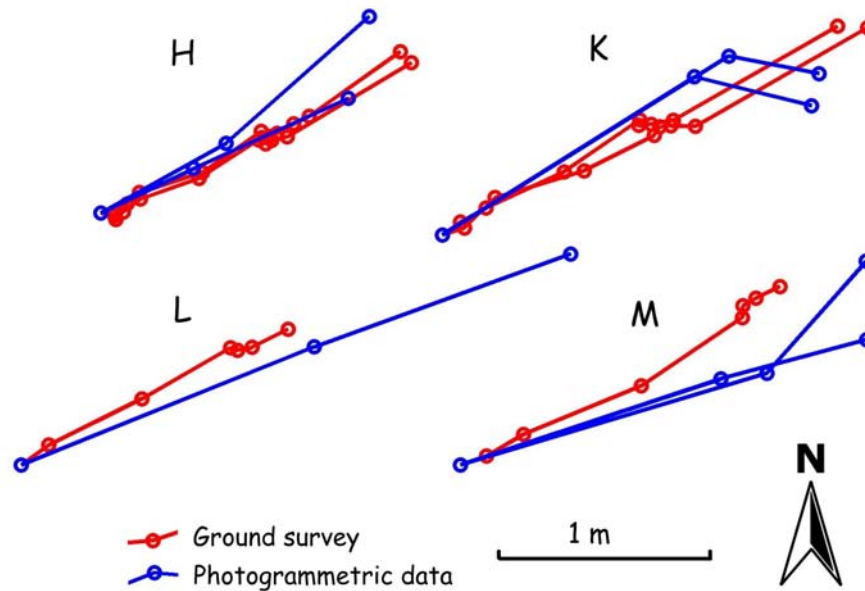
Figure 5.43. Comparison of four monitoring points; the numbers refer to landslide elements in Figure 5.4; ground survey data are yearly records from 1990-2002 from Waltham & Dixon (2000) and Rutter et al. *(2003), while photogrammetric data comprise the 1990, 1995 and 1999 epochs.*

Additionally, calculated movement rates were compared with values obtained from the ground surveying. Mean horizontal displacement of the landslide over the period from 1953 to 1999 was found to be ≃0.21 m/yr, varying from ≃0.09 m/yr at the toe up to ≃0.74 m/yr in the central part. These values are of comparable size to movement rates found by Rutter *et al.* (2003), 0.04-0.35 m/yr during last century and up to 0.50 m/yr in recent years. Figure 5.44 shows in some more detail the movement rates of one particular monitoring point obtained by land surveying and by photogrammetric analysis. Because of the difference in measurement frequency between the two sources, direct comparison was not possible. Therefore the yearly data from the ground surveying were averaged to two intervals of respectively 5 and 4 years, corresponding with the intervals between the image epochs (1990-1995 and 1995-1999). The resulting trends are consistent with each other; both sources show a decreasing movement rate over this period.
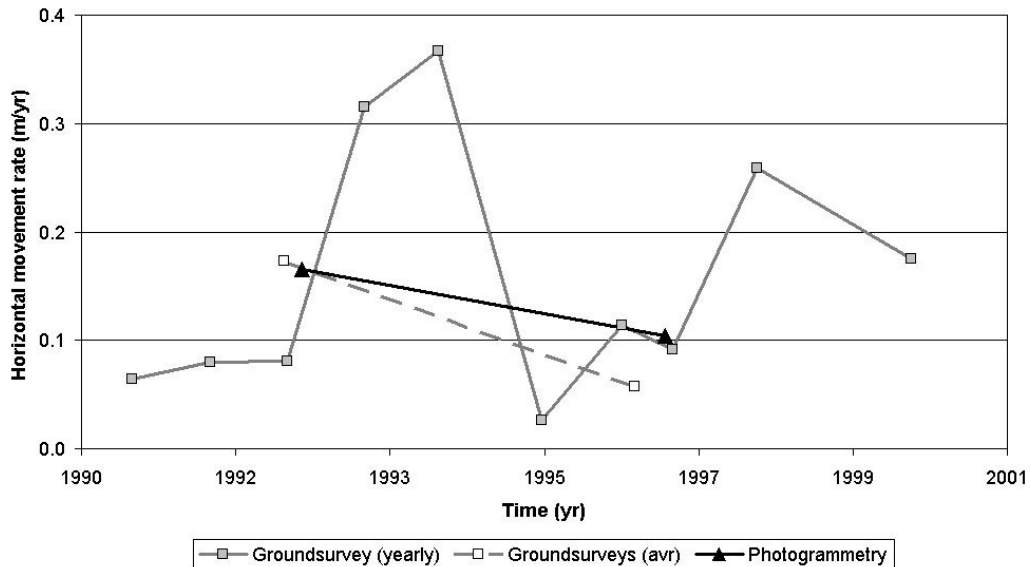
Figure 5.44. Movement rates from ground surveyed and photogrammetric data.

5.5.5 Animations

An animation was created from a sequence of orthophotos of the central part of the landslide (Figure 5.45). The animation clearly visualises the progressive change of the surface; especially the displacement and disintegration of the road is striking. Also a fly-through animation was created, using the DEM and orthophoto from the 1999 epoch, providing a very realistic impression of the landslide area (Figure 5.46). These animations are accessible via internet (Walstra 2006).

Such powerful visualisations can exclusively be acquired using photogrammetric techniques, adding another advantage of photogrammetry over other surveying methods.

5.6 Landslide mechanisms

Due to its limited accuracy, the height data was not suitable for quantitative analysis. This implied that the 'DEMs of difference' could not be used to detect significant transportation of ground volumes, and neither was it possible to make statements on the position and shape of the slip surface.
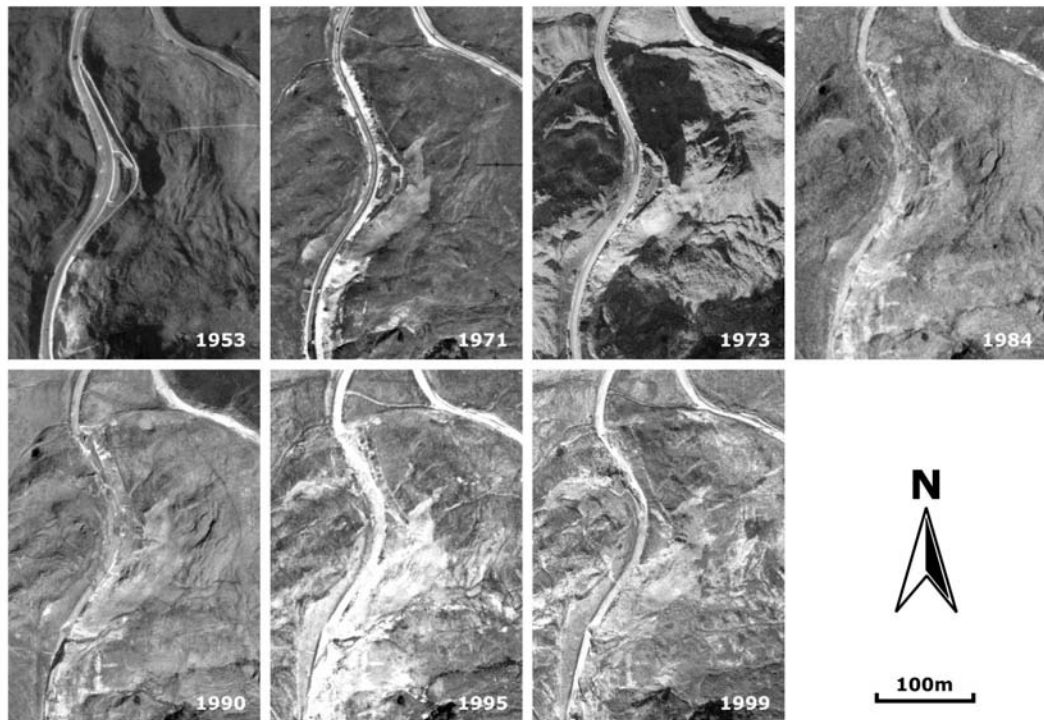
Figure 5.45. Sequence of orthophotos showing the progressive surface change of the central part of the Mam Tor landslide.

Figure 5.46. Realistic 3D view of Mam Tor, created by draping an orthophoto over a DEM, both acquired from the 1999 images.

Qualitative interpretation of the photographs allowed identification of the main landslide elements and indications for their movement mechanisms. All surface features clearly indicate a rotational type of movement in the upper part (arc-shaped scarp, transverse cracks dividing the upper body into several blocks, en-echelon cracks along the sides, bulging at the foot) and a flow slide in the lower part (transverse pressure ridges, radial cracks and drainage pattern in lobe).

The observed horizontal movement pattern matches the morphological interpretation. The predominantly south-eastern direction of the movements in the upper part of the slide suggests that the slip surface is largely controlled by the dip of the geological strata. In the lower part the movement direction suggest that the slip surface is controlled by the original hill slope. At the toe, movements tend to be slightly outwards directed, which suggests an outward spreading of the earthflow lobe. The contour plot of displacements shows a zone of extension in the upper part, which corresponds with the observed transverse cracks this area. A zone of compression below the road sections coincides with the observed pressure ridges.

The temporal pattern of movement rates is showing increased activity during the 1970s and 1990s, while movements slowed down in the late 1980s. The high rates during the 1971-73 period should be interpreted with care, since the measurement error is relatively large over such a short time interval. The period 1973-84 includes the two years of large recorded movements (1977 and 1978), that were responsible for the final road closure. 1994 and 1995 are known to be very wet years causing increased movement rates during the 1990s. During the late 1980s there were some major displacements recorded as well, which do not correlate with the slow rates between 1984 and 1990; maybe the movement was very small in the other years. Table 5.30 shows the number of years that rainfall thresholds for accelerated movement were exceeded during each time interval and the average movement rate of one of the monitoring points. There is no obvious

Table 5.30. Exceeding of rainfall thresholds and average movement rates for each interval.

	Threshold exceeded	Return period	Movement rate
1953-1971	3	9.3	0.83
1971-1973	0	0	1.33
1973-1984	3	3.7	0.98
1984-1990	2	3	0.14
1990-1995	2	2.5	0.72
1995-1999	0	0	0.45

relation between the two values, but the main difficulty preventing a thorough comparison is the limited time resolution of the image epochs.

5.7 Summary

This chapter described a case study on the Mam Tor landslide, intended to develop the methodologies to extract meaningful data from historical photography for quantifying landslide dynamics. The landslide originated 3,600 years ago, but is still moving at present, at rates which are closely related to rainfall characteristics.

Eight different image epochs were acquired, covering a time span of 46 years between 1953 and 1999. The epochs included a wide range of material, in terms of quality, media and format. This provided a good opportunity to assess the data that can be achieved by applying the techniques to commonly available material.

From all epochs, high-resolution DEMs and orthophotos were created and used for further analysis. A geomorphological map was produced only from the 1990 epoch through photo-interpretation, allowing identification of the main elements within the landslide. Quantitative analysis comprised the production of 'DEMs of difference' and measurement of displacement vectors. The vertical accuracy of the data was rather limited, especially compared to the size of vertical displacements. The horizontal data were more useful, because of their generally better accuracy and the larger displacements horizontally; the observed movement pattern could be related to the morphological interpretation. Attempts to extract displacement vectors from orthophotos through automatic image matching techniques were ultimately unsuccessful, due to the absence of distinct features on the ground surface.

Comparison of the photogrammetric measurements with ground surveyed data showed a good consistency. A rigorous comparison was not possible, since the frequency of the image epochs was much lower than the ground surveys, and the position of the ground survey points could not be exactly identified on the photographs. Nevertheless it was evident that direction and magnitude of the movements compared very well.

Due to the limited frequency of the epochs, it appeared to be difficult to relate the observed temporal movement pattern to rainfall data.

Chapter 6

6 Case study East Pentwyn

This chapter describes a case study on the East Pentwyn landslide. This site was used to validate the techniques that were developed in the previous case study on Mam Tor. The landslide was initiated recently and its development well documented. Of particular interest is that the entire development of the landslide is recorded by historical aerial photographs.

The structure of this chapter is similar to that adapted in Chapter 5. First a brief description of the site will be given. Then, the processing of the acquired photographs will be described and the extracted data presented.

6.1 Study area

The East Pentwyn landslide is situated on the eastern face of Ebbw Fach valley, south of Blaina, in the South-Wales Coalfield (OS coordinates SO207075). This region is notorious for its many landslides; an extensive survey during the 1970s by the British Geological Survey identified 579 landslips in the entire region, of which 26 involved deep-seated rotational failures. The majority of these landslides typically occur at the junction of Pennant Sandstone with underlying argillaceous sequences and can be associated with a combination of factors: steep valley sides, thick argillaceous strata to facilitate a curved failure surface, groundwater

conditions providing a piezometric head, and effects of mining subsidence (Conway *et al.* 1980).

   The East Pentwyn landslide is a typical example of such deep-seated rotational failures. The primary failure was triggered as recently as 1954. Two earthflow lobes developed from the displaced block and advanced further downhill, eventually leading to abandonment of 12 houses (Siddle 2000). Remedial measures during the 1980s attempted to stabilise the sliding mass and slow down its continuing movements. Ground movements have been monitored to quantify the effects of the remedial works and observe further development of the slide (Jones & Siddle 1988).

Figure 6.1. The East Pentwyn landslide.

6.1.1 Geology

The geology in this area is not very complicated. Hughes and Brithdir Sandstones are exposed in the backscar of the landslide, overlying the extensively worked Tillery Seam (see Figure 6.2). Beneath are the argillaceous Rhondda Beds, notorious in this part of the Coalfield for its many landslides. The strata dip 5° in south-western direction, slightly outwards of the hillside. High-angle joint sets in the Hughes Sandstone in combination with moderately spaced bedding planes give the backscar a cubical structure. A northwest trending minor fault crosses the landslide area with 5 m downthrow to the southwest. The larger Brynmawr Fault is

250 m west of the site. The hillsides north and south of the landslip are covered with a layer of colluvium of periglacial origin. The Tillery and Hughes Sandstones form an unconfined aquifer, giving rise to a spring line at the crop of the Tillery Seam (Jones & Siddle 1988).
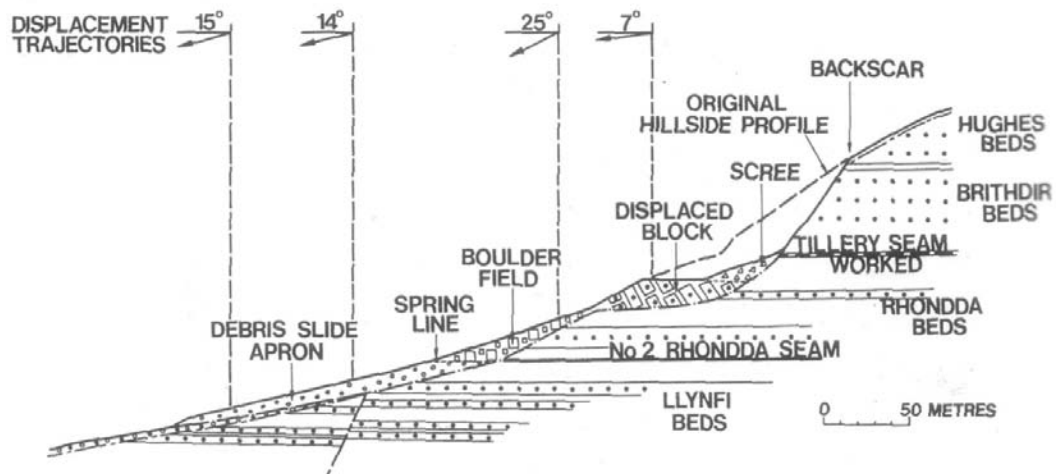
Figure 6.2. Cross-section through the East Pentwyn landslide, showing the geological strata (Siddle 2000).

6.1.2 Morphology

The dimensions of the landslide are approximately 470 m in length and 300 m wide; elevation ranges from 500 m at top of the backscar down to 325 m at the bottom toe.

The arched backscar originates from the initial failure in 1954 but has since regressed due to active rockfall and toppling. The rock face stands to a height of 40-70 m in sandstone and is inclined at 60-70°. In the hillside just behind the backscar some opened fissures are present.

The landslide mass forms a cascading system consisting of three interacting components (Halcrow 1983; Siddle 2000):

1. A displaced block composed of disaggregated sandstone boulders, up to 15 m thick. The block is slightly back-tilted which indicates a rotational failure. Movement is controlled by a weak layer in the underlying Rhondda Beds and maintained by loading of continuing rockfall from the backscar.

2. The central part consists of a boulder field, extending 100 m downslope, 4-9 m thick and resting on Rhondda Beds. Pronounced lateral shears mark the edges of current movements. Heaved ridges at the foot depict a

shallow non-circular slide. At the toe of the boulder field, perched groundwater forms a permanent spring line.

3. Two earthflow lobes originate from 4-5 m high backscars on the downhill side of the boulder field. The lobes are about 6 m thick, and partly consist of overridden and re-activated solifluction sheets. In their early stages material was derived from the argillaceous Rhondda Beds, later replaced by sandstone fragments. Their elongated shape and lateral fissuring on the surface indicate a plastic flow type of movement.
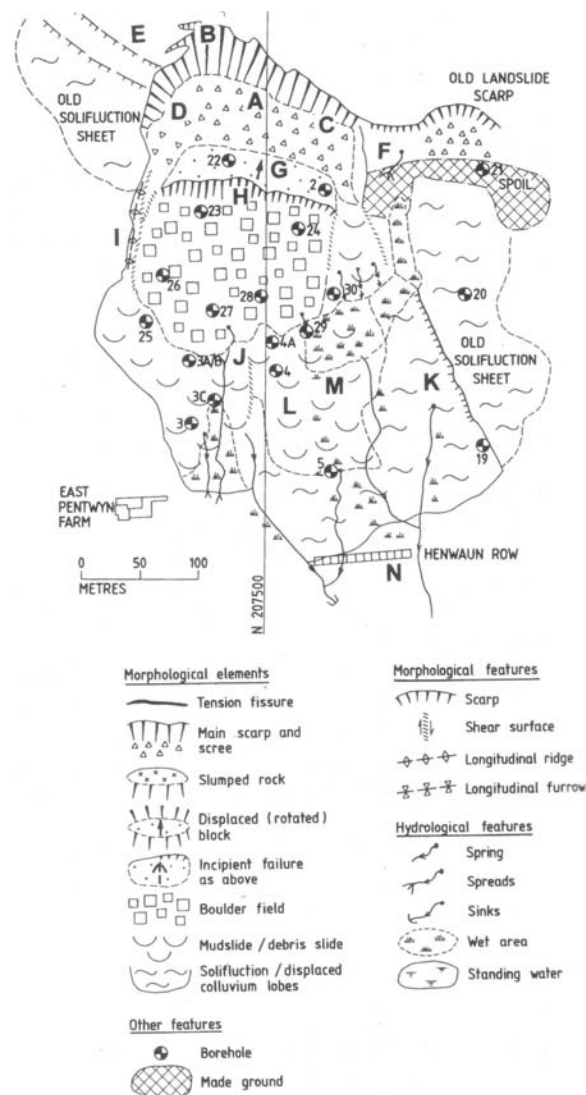
Figure 6.3. Geomorphological map of the East Penwtyn landslide (Siddle 2000).

6.1.3 Movement history

Compared to the Mam Tor landslide in Chapter 5, this failure is very recent and hence its complete development has been well documented and can be observed from historical aerial photographs.

Bulging and fissuring of the ground downhill of the outcropping sandstone sequences are already visible on 1951 aerial photographs (Figure 6.20). The rear scarp was first observed on 22 January 1954, progressively exposed by a rotating block of sandstone. Large-scale movements started on 5 February when groundwater burst out of the displaced block and earthflows moved downhill at rates up to several meters a day. Loading of old landslide deposits resulted in their reactivation. By 8 March the earthflow lobes arrived within reach of housing in 'Henwaun Row' which was subsequently evacuated. Since then slower displacements have continued, maintained by active rockfall entering the cascading landslide system from above (Siddle 2000).

The geological context of the site shows a situation prone to slope instability, controlled by weak argillaceous rock beneath the Tillery Seam, and the effects of cambering in the steep valley side (Halcrow 1983). However, there are strong indications that mining activity has played a vital role in triggering this failure. Computer modelling has demonstrated the importance of critical changes in stress regime within slopes resulting from shallow mining, such as at East Pentwyn (Jones & Siddle 2000). Moreover, groundwater flows were concentrated along the mine roadways in the Tillery Seam and introduced into the landslide area. This may have been responsible for further softening of the Rhondda Beds (Halcrow 1983).

High movement rates during the early 1980s raised concerns for the safety of a housing estate and a nearby farm. Halcrow was commissioned to investigate the site and study remedial measures. The extensive site investigation included sinking boreholes and trial pits to establish the geological structure (Figure 6.2); laboratory testing of soil and rock samples; flow measurements, tracer tests, installation of piezometers and a rainfall gauge to study the hydrogeological conditions; morphological mapping (Figure 6.3); and monitoring of surface movements (Figure 6.4). The collected data were used to perform a stability analysis and design remedial measures (Halcrow 1981; Halcrow 1983).

The results of movement monitoring were of significant interest in the context of this study. Movement markers were installed across the landslide surface in order to measure the effect of the stabilisation works. Records of monthly

displacements are available for the period between 1982 and 1988 (Halcrow 1989). Throughout this period, movement rates were highest in the boulder field (up to 6 m/yr). The movements also showed a clear seasonal pattern, with greatest displacements taking place in the period September-March (Halcrow 1983). The strong correlation of movement rate with rainfall is shown in Figure 6.4. Figure 6.5 presents the spatial variation of movement during two periods (before and after remedial measures were carried out). These recorded movements were ideal to validate the measured displacements in this study (see Section 6.5.4).

The stabilisation measures that where carried out during the 1980s comprised (Jones & Siddle 1988):

1. A drainage blanket surrounding the toe of the earthflow lobes, resulting in underdrainage whilst overridden, and hence reducing downslope extension;

2. Lined drains across the landslide to intercept issues of groundwater and limit surface infiltration;

3. Deep drains in the southern side of the boulder field and the displaced block to intercept groundwater and reduce seepage into the debris.
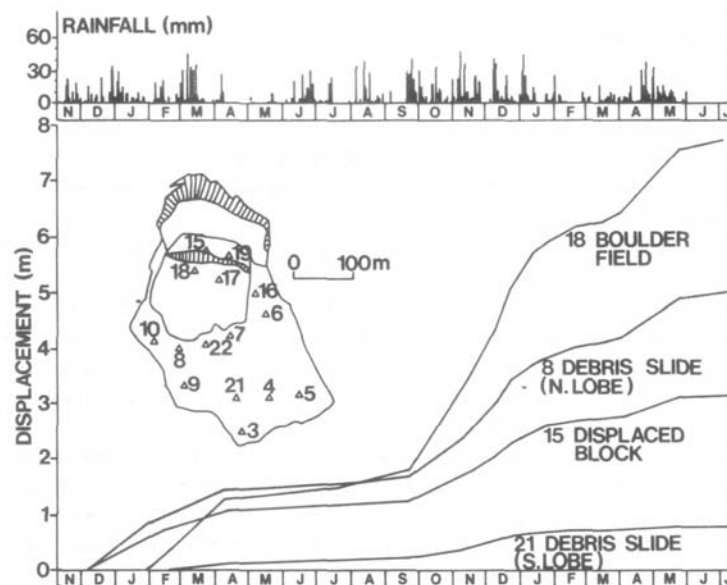
Figure 6.4. Progressive displacement of movement markers in different parts of the East Pentwyn landslide, November 1981-July 1983 (Jones & Siddle 1988).
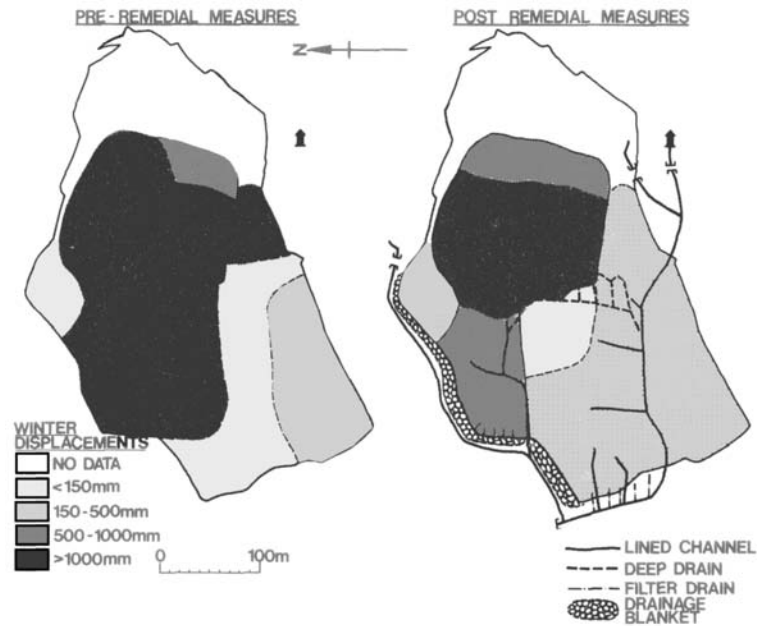
Figure 6.5. Movement rates of East Pentwyn landslide during two periods, 1982-83
and 1987-88, respectively before and after remedial works (Jones & Siddle 1988).

Construction of additional works in the original recommendations, such as an anchored structure between the boulder field and the displaced block were not implemented. Their costs were considered disproportionate to the potential losses of property, and could not resist a potential collapse of the backscar. It was therefore decided to attempt control over the movements in the lower part of the landslide and implement a continuous monitoring scheme. Despite the limited scale of the works, significant reductions in the movements were achieved (Figure 6.5). Greatest improvements were in the southern side of the landslide, where the majority of works had been carried out (Jones & Siddle 1988).

6.2 Acquired photographs

A search for aerial photography by the Central Register of Air Photography for Wales (CRAPW) resulted in a large amount of imagery covering the study area. Although it was recognised that the quality of RAF photography from the 1950s is rather limited for photogrammetric purposes, they did offer a unique opportunity to present images from close before and after the landslide failure. For this reason it was decided to acquire pairs of photographs from 1951 and 1955. The images provide a fairly good definition of the site, but on the 1955 images the backscar of the landslide is obscured through shadows.

The 1971 and 1973 epochs were selected because of their potential for extracting displacement vectors. The quality of the images appeared good and their similar lighting conditions gave hopes for automated vector extraction (Section 6.5.3). If displacement rates during this period were of the same magnitude as in the period 1982-83 (up to 6 m/yr; Halcrow 1983) these would be sufficiently large to be detected.

The CRAPW held the original films of the RAF imagery and the 1973 epoch (originally by Meridian Airmaps Ltd.), and provided photogrammetric-quality scans at high resolution. Scanned diapositives of the 1971 photographs were obtained from their original source; BKS. Characteristics of the imagery at the four epochs are presented in Table 6.1.

Table 6.1. Acquired photographs.

Date	Source	Scale	Focal length	Scan resolution	Ground resolution	Image type*	Format	Original media
1951	CRAPW	1/9,800	20 inch	14 µm	0.14 m	B/W Vert.	18x21 cm	Diapositives
1955	CRAPW	1/9,200	20 inch	14 µm	0.13 m	B/W Vert.	18x21 cm	Diapositives
1971	BKS	1/13,000	153 mm	14 µm	0.18 m	B/W Vert.	23x23 cm	Diapositives
1973	CRAPW	1/8,000	152 mm	16 µm	0.13 m	B/W Vert.	23x23 cm	Diapositives

* B/W = black-and-white, Vert. = vertical

6.3 Ground control collection

The ground control data was collected using differential GPS. Two real-time kinematic (RTK) dual frequency receivers (Leica System 500) were used, which allowed real-time data acquisition (Section 4.2.2). One of the receivers was based at the East Pentwyn farm, near the toe of the landslide. The other receiver was moved around the area to collect data in a stop-and-go survey.

The majority of control points were located in the valley around Blaina, and a small number in the adjacent valley of Cmwtillery. These valleys have undergone some major changes in land use since mining activities ceased; slag heaps have been resurfaced and many constructions demolished. For this reason it was sometimes difficult to find suitable ground control that could be identified on 50 year old aerial photographs. Another obstacle was the hill ridge Mynydd James, which covers a considerable area on the photographs, but does not offer any suitable targets (Figure 6.6). Typical natural control points were corners of old buildings, stonewalls and gravestones (Figure 6.7).
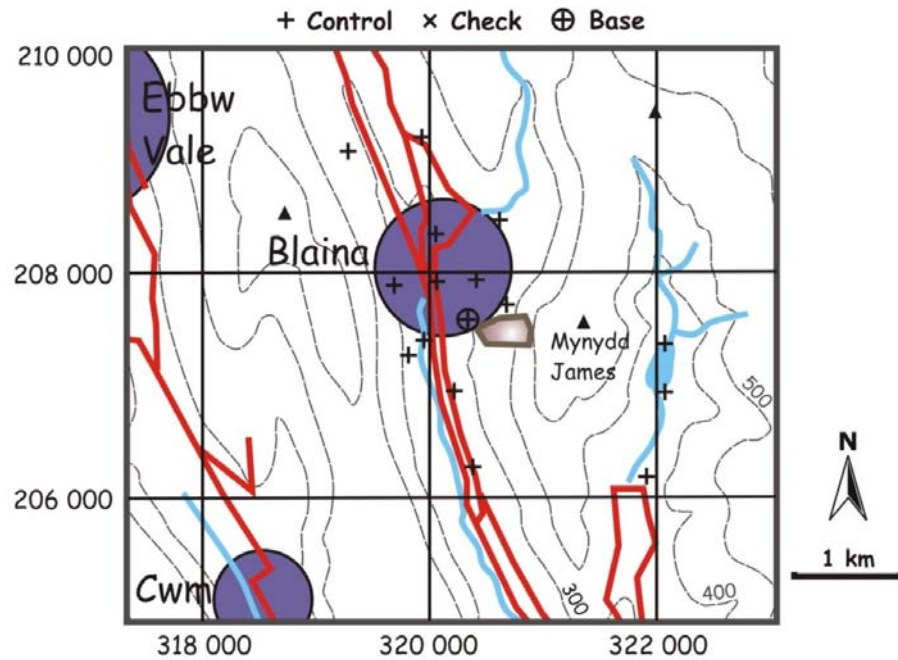
Figure 6.6. Distribution of control and check points, East Pentwyn (each point represents a cluster of points, which cannot be displayed individually at this scale).

Figure 6.7. Typical targets for ground control: corner of an old barn and a gravestone.

GPS data from the active station in Cardiff were downloaded from the National GPS Network website and used for post-processing, similar to the Mam Tor case study. Although real-time data were collected, the post-processing was still needed to reference the data accurately to the National Grid. Coordinates of 59 control points were successfully recovered to a precision of approximately 0.01 m. One third of the points were used as checkpoints during the photogrammetric processing. The distribution of control and check points is displayed in Figure 6.6.

6.4 Photogrammetric processing

6.4.1 Restitution

Photogrammetric restitution was straightforward for the 1971 images, as these were provided with a camera calibration certificate (Figure 6.8, Table 6.2). Compared to the other epochs, its small scale and hence large coverage in combination with a relatively recent age resulted in sufficient availability of ground control; 22 control points were used to define the photogrammetric model (Figure 6.10). A limitation of these images was the presence of a high degree of radiometric noise, forming a 'salt and pepper' pattern. This noise prevented the accurate definition of features and also deteriorated the performance of image matching. It was judged useful to remove this noise before the processing could proceed. A quick but satisfying method was applying the 'Jaggy despeckle' filter in Corel Photo-Paint (Version 10). This filter removed the noise while causing only minimal spatial distortion to the image, as stated by the software's manual and confirmed through visual inspection (Figure 6.9). Using the de-noised images, the image matching for automatic tie point generation was much improved. Tie points in the uphill area of Mynydd James remained difficult due to low image contrast. Because of the bad radiometric quality of the images, the standard deviation of image measurements was increased to 0.30 pixels. Accuracy of the solution was good, judging residuals of less than 0.2 m in plan and 0.6 m in height (Table 6.3).

The 1973 images were lacking a calibration certificate, but obviously captured with a metric camera; clear fiducial marks were present in the corners allowing accurate estimates of the principal point position (Figure 6.11). Values for focal length (152.05 mm) and flying height (1530 m) were displayed on the data strip of the frames. The image pair was aligned along the valley, with the result that control points were mainly distributed along the central part of the photographs (Figure 6.12), and only tie points in the uphill regions on both sides. An attempt to improve the estimates for the interior orientation of the camera in a self-calibration procedure resulted in unrealistic values (Table 6.5), whereas the residuals of the solution were only slightly better than using the original estimates (see Table 6.6). It was suspected that the poor distribution of control was responsible for high correlation of interior with exterior orientation, hence giving rise to inaccurate parameters. Use of this unrealistic camera model resulted in systematic errors that became very pronounced in the created orthophotos:

deviations up to 3.8 m compared to an orthophoto from the 1971 epoch. In situations where additional parameters are correlated, they should be removed from the solution, as explained in Section 3.2.2. Independent checks suggested the decision to neglect the self-calibration procedure proved valid. The residuals of the photogrammetric solution were acceptably low (object residuals of checkpoints smaller than 0.5 m in plan), while the systematic errors in the orthophotos were reduced to less than 1 m.

Figure 6.8. Frame 648030 of the 1971 epoch (© copyright BKS).
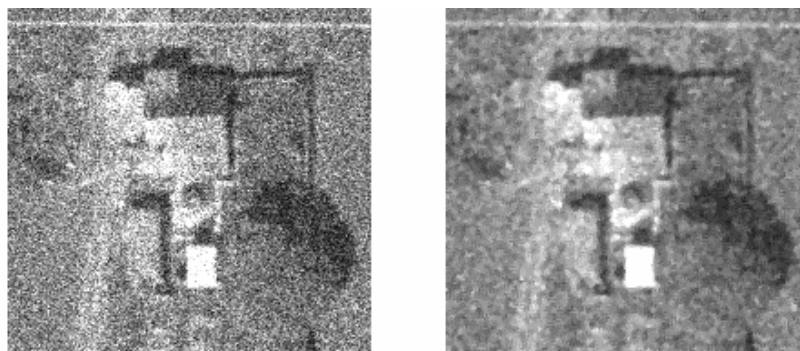
Figure 6.9. Original image (left) and after noise removal (right).
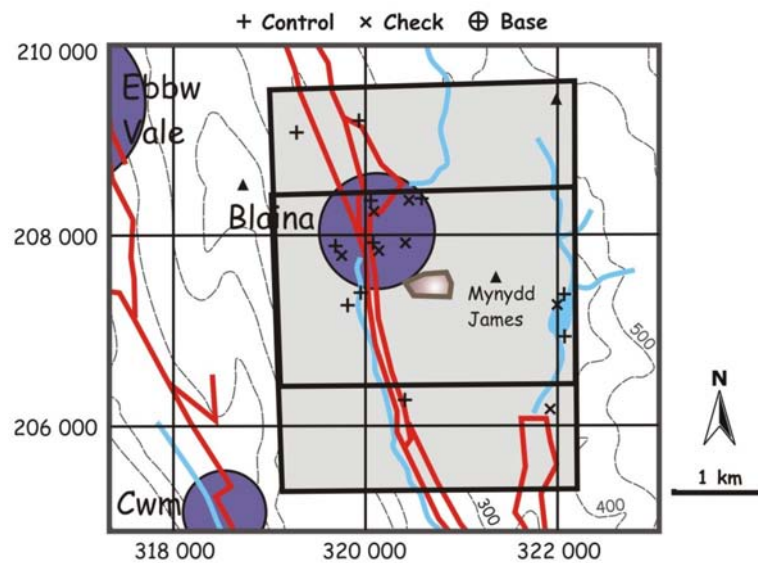
Figure 6.10. Coverage of the 1971 images and distribution of ground control and check points.

Table 6.2. Details of the 1971 epoch.

Source	BKS
Media	Scanned B&W diapositives
Frame numbers	648030 & 648031
Date	1 June 1971
Scale	1/13,000
Resolution	14 µm
Ground resolution	0.18 m
Flying height	2330 m
B/H ratio	1/1.90
Focal length	152.85 mm
x_0	-0.005 mm
y_0	-0.011 mm

Table 6.3. Results from the bundle block adjustment, 1971 epoch.

			x	y	z
Control points	22				
Tie points	275	Image residuals control (µm)	13.31	14.19	
Checkpoints	10	Image residuals check (µm)	12.30	16.18	
Std. photo (pixels)	0.30	Ground residuals control (m)	0.007	0.008	0.005
Std. ground (m)	0.01	Ground residuals check (m)	0.19	0.18	0.58

Figure 6.11. Frame 7333 of the 1973 epoch (© copyright reserved); the enlargement shows one of the uncalibrated fiducials.
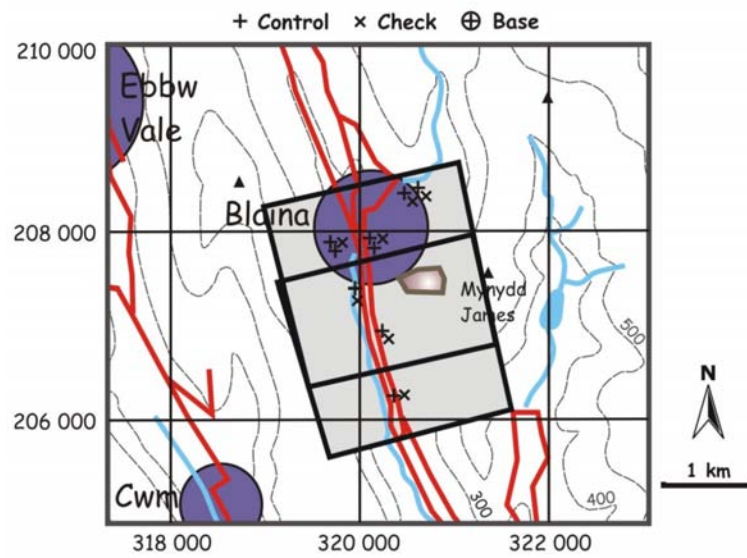
Figure 6.12. Coverage of the 1973 images and distribution of ground control.

Table 6.4. Details of the 1973 epoch.

Source	CRAPW (Meridian)
Media	Scanned B&W diapositives
Frame numbers	7332 & 7333
Date	14 June 1973
Scale	1/8,000
Resolution	16 µm
Ground resolution	0.13 m
Flying height	1575 m
B/H ratio	1/1.67

Table 6.5. Comparing the interior orientation parameters estimated in a self-calibrating bundle adjustment and without calibration, 1973 epoch.

	No calibration	Self-calibration
Focal length	152.05 mm (fixed)	152.05 mm (fixed)
x_0	0 (fixed)	6.91 ± 0.28 mm
y_0	0 (fixed)	-2.63 ± 0.21 mm
k_1	0 (fixed)	-0.13 ± 0.01
k_2	0 (fixed)	0.3 ± 0.3

Table 6.6. Comparing the results from the bundle block adjustment, using the self-calibrated parameters and an uncalibrated camera model, 1973 epoch.

Control points	8					
Tie points	115					
Check points	6					
St. dev. photo (pixels)	0.20					
St. dev. ground (m)	0.01					

	Self-calibrated camera model			No calibration		
	x	*y*	*z*	*x*	*y*	*z*
Image res. control (µm)	26.43	18.39		30.60	33.26	
Image residuals check (µm)	30.87	27.54		31.55	37.43	
Ground residuals control (m)	0.016	0.009	0.002	0.019	0.010	0.006
Ground residuals check (m)	0.16	0.22	0.84	0.49	0.13	0.78

The RAF imagery from 1951 and 1955 presented more challenges for restitution of a satisfactory photogrammetric model. First of all, these old RAF images were rather blurred and had a poor base to height ratio (Figure 6.13 and Figure 6.15). No calibration data was available and their spatial arrangement rather poor in relation to the distribution of ground control (Figure 6.14 and Figure 6.16). All these limitations could still not explain the very poor results that initially were achieved; large systematic errors were identified in both pairs, in particular in the control points tying the two frames together (residuals up to 0.4 m in object space and more than 200 µm in the images).

Inspection of the manually measured coordinates of the reference marks on the frames used for fiducials, revealed large discrepancies between the two frames in both pairs. Measurement of the distances between the marks showed that the error could be mainly attributed to the right-hand fiducial mark in both cases (distortions exceeded 100 µm across the frames, see Table 6.8 and Table 6.12). There could be several explanations for these large distortions; deficiencies during image capture, distortion of the film during storage or irregularities during the scanning procedure. However, there was no sign of distortion apparent upon visual inspection of the frames. Irrespective of the causes, a first solution was to avoid this part of the images during the photogrammetric restitution; the interior orientation was defined based on the three remaining reference marks, and the control points in these areas were ignored. Still, only a poor photogrammetric solution could be obtained, which implied that the distortion was not restricted to just this part of the image.

Another possible solution would be to accept the systematic distortion and attempt to account for it in the camera model by using the available parameters in the self-calibration adjustment. Experiments were carried out implementing a differential x-scale factor and using different camera models for each frame. Although the residuals were greatly reduced, the resulting camera parameters were completely unrealistic (change in focal length of several 100s of mm, principal point offsets of many centimetres). It again appeared that the models were over-parameterised, and there was a high correlation between the parameters. It was decided to use rather a crude model that was more realistic and accept the consequently larger residuals. For both epochs it was decided to fix the focal length, since this parameter was highly correlated with flying height in the bundle adjustment, and the expected accuracy in height was low anyway. Self-calibration

Figure 6.13. Frame 4263 of the 1951 epoch (RAF).
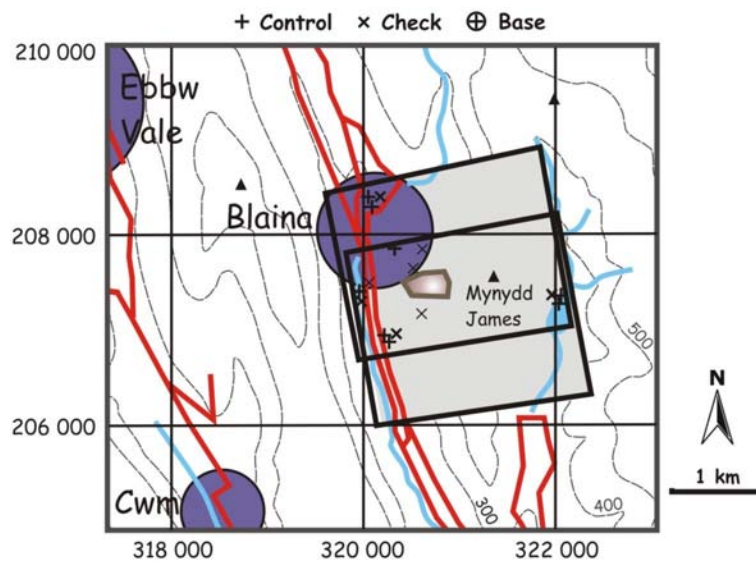
Figure 6.14. Coverage of 1951 images and distribution of ground control.

Table 6.7. Characteristics of the 1951 epoch.

Source	CRAPW
Media	Scanned B&W diapositives
Frame numbers	4262 & 4263
Date	12 May 1951
Scale	1/9,800
Scan resolution	14 µm
Ground resolution	0.14 m
Flying height	5,400
B/H ratio	1/6.8

Table 6.8. Measurement of the reference marks on the 1951 images.

	Frame 4262		Frame 4263		Difference	
	x (mm)	*y (mm)*	*x (mm)*	*y (mm)*	*x (µm)*	*y (µm)*
1	84.71	0.00	84.68	0.00	-27.04	0.00
2	0.26	-102.61	0.23	-102.61	-28.08	-2.37
3	-84.47	0.00	-84.58	0.00	-105.97	0.00
4	-0.25	97.20	-0.22	97.25	26.49	51.80

Table 6.9. Estimated interior orientation parameters from a self-calibrating bundle adjustment using different models, 1951 epoch.

	No calibration	No radial distortion	Incl. radial distortion
Focal length	508 mm (fixed)	508 mm (fixed)	508 mm (fixed)
x_0	0 (fixed)	-3.82 ± 0.34 mm	-2.77 ± 0.38 mm
y_0	0 (fixed)	-31.29 ± 0.61 mm	-24.65 ± 0.83 mm
k_1	0 (fixed)	0 (fixed)	0.25 ± 0.02
k_2	0 (fixed)	0 (fixed)	-2.9 ± 0.8

Table 6.10. Comparison of results from the bundle block adjustments, using different camera models, 1951 epoch.

Control points	9		
Tie points	49		
Check points	8		
St. dev. photo (pixels)	0.5		
St. dev. ground (m)	0.01		

	No calibration			No radial distortion			Incl. radial dist.		
	x	*y*	*z*	*x*	*y*	*z*	*x*	*y*	*z*
Image res. control (µm)	28.13	54.72		21.93	28.56		24.76	35.28	
Image res. check (µm)	3.70	39.73		4.28	35.92		6.05	45.13	
Ground res. control (m)	0.013	0.008	0.001	0.007	0.004	0.001	0.009	0.005	0.001
Ground res. check (m)	9.25	2.60	24.13	1.65	1.05	8.03	1.26	1.62	13.86

Figure 6.15. Frame 6209 of the 1955 epoch (RAF).
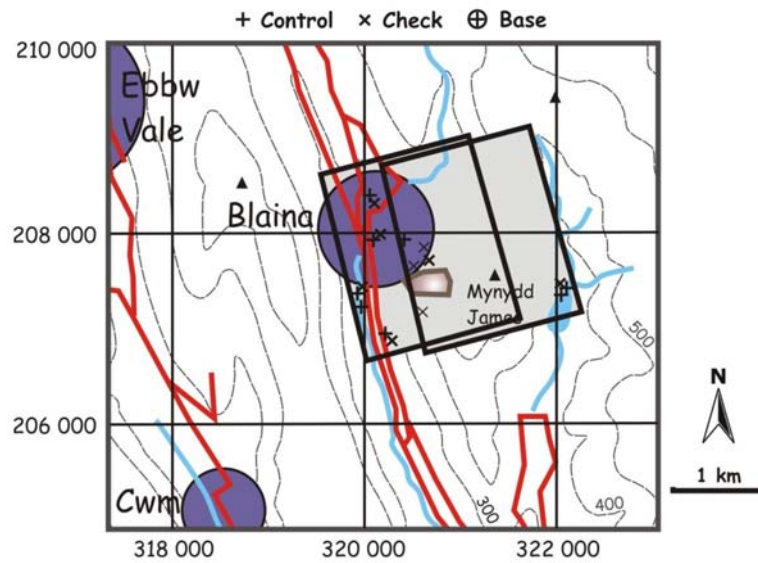
Figure 6.16. Coverage of the 1955 images and distribution of ground control.

Table 6.11. Characteristics of the 1955 epoch.

Source	CRAPW
Media	Scanned B&W diapositives
Frame numbers	209 & 210
Date	14 April 1955
Scale	1/9,200
Scan resolution	14 µm
Ground resolution	0.13 m
Flying height	5,100
B/H ratio	1/7.6

Table 6.12. Measurement of the reference marks on the 1955 images.

	Frame 4262		Frame 4263		Difference	
	x (mm)	y (mm)	x (mm)	y (mm)	x (µm)	y (µm)
1	-85.03	-0.25	-84.96	-0.25	70.49	-2.64
2	84.29	0.25	84.12	0.25	-168.31	2.33
3	0.00	97.61	0.00	97.63	0.00	22.24
4	0.00	-101.87	0.00	-101.88	0.00	-9.96

Table 6.13. Estimated interior orientation parameters from a self-calibrating bundle adjustment using different models, 1955 epoch.

	No calibration	No radial distortion	Incl. radial dist.
Focal length	508 mm (fixed)	508 mm (fixed)	508 mm (fixed)
x_0	0 (fixed)	-1.51 ± 0.59	-3.72 ± 0.55
y_0	0 (fixed)	-28.52 ± 0.29	-34.97 ± 0.43
k_1	0 (fixed)	0 (fixed)	0.40 ± 0.03
k_2	0 (fixed)	0 (fixed)	1.9 ± 0.5

Table 6.14. Comparison of results from the bundle block adjustment, using different camera models, 1955 epoch.

Control points	8								
Tie points	76								
Check points	9								
St. dev. photo (pixels)	0.5								
St. dev. ground (m)	0.01								
	No calibration			No radial dist.			Incl. radial distortion		
	x	y	z	x	y	z	x	y	z
Image res. control (µm)	94.23	112.6		29.24	45.74		21.78	40.21	
Image res. check (µm)	62.56	90.13		26.51	29.45		25.37	30.55	
Ground res. control (m)	0.020	0.024	0.003	0.009	0.010	0.003	0.007	0.008	0.002
Ground res. check (m)	1.21	6.09	21.68	0.92	0.62	10.85	0.46	1.99	9.05

adjustments were carried out both including and excluding the additional parameters for radial distortion (Table 6.9 and Table 6.13). Although the residuals of the control points were lower when including radial distortion, the checkpoints showed a better accuracy when these were excluded. The estimates for the principal point offsets were still excessively large, but the accuracy in object space was significantly better than using no additional parameters at all. Additional checkpoints were measured in the 1971 stereomodel and confirmed the satisfactory solution that was achieved. The achieved accuracy of less than 1 m in object space was considered the optimum for such poor quality images, and so this simple camera model was used for further processing. Comparisons of the different photogrammetric restitutions for the two epochs are tabulated in Table 6.10 and Table 6.14.

6.4.2 DEM extraction

Automatically extracted DEMs were produced from all epochs. A grid spacing of 1 m was used for the 1970s images and of 2 m for the 1950s epochs. Optimum results were achieved using the 1973 images, since these had the best contrast to suit image matching. Because of their lower contrast, the threshold correlation coefficient was lowered for the other epochs. The low contrast of the uphill area adjacent to the landslide and the steep valley sides proved to be particularly difficult for DEM extraction. Values for the DEM extraction strategy parameters are shown in Table 6.15.

Table 6.15. DEM extraction parameters for the four epochs.

	1951	1955	1971	1973
Search Size	9x3	9x3	15x3	27x3
Correlation Size	7x7	7x7	7x7	7x7
Coefficient Limit	0.70	0.70	0.75	0.80
Topographic Type	RH*	RH	RH	RH
Object Type	OA**	OA	OA	OA
DTM Filtering	High	High	High	High
Cell Size (m)	2	2	1	1
Mass points (per ha)	140	89	235	781
Number of checkpoints	13	5	18	4
Mean error checkpoints (m)	1.47	15.0	-0.77	0.44
Standard error checkpoints (m)	7.91	7.80	1.75	1.76

* RH = Rolling Hills; ** OA = Open Area
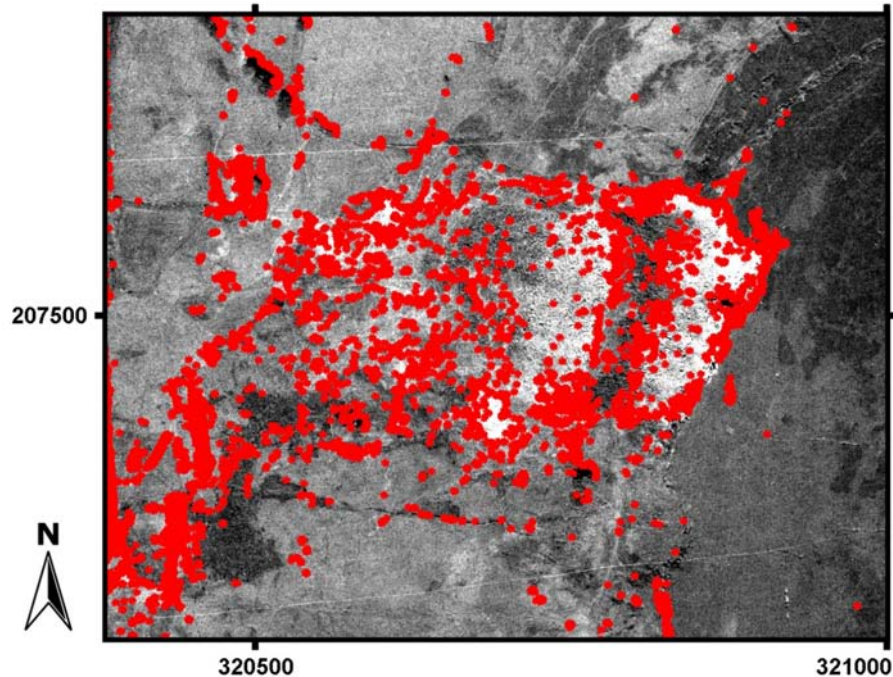
Figure 6.17. Distribution of mass points for DEM extraction, 1971 epoch.

6.4.3 DEM Quality

The amount of mass points gives an indication of the success of the image matching procedure during the DEM extraction (Section 4.2.4). The values in Table 6.15 show a very low density in most of the epochs, due to the limited contrast in the images. Figure 6.17 shows the very low density of mass points in extensive areas in the 1971 images.

The RMS error of checkpoints provided an indication for the accuracy of the DEMs. However, these values can be regarded as very optimistic. The checkpoints are all located in centre of the valley; due to the limited accuracy in height of the photogrammetric models (especially the RAF imagery) and little mass points in the uphill area, the DEM accuracy can be expected to be much lower in these areas.

6.4.4 Orthophoto generation

Orthophotographs were generated using a resolution corresponding to the ground resolution of the original images at the landslide area. Additionally, orthophotos at an identical resolution were required as a basis for automated extraction of displacement vectors; therefore from the 1971 and 1973 epoch orthophotos at 0.2 m resolution were created. An example of an orthophoto is presented in Figure 6.18, created from the 1971 images.

Visual inspection of the orthophotos showed that poor DEM accuracy had a significant effect on the orthophotos. In particular in the uphill areas the planar distortion of features was very large and resulted in deviations between the different epochs. On the valley floor the DEMs were more accurate and hence, consistency between the orthophotos is much better. Figure 6.19 displays large distortions in the orthophoto from the 1971 epoch, caused by poor DEM quality.

Four checkpoints were used to provide an indication of the accuracy of the orthophotos (Table 6.16). The values for 1955 and 1973 should be considered with caution as only two checkpoints were covered by the orthophoto. In the 1971 epoch, the significant effect of poor DEM quality is evident: horizontal accuracy achieved in the bundle adjustment was 0.26 m, while this exceeded 1 m in the orthophoto.
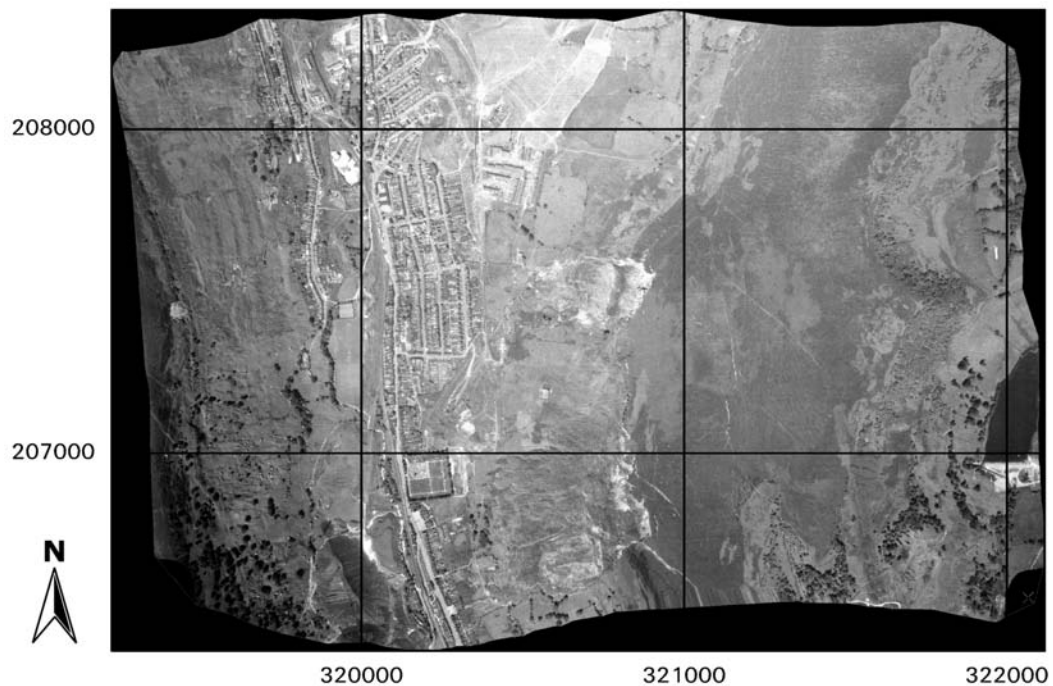
Figure 6.18. Orthophoto created from the 1971 epoch.

Figure 6.19. Detail of the 1971 orthophoto showing distortions caused by the poor-quality DEM used for its creation.

Table 6.16. Accuracy of the orthophotos.

Epoch	Resolution	Mean error checkpoints	Standard error checkpoints
1951	0.14 m	1.82	0.72
1955	0.13 m	0.57	0.06
1971	0.18 m	1.18	1.11
1973	0.13 m	0.53	0.54

6.5 Visualisation and analysis

6.5.1 Geomorphological maps

Although the quality of the 1951 and 1955 RAF imagery was limited for accurate quantitative measurements, they did offer a good opportunity for qualitative analysis. Geomorphological maps were created using the legend from Figure 4.6. Comparison of the maps from 1951 and 1955 (Figure 6.20) clearly shows the extent of the major failure that occurred in 1953.

On the 1951 photographs tension fissures were visible at the position of the scarp later formed by the failure. Some recent minor mass movements were observed, and a large part of the slope was covered with ancient solifluction sheets.

On the 1955 photographs the extend of the major failure was evident. Earthflow lobes override and reactivated the old solifluction lobes, reaching all the way down to the houses of 'Henwaun Row'. The linear ridges across the lobes suggested a plastic flow. The upper part of the mass was covered with scree and boulders. Unfortunately, the main scarp was obscured by shadows.
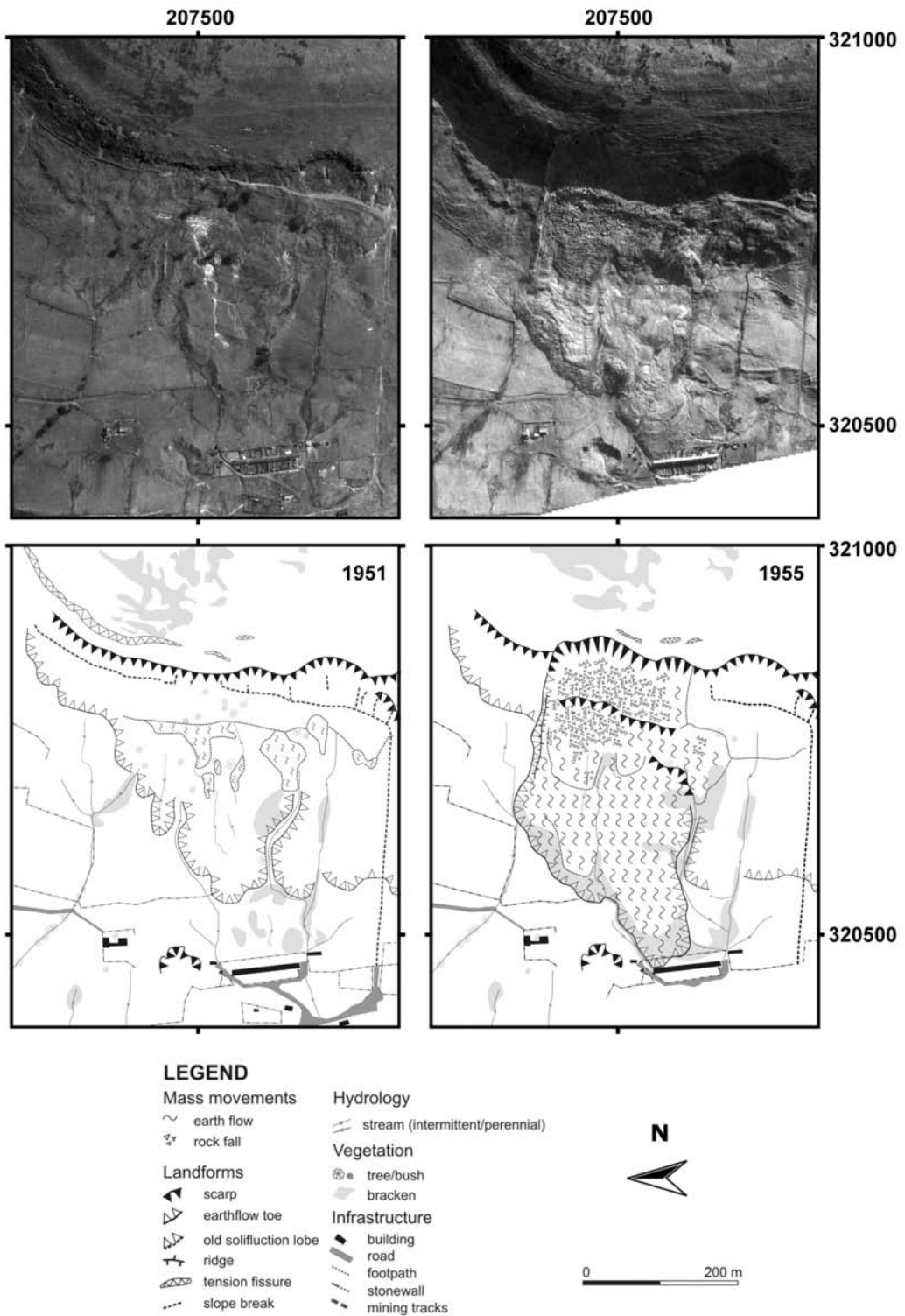
Figure 6.20. Orthophotos and geomorphological maps from the 1951 and 1955 epoch, showing the extent of the East Pentwyn failure.

6.5.2 *'DEMs of difference'*

Due to the poor DEM quality it was not practical to create 'DEMs of difference' that were able to detect significant surface changes. This can be illustrated with the 'DEM of difference' for the period 1973-71 shown in Figure 6.21. Large systematic errors existed between the DEMs of the two epochs. These could be mainly attributed to the poor mass point distribution of the 1971 epoch (see Figure 6.17). Analysis of the statistics of differences in three sub-areas revealed that these were in fact larger in the areas surrounding the landslide than on the landslide itself (Table 6.17). Hence, it was concluded that after correction for these systematic errors, significant changes would still be undetectable.
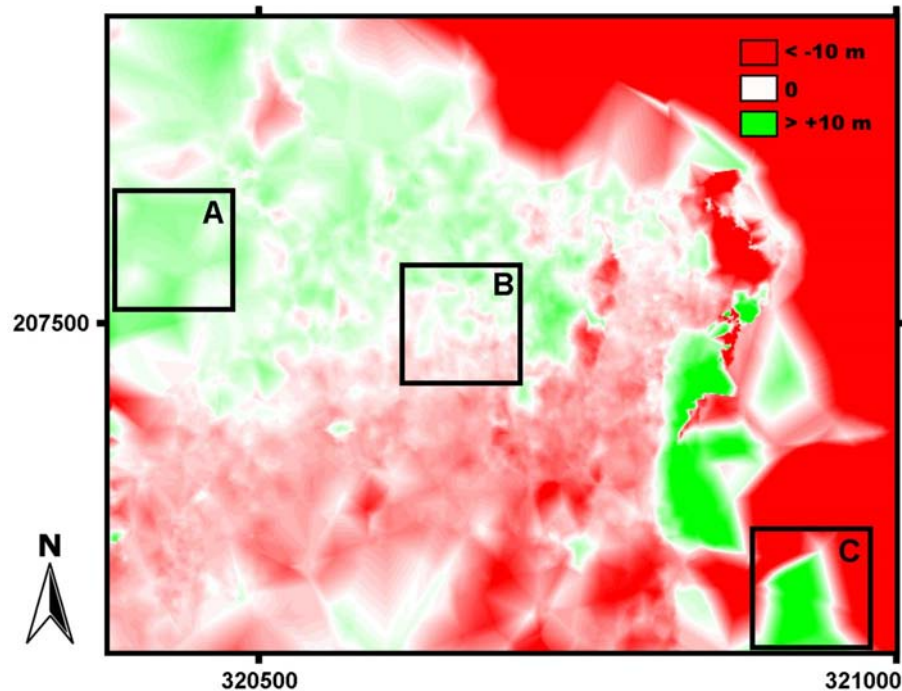
Figure 6.21. 'DEM of difference' 1973-71; the statistics of the three boxes are presented in Table 6.17.

Table 6.17. Statistics of 'DEM of difference' 1973-71 in three sub-areas.

Area	Mean difference	Standard difference
A	2.79	1.49
B	0.98	1.41
C	-7.68	12.3

6.5.3 Displacement vectors

The 1971 and 1973 epochs were specifically selected because of their potential for automated extraction of displacement vectors. On these photographs the landslide surface was not obscured by vegetation cover and mainly consisted of large boulders that could be individually identified. Also, the sorties were flown at about the same time of the year, at similar times of the day (afternoon in June), and consequently under similar lighting conditions. Unfortunately, a lot of radiometric noise was present in the 1971 images, as discussed in Section 6.4.1. Although the noise was largely removed, there was still considerably less contrast and detail present in these images (Figure 6.22).
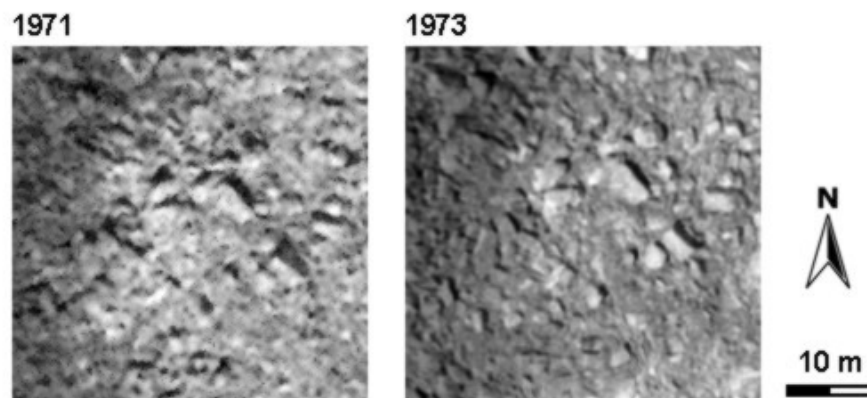
Figure 6.22. Detail of the orthophotos from 1971 and 1973, showing large boulders covering the landslide surface. Note that although lighting conditions are similar the 1971 image is less sharp.

Manual measurements of 28 points on and 4 off the landslide, using Erdas' StereoViewer tool revealed that the displacements were large enough to be detected from these photographs. The statistics from the four stable points provided data for assessing the accuracy of the measured displacements; co-variances of the errors between the two epochs allowed the creation of error-ellipses, as described in Section 4.3.3. The measured displacements were significant, up to 18.5 m in horizontal direction and variable over the whole landslide area. In most cases, the statistical threshold at a 95% confidence level was easily exceeded for horizontal displacements (i.e. larger than 2.62 m). As was also experienced in the Mam Tor case-study, the vertical accuracy of the data was poorer than horizontally. Consequently, vertical displacements needed to be larger (exceeding 3.79 m) in order to be accepted; this was only the case in a limited number of the 28 measured points. The measured displacements are tabulated

(Table 5.27) and plotted on an orthophoto (Figure 6.23). Although the point density was rather low, the measurements were also interpolated and presented in the form of a contour plot and a grid surface (Figure 6.24).

Table 6.18. Measured displacements between the 1971 and 1973 epochs; the first four points are stable points off the landslide used for accuracy assessment. Italic numbers represent insignificant displacements at 95% confidence level.

	1971			1973			Change	
Point	*x*	*y*	*z*	*x*	*y*	*z*	*dxy*	*dz*
1	320490.77	207620.82	333.66	320491.46	207621.27	335.75	*0.83*	*2.09*
2	320634.66	207633.40	366.86	320634.37	207632.94	364.88	*0.55*	*-1.98*
3	320694.28	207336.00	381.12	320696.02	207336.94	379.57	*1.98*	*-1.55*
4	320455.56	207396.20	325.88	320455.94	207396.74	325.13	*0.66*	*-0.75*
5	320821.17	207551.81	425.64	320820.37	207552.87	425.69	*1.33*	*0.05*
6	320820.90	207544.85	427.78	320816.96	207546.99	427.78	4.49	*0.00*
7	320815.62	207474.29	428.02	320815.55	207475.39	424.53	*1.11*	*-3.49*
8	320817.84	207469.58	432.29	320818.30	207471.82	428.13	*2.29*	-4.16
9	320782.47	207462.65	418.43	320782.16	207463.02	416.10	*0.49*	*-2.32*
10	320781.98	207516.45	426.18	320778.45	207518.52	423.46	4.10	*-2.72*
11	320755.72	207574.66	410.13	320744.03	207577.07	405.87	11.94	-4.26
12	320750.86	207449.92	408.38	320739.04	207451.45	400.35	11.92	-8.03
13	320741.39	207426.88	407.14	320738.46	207428.31	402.53	3.26	-4.61
14	320734.60	207450.32	403.14	320716.38	207453.58	392.20	18.51	-10.94
15	320725.87	207446.56	401.12	320709.09	207448.80	389.61	16.93	-11.52
16	320686.39	207505.08	380.17	320679.77	207504.45	378.12	6.66	*-2.05*
17	320667.65	207491.84	377.71	320660.49	207491.75	376.07	7.16	*-1.65*
18	320679.80	207551.66	385.16	320668.21	207553.94	382.26	11.81	*-2.90*
19	320649.15	207541.10	376.72	320640.66	207542.08	373.57	8.55	*-3.14*
20	320620.23	207533.93	364.66	320613.19	207533.62	365.09	7.05	*0.43*
21	320627.71	207510.70	367.72	320624.08	207512.22	367.42	3.94	*-0.30*
22	320605.53	207556.23	365.46	320598.24	207556.01	363.93	7.29	*-1.53*
23	320558.48	207531.14	351.15	320554.43	207533.34	350.95	4.61	*-0.20*
24	320553.89	207544.30	350.05	320547.67	207545.47	349.30	6.32	*-0.75*
25	320552.22	207452.64	350.07	320550.07	207452.70	347.47	*2.15*	*-2.60*
26	320521.83	207462.59	344.60	320520.25	207463.16	343.55	*1.68*	*-1.04*
27	320494.89	207392.14	333.13	320494.41	207391.67	329.87	*0.67*	*-3.26*
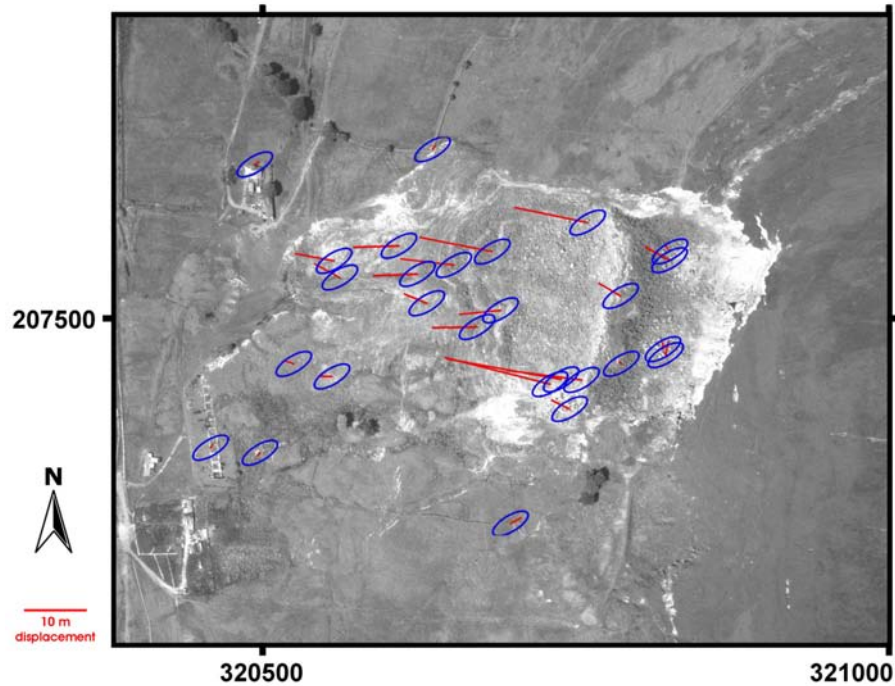
Figure 6.23. Horizontal displacement vectors 1971-1973.
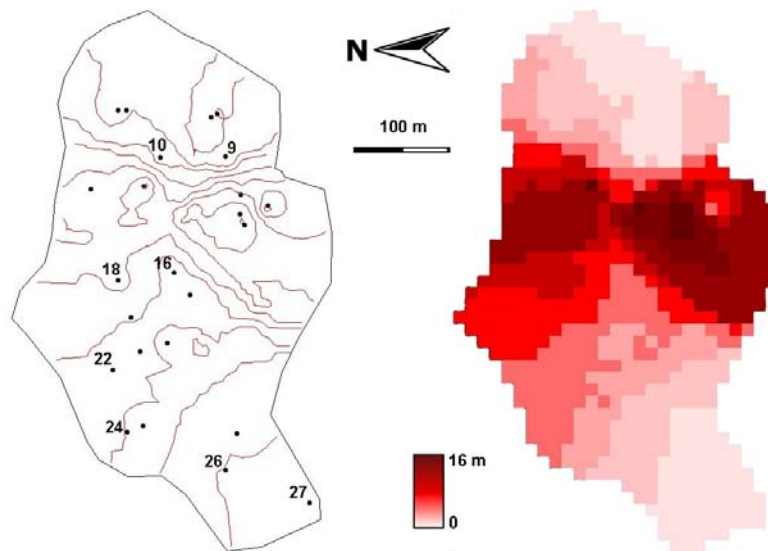
Figure 6.24. Interpolated displacements, using an 'Inverse Distance Weighted' mean of 5 neighbouring points and a grid cell of 10 m; contours shown have an interval of 2 m. In spite of the low density, a clear pattern is evident with largest displacements in the central part of the landslide. Numbered points refer to Table 6.19.

Although expectations were high for automatic image matching between the two orthophotos, the attempts did not lead to any success. Inputs for the algorithm were the two orthophotos, one from each epoch, generated at identical ground resolution of 0.2 m. The search window size that was used was based on the manual measured displacements. The maximum displacement was about 18 m in x-direction and 4 m in y-direction, so a slightly larger search window of 20x5 m (101x25 pixels) was adopted. A rectangular rather than square search window size was used to reduce processing time and minimise the chance on mismatches. The values for template size and correlation threshold were varied, but none of the attempts led to reliable results. Striking are the many large 'displacements' appearing on stable grounds. Part of these apparent displacements may be attributed to distortions in the orthophotos through the poor quality of the DEMs used for their creation (as discussed in Section 6.4.4; especially the hillslopes outside the landslide area that suffered from a lack of mass points and hence inaccuracies of the DEM), but their large size clearly suggested faulty matches. For this reason it could be assumed that many of the vectors in the landslide area were actually related to mismatches rather than genuine movements. Attempts to eliminate mismatches through increasing the correlation coefficient threshold value or applying larger templates were unsuccessful (Figure 6.25).

6.5.4 *Comparing with ground survey data*

The manual measured displacements between the 1971 and 1973 epochs were compared to independent monitoring data provided by Halcrow. The Halcrow data comprised repeated monitoring of movement markers located on the different landslide elements (see Section 6.1.3). Displacements of some typical points from both datasets are tabulated below (Table 6.19). Care must be taken in this comparison, since displacements are strongly temporally and spatially variable. Nevertheless, there is a striking resemblance regarding magnitude and direction of the movements. Highest rates were observed in the boulder field (almost 6 m/yr) and the northern earthflow lobe (more than 3 m/yr). The movements of the displaced block and the southern earthflow lobe were much smaller, and in some cases undetected at a confidence level of 95%. For completeness, the slopes of movement are also displayed. However, the photogrammetrically derived slopes were unreliable; especially in the case of small displacements where the uncertainty in measurements were relatively large this resulted in odd values (e.g. points 9 and
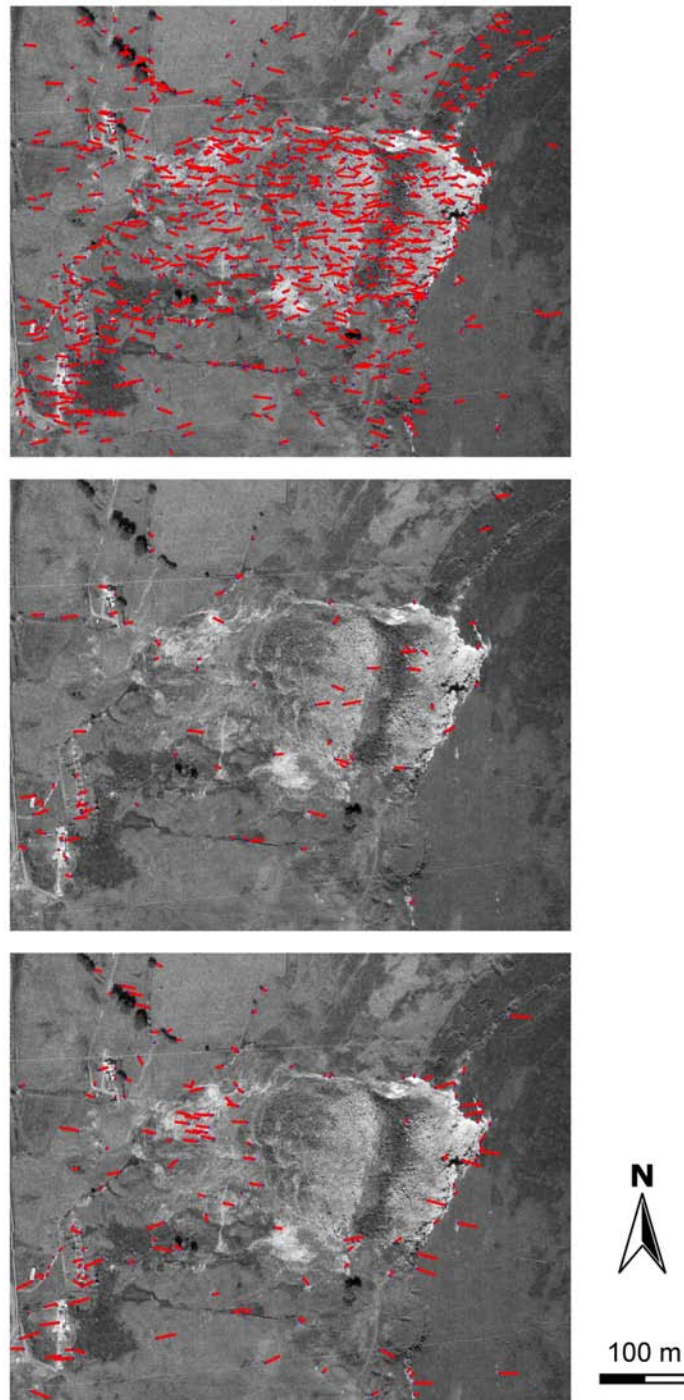
Figure 6.25. Attempts to automatic extraction of displacement vectors from the 1971 and 1973 orthophotos, using different parameter values: template size 7x7, correlation coefficient 0.70 (upper); template size 7x7 and correlation coefficient 0.90 (middle); template size 15x15 and correlation coefficient 0.80 (bottom). Note the persistent occurrence of mismatches on stable ground resulting in faulty vectors.

27 in Table 6.19). Nevertheless, the measured slopes of points that moved over larger distances are very similar to the Halcrow data (e.g. points 18 and 22).

Table 6.19. Comparison of the photogrammetric-derived horizontal displacements with ground surveyed data; displacements are converted to yearly rates. Numbers in italic are statistically insignificant at 95% confidence level. Location of the points are indicated in Figure 6.4 (Halcrow data) and Figure 6.24 (photogrammetric data).

Halcrow data (1982-83)				**Photogrammetric measurements (1971-73)**			
Point ID	*Displacement (m/yr)*	*Bearing (degrees)*	*Slope (degrees)*	*Point ID*	*Displacement (m/yr)*	*Bearing (degrees)*	*Slope (degrees)*
Displaced Block							
15	1.98	267	9	10	2.05	300	*34*
19	1.39	268	7	9	*0.24*	*320*	*78*
Boulder Field							
17	5.46	265	24	16	3.33	265	*17*
18	5.88	278	15	18	5.91	281	*14*
Earthflow (North Lobe)							
8	2.99	266	14	22	3.65	268	*12*
9	3.48	276	15	24	3.16	281	*7*
Earthflow (South Lobe)							
21	0.67	269	8	26	*0.84*	*290*	*32*
4	0.35	263	0	27	*0.34*	*226*	*78*

6.6 Summary

This chapter described the work conducted in the second case-study, on the East Pentwyn landslide. This landslide is located in the South Wales Coalfield and was triggered in 1953, due to extensive mining activities in the hillside. Movements have continued since, but considerably slowed down through stabilisation measures in the 1980s.

The initial failure of the slide could be observed on historical aerial photographs dated just before and after the event. Unfortunately, the quality of this RAF imagery was insufficient to allow accurate quantitative analysis.

Two photographic epochs from the 1970s were successfully used for quantitative measurement of the continuing surface movements. Accuracy of the data allowed detection of horizontal displacements and its spatial variation within the landslide area. The movement rates showed consistency with monitoring data

from ground surveys during the 1980s, in spite of the different period covered. Accuracy in height was insufficient to measure significant vertical changes.

The aerial photographs from the 1970s were specially selected because of their potential for automatic extraction of displacement vectors. In contrast to experiences in the case-study on Mam Tor, the surface of this landslide was not obscured by vegetation and the lighting conditions of the two epochs were very similar. Unfortunately, the developed image matching algorithm proved still unsuccessful. This failure is most likely due to the high radiometric noise in one set of photographs; even after removal of this noise, image contrast was still low and hampered detection of distinct features through image matching.

Chapter 7

7 Discussion

This chapter combines the findings from the two case-studies and discusses their implications for landslide research. The diverse range of photo sources and quality that was used, allows the identification of the main controls on data quality, and an attempt is made to formulate the relation between these. Also some weaknesses of this study are identified culminating in recommendations for further research. Finally, a short overview is given of the different data types proven to be relevant in landslide investigations.

7.1 Restitution

In Chapter 3 it was shown that the bundle adjustment allows propagation of the stochastic properties of measurements through the functional model. It is important that there is an appropriate balance between the functional and stochastic models. The appropriateness of the stochastic model can be analysed by comparing the *a priori* value of the variance factor with the *a posteriori* value, which should be identical. *A priori* analysis allows a covariance matrix of the estimated parameters to be obtained, based on the statistical weights assigned to the measurements. This also allows an estimation of the precision of the output data.

The *a posteriori* variance factor is based on the residuals in the bundle adjustment, in relation to the assigned weightings. A significant difference between these two variance factors can have the following causes (Cooper 1987):

- Error in computations;

- Undetected systematic error or blunder;

- Inaccurate linearisation of the functional model;

- Wrong stochastic model.

The only global indicator for the quality of the adjustment provided by LPS, is the 'total RMS error of solution'. This indicator does not relate to classical error theory described above, but is useful for the layperson, since it is based on the residuals of the adjustment and expressed in image coordinate units. The only guidance provided by LPS is that the value should be less than a pixel size of the original imagery (Leica Geosystems 2003).

In the following analysis, the variance in the output data was analysed in order to evaluate the stochastic models used and to indicate the main variables controlling data accuracy. It should be noted that this approach is rather speculative and based on certain assumptions, as there were only limited datasets available. In this analysis datasets from both case-studies were combined.

It was assumed that any gross errors in the bundle adjustment were successfully removed, and hence all errors in the final data were solely due to random errors and unresolved systematic errors. The (root-) mean-square-error of measurements is a common measure of accuracy and is defined as the sum of variances of random errors and bias (Mikhail & Gracie 1981); see Equation 7.1. This way of describing accuracy is similar to the adopted approach in this study for assessing DEM accuracy by mean and standard errors (Section 4.2.4; p. 75).

$$MSE = \sigma^2 + \beta^2 \quad (7.1)$$

Where σ^2 is a measure of the variance of random errors and β^2 represents the variance of bias (defined as the difference between mean value and true value).

As previously discussed (Sections 3.2.3), random errors are inherent to the measurement of any quantity (Cooper & Cross 1988) and are dependent on the precision of the source data and measurement procedures. The precision of

measurements derived from digital photographs primarily depends on the scanning resolution, which is usually worse than the resolution of the original film or camera lens (Section 3.6.1, p.49). Depending on the target and image contrast, image features can be measured to sub-pixel precision (Section 3.6.1, p.50). In line with this assumption, a standard deviation of ±0.2 pixels was assigned initially in the bundle adjustments. An approximate estimate of horizontal image precision in object dimensions could be derived by multiplying by the image scale. Similarly, an approximate estimate of vertical precision from image measurements was obtained by multiplying this value with the inverse base/height ratio (Equation 3.10; repeated below).

$$\sigma_{x,y} = 0.2 \cdot pixelsize \cdot scalenumber$$
$$\sigma_z = 0.2 \cdot pixelsize \cdot scalenumber \cdot \frac{H}{B} \qquad (7.2)$$

Where $\sigma_{x,y}$ is the precision in any of the horizontal directions (not to be confused with covariance) and σ_z is precision in height.

Another source of random errors was introduced into the adjustment through the measurements of ground control points. The precision of the differential GPS systems used for the ground control was ±0.01 m (Section 4.2.2; p.69) and therefore this value was assigned initially to the control points in the bundle adjustment. This contribution would be significant compared to the image ground resolution only in the case of large-scale imagery (e.g. Mam Tor 1973 epoch).

Hence, a simplified way of estimating the expected precision in a bundle adjustment would be by summing the contributing variances from image measurements and ground measurements (Equation 7.3).

$$\sigma^2 = \sigma_o^2 + \sigma_i^2 \qquad (7.3)$$

Where σ^2 is a measure of the total variance in the bundle adjustment; σ_o^2 is a measure of the variance of errors in object measurements and σ_i^2 the variance of errors in image measurements.

A priori estimates of the precision of the bundle adjustment for each epoch were computed using Equations 7.2 and 7.3, based on the approximate image scale at

the position of the landslide. The obtained values were compared to the real errors as observed from checkpoints (Table 7.1). Since a single value for horizontal precision would be more useful rather than separate values for arbitrary x and y directions, these were combined through vector summation. Table 7.1 shows that the observed accuracy in all cases is clearly worse than the expected precision. This suggests either the presence of large unresolved systematic errors, which was unlikely in the case of the epochs with full camera calibration data available, or significant underestimation of the effects of random errors in the stochastic model.

Table 7.1. Comparison between measures of expected precision (σ) and observed accuracy (RMS error); note that σ(x,y) represents precision in either x or y, whereas σ(xy) are their summed standard errors.

	Expected precision			Observed accuracy			
Epoch	*σ (x, y)*	*σ (z)*	*σ (xy)*	*RMSE (x)*	*RMSE (y)*	*RMSE (z)*	*RMSE(xy)*
MT1953	0.090	0.72	0.13	0.55	1.40	4.21	1.50
MT1971	0.055	0.18	0.077	0.46	0.42	1.16	0.62
MT1973	0.016	0.034	0.023	0.14	0.28	0.54	0.31
MT1984	0.082	0.14	0.12	0.45	0.40	1.67	0.60
MT1990	0.037	0.066	0.053	0.26	0.34	0.41	0.43
MT1995	0.050	0.094	0.071	0.35	0.24	0.47	0.42
MT1999	0.052	0.098	0.074	0.26	0.30	0.74	0.40
EP1951	0.029	0.19	0.041	1.65	1.05	8.03	1.96
EP1955	0.028	0.20	0.039	0.92	0.62	10.85	1.11
EP1971	0.038	0.070	0.053	0.19	0.18	0.58	0.26
EP1973	0.027	0.045	0.039	0.49	0.13	0.78	0.51

The data from Table 7.1 are graphically displayed in Figure 7.1, to look for any obvious trends. The epochs were grouped according to the calibration data that were used:

• Full calibration available – no systematic effects arising from unknown geometry, hence accuracy was expected to be close to the expected precision (epochs MT1973, MT1984, MT1990, MT1995, MT1999 and EP1971);

• Self-calibration – camera model was successfully estimated in a self-calibrating bundle adjustment; nevertheless some systematic errors may be left unresolved due to the use of poor-quality scanned prints (MT1953, MT1971);

- No calibration; however, a metric camera was used and reasonable estimates for camera geometry were available, and therefore only limited systematic effects were expected (EP1973);

- Very large systematic errors that could not be resolved through a self-calibration (EP1951 and EP1955). Because of their inconsistency, these epochs were left out in the further analysis below.

For the epochs with fully calibrated camera models, it would perhaps be expected that the relation between precision and accuracy would approximate a linear 1:1 line through the origin. Although a clear linear relation is apparent in Figure 7.1, its slope appeared well below 1:1, suggesting that the stochastic model adopted initially was not appropriate.

An obvious explanation would be that the precision of ground control and/or image measurements were overestimated. Regarding the ground control, in the Mam Tor case-study, a check on using different active stations to reference the base-station to, revealed an inconsistency of 0.5 m (Section 5.3; p.95). Within the control network the base lengths were much shorter than the distance to the active stations, but it suggested that the indicated precision of 0.01 m was perhaps too optimistic. Regarding image measurements, the natural features used as control points were rarely sufficiently distinctive, suggesting that the stated precisions were
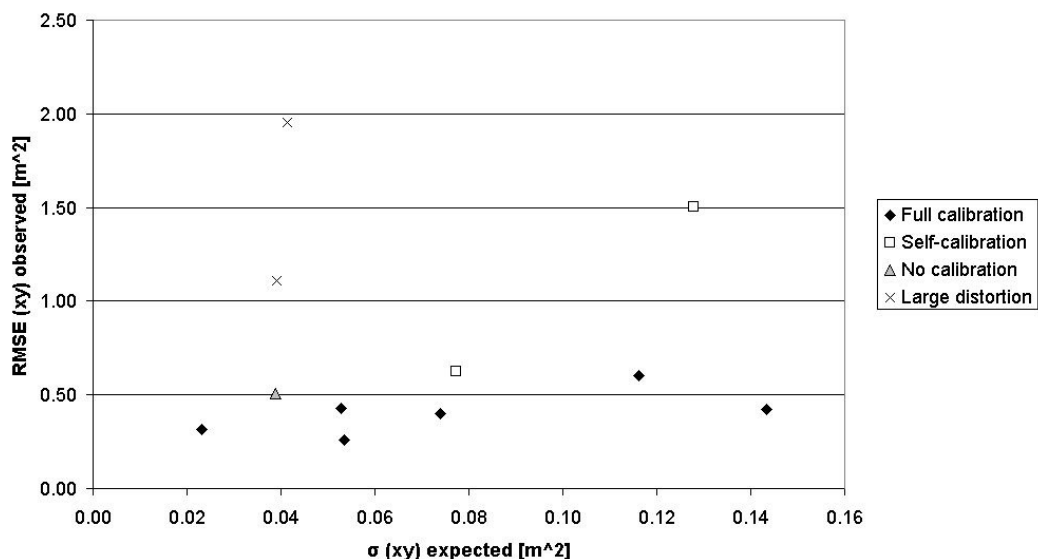
Figure 7.1. Comparison between expected horizontal precision (σ) and observed accuracy (RMS error); the epochs are grouped according to their calibration mode.

too optimistic. Further uncertainties could arise due to difficulties in correlating image features to the corresponding feature in the field; differences in shading and angle of view may lead to 'mismatching'. In the case of archival images, more uncertainty is added whether a feature did actually remain unchanged between image capture and ground measurement. These issues only apply to control points, which need to be linked to measured ground objects; tie-points require only image measurements, and hence the quoted theoretical precision would indeed be valid.

It was explored how these uncertainties could best be reflected in the stochastic model, to find a better balance. Assuming systematic effects were negligible, the variance in the bundle adjustment would be entirely due to random errors in the measurements and from previous equations, Equation 7.4 could be derived.

$$MSE = \sigma_o{}^2 + \sigma_i{}^2 \qquad (7.4)$$

Where MSE is mean-square-error, $\sigma_o{}^2$ a measure of the variance of errors in object measurements and $\sigma_i{}^2$ the variance of errors in image measurements.

Let the unknown weights that should be assigned to the measurements be *a* and *b* (respectively corresponding to the previously used 0.2 of pixel size and 0.01 m); their horizontal variance (vector summation of x and y) would then be represented by Equation 7.5.

$$\sigma_i{}^2 = 2(a \cdot pixelsize \cdot scalenumber)^2$$
$$\sigma_o{}^2 = 2b^2 \qquad (7.5)$$

Where $\sigma_o{}^2$ refers to the variance of errors in object measurements and $\sigma_i{}^2$ to the variance of errors in image measurements

Substituting these equations into Equation 7.4 effectively provided a linear relation between the squared ground resolution and the observed mean-square-error (see Equation 7.6), since *b* was constant for all epochs (because the same source for ground control was used).

$$MSE_{xy} = 2a^2 \cdot gres^2 + 2b^2 \qquad (7.6)$$

Where a and b are the unknown weights and $gres$ is ground resolution distance (pixel size multiplied by scale number).

The term $2a^2$ corresponds to the slope of this linear relation; $2b^2$ to the intercept. These terms were determined through regression (see Figure 7.2) and provided the optimum values for the weights a and b (respectively 0.92 and 0.19). Using these stochastic constraints in the bundle adjustment should provide a better balance in the stochastic model.

Similarly, a relation was established for the self-calibrated epochs, in an attempt to account for additional errors inherent to using low-quality scanned prints. Since the same control was used, it was assumed that precision in the object measurements would be identical; hence the intercept should be the same as for the fully calibrated cameras. Regression revealed a value of 2.25 for weighting parameter a.

Up to now, only horizontal accuracy was considered. Vertical precision from image measurements was obtained through multiplying the horizontal image precision (in x direction) with the inverse base/height ratio (Equation 7.2). The parameters a and b were used for estimating the vertical precision of all epochs and compare these with the observed vertical accuracy (Figure 7.3). The points all approximated to the 1:1 line, demonstrating the validity of the approach adopted. Only one of the epochs (MT1984) showed a large deviation from this line. However, the data set was insufficient to find an explanation for this particular discrepancy; perhaps it was caused by poor ground control distribution.

A brief test was carried out to validate the logic of the argued above and improve the stochastic model, using the optimised weights in the bundle adjustment. Standard deviations of 0.92 pixels and 0.19 m were used in the adjustments for the 1973 and 1995 Mam Tor epochs. Although, as expected, the accuracy of the adjustments did barely change, at least these were now in better agreement with the variance of the measurements (compare 'new' precision and accuracy values in Table 7.2).

Also the 'accuracy' estimates provided in the LPS triangulation report were evaluated and it was hoped that these would confirm the improvements made in
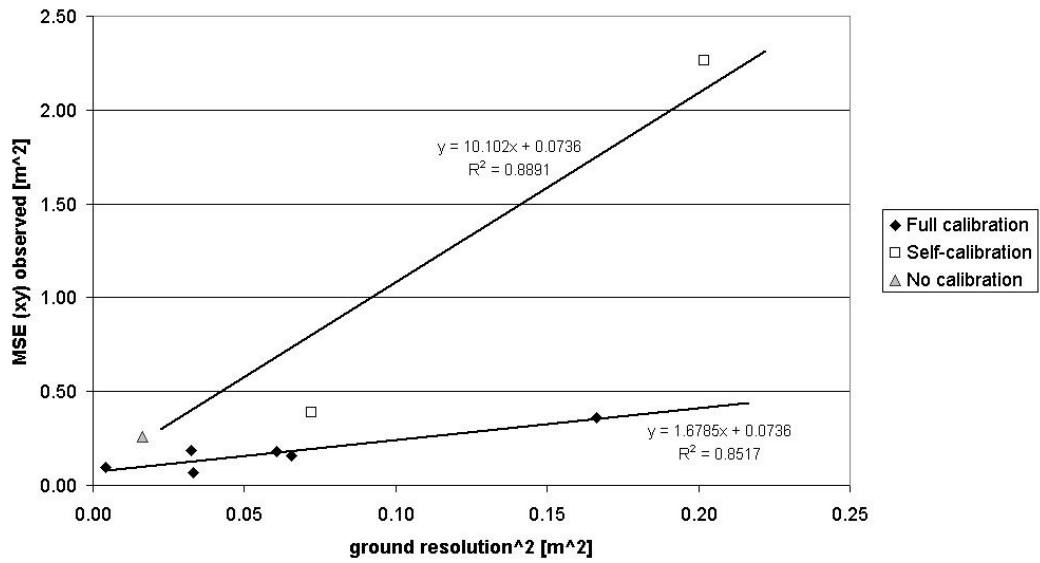
Figure 7.2. Relation between ground resolution and observed accuracy.
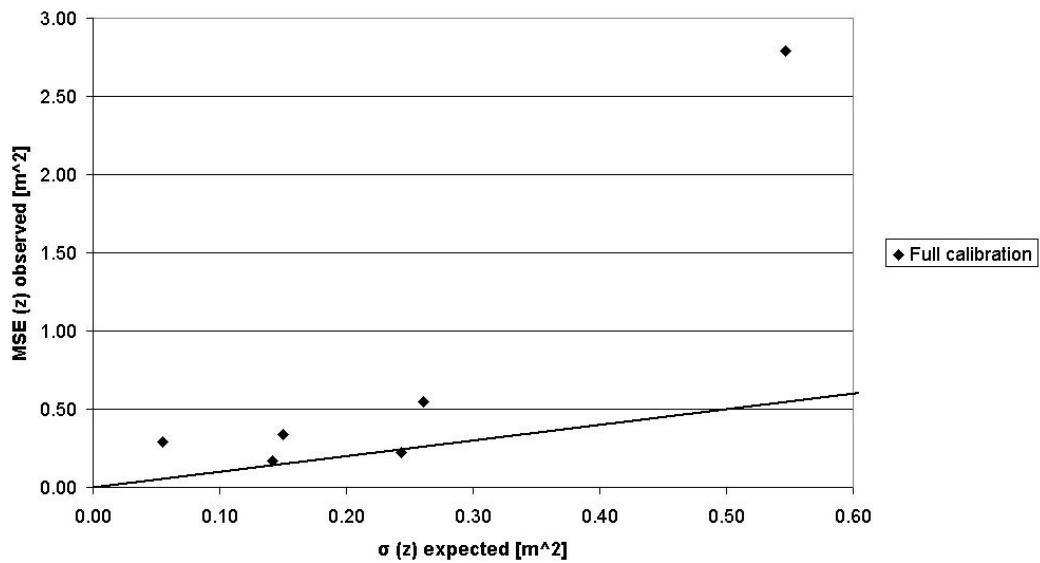
Figure 7.3. Estimated vertical standard error versus observed MSE; the black line represents the 1:1 line.

the model. Unfortunately, these 'accuracy' estimates were rather difficult to interpret. They are based on the stochastic model propagated through the functional model to derive a cofactor matrix; this is then scaled by multiplying by the variance factor (Equation 7.7; Cooper 1987), itself derived by the ratio of residuals to the standard deviation of each measurement. The changes to the functional model due to the modified stochastics were only marginal, and consequently so were the changes to the residuals in the adjustment. Therefore, the LPS 'accuracy' estimates were not expected to have changed significantly either

(Table 7.2); because the actual variance factor is not provided by LPS, this measure was not very helpful.

$$C_x = \sigma_o^2 (A^t Q_l^{-1} A)^{-1} \qquad (7.7)$$

Where C_x is the covariance matrix of the coordinates, σ_o^2 the variance factor, A the design matrix, and Q_l the cofactor matrix.

Table 7.2. Comparing the effects of the modified weights in the stochastic model: estimated precision (using Equation 7.2), LPS 'accuracy', and accuracy from checkpoints. Initial adjustments used weights of 0.2 pixel and 0.01 m; new weights were 0.92 pixel and 0.19 m.

	Estimated precision		LPS 'accuracy' estimate			Accuracy from checkpoints		
	$\sigma\ (x,y)$	$\sigma\ (z)$	$\sigma\ (x)$	$\sigma\ (y)$	$\sigma\ (z)$	RMSE (x)	RMSE (y)	RMSE (z)
1973								
Initial	0.016	0.034	0.024	0.026	0.047	0.11	0.28	0.39
New	0.20	0.24	0.059	0.053	0.071	0.11	0.28	0.39
1995								
Initial	0.050	0.094	0.11	0.10	0.38	0.35	0.24	0.47
New	0.30	0.47	0.11	0.10	0.36	0.35	0.24	0.48

Apart from the improvements to the stochastic model, Equation 7.6 also provides a means to estimate the accuracy that can be expected, based on scanning resolution and image scale. Furthermore, the analysis showed that the accuracy that can be achieved from scanned prints is approximately 2.5 times (2.25/0.92) worse than from scanned diapositives. It should be kept in mind that this value may be of limited significance, since it is based on only a few observations. It did however give a clear indication of the degenerating effect on accuracy, when scanned prints are used instead of diapositives, and the associated larger standard deviations that should be used in the stochastic model.

It should be noted that also other factors have influence on data accuracy, such as amount and distribution of control points and quality of camera calibration data. The datasets in the two case-studies provided insufficient data to quantify each one of these factors separately. Figure 7.4 illustrates the limiting effects of these various factors. The top of this diagram represents the best data quality that can be achieved (depending in image scale), using high-quality scanned contact-

diapositives, a calibrated metric camera to capture the original images, and good control data. Quality of the source data degrades down to worst results when prints are used, scanned with a desktop scanning device; this was the only category quantified at a factor of 2.5. Regarding the camera calibration, still reasonable results can be achieved when the camera geometry is estimated in a self-calibrating bundle adjustment, although this is also strongly depending on the availability of good ground control. Worst data quality can be expected when a uncalibrated non-metric camera is used. Ground control can be a limiting factor, when its accuracy is low or its spatial distribution within the images limited. This factor could not be quantified in this study, since the same source for control points was used for all epochs and generally their distribution was sufficient. Hence, the scale bar provided in Figure 7.4 is only a rough estimate.

A more global factor for long-term stability of the photographic record could also be considered in such analysis. Such a term would incorporate different effects such as camera and film quality, and reliability of ground control. These factors all deteriorate with increasing age but their effects are difficult to separate.

It should also be noted that even if each factor were quantified, a single accuracy value for a bundle adjustment does not account for the variability within the block of images, depending on the configuration of images and control points, and the position of the required measurement.
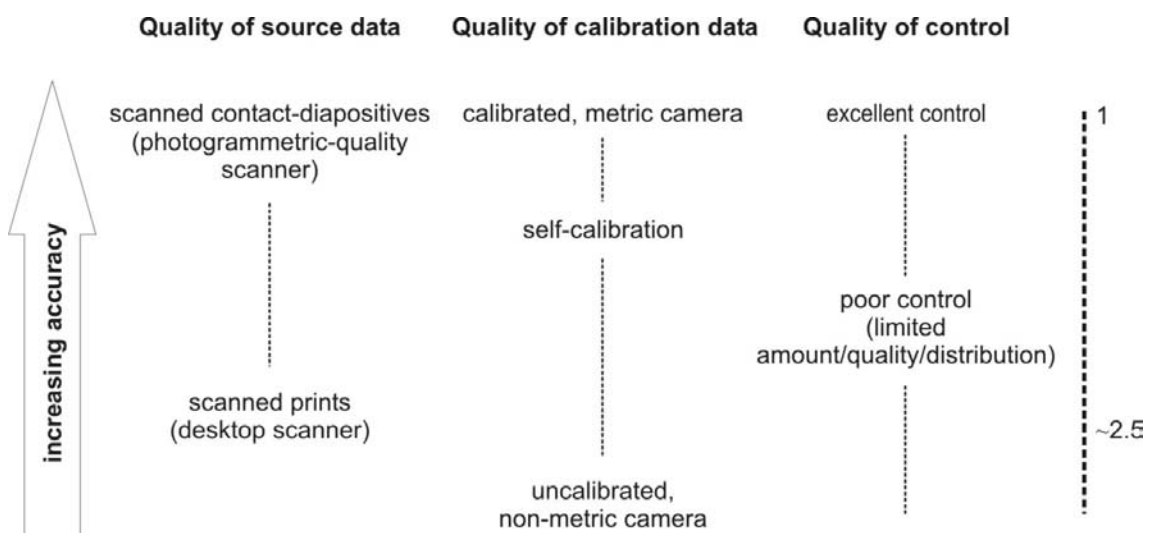
Figure 7.4. The effects of various factors on data accuracy; the categories on top provide highest achievable accuracy, decreasing downwards. The scale bar on the right side is only for indication.

An additional study could be identified, in which systematically any of these variables is changed and its effect on data accuracy evaluated. For example, one would use only one set of photographs and then compare the results achieved from scanning prints and diapositives, a variety of scanning resolutions, using different amount and quality of ground control, and using different quality of calibration data. If the effects of each of these variables were quantified, Figure 7.4 could be expanded with absolute values, and these could also be included in Equation 7.5, providing a reliable *a priori* estimate of accuracy, achievable using different media, quality of control and calibration data.

7.2 DEMs

An accurate bundle adjustment does not guarantee accurate DEM generation when using automatic techniques (Section 3.6.2; p.51). Insufficient contrast and geometric distortion due to relief displacement may lead to mismatches or low density of mass points. The accuracy of an interpolated surface also depends on its resolution in relation to terrain characteristics; a rough terrain surface requires a higher mass point density for its accurate representation than a smooth surface. In this context it is advantageous that surface roughness and image contrast are usually positively correlated, due to associated variances in shading, soil and vegetation. This was apparent in both case studies, where in general the mass point density was much higher on the irregular landslide surface, compared to the surrounding homogeneous grounds (e.g. see Figure 6.17). Ironically, the related higher accuracy did not help the detection of significant changes on the landslide surface, due to the lower accuracy of the surrounding reference data. It was not possible to measure the accuracy directly on the landslide itself, since the surface had been subject to changes.

Numerous studies have investigated the effect of DEM resolution on the accuracy of surface representation (e.g. (Gong *et al.* 2000; Lane *et al.* 1994), showing that DEM accuracy decreases with larger sampling interval. In this study high resolutions were adopted for all epochs (1 or 2 m), to reduce this data loss as much as possible. On the other hand, it was observed that such high resolutions prevented outliers from being filtered out, and consequently resulted in irregular noise.

Visual inspection of the DEMs showed that certain areas were vulnerable to mismatches or disproportionate interpolation. This was particularly the case in areas of steep relief (such as the main scarp of the landslide), low contrast (large patches of the surrounding hill slopes) and shadows (usually associated with steep relief). The large errors in these image patches were not represented in the error statistics provided by checkpoints. Although the checkpoints were generally located in areas relatively favourable for image matching, they also represented break lines in the terrain surface (corners of buildings, stone walls), which would be smoothed out at a coarse DEM ground resolution. This observation confirmed the statements by several researchers (Florinsky 1998) that for an appropriate assessment of DEM accuracy, the use of checkpoint statistics is insufficient. Lacking a more accurate DEM from an alternative source, this was yet the only way available in this study.

In spite of these issues, Figure 7.5 shows a strong correlation between the accuracy measures of the bundle adjustments and the resulting DEMs (R^2 of 0.98 for the Mam Tor images). Both accuracy measures were based on the RMS errors of checkpoints (see tabulated values from Sections 5.4 and 6.4; combined in Table 7.3). As expected, the accuracy of the DEM is lower than the vertical accuracy in the adjustment, due to a certain degree of interpolation. However, the strong correlation suggests that the errors associated with interpolation are only small compared to the uncertainty of the measurements. This also implies that the

Table 7.3. Accuracy measures for the bundle adjustments (RMSE), the extracted DEMs (standard error) and mass point densities for all epochs.

Epoch	RMSE (z) bundle adj.	Mass point dens. (pts/ha)	Std. error DEM
MT1953	4.21	751	5.22
MT1971	1.16	5,921	1.34
MT1973	0.54	5,108	0.76
MT1984	1.67	470	1.58
MT1990	0.41	2,424	0.83
MT1995	0.47	1,029	0.76
MT1999	0.74	1,031	1.13
EP1951	8.03	140	7.91
EP1955	10.9	89	7.80
EP1971	0.58	235	1.75
EP1973	0.78	781	1.76

controls on the bundle adjustment, such as image resolution, are also the primary factor for DEM quality. Separate lines for both case-study sites were displayed in the figure, since the different terrain characteristics have influence on this relationship as well.
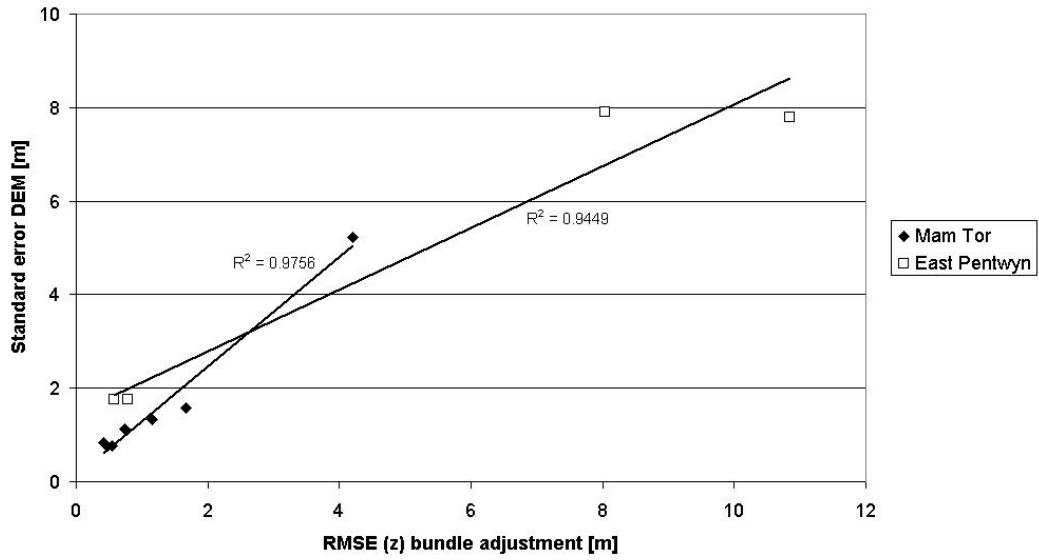
Figure 7.5. Accuracy of DEM versus bundle adjustment (data from Table 7.3, MT = Mam Tor, EP = East Pentwyn).
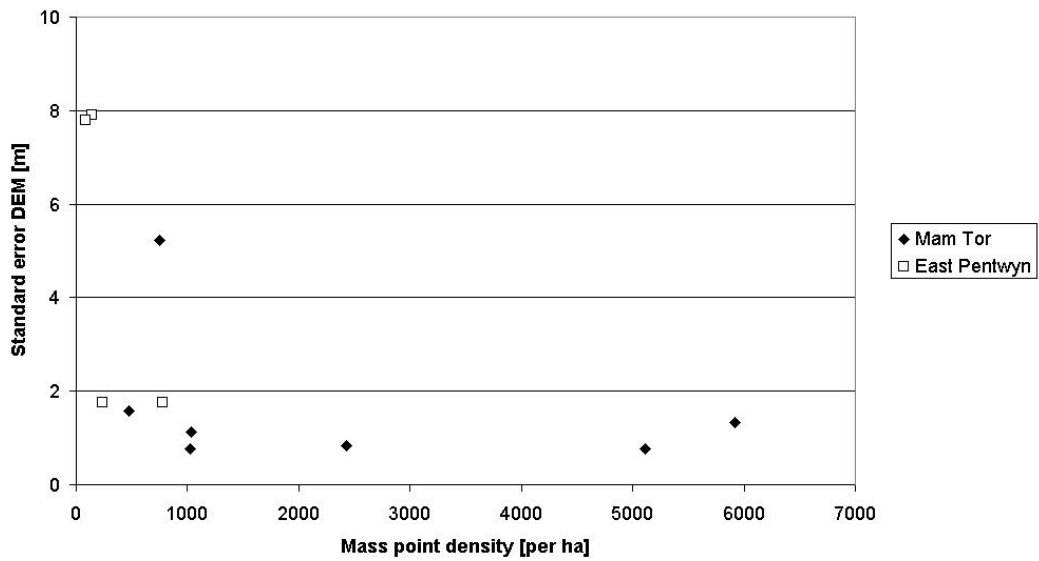
Figure 7.6. DEM accuracy versus mass point density.

Since the degree of surface interpolation is controlled by the density of mass points, a plot of DEM accuracy versus mass point density would indicate the influence of interpolation on DEM quality. However, Figure 7.6 confirms that there is no clear relationship between these two variables. Even in the two East Pentwyn epochs (1951 and 1955), with their poor point densities, the low DEM accuracy can be largely attributed to the systematic errors that occurred in the bundle adjustments. However, this conclusion should be taken with caution, because the average mass point density may not be representative for the whole area, in particular with respect to the locations of the few checkpoints.

The significance of errors in the DEMs became greater, when they were subtracted from each other to obtain 'DEMs of difference'. The elevation differences were small, whereas their uncertainty was larger than in any of the individual DEMs due to propagation of errors. Some researchers (e.g. Kääb & Vollmer 2000) have suggested the use of low-pass filters to 'DEMs of difference', which remove small-scale noise without losing overall accuracy. This would however not eliminate the gross errors caused by mismatches in 'difficult' areas, and discrepancies due to interpolation of steep scarps (e.g. Figure 5.34).

The large errors associated with steep relief are in accordance with Gong *et al*. (2000), who concluded that DEM accuracy decreases with increase in relief, and recommend to include manual measurements. It is therefore advisable to improve the surface representation through manual removal of spurious spikes and ridges associated with mismatches and include measured spot heights at strategic positions, where automated image matching failed (Kerle 2002). Areas lacking sufficient mass points can be identified from the mass point distribution image created during DEM extraction; additional spot heights can be readily measured using the StereoAnalyst tool and then added. Obviously, manual measurement is very laborious and the point densities that can be achieved are much lower than those achieved automatically.

7.3 Orthophotographs

It was anticipated that the accuracy of orthophotos would be mainly controlled by the accuracies of the bundle adjustment and the DEMs that were used for their creation. Accuracy measures for the bundle adjustments, DEMs and orthophotos, all

based on checkpoints, were presented in earlier chapters (Sections 5.4 and 6.4) and are combined here in Table 7.4. A graphical representation of these data is provided in Figure 7.7 and Figure 7.8, in which the RMS errors of the orthophotos are plotted against respectively horizontal RMS errors in the bundle adjustments and DEM standard errors. The Horizontal RMS errors were obtained by vector summation of RMS errors in x and y.

Figure 7.7 shows that in general, the accuracy of the orthophotos was slightly worse than the horizontal accuracy of the corresponding bundle adjustment, although their correlation is weak (R^2 of 0.59 for Mam Tor images). Diffusion of data points from this direct relation may be explained by errors in the DEMs; for example in the case of the Mam Tor 1984 and East Pentwyn 1971 epochs, the relatively large errors in the orthophoto could well be attributed to low-quality DEMs. However, Figure 7.8 illustrates there is no clear pattern between DEM accuracy and the errors in the resulting orthophoto, suggesting this is not a principal factor. These results confirm the findings by Krupnik (2003) who indicated that orthophotos are more sensitive to errors in the bundle adjustment than to DEM errors.

Krupnik (2003) also showed that steep relief can locally cause large distortions in the orthophotos. Hence, the same caution should be kept in mind as for DEMs; areas exhibiting difficulties in image matching may not be well represented by the limited amount of checkpoints, and their RMS error may overestimate overall accuracy. It was also observed that if gross errors were not removed from the DEM, these would cause large distortions in the orthophoto.

Table 7.4. Accuracy measures of the bundle adjustments, DEMs and orthophotos.

Epoch	RMSE (xy) adjustment	Std. error DEM	RMSE (xy) orthophoto
MT1953	1.50	5.22	1.65
MT1971	0.62	1.34	0.86
MT1973	0.31	0.76	0.88
MT1984	0.60	1.58	1.38
MT1990	0.43	0.83	0.34
MT1995	0.42	0.76	0.69
MT1999	0.40	1.13	0.34
EP1951	1.96	7.91	1.93
EP1953	1.11	7.80	0.47
EP1971	0.26	1.75	1.45
EP1973	0.51	1.76	0.84

As discussed in the previous section, in both case-studies the landslide surface itself provided good targets for automated DEM extraction. Therefore, the effects of distortions in the orthophotos due to gross errors in the DEM would be of little importance regarding the measurement of landslide displacements. However, when steep terrain sections need to be mapped, for example a retreating head scarp, the orthophoto may be unreliable. Either the DEM should be corrected or measurements should be done directly from the stereo-model, using for example the StereoAnalyst tool.
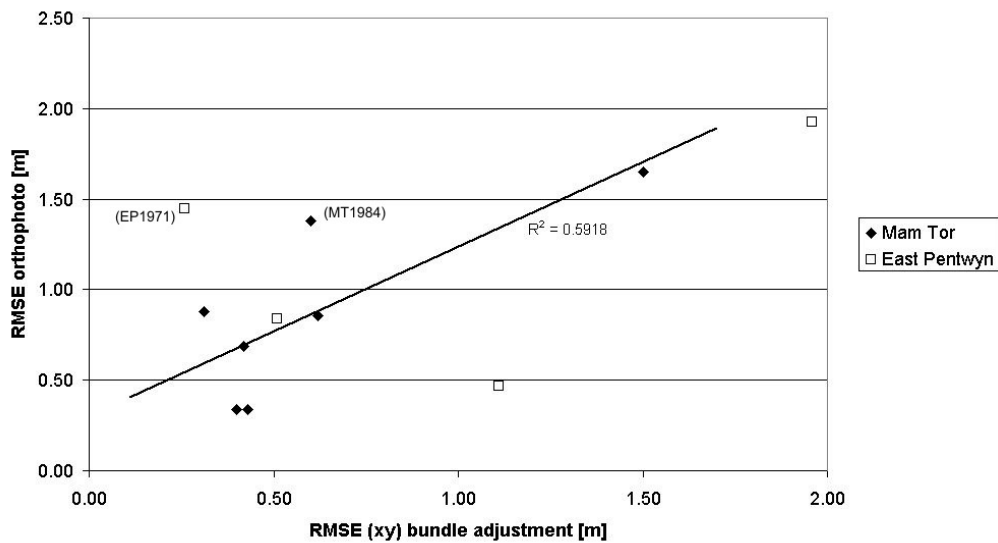
Figure 7.7. Relation between the accuracy of orthophotos and bundle adjustment.
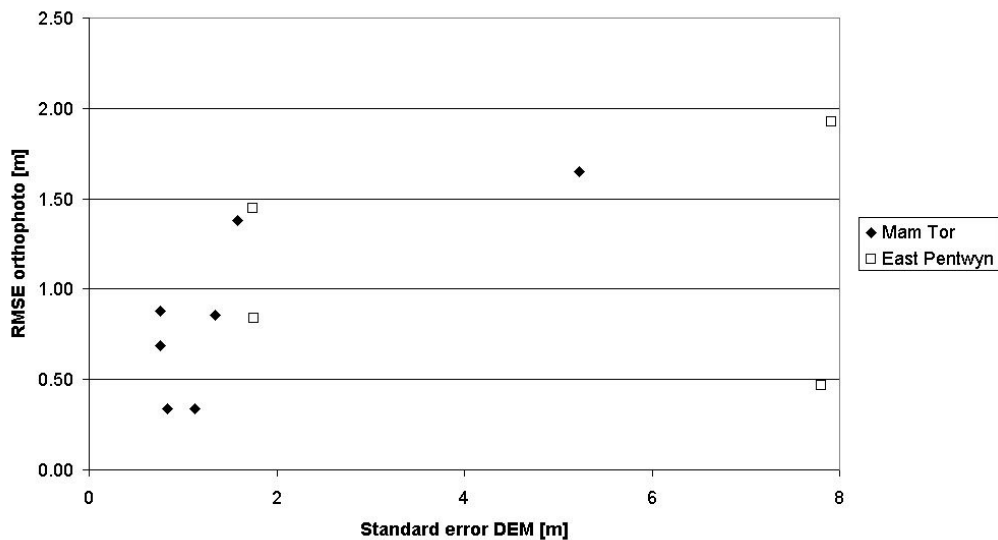
Figure 7.8. Relation between the accuracy of orthophotos and quality of the DEM used for its creation.

7.4 Displacement vectors

The experiments for automated extraction of displacement vectors were unsuccessful in this study. In the case of the Mam Tor images, this could be explained by the lack of suitable targets; vegetation cover and different illumination conditions obscured the changes of the ground surface between the epochs, and no clear maximum in the cross-correlation could be found. This issue did not affect the various studies that successfully applied similar techniques, as these were all situated in alpine environments, characterised by a bare and coarse-textured terrain surface (e.g. Kääb & Vollmer 2000; Kaufmann & Ladstädter 2002; Delacourt *et al.* 2004).

In the East Pentwyn case-study, vegetation cover was sparse and a large part of the landslide surface exposed boulders, potentially providing a good texture for automated matching. The images were selected carefully to assure similar illumination conditions. Nevertheless, multi-epoch image matching failed again, this time most likely due to the radiometric noise present in one of the epochs. The effects of this salt-and-pepper had hampered automated DEM extraction as well, but this could be solved by applying a filter (p.148). However, removal of the noise reduced the distinctive features of individual boulders, and hence matching performance with the other epoch did not improve.

Initially, it was assumed that the distinct features in the East Pentwyn boulder field would be in the order of 2-3 meters in size, and the template window was adjusted to this accordingly (7-15 pixels). However, the presence of noise prevented a clear match to be established. It could be argued that a larger template size should have been used to reduce this effect. A brief experiment was carried out to evaluate the effect of template size on the matching performance. A particular template window was extracted from one image, and its correlation values in a search area of the second image displayed. This procedure was repeated for different template sizes (see Figure 7.9). It now became clear that a small template size resulted in many high peaks in the correlation surface, which indicated that mismatches were likely to occur. When the template size was considerably increased (up to 45 pixels), a single distinct peak was visible. Hence, although the absolute correlation values were generally lower (compare the scales of the z-axes in Figure 7.10), features were much more pronounced and the chance of mismatches reduced. The downside of using larger templates would be a lower

precision, since a displacement would represent a larger area (45 pixels corresponded to 9 meters). However, when this template size was used for extracting displacements vectors, false matches on stable grounds still remained (Figure 7.11). This indicated that the algorithm was still unreliable and would need further improvement.

Despite the disappointments of the automated algorithm, manual measurement of vectors in both case-studies showed that the geometries of the stereo-models were accurate enough to detect significant horizontal displacements (Sections 5.5.3 and 6.5.3). Furthermore, it was concluded in the previous section that the accuracies of orthophotos were only slightly worse than their corresponding bundle adjustments, and poor-quality DEMs did not cause major distortions on the landslide surface itself (Section 7.3). Hence, the great efforts to avoid inaccuracies due to low-quality DEMs (e.g. Kaufmann & Ladstädter 2004; Casson *et al.* 2003) would not been justified in these two case-studies. Also, the rigorous method presented by Kaufmann & Ladstädter (2002; 2004) to measure displacements in three dimensions, would not be relevant in these cases, as the vertical accuracy of the stereo-models was too low anyway. It should be realized
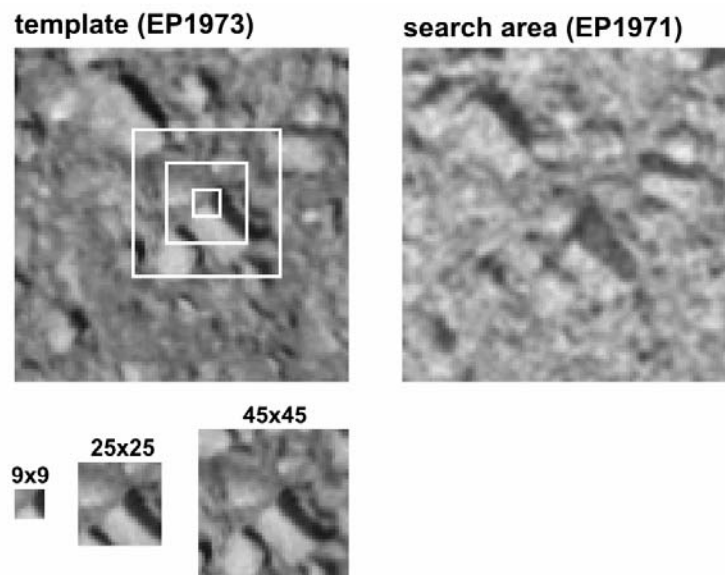
Figure 7.9. Different template sizes extracted from the 1973 image (left): 9x9, 25x25 and 45x45 pixels; corresponding search area in the 1971 image (right).
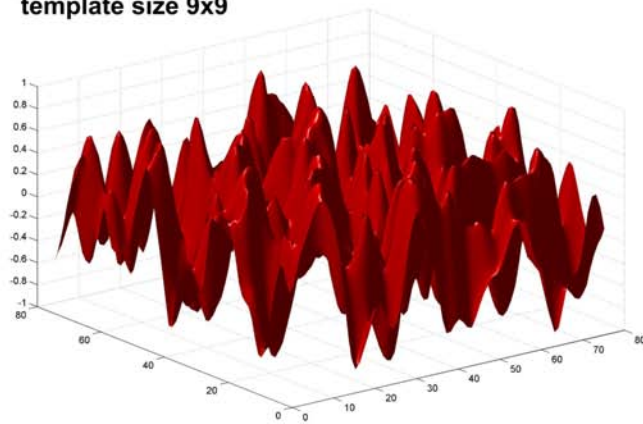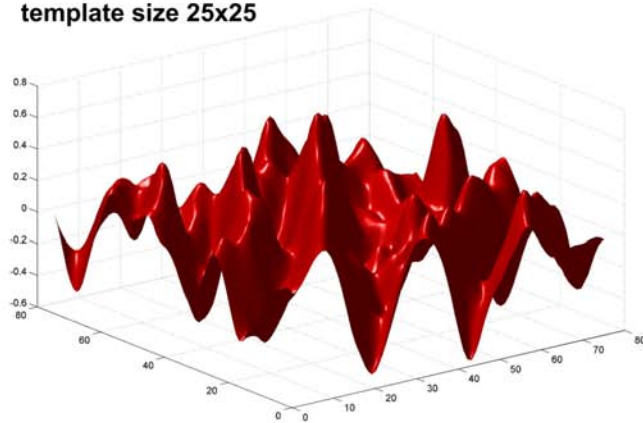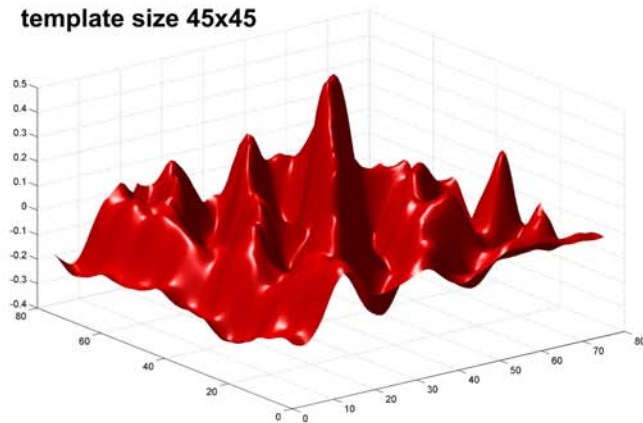
Figure 7.10. The effect of different template sizes on cross-correlation (template and search area displayed in Figure 7.9); note the distinct peak when using larger templates.
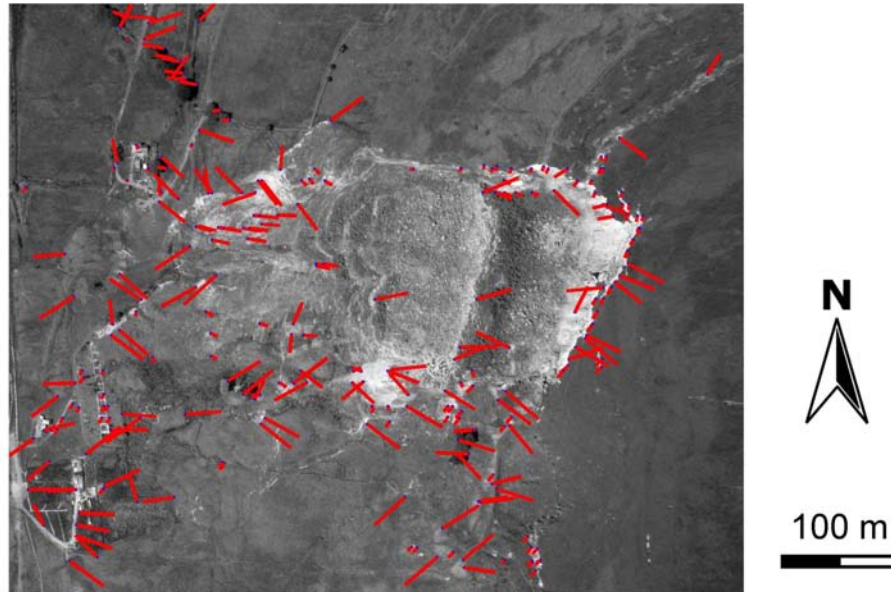
Figure 7.11. Displacement vectors, obtained by using a template size of 45 pixels during image matching and correlation threshold of 0.70; note the mismatches in the area surrounding the landslide.

that these studies were situated in alpine environments, where steep relief may have constrained DEM quality more severely than in this study, and also the mass movements involved a more significant vertical component.

The experiences in this study suggested that the automated extraction of displacement vectors has high requirements in terms of image quality. Although the geometric quality in both case-studies was sufficient to detect and quantify ground movements horizontally, radiometric image requirements and its consistency among multiple epochs were difficult to meet, using archival imagery.

7.5 Obliques

The oblique images in the Mam Tor case-study showed that accurate results can be achieved from this type of imagery. As mentioned previously (p.21), they provide a more familiar view of the landscape than vertical images, which makes it easier to interpret ground features and identify control points (Figure 7.12). However, in the case of high-oblique images (i.e. large angle with vertical), parts of the terrain may be obscured behind tall objects.
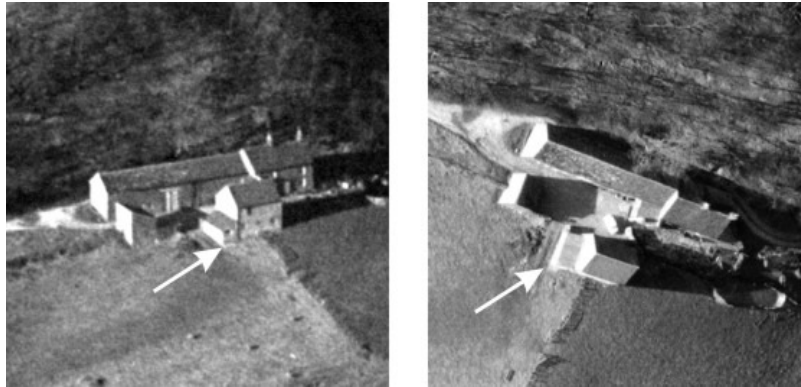
*Figure 7.12. Better view on control point (indicated by arrow) on oblique image (left)
compared to vertical (right); both images from the Mam Tor sequence, 1973.*

The geometry of obliques makes them more suitable for recovering the camera model in a self-calibrating bundle adjustment, as there is no strong correlation between focal length and flying height. Consequently, often a better accuracy in height can be achieved than from comparable vertical imagery. In the case of the Mam Tor images, the vertical accuracy from the obliques proved better than from verticals of the same date (RMS errors of respectively 0.21 and 0.39 m), in spite of a non-metric camera used to capture them. A disadvantage of obliques is their variable scale; as a consequence, the accuracy of measurements will decrease with increasing object distance, showing great spatial variability across a site.

Although a large base/distance ratio provides stronger geometry for the bundle adjustment, it appeared that conversely this hampered automatic matching procedures. In this study, it was experienced that automatic DEM extraction was only successful when the base/distance ratio of the pair was smaller than 1/3 (Section 5.4.2). Even if matching was successful, the accuracy of extracted DEMs was rather low. This can be explained by the high angle of the images that obscured parts of the ground surface, especially in undulating and vegetated terrain. This widespread occurrence of 'dead-ground' also strongly affected the orthophotos.

The value of oblique photographs has been especially appreciated for mapping of steep cliff faces (Chandler 1989; Kalaugher *et al.* 1987). In such situations, they may provide a much better view of the slope than vertical images, and the problems associated with DEM extraction in steep areas are avoided. The optimum orientation of obliques would be perpendicular to the slope under investigation. The obliques in the Mam Tor case-study would have been valuable if their orientation was more favourable regarding the aspect of the main scarp face,

which caused difficulties in DEMs from vertical imagery. However, for the relatively low slope angles of the whole landslide surface, vertical imagery provided more suitable geometry.

7.6 Implications for landslide studies

This study showed that archival aerial photographs have the potential of providing a wide range of information, both qualitative and quantitative. This section summarises the different types of products that can be acquired and their relevance in studies on landslide dynamics. The various products and their interrelationships are also presented in Figure 7.13.

First of all, aerial photographs provide an overall view of the study area, generally better than can be achieved from a ground perspective. Qualitative data can be obtained through aerial photo-interpretation. Surface features can be identified and mapped from aerial photographs, depending on the image resolution and contrast. In this way, different geomorphological elements within a landslide can be delineated; their interpretation may be indicative for particular types of movement. Analysis of drainage and vegetation patterns, ground material, and geological sequences may be useful for assessing slope stability conditions. Temporal changes of these elements can be observed from image sequences and indicate the progressive development of unstable slopes.

Photogrammetric techniques can be applied to acquire accurate quantitative data. Automated techniques provided by modern software packages allow high-resolution DEMs and orthophotos to be extracted easily. A DEM can be used as a source for various parameters relevant for slope stability modelling, such as slope angle, direction and length. Subtracting DEMs from different epochs is a useful approach to quantify changes in landforms; they show areas where material has been removed or deposited, and the volumes of transported material can be quantified. However, the use of 'DEMs of difference' may be limited by the accuracy of the data; in this study vertical changes in the terrain were generally too small to be quantified. In other studies, in which this approach was applied more successfully, the elevation changes were much larger (see Table 3.1). Hence, this type of analysis is only useful when large ground masses have been displaced. Displaced ground masses can also be visualised by sequential cross-sections through the slope profile.

A common use of orthophotographs is to provide a base-map. In this respect, they assure that photo-interpreted information is geometric-correctly mapped, and comparisons can be made between maps from different epochs. When distinct features can be identified on the landslide surface, their horizontal displacements can be measured from sequential orthophotos. This allows spatial and temporal displacement patterns to be analysed. The spatial patterns may be related to different elements within the landslide body, or used for strain analysis.

Three-dimensional measurement of displacement vectors would allow estimates of the underlying slip surface. Horizontal accuracy is usually better than vertical, allowing relatively small displacements to be detected. Also, the measurement of displacement vectors is limited to situations where the surface integrity has remained, so that features can be identified on the different images. Hence this type of analysis is particularly useful when ground movements are relatively small.

In addition to providing a source for quantitative data, DEMs and orthophotos are essential sources for visualisation. Realistic 3D views of the area from any perspective can be created, which are helpful for interpretation and presentation. Animated sequences of images provide a very useful tool for illustrating the progressive change occurring within a landslide.

A very important aspect of quantitative analysis is the requirement of assessing the quality of data. In the previous sections it appeared that the input data is of primary importance for the final data accuracy. However, when using archival material, there is only little control over data quality, and the desirable accuracy should be considered beforehand. The results of this study indicate that even when the data captured in archival imagery may be sufficiently accurate for quantifying landslide dynamics, the application of automated techniques needs caution, and manual intervention is needed to guarantee optimal data accuracy.

7.7 Summary

The diverse range of photo sources and quality that was used in this study, allowed identification of the main controls on data quality. An analysis of the combined datasets showed that the precision of the control data was overestimated, and accordingly the stochastic model was improved. This analysis also allowed to formulate a relation between image ground resolution and the accuracy achievable.

It was apparent that uncorrected systematic effects provided a further limiting constraint to data quality. For example, accuracy achievable from scanned prints was a factor 2.5 times worse than from photogrammetric-quality scans of diapositives. The datasets proved insufficient to quantify the effects of other factors individually; this requires additional research.

Accurate bundle adjustment appeared to be the principal control on the quality of DEM extraction, although high accuracy is not guaranteed when using automated techniques. It was recognised that the distribution of mass points is another important control, but the use of checkpoints is not suitable for a rigorous assessment. Especially areas of limited contrast and steep relief are not suited for automated matching and require manual intervention.

Regarding orthophotos; these appeared more sensitive to uncertainties in the bundle adjustment than to DEM errors, although again the limitations of using checkpoints for accuracy assessment were acknowledged.

The experiments for automatic extraction of displacement vectors were unsuccessful in this study. This could be explained either by the lack of distinct targets on the ground surface, or limitations in terms of radiometric quality of the images. It was proven that geometrically, the image accuracy is usually sufficient to detect and quantify ground movements; however the radiometric requirements and its consistency among multiple epochs are difficult to meet when using archival imagery.

The use of obliques is strongly dependent on their geometry. Although a large base/distance ratio provides a strong bundle adjustment, it conversely hampers automatic matching procedures.

Summarising, photogrammetric techniques have the capability to deliver a wide range of relevant data for studying landslide dynamics. 'DEMs of difference' are especially useful for quantifying terrain changes associated with displacement of relatively large ground masses. Displacement vectors can be measured where the integrity of the displaced terrain surface has remained and are consequently better suited for more modest displacements. Qualitative photo-interpreted information is essential during analysis of these quantitative data. It is also of vital importance to be aware of the data quality that is derived.
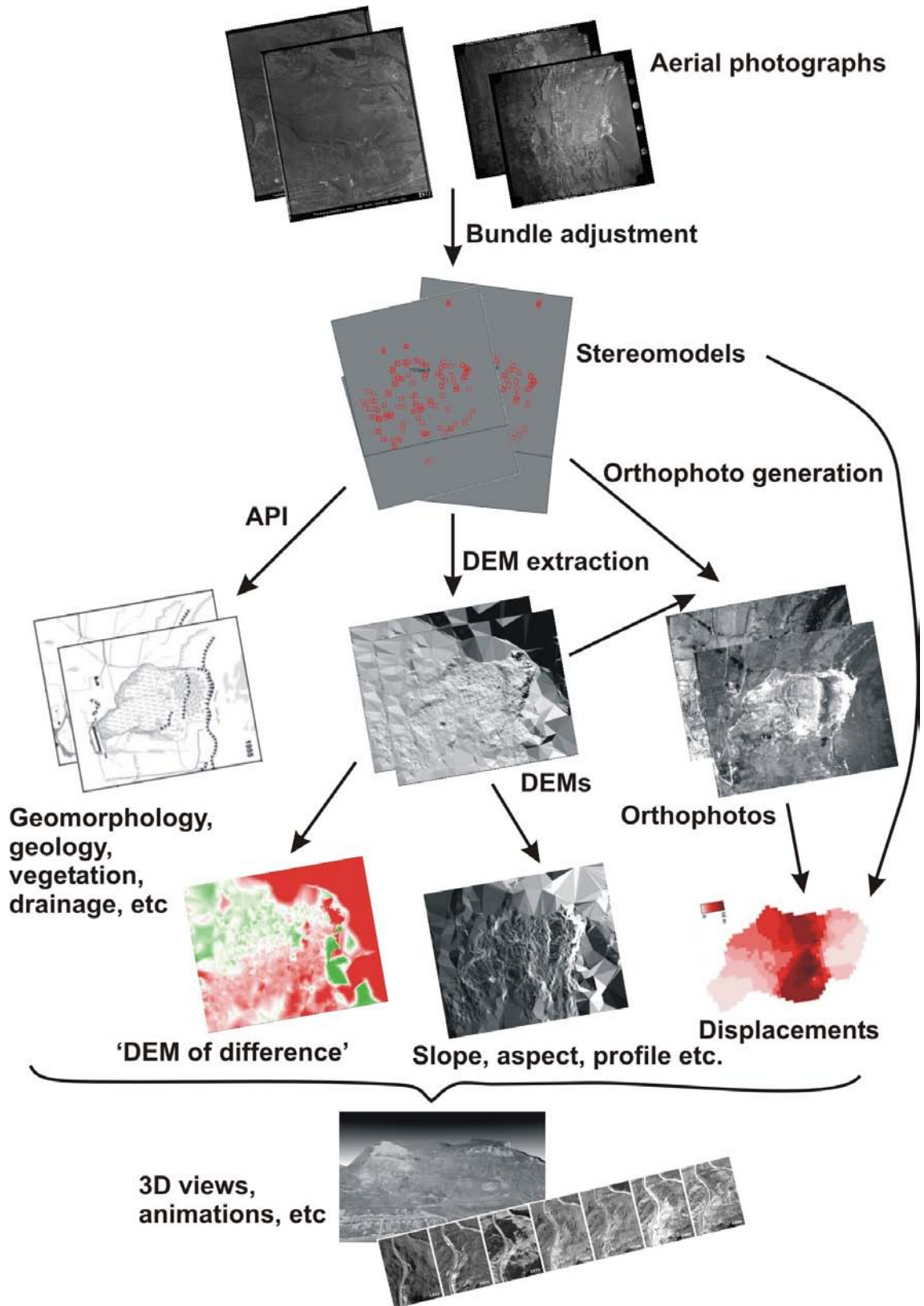
Figure 7.13. Overview of products from aerial photographs, relevant for monitoring landslide dynamics.

Chapter Eight

8 Conclusion

This study demonstrated the value of historical aerial photographs to the long-term monitoring of landslides. A sequence of aerial photographs captures morphological change, which can be unlocked by using appropriate photogrammetric methods. Owing to the flexibility and high degree of automation of modern digital photogrammetric techniques, it is possible to derive accurate quantitative data. Hence, the aerial photographic archive provides a great source for studying landslide evolution.

The aim of this study, *"to evaluate the use of historical aerial photographs and latest digital photogrammetric techniques for investigating past landslide dynamics"*, was accomplished through an extensive literature review and two landslide case-studies (Mam Tor and East Pentwyn).

8.1 Literature review

The literature review identified quantitative data on surface movements as a key element required for analysing landslide mechanisms. Distinct advantages of using aerial photographs are the possibility to monitor inaccessible terrain, and measurement of past movements using archival imagery. The approaches to measure progressive landform change from sequences of aerial photographs can be

divided into three categories: based on qualitative photo-interpretation, DEMs and displacement vectors. It is essential to evaluate the quality of derived data, but there appeared to be only scarce research available on the value of commonly available material, hence the motivation of this study.

8.2 Case-studies

Two landslide case-studies (the Mam Tor and East Pentwyn landslides) were used to explore the photogrammetric techniques for extracting meaningful, high-resolution data from historical aerial photographs. A wide range of imagery was used in terms of quality, media and format, providing the opportunity to assess data quality achievable from generally available material. The derived products comprised geomorphological maps (through photo-interpretation), automatically derived 'DEMs of difference', and displacement vectors. In both case-studies, the vertical component of measurements was of limited use, due to the large contribution of errors in relation to the measured change. The horizontal data proved to be more useful, and their spatial patterns could be related to the morphological interpretation. Comparison of measured displacements with independent ground surveyed data showed good consistency, even though a rigorous comparison was not possible, since the temporal frequency of the photogrammetrically derived data was much lower, or covering a different period of time.

8.3 Data quality issues

The bundle adjustment is a flexible way of establishing a photogrammetric model, requiring only limited ground control, and allowing the incorporation of additional parameters for estimating unknown camera parameters and other systematic distortions. Inclusion of a stochastic model allows measurements of differing quality to be combined and *a priori* estimation of precision that can be achieved, based on quality of source data. Analysis of the combined datasets from both case-studies resulted in improvements of the stochastic model. A linear relation was established between image ground resolution and data accuracy. Undetected systematic errors provided a further limiting constraint on the accuracy of derived data; e.g. the accuracy from low-quality scanned prints appeared a factor 2.5 times worse than could be achieved from photogrammetric-quality scanned diapositives. There was

insufficient data available to quantify the individual effects of other factors on accuracy, such as availability of camera calibration, and quality of ground control.

An important advancement in digital photogrammetry is image matching, which allows automation of various stages in the photogrammetric working chain, and hence a fast way of extracting large quantities of data, such as DEMs and orthophotos. Although an accurate bundle adjustment is a prerequisite, it does not guarantee accurate results using automatic techniques. Areas of limited contrast or steep relief are in particular ill-suited for automated image matching. In these cases manual intervention may be required to assure good results. It was also recognised that checkpoints may not provide a good representation of overall accuracy.

Under favourable conditions image matching may be employed using multi-temporal photographs for extracting displacement vectors. In this study, a Matlab script was written to perform this procedure, but the algorithm was ultimately unsuccessful in both case-studies. This failure could be attributed to the absence of distinct features on the ground surface and/or different photo-quality. It was concluded that the high requirements in terms of radiometric photo quality, and in particular its consistency were difficult to meet while using archival imagery.

Although providing a more familiar view than vertical imagery, the value of obliques for quantitative analysis strongly depends on its orientation with respect to the slope under investigation. Its height accuracy may be better than using conventional vertical images, and a larger base/distance ratio can provide a strong bundle adjustment. Conversely, it appeared that a too large base/distance ratio hampered automatic matching procedures, and hence extraction of accurate DEMs and orthophotos.

8.4 Relevance to landslide studies

This study showed that a wide range of information can be provided from archival aerial photographs, both qualitative and quantitative. Landslides and their progressive evolution can be visualised using 3D views and animations created from sequential images. Surface features can be identified and mapped through photo-interpretation, providing useful information for assessing slope stability conditions, and to support interpretation of quantitative data products.

Photogrammetric techniques can provide accurate quantitative data. DEMs are a source for various parameters relevant for slope stability modelling. Multi-temporal elevation models are especially useful for quantifying terrain changes associated with large ground displacements. Displacement vectors can be measured when the integrity of the displaced terrain surface has remained. Such vectors are valuable for analysing spatial and temporal displacement patterns, and estimation of the underlying slip surface.

8.5 Recommendations

An additional study is needed to separate the effects of different variables on data accuracy, such as camera calibration and the quality of ground control. This would then provide a reliable *a priori* estimate of achievable accuracy, based on the quality of source data and the amount of effort to establish the photogrammetric model.

Extra work could be carried out to assess the effects of errors occurring during automated procedures. It appeared that especially in areas of low contrast and steep relief mismatches and interpolation can lead to inaccurate data, which may not always be evident in accuracy assessments. It is desirable to investigate how these errors can be better evaluated and their effects decreased, for example through manual intervention.

Vector determination using an automatic image matching algorithm was ultimately unsuccessful in both case-studies, due to absence of distinct surface features or differing image quality. Simply changing the values for the various parameters in the algorithm did not lead to significant improvements. A more sophisticated matching procedure is required, which perhaps imitates human intelligence more closely.

Finally, it would be interesting to extend the data sequences of the two case-studies and relate the long-term landslide evolution to climatic factors. It was however recognised that an important difficulty in establishing such a relationship would be the difference between the frequency of measurements and the variability of landslide activity. Although the time span of the image sequences would cover medium long-term climatic changes (up to 50 years), their intervals mask the response of the landslides to short-term climatic variability (typically yearly).

References

Adams, J. C. and Chandler, J. H. (2002). Evaluation of Lidar and Medium Scale Photogrammetry for Detecting Soft-Cliff Coastal Change. *Photogrammetric Record* 17 (99): pp. 405-418.

Ager, G., Marsh, S., Hobbs, P., Chiles, R., Haynes, M., Thurston, N. and Pride, R. (2004). Towards Automated Monitoring of Ground Instability Along Pipelines. *Proceedings of the Institute of Civil Engineers, Geopipe 2004 Conference, London, UK*.

Al-Dabbagh, T. H. (1985). *Study of Residual Shear Strength of Namurian Shale in Respect of Slopes in North Derbyshire* (PhD Thesis). Sheffield University, Sheffield.

Al-Dabbagh, T. H. and Cripps, J. C. (1987). Planning and Engineering Geology. In: Culshaw, M. G., Bell, F. G., Cripps, I. C. and O'Hara, M. (eds.) *Planning and Engineering Geology*. Geological Society, London: pp. 101-114.

Baily, B., Collier, P., Farres, P. J., Inkpen, R. and Pearson, A. (2003). Comparative Assessment of Analytical and Digital Photogrammetric Methods in the Construction of DEMs of Geomorphological Forms. *Earth Surface Processes and Landforms* 28 (3): pp. 307-320.

Baldi, P., Fabris, M., M., M. and Monticelli, R. (2005). Monitoring the Morphological Evolution of the Sciara Del Fuoco During the 2002-2003 Stromboli Eruption Using Multi-Temporal Photogrammetry. *ISPRS Journal of Photogrammetry & Remote Sensing* 59 (4): pp. 199-211.

Baltsavias, E. P. (1999). On the Performance of Photogrammetric Scanners. *Proceedings of the Photogrammetric Week '99, Stuttgart*. pp. 155-173.

Barsch, D. and Hell, G. (1975). Photogrammetrische Bewegungsmessungen Am Blockgletscher Murtèl I, Oberengadin, Sweizer Alpen. *Zeitschrift für Gletscherkunde und Glazialgeologie* 11 (2): pp. 111-142.

Baum, R. L., Messerich, J. and Fleming, R. W. (1998). Surface Deformation as a Guide to Kinematics and Three-Dimensional Shape of Slow-Moving, Clay-Rich Landslides, Honolulu, Hawaii. *Environmental & Engineering Geoscience* IV (3): pp. 283-306.

Bell, F. G. (2003). *Geological Hazards. Their Assessment, Avoidance and Mitigation*. Spon Press, London/New York: 648 pp.

Betts, H. D. and DeRose, R. C. (1999). Digital Elevation Models as a Tool for Monitoring and Measuring Gully Erosion. *International Journal of Applied Earth Observation and Geoinformation* 1 (2): pp. 91-101.

Betts, H. D., Trustrum, N. A. and DeRose, R. C. (2003). Geomorphic Changes in a Complex Gully System Measured from Sequential Digital Elevation Models, and Implications for Management. *Earth Surface Processes and Landforms* 28 (10): pp. 1043-1058.

Bitelli, G., Dubbini, M. and Zanutta, A. (2004). Terrestrial Laser Scanning and Digital Photogrammetry Techniques to Monitor Landslide Bodies. *Proceedings of the 20th ISPRS Conference, Istanbul, Turkey*. Vol. XXXV, part B5, pp. 246-251.

Brardinoni, F., Slaymaker, O. and Hassan, M. A. (2003). Landslide Inventory in a Rugged Forested Watershed: A Comparison between Air-Photo and Field Survey Data. *Geomorphology* 54 (3-4): pp. 179-196.

Brown, D. C. (1956). *The Simultaneous Determination of the Orientation and Lens Distortion of a Photogrammetric Camera. RCA Data Reduction Technical Report.*

Brown, D. C. (1971). Analytical Calibration of Close-Range Cameras. *Photogrammetric Engineering* 37 (8): pp. 855-866.

Brown, D. G. and Arbogast, A. F. (1999). Digital Photogrammetric Change Analysis Applied to Active Coastal Dunes in Michigan. *Photogrammetric Engineering & Remote Sensing* 65 (4): pp. 467-474.

Brunsden, D. (1984). Mudslides. In: Brunsden, D. and Prior, D. B. (eds.) *Slope Instability*. John Wiley & Sons, Chichester: pp. 363-418.

Brunsden, D. (1993). Mass Movement; the Research Frontier and Beyond: A Geomorphological Approach. *Geomorphology* 7 (1-3): pp. 85-128.

Brunsden, D. and Chandler, J. H. (1996). Development of an Episodic Landform Change Model Based Upon the Black Ven Mudslide, 1946-1995. In: Anderson, M. G. and Brooks, S. M. (eds.) *Advances in Hillslope Processes*. John Wiley & Sons Ltd., Chichester: pp. 869-896.

Brunsden, D., Doornkamp, J. C., Fookes, P. G., Jones, D. K. C. and Kelly, J. M. H. (1975). Large Scale Geomorphological Mapping and Highway Engineering Design. *Quarterly Journal of Engineering Geology* 8: pp. 227-530.

Brunsden, D. and Ibsen, M.-L. (1996). Mudslide. In: Dikau, R., Brunsden, D., Schrott, L. and Ibsen, M.-L. (eds.) *Landslide Recognition. Identification, Movement and Causes*. John Wiley & Sons, Chichester: pp. 103-119.

Brunsden, D. and Prior, D. B. (eds.) (1984) *Slope Instability,* John Wiley & Sons, Chicester: 620 pp.

Buckley, S. J. (2003). *A Geomatics Data Fusion Technique for Change Monitoring* (PhD Thesis). School of Civil Engineering and Geosciences, University of Newcastle upon Tyne, Newcastle: 258 pp.

Buckley, S. J., Mills, J. P., Clarke, P. J., Edwards, S. J., Pethick, J. and Mitchell, H. L. (2002). Synergy of Gps, Photogrammetry and Insar for Coastal Zone Monitoring. *International Archives of Photogrammetry and Remote Sensing* 34 (part 4).

Buma, J. and Van Asch, T. W. J. (1996). Slide (Rotational). In: Dikau, R., Brunsden, D., Schrott, L. and Ibsen, M.-L. (eds.) *Landslide Recognition. Identification, Movement and Causes*. John Wiley & Sons, Chichester: pp. 43-61.

Burrough, P. A. and McDonnel, R. A. (1998). *Principles of Geographical Information Systems*. Oxford University Press, Oxford: 333 pp.

Butler, J. B., Lane, S. N. and Chandler, J. H. (1998). Assessment of DEM Quality for Characterizing Surface Roughness Using Close Range Digital Photogrammetry. *Photogrammetric Record* 16 (92): pp. 271-291.

Carrara, A., Cardinali, M., Guzzetti, F. and Reichenbach, P. (1995). Gis-Based Techniques for Mapping Landslide Hazard. In: Carrara, A. and Guzzetti, F. (eds.) *Geographical Information Systems in Assessing Natural Hazards*. Kluwer Academic Publishers, Dordrecht, The Netherlands: pp. 135-176.

Carter, M. and Bentley, S. P. (1985). The Geometry of Slip Surfaces beneath Landslides: Predictions from Surface Measurements. *Canadian Geotechnical Journal* 22: pp. 234-238.

Casale, R., Fantechi, R. and Flageollet, J.-C. (eds.) (1994) *Temporal Occurrence and Forecasting of Landslides in the European Community - Final Report,* European Community, Programme EPOCH (Contract No. 90 0025) 957 pp.

Casson, B., Delacourt, C., Baratoux, D. and Allemand, P. (2003). Seventeen Years of the "La Clapière" Landslide Evolution Analysed from Ortho-Rectified Aerial Photographs. *Engineering Geology* 68 (1-2): pp. 123-139.

Chadwick, J., Dorsch, S., Glenn, N., Thackray, G. and Shilling, K. (2005). Application of Multi-Temporal High-Resolution Imagery and Gps in a Study of the Motion of a Canyon Rim Landslide. *ISPRS Journal of Photogrammetry & Remote Sensing* 59 (4): pp. 212-221.

Chandler, J. H. (1989). *The Acquisition of Spatial Data from Archival Photographs and Their Application to Geomorphology* (PhD Thesis). Department of Civil Engineering, The City University, London: 300 pp.

Chandler, J. H. (1999). Effective Application of Automated Digital Photogrammetry for Geomorphological Research. *Earth Surface Processes and Landforms* 24 (1): pp. 51-63.

Chandler, J. H. (2001). Terrain Measurement Using Automated Digital Photogrammetry. In: Griffiths, J. S. (ed.) *Land Surface Evaluation for Engineering Practice*. Geological Society, London: pp. 13-18.

Chandler, J. H. and Brunsden, D. (1995). Steady State Behaviour of the Black Ven Mudslide: The Application of Archival Analytical Photogrammetry to Studies of Landform Change. *Earth Surface Processes and Landforms* 20 (3): pp. 255-275.

Chandler, J. H. and Cooper, M. A. R. (1989). The Extraction of Positional Data from Historical Photographs and Their Application to Geomorphology. *Photogrammetric Record* 13 (73): pp. 69-78.

Cheng, H.-H. (2000). Photogrammetric Digital Data Processing of Tsau-Lin Big Landslide. *Proceedings of the 21st Asian Conference on Remote Sensing, Taipei, Taiwan*.

Clarke, J. S. and Chandler, J. H. (1992). 'the Archival Photogrammetric Technique: Further Application and Development. *Photogrammetric Record* 14 (80): pp. 241-247.

Conway, B. W., Forster, A., Northmore, K. J. and Barclay, W. J. (1980). *South Wales Coalfield Landslip Survey: Volume 1 - Text*. Institute of Geological Sciences, 218 pp.

Cooke, R. U. and Doornkamp, J. C. (1990). *Geomorphology in Environmental Management*. Clarendon Press, Oxford, UK: 410 pp.

Cooper, M. A. R. (1987). *Control Surveys in Civil Engineering*. Collins, London: 381 pp.

Cooper, M. A. R. and Cross, P. A. (1988). Statistical Concepts and Their Application in Photogrammetry and Surveying. *Photogrammetric Record* 12 (71): pp. 637-663.

Crozier, M. J. (1984). Field Assessment of Slope Instability. In: Brunsden, D. and Prior, D. B. (eds.) *Slope Instability*. John Wiley & Sons Ltd., Chichester, UK: pp. 103-142.

Crozier, M. J. (1986). *Landslides: Causes, Consequences and Environment*. Croom Helm, London: 252 pp.

Crozier, M.J. (2004). *Landslides.* In: Goudie, A.S. (ed.) *Encyclopedia of Geomorphology.* Routledge, London, UK: pp. 605-608.

Dare, P. M., Hanley, H. B., Fraser, C. S., Riedel, B. and Niemeier, W. (2002). An Operational Application of Automatic Feature Extraction: The Measurement of Cracks in Concrete Structures. *Photogrammetric Record* 17 (99): pp. 453-464.

De Graaff, L. W. S., De Jong, M. G. G., Rupke, J. and Verhofstad, J. (1987). A Geomorphological Mapping System at Scale 1:10,000 for Mountainous Areas. *Zeitschrift für Geomorphologie* 31 (2): pp. 229-242.

Delacourt, C., Allemand, P., Casson, B. and Vadon, H. (2004). Velocity Field of the "La Clapière" Landslide Measured by the Correlation of Aerial and Quickbird Satellite Images. *Geophysical Research Letters* 31 (L15619): pp. 5.

Derbyshire County Council (1978). *Principal Road A625, Hope to Chapel-En-Le-Frith, Landslip at Mam Tor. Report No. 25 of the County Surveyor, Derbyshire County Council*.

Desmond, R. (2004). *Personal correspondence during visit to CUCAP library, October 2004*.

Dikau, R., Brunsden, D., Schrott, L. and Ibsen, M. (eds.) (1996) *Landslide Recognition. Identification, Movement and Causes,* John Wiley & Sons, Chicester: 251 pp.

Drury, S. A. (1987). *Image Interpretation in Geology*. Allen & Unwin, London: 243 pp.

Evin, M. and Assier, A. (1982). Mise En Évidence De Mouvements Sur Le Glacier Rocheux Du Pic D'asti (Queyras - Alpes Du Sud - France). *Revue de Géomorphologie Dynamique* 31 (4): pp. 127-136.

Fisher, R., Perkins, S., Walker, A. and Wolfart, E. 2003. *The Hypermedia Image Processing Reference* [online]. Available at: <http://homepages.inf.ed.ac.uk/rbf/HIPR2/hipr_top.htm> [Accessed 10 May 2006].

Florinsky, I. V. (1998). Combined Analysis of Digital Terrain Models and Remotely Sensed Data in Landscape Investigations. *Progress in Physical Geography* 22 (1): pp. 33-60.

Ford, T. D. and Rieuwerts, J. H. (1976). Odin Mine Castleton, Derbyshire. *Bulletin of the Peak District Mines Historical Society* 6 (4): pp. 1-54.

Fox, H. and Nuttall, A.-M. (1997). Photogrammetry as a Research Tool for Glaciology. *Photogrammetric Record* 15 (89): pp. 725-737.

Franklin, J. A. (1984). Slope Instrumentation and Monitoring. In: Brunsden, D. and Prior, D. B. (eds.) *Slope Instability*. John Wiley & Sons, Chichester: pp. 143-169.

Fricker, P., Sandau, R. and Walker, A.S. (2000). Progress in the Development of a High Performance Aerial Digital Sensor. *Photogrammetric Record* 16 (96): 911-927.

Fryer, J. G., Chandler, J. H. and Cooper, M. A. R. (1994). On the Accuracy of Heighting from Aerial Photographs and Maps: Implications to Process Modellers. *Earth Surface Processes and Landforms* 19 (6): pp. 577-583.

Gentili, G., Giusti, E. and Pizzaferri, G. (2002). Photogrammetric Techniques for the Investigation of the Corniglio Landslide. In: Allison, R. J. (ed.) *Applied Geomorphology*. John Wiley & Sons, Chichester, UK: pp. 39-48.

Gili, J. A., Corominas, J. and Rius, J. (2000). Using Global Positioning System Techniques in Landslide Monitoring. *Engineering Geology* 55 (3): pp. 167-192.

Gong, J., Li, Z., Zhu, Q., Sui, H. and Zhou, Y. (2000). Effects of Various Factors on the Accuracy of DEMs: An Intensive Experimental Investigation. *Photogrammetric Engineering & Remote Sensing* 66 (9): pp. 1113-1117.

Gorbunov, A. P., Titkov, S. N. and Polyakov, V. G. (1992). Dynamics of Rocks Glaciers of the Northern Tien Shan and the Djungar Ala Tau, Kazakhstan. *Permafrost and Periglacial Processes* 3 (1): pp. 29-29.

Graham, R. (1998). *Digital Imaging*. Whittles, Caithness: 212 pp.

Granshaw, S. I. (1980). Bundle Adjustment Methods in Engineering Photogrammetry. *Photogrammetric Record* 10 (56): pp. 181-207.

Greenway, D. R. (1987). Vegetation and Slope Stability. In: Anderson, M. G. and Richards, K. S. (eds.) *Slope Stability. Geotechnical Engineering and Geomorphology*. John Wiley & Sons, Chichester: pp. 187-230.

Gruen, A.W. (1985). Adaptive Least Squares Correlation: A Powerful Image Matching Technique. *South African Journal of Photogrammetry, Remote Sensing and Cartography*. 14 (3): pp. 175-187.

Halcrow (1981). *Preliminary Study of Possible Remedial Measures to the Landslips at East Pentwyn and Bournville, Gwent*. Sir William Halcrow & Partners.

Halcrow (1983). *East Pentwyn Landslip: First Report on Geotechnical Investigations.* Sir William Halcrow & Partners.

Halcrow (1989). *East Pentwyn & Bournville Landslips: Monitoring Report 1987-1989*. Sir William Halcrow & Partners.

Hall, G., Groves, K., Ogle, R., Spiers, D. and Runciman, C. (2003). *NMR Archives. An Overview of the Aerial Photograph Collections of the NMR*. The National Monuments Record, 14 pp.

Hannah, M. J. (1981). Error Detection and Correction in Digital Terrain Models. *Photogrammetric Engineering & Remote Sensing* 47 (1): pp. 63-69.

Hansen, A. (1984a). Landslide Hazard Analysis. In: Brunsden, D. and Prior, D. B. (eds.) *Slope Instability*. John Wiley & Sons, Chichester: pp. 523-602.

Hansen, M. J. (1984b). Strategies for Classification of Landslides. In: Brunsden, D. and Prior, D. B. (eds.) *Slope Instability*. John Wiley & Sons, Chichester: pp. 1-25.

Hapke, C. J. (2005). Estimation of Regional Material Yield from Coastal Landslides Based on Historical Digital Terrain Modelling. *Earth Surface Processes and Landforms* 30 (6): pp. 679-697.

Hapke, C. J. and Richmond, B. (2000). Monitoring Beach Morphology Changes Using Small-Format Aerial Phtography and Digital Softcopy Photogrammetry. *Environmental Geosciences* 7 (1): pp. 32-37.

Hartlen, J. and Viberg, L. (1988). Evaluation of Landslide Hazard. *Proceedings of the 5th International Symposium on Landslides, Lausanne, Switzerland*. pp. 1037-1057.

Hayden, R. S. (1986). Mapping. In: Short, S., N.M. and Blair, S., R.W. (eds.) *Geomorphology from Space. A Global Overview of Regional Landforms*. NASA.

Heipke, C. (1997). Automation of Interior, Relative, and Absolute Orientation. *ISPRS Journal of Photogrammetry & Remote Sensing* 52 (1): pp. 1-19.

Hencher, S. R. (1987). The Implications of Joints and Structures for Slope Stability. In: Anderson, M. G. and Richards, K. S. (eds.) *Slope Stability. Geotechnical Engineering and Geomorphology*. John Wiley & Sons, Chichester: pp. 145-186.

Hervás, J., Barredo, J. I., Rosin, P. L., Pasuto, A., Mantovani, F. and Silvano, S. (2003). Monitoring Landslides from Optical Remotely Sensed Imagery: The Case History of Tessina Landslide, Italy. *Geomorphology* 54 (1-2): 63-75.

Hinz, A. and Heier, H. (2000). The Z/I Imaging Digital Camera System. *Photogrammetric Record* 16 (96): 929-936.

Hoittier, P. (1976). Accuracy of Close Range Analytical Solutions. *Photogrammetric Engineering & Remote Sensing* 42 (3): pp. 345-375.

Hutchinson, J. N. (1968). Mass Movement. In: Fairbridge, R. W. (ed.) *Encyclopaedia of Earth Sciences Series Iii*. Reinhold Publishers, New York: pp. 688-695.

Hutchinson, J. N. (1988). General Report: Morphological and Geotechnical Parameters of Landslides in Relation to Geology and Hydrogeology. *Proceedings of the 5th International Symposium on Landslides, Lausanne, Switserland*. Vol. 1, pp. 3-35.

Ibsen, M.-L., Brunsden, D., Bromhead, E. and Collison, A. (1996). Slab Slide. In: Dikau, R., Brunsden, D., Schrott, L. and Ibsen, M.-L. (eds.) *Landslide Recognition. Identification, Movement and Causes*. John Wiley & Sons, Chichester: pp. 78-84.

Jacobsen, K. 2005. *Integrated Sensor Orientation Course* [online]. Available at: <http://www.ipi.uni-hannover.de/elan/iso/index.htm> [Accessed 10/05/2006].

Jones, D. B. and Siddle, H. J. (1988). Geotechnical Parameters for Stabilisation Measures to a Landslide. *Proceedings of the 5th International Symposium on Landslides, 10-15 July 1988, Lausanne*.

Jones, D. B. and Siddle, H. J. (2000). Effect of Mining on Hillslope Stability. In: Siddle, H. J., Bromhead, E. N. and Bassett, M. G. (eds.) *Landslides and Landslide Management in South Wales*. National Museums & Galleries of Wales, Cardiff: pp. 40-43.

Kääb, A. (2002). Monitoring High-Mountain Terrain Deformation from Repeated Air- and Spaceborn Optical Data: Examples Using Digital Aerial Imagery and Aster Data. *ISPRS Journal of Photogrammetry & Remote Sensing* 57 (1): pp. 39-52.

Kääb, A., Haeberli, W. and Hilmar Gudmundsson, G. (1997). Analysing the Creep of Moutain Permafrost Using High Precision Aerial Photogrammetry: 25 Years of Monitoring Gruben Rock Glacier, Swiss Alps. *Permafrost and Periglacial Processes* 8 (4): pp. 409-426.

Kääb, A., Hilmar Gudmundsson, G. and Hoelzle, M. (1998). Surface Deformation of Creeping Mountain Permafrost. Photogrammetric Investigations on Rock Glacier Murtèl, Swiss Alps. *Proceedings of the 7th International Conference on Permafrost, Yellowknife, Canada*. pp. 531-537.

Kääb, A. and Vollmer, M. (2000). Surface Geometry, Thickness Changes and Flow Fields on Creeping Mountain Permafrost: Automatic Extraction by Digital Image Analysis. *Permafrost and Periglacial Processes* 11 (4): pp. 315-326.

Kalaugher, P. G., Grainger, P. and Hodgson, R. L. P. (1987). Cliff Stability Evaluation Using Geomorphological Maps Based Upon Oblique Aerial Photographs. In: Culshaw, M. G., Bell, F. G., Cripps, I. C. and O'Hara, M. (eds.) *Planning and Engineering Geology*. Geological Society, London: pp. 163-170.

Kaufmann, V. (1996). Geomorphometric Monitoring of Active Rock Glaciers in the Austrian Alps. *Proceedings of the 4th International Symposium on High Mountain Remote Sensing Carthography, Karlstad-Kiruna-Tromsø*. pp. 97-113.

Kaufmann, V. (2002). Morphometric Documentation and Computer-Based Visualization of Slope Deformation and Slope Creep of the Blaubach Landslide (Salzburg, Austria). *Proceedings of the 7th International Symposium on High Mountain Remote Sensing Cartography, Bishkek, Kyrgyzstan*.

Kaufmann, V. and Ladstädter, R. (2000). Spatio-Temporal Analysis of the Dynamic Behaviour of the Hochebenkar Rock Glaciers (Oetztal Alps, Austria) by Means of Digital Photogrammetric Methods. *Proceedings of the 6th International*

Symposium on High Mountain Remote Sensing Cartography, Graz, Austria. Grazer Schriften der Geographie und Raumforschung, Vol. 37, pp. 119-139.

Kaufmann, V. and Ladstädter, R. (2002). Monitoring of Active Rock Glaciers by Means of Digital Photogrammetry. *International Archives of Photogrammetry and Remote Sensing* XXXIV, Part 3B: pp. 108-111.

Kaufmann, V. and Ladstädter, R. (2004). Documentation of the Movement of the Hinteres Langtalkar Rock Glacier. *International Archives of Photogrammetry and Remote Sensing* XXXV, part B7: pp. 893-898.

Kenefick, J. F., Gyer, M. S. and Harp, B. F. (1972). Analytical Self-Calibration. *Photogrammetric Engineering* 38 (11): pp. 1117-1126.

Kerle, N. (2002). Volume Estimation of the 1998 Flank Collapse at Casita Volcano, Nicaragua: A Comparison of Photogrammetric and Conventional Techniques. *Earth Surface Processes and Landforms* 27 (7): pp. 759-772.

Konecny, G. (1964). Glacial Surveys in Western Canada. *Photogrammetric Engineering* 30 (1): pp. 64-82.

Konecny, G. (1985). The International Society for Photogrammetry and Remote Sensing - 75 Years Old, or 75 Years Young. *Photogrammetric Engineering & Remote Sensing* 51 (7): pp. 919-933.

Krupnik, A. (2003). Accuracy Prediction for Ortho-Image Generation. *Photogrammetric Record* 18 (101): pp. 41-58.

Lane, S. N. (2000). The Measurement of River Channel Morphology Using Digital Photogrammetry. *Photogrammetric Record* 16 (96): pp. 937-961.

Lane, S. N., Chandler, J. H. and Richards, K. S. (1994). Developments in Monitoring and Modelling Small Scale River Bed Topography. *Earth Surface Processes and Landforms* 19: pp. 349-368.

Lane, S. N., James, T. D. and Crowell, M. D. (2000). Application of Digital Photogrammetry to Complex Topography for Geomorphological Research. *Photogrammetric Record* 16 (95): pp. 793-821.

Lane, S. N., Richards, K. S. and Chandler, J. H. (1993). Developments in Photogrammetry; the Geomorphological Potential. *Progress in Physical Geography* 17: pp. 306-328.

Leica Geosystems (2003). *Leica Photogrammetry Suite Orthobase & Orthobase Pro User's Guide*. Leica Geosystems GIS & Mapping, LLC, Atlanta, Georgia: 516 pp.

Leick, A. (1990). *Gps Satellite Surveying*. John Wiley & Sons, New York, USA: 352 pp.

Li, Z. (1988). On the Measure of Digital Terrain Model Accuracy. *Photogrammetric Record* 12 (72): pp. 873-877.

Lillesand, T. M. and Kiefer, R. W. (1994). *Remote Sensing and Image Interpretation*. John Wiley & Sons, New York, USA: 750 pp.

Lo, C. P. (1976). *Geographical Applications of Aerial Photography*. David & Charles, Newton Abbot, UK: 330 pp.

Mantovani, F., Soeters, R. and Van Westen, C. J. (1996). Remote Sensing Techniques for Landslide Studies and Hazard Zonation in Europe. *Geomorphology* 15 (3-4): pp. 213-225.

Matthys, D. 2001. *Digital Image Processing* [online]. Available at: <http://academic.mu.edu/phys/matthysd/web226/index.htm> [Accessed 10 May 2006].

Mikhail, E. M. and Gracie, G. (1981). *Analysis and Adjustment of Survey Measurements*. Van Nostrand Reinhold Company, New York: 340 pp.

Mills, J.P. (2006). *Personal correspondence during viva, 31 August 2006*.

Mills, J. P., Buckley, S. J., Mitchell, H. L., Clarke, P. J. and Edwards, S. J. (2005). A Geomatics Data Integration Technique for Coastal Change Monitoring. *Earth Surface Processes and Landforms* 30 (6): pp. 651-664.

Mora, P., Baldi, P., Casula, G., Fabris, M., Ghirotti, M., Mazzini, E. and Pesci, A. (2003). Global Positioning Systems and Digital Photogrammetry for the Monitoring of Mass Movements: Application to the Ca' Di Malta Landslide (Nothern Apennines, Italy). *Engineering Geology* 68 (1-2): pp. 103-121.

NAPLIB (1999). *Directory of Aerial Photographic Collections in the United Kingdom*. 132 pp.

Nash, D. F. T. (1984). A Comparative Review of Limit Equilibrium Methods of Stability Analysis. In: Anderson, M. G. and Richards, K. S. (eds.) *Slope Stability. Geotechnical Engineering and Geomorphology*. John Wiley & Sons, Chichester: pp. 11-75.

Nikon 2006. *Microscopyu. The Source for Microscopy Education* [online]. Available at: <http://www.microscopyu.com/> [Accessed 10 May 2006].

Norman, J. W., Leibowitz, T. H. and Fookes, P. G. (1975). Factors Affecting the Detection of Slope Instability with Air Photographs in an Area near Sevenoaks, Kent. *Quarterly Journal of Engineering Geology* 8: pp. 159-176.

Ordnance Survey 2006a. *Aerial Photography* [online]. Available at: <http://www.ordnancesurvey.co.uk/oswebsite/products/aerialphotography/index.html> [Accessed 10 May 2006].

Ordnance Survey 2006b. *OS Net* [online]. Available at: <http://www.ordnancesurvey.co.uk/oswebsite/gps/> [Accessed 10 May 2006].

Parise, M. (2003). Observation of Surface Features on an Active Landslide, and Implications for Understanding Its History of Movement. *Natural Hazards and Earth System Sciences* 3 (6): pp. 569-580.

Patias, P. and Streilein, A. (1996). Contribution of Videogrammetry to the Architectural Restitution - Results of the CIPA "O. Wagner Pavillon" Test. *International Archives of Photogrammetry and Remote Sensing* XXI (B5): pp. 457-462.

Petley, D. N. (2004). The Evolution of Slope Failures: Mechanisms of Rupture Propagation. *Natural Hazards and Earth System Sciences* 4 (147-152):

Petley, D. N., Mantovani, F., Bulmer, M. H. and Zannoni, A. (2005). The Use of Surface Monitoring Data for the Interpretation of Landslide Movement Patterns. *Geomorphology* 66 (1-2): pp. 133-147.

Powers, P. S., Chiarle, M. and Savage, W. Z. (1996). A Digital Photogrammetric Method for Measuring Horizontal Surficial Movements on the Slumgullion Earthflow, Hinsdale County, Colorado. *Computers & Geosciences* 22 (6): pp. 651-663.

Pyle, C. J., Richards, K. S. and Chandler, J. H. (1997). Digital Photogrammetric Monitoring of River Bank Erosion. *Photogrammetric Record* 15 (89): pp. 753-764.

Remondino, F. and Fraser, C. (2006). Digital Camera Calibration Methods: Considerations and Comparisons. *International Archives of Photogrammetry and Remote Sensing* XXXVI (Part 5): pp. 266-272.

Rib, H. T. and Liang, T. (1978). Recognition and Identification. In: Schuster, R. L. and Krizek, R. J. (eds.) *Landslides Analysis and Control*. National Academy of Sciences, Washington, D.C.: pp. 34-80.

Robson, S. and Shortis, M. R. (1998). Practical Influences of Geometric and Radiometric Image Quality Provided by Different Digital Camera Systems. *Photogrammetric Record* 16 (92): pp. 225-248.

Russ, J. C. (2002). *The Image Processing Handbook*. CRC Press LLC, Boca Raton, Florida: 732 pp.

Rutter, E. H., Arkwright, J. C., Holloway, R. F. and Waghorn, D. (2003). Strains and Displacements in the Mam Tor Landslip, Derbyshire, England. *Journal of the Geological Society* 160 (5): pp. 735-744.

Saleh, R. A. and Scarpace, F. L. (2000). Image Scanning Resolution and Surface Accuracy; Experimental Results. *International Archives of Photogrammetry and Remote Sensing* XXXIII, Part B2: pp. 482-485.

Savigear, R. A. G. (1965). A Technique of Morphological Mapping. *Annals of the Association of American Geographers* 55: pp. 514-538.

Scambos, T. A., Dutkiewicz, M. J., Wilson, J. C. and Bindschadler, R. A. (1992). Application of Image Cross-Correlation to the Measurement of Glacier Velocity Using Satellite Image Data. *Remote Sensing of Environment* 42 (3): pp. 177-186.

Schenk, A. F. (1996). Automatic Generation of Dem's. In: Cary, T., Jensen, J. and Nyquist, M. (eds.) *Digital Photogrammetry. An Addendum to the Manual of Photogrammetry*. American Society for Photogrammetry and Remote Sensing, Bethesda, Maryland: pp. 247-250.

Schenk, T. (1997). Towards Automatic Aerial Triangulation. *ISPRS Journal of Photogrammetry & Remote Sensing* 52 (3): pp. 110-121.

Schuster, R. L. and Smith, W. K. (1996). Retreat of the Slumgullion Main Scarp. In: Varnes, D. J. and Savage, W. Z. (eds.) *The Slumgullion Earth Flow: A Large-Scale Natural Laboratory. U.S. Geological Survey Bulletin 2130*. U.S. Government Printing Office, Washington, USA.

Selby, M. J. (1993). *Hillslope Materials and Processes*. Oxford University Press, Oxford: 451 pp.

Siddle, H. J. (2000). East Pentwyn Landslide, Blaina. In: Siddle, H. J., Bromhead, E. N. and Bassett, M. G. (eds.) *Landslides and Landslide Management in South Wales*. National Museums & Galleries of Wales, Cardiff: pp. 77-80.

Simmons Aerofilms Ltd. 2006. *Historic Image Library* [online]. Available at: <http://www.simmonsaerofilms.com/imglib/index_ektid51.aspx> [Accessed 10 May 2006].

Skempton, A. W., Leadbeater, A. D. and Chandler, R. J. (1989). The Mam Tor Landslide, North Derbyshire. *Philosophical Transactions of the Royal Society of London A* 329: pp. 503-747.

Slama, C. C. (1980). *The Manual of Photogrammetry (4th Edition)*. American Society for Photogrammetry, Falls Church: 1056 pp.

Smith, W. K. (1996). Photogrammetric Determination of Slope Movements on the Slumgullion Landslide. In: Varnes, D. J. and Savage, W. Z. (eds.) *The Slumgullion Earth Flow: A Large-Scale Natural Laboratory. U.S. Geological Survey Bulletin 2130*. U.S. Government Printing Office, Washington.

Soeters, R. and Van Westen, C. J. (1996). Slope Instability Recognition, Analysis, and Zonation. In: Turner, A. K. and Schuster, R. L. (eds.) *Landslides. Investigation and Mitigation*. National Academy Press, Washington D.C.: pp. 129-177.

Sorriso-Valvo, M. and Gullà, G. (1996). Rock Slide. In: Dikau, R., Brunsden, D., Schrott, L. and Ibsen, M.-L. (eds.) *Landslide Recognition. Identification, Movement and Causes*. John Wiley & Sons, Chichester: pp. 85-96.

Squarzoni, C., Delacourt, C. and Allemand, P. (2003). Nine Years of Spatial and Temporal Evolution of the La Valette Landslide Observed by Sar Interferometry. *Engineering Geology* 68 (1-2): pp. 53-66.

Squarzoni, C., Delacourt, C. and Allemand, P. (2005). Differential Single-Frequency Gps Monitoring of the La Valette Landslide (French Alps). *Engineering Geology* 79 (3-4): pp. 215-229.

Stojic, M., Chandler, J. H., Ashmore, P. and Luce, J. (1998). The Assessment of Sediment Transport Rates by Automated Digital Photogrammetry. *Photogrammetric Engineering & Remote Sensing* 64 (5): pp. 387-395.

Tait, D. A. (1970). Photo-Interpretation and Topographic Mapping. *Photogrammetric Record* 6 (35): pp. 466-479.

Tarchi, D., Casagli, N., Fanti, R., Leva, D. D., Luzi, G., Pasuto, A., Pieracccini, M. and Silvano, S. (2003). Landslide Monitoring by Using Ground-Based Sar Interferometry: An Example of Application to the Tessina Landslide in Italy. *Engineering Geology* 68 (1-2): pp. 15-30.

Unit for Landscape Modelling 2001. *Unit for Landscape Modelling - the Library* [online]. Available at: <http://www.uflm.cam.ac.uk/library_page.htm> [Accessed 10 May 2006].

Uren, J. and Price, W. F. (2006). *Surveying for Engineers*. Palgrave Macmillan, Basingstoke/New York: 824 pp.

USGS 2004. *Landslide Types and Processes* [online]. Available at: <http://pubs.usgs.gov/fs/2004/3072/pdf/fs2004-3072.pdf> [Accessed 10/05/2006].

Van Westen, C. J. (1993). *Gissiz Training Package for Geographic Information Systems in Slope Instability Zonation. Part 1: Theory*. ITC, Enschede, The Netherlands: 245 pp.

Van Westen, C. J. and Getahun, F. L. (2003). Analyzing the Evolution of the Tessina Landslide Using Aerial Photographs and Digital Elevation Models. *Geomorphology* 54 (1-2): pp. 77-89.

Van Westen, C. J., Seijmonsbergen, A. C. and Mantovani, F. (1999). Comparing Landslide Hazard Maps. *Natural Hazards* 20 (2-3): pp. 137-158.

Van Zuidam, R. A. (1985). *Aerial Photo-Interpretation in Terrain Analysis and Geomorphological Mapping*. Smits Publishers, The Hague: 442 pp.

Vanapalli, S. K., Fredlund, D. G., Pufahl, D. E. and Clifton, A. W. (1996). Model for the Prediction of Shear Strength with Respect to Soil Suction. *Canadian Geotechnical Journal* 33 (3): pp. 379-392.

Varnes, D. J. (1958). Landslide Types and Processes. In: Eckel, E. B. (ed.) *Landslides and Engineering Practice, Highway Research Board Special Report 29*. The National Academy of Sciences, Washington, D.C.: pp. 21-47.

Varnes, D. J. (1978). Slope Movement Types and Processes. In: Schuster, R. L. and Krizek, R. J. (eds.) *Landslides - Analysis and Control, Transportation Research Board Special Report 176*. National Academy of Sciences, Washington D.C.: pp. 12-33.

Varnes, D. J. (1984). *Landslide Hazard Zonation: A Review of Principles and Practice*. UNESCO: 63 pp.

Wales on the Web 2006. *Wales on the Web - the All Wales Portal* [online]. Available at: <http://www.walesontheweb.org/> [Accessed 10 May 2006].

Walker, S. and Petrie, G. (1996). Digital Photogrammetric Workstations 1992-1996. *International Archives of Photogrammetry and Remote Sensing* 31 (2): pp. 384-395.

Walstra, J. (2006). *Historical Aerial Photographs and Digital Photogrammetry for Landslide Assessment - Animations* [online]. Available at:

<http://civil-unrest.lboro.ac.uk/cvjhc/jan/> [Accessed 22 October 2006].

Waltham, A. C. and Dixon, N. (2000). Movement of the Mam Tor Landslide, Derbyshire, Uk. *Quarterly Journal of Engineering Geology and Hydrogeology* 33 (2): pp. 105-123.

Weibel, R. and Heller, M. (1991). Digital Terrain Modelling. In: Maguire, D. J., Goodchild, M. F. and Rhind, W. D. (eds.) *Geographical Information Systems: Principles and Applications*. Longman, London: pp. 269-297.

Welch, R. and Howarth, P. J. (1968). Photogrammetric Measurements of Glacial Landforms. *Photogrammetric Record* 6 (34): pp. 75-96.

Wolf, P. R. and Dewitt, B. A. (2000). *Elements of Photogrammetry. With Applications in GIS*. McGraw-Hill, Boston: 608 pp.

WP/WLI (1993). *The Multilingual Landslide Glossary*. Bitech Press, Vancouver.

Appendix 1

Publications

Parts of this study were published in the following papers:

Chandler, J. H., Lane, S. and Walstra, J. (2006). Quantifying Landform Change. In: Fryer, J., Mitchell, H. and Chandler, J. H. (eds.) *Applications of 3D Measurement from Images*. Whittles Publishing.

Walstra, J., Chandler, J. H., Dixon, N. and Dijkstra, T. A. (2004). Extracting Landslide Movements from Historical Aerial Photographs. In: Lacerda, W., Erlich, M., Fontoura, S. A. B. and Sayao, A. S. F. (eds.) *Landslides: Evaluation and Stabilization*. Taylor & Francis, London: pp. 843 - 850.

Walstra, J., Chandler, J. H., Dixon, N. and Dijkstra, T. A. (2004). Time for Change - Quantifying Landslide Evolution Using Historical Aerial Photographs and Modern Photogrammetric Methods. *The International Archives of the Photogrammetry, Remote Sensing and Spatial Information Sciences* XXXV (part B4): pp. 475-480.

Walstra, J., Chandler, J. H., Dixon, N. and Dijkstra, T. A. (2005). Use of Historical Aerial Photographs for Monitoring the Evolution of the Mam Tor Landslide. *Proceedings of the RSPSoc 2005 conference: Measuring, Mapping and Managing a Hazardous World, Portsmouth*.

Walstra, J., Chandler, J. H., Dixon, N. and Dijkstra, T. A. (2006). Aerial Photography and Digital Photogrammetry for Landslide Monitoring. In: *Mapping Hazardous Terrain Using Remote Sensing*. Geological Society Special Publications.

Appendix 2

Sources for aerial photography

Agricultural Development and Advisory Service (ADAS)

Contact: Pat Evans

Address:
ADAS Aerial Photography
Woodthorne
Wergs Road
Wolverhampton
WV6 8TQ

Tel: 01902 693199

BKS

Contact: Mervyn Adams

Address:
BKS Surveys Ltd.
47 Ballycairn Road
Coleraine
Northern Ireland
BT51 3HZ

Tel: 028 70352311
Fax: 028 70357637
Email: madams@bks.co.uk
Web: http://www.bks.co.uk

Cambridge University Collection of Aerial Photographs (CUCAP)

Contact: Rose Desmond

Air Photo Library
Unit for Landscape Modelling - CUCAP
University of Cambridge
Sir William Hardy Building
Tennis Court Road
Cambridge, CB2 1QB

Tel: 01223 764377
Fax: 01223 764381
Email: library@uflm.cam.ac.uk
Web: http://venus.uflm.cam.ac.uk/

Central Register of Air Photography for Wales (CRAPW)

Contact: Vivien Davies

Address:
The Aerial Photography Unit
Room G-073a
National Assembly for Wales
Crown Offices, Cathays Park
Cardiff, CF10 3NQ

Tel: 029 2082 3819
Fax: 029 2082 3080
Email: air_photo_officer@wales.gsi.gov.uk

Infoterra

Contact: Dave Reed

Address:
Infoterra Ltd.
Atlas House
41 Wembley Road
Leicester, LE3 1UT

Tel: 0116 273 2314
Email: david.reed@infoterra-global.com
Web: http://www.infoterra.co.uk/airphotos.html

National Monuments Record (NMR)

Address:
NMR Enquiry and Research Services
English Heritage
Kemble Drive
Swindon, SN2 2GZ

Tel: 01793 414 600
Fax: 01793 414606
Email: nmrinfo@english-heritage.org.uk
Web: http://www.english-heritage.org.uk/server/show/nav.8502

Ordnance Survey (OS)

Ordnance Survey Options outlets:
http://www.ordnancesurvey.co.uk/oswebsite/business/howtobuy/options.html

e.g.
The Map Shop
30a Belvoir Street
Leicester, LE1 6QH

Tel: 0116 247 1400
Fax: 0116 247 1401
Email: sales@mapshopleicester.co.uk
Web: http://www.mapshopleicester.co.uk/

Simmons Aerofilms

Contact: Michael Willis

Address:
Library
Simmons Aerofilms Ltd.
32-34 Station Close
Potters Bar
Herts, EN6 1TL

Tel: 01707 648398
Fax: 01707 648399
Email: library@aerofilms.com
Web: http://www.simmonsaerofilms.com/imglib/form.aspx

Appendix 3

Matlab scripts

Automatic extraction of displacement vectors – main script:

```
%-------------------------------------------------------------------------
% Automatic displacement measurement
%
% Script for automatic measurement of displacement vectors from two images;
% selection of targets points based on image texture; image matching using
% a cross-correlation algorithm.
% Input: two greyscale tif images (identical dimensions and ground
% resolution) + covariance matrix for accuracy assessment of extracted
% vectors + values for arbitrary thresholds and search windows.
% Output: displacement vectors.
%
% JW 16 Dec 2004, 9 Dec 2005, 24 Feb 2006
%-------------------------------------------------------------------------

% Define input files
image1 = imread('1990.tif');
image2 = imread('1995.tif');
covarmatrix = dlmread('covar9095.dat');
% Define parameters
texwindowsize = 40;      % Window size to find maximum texture
texthres = 220;          % Texture threshold
searchsize = 15;         % Search window size
templatesize = 9;        % Template size
corrthreshold = 0.75;    % Correlation threshold
vectorscale = 5;         % Scale factor for display of vectors
confidence = 0.95;       % Confidence level for display of ellipses
% Define output file for vectors
outputfile = 'displacement9599.txt';
%-------------------------------------------------------------------------

% Display images and determine dimensions
figure(1), imshow(image1);
[dimx1,dimy1,a1] = getimage(1);
figure(2), imshow(image2);
[dimx2,dimy2,a2] = getimage(2);

% Texture function
hightex = texture_log(image1, texwindowsize, texthres);

% Determine number first and last columns/rows; to avoid edges of image
xstart=(searchsize+1)/2;
xend=dimx1(2)-xstart;
ystart=(searchsize+1)/2;
yend=dimy1(2)-ystart;
numbercols=xend-xstart;
numberrows=yend-ystart;

figure(1);
hold on
```

```matlab
% Index for measured displacement vectors
i=1;

for ypos = ystart:numberrows
    for xpos = xstart:numbercols
        if hightex(ypos,xpos)==1

            % Isolate template from first image, centred around selected
            % point
            xt = xpos - (templatesize-1)/2;
            yt = ypos - (templatesize-1)/2;
            template = imcrop(image1,[xt yt (templatesize-1) (templatesize-1)]);

            % Isolate search window from second image, centred around same
            % coordinates
            xs = xpos - (searchsize)/2;
            ys = ypos - (searchsize)/2;
            searchwindow = imcrop(image2,[xs ys (searchsize-1) (searchsize-1)]);

            % Calculate normalised correlation;
            corrmatrix = normxcorr2(template,searchwindow);

            % Determine position of maximum correlation
            maxrow = max(corrmatrix);
            maxval = max(maxrow);
            % Determine size of matrix
            matrize = size(corrmatrix);

            % Accept matched point only if correlation exceeds defined
            % threshold value
            if maxval>corrthreshold

                % Determine position of match to sub-pixel precision, using
                % centre of gravity operator
                centrepos = cofgravity(corrmatrix);

                % Store coordinates of matched point in first image
                displacement(i,1) = xpos;
                displacement(i,2) = ypos;
                % Calculate and store displacement of point
                displacement(i,3) = centrepos(1)- (matrize(2)+1)/2;
                displacement(i,4) = centrepos(2)- (matrize(1)+1)/2;
                % Store correlation coefficient
                displacement(i,5) = maxval;

                % Plot displacement vectors
                plot(xpos,ypos,'-r.','MarkerSize',8,'LineWidth',2);

line([xpos,xpos+displacement(i,3)*vectorscale],[ypos,ypos+displacement(i,4)*vectorscale]
,'Color','r','LineWidth',2.5);
                % Plot error ellipse around vector
                error_ellipse(vectorscale^2*covarmatrix,[xpos,ypos],confidence)

                i=i+1;
            end
        end
        xpos=xpos+1;
    end
    ypos=ypos+1;
end

% Write data to textfile
dlmwrite(outputfile, displacement);
```

Function for selecting target points for image matching:

```
function hightex = texture(image1, texwindowsize, texthres);

%--------------------------------------------------------------------------
% Function for determining image texture using a 5x5 Laplace filter, and
% selecting locations of maximum values
% 'image1' is input image;
% 'texwindowsize' is size of search window to find maximum texture;
% 'textresh' is texture threshold value;
% Output is a binary image, containing positions of the selected points.
%
% JW, 19 dec 2004, 24 feb 2006
%--------------------------------------------------------------------------

% Applying 5x5 Laplace filter to input image; image stretching only for
% display purposes
logfilter= fspecial('log',15,3);
teximage= imfilter(image1,logfilter);
stretchimage = imadjust(teximage);
figure(3),imshow(stretchimage), title('Filtered Image');

% Determine dimensions of input image; create zero matrix of similar size to
% contain positions of selected points
imagesize=size(teximage);
hightex=zeros(imagesize(1),imagesize(2));

% Avoid edge effects; convert edges of texture image into zeros
edge=(texwindowsize-1)/2;
teximage(1:edge,:)=0;
teximage((imagesize(1)-edge):imagesize(1),:)=0;
teximage(:,1:edge)=0;
teximage(:,(imagesize(2)-edge):imagesize(2))=0;

% Divide texture image in segments; determine number of columns and rows
numbercol=fix(imagesize(2)/texwindowsize);
numberrow=fix(imagesize(1)/texwindowsize);

figure(3)
hold on
ypos=1;
for i = 1:numberrow        % Row
    xpos=1;
    for j = 1:numbercol    % Column

        % Isolate segment from texture image; determine maximum texture
        searchsegment = imcrop(stretchimage,[xpos ypos (texwindowsize-1) (texwindowsize-
1)]);
        maxrow = max(searchsegment);
        maxval = max(maxrow);

        % Accept if texture is larger than threshold value, determine
        % position of maximum within segment
        if maxval>texthres
            for k = 1:texwindowsize
                for l = 1:texwindowsize
                    if searchsegment(k,l)==maxval;
                        positionmaxx=l;
                        positionmaxy=k;
                    end
                end
            end

            % Determine position of selected point within entire image
            absposx=xpos+positionmaxx-1;
            absposy=ypos+positionmaxy-1;

            % Plot selected point
```

```
        plot(absposx,absposy,'-rx','MarkerSize',8,'LineWidth',2);

        % Store selected point in binary image
        hightex(absposy,absposx)=1;
    end
    xpos=xpos+texwindowsize;
  end
  ypos=ypos+texwindowsize;
end
```

Function for obtaining centre of gravity:

```
function position = cofgravity(corrmatrix);

%-------------------------------------------------------------------------
% Returns the position of the maximum within image segment using centre of
% gravity; using a local threshold based upon maximum pixel value (Russ,
% 2000: 'The Image Processing Handbook')
% 'corrmatrix' is the input correlation matrix
%
% JC 17 Jun 2003, modified JW 24 Feb 2006
%-------------------------------------------------------------------------

sumxi=0; sumyi=0; sumx=0; sumy=0;

% Define dimensions of input matrix
matrize = size(corrmatrix);

% Define local threshold
maxrow=max(corrmatrix);
maxval=max(maxrow);
threshold = maxval-0.1;

% Determine centre of gravity
for i = 1:matrize(1)
    for j = 1:matrize(2)
        if corrmatrix(i,j) > threshold;
            sumxi = sumxi + corrmatrix(i,j) * j;
            sumx = sumx + corrmatrix(i,j);
        end
        if corrmatrix(j,i) > threshold;
            sumyi = sumyi + corrmatrix(j,i) * j;
            sumy = sumy + corrmatrix(j,i);
        end
    end
end
position(1) = sumxi/sumx ;
position(2) = sumyi/sumy ;
end
```

Function for plotting error ellipses (Kaplan 2005):

```
function h=error_ellipse(varargin)

% ERROR_ELLIPSE - plot an error ellipse, or ellipsoid, defining confidence region
%    ERROR_ELLIPSE(C22) - Given a 2x2 covariance matrix, plot the
%    associated error ellipse, at the origin. It returns a graphics handle
%    of the ellipse that was drawn.
%
%    ERROR_ELLIPSE(C33) - Given a 3x3 covariance matrix, plot the
%    associated error ellipsoid, at the origin, as well as its projections
%    onto the three axes. Returns a vector of 4 graphics handles, for the
%    three ellipses (in the X-Y, Y-Z, and Z-X planes, respectively) and for
%    the ellipsoid.
%
%    ERROR_ELLIPSE(C,MU) - Plot the ellipse, or ellipsoid, centered at MU,
%    a vector whose length should match that of C (which is 2x2 or 3x3).
%
%    ERROR_ELLIPSE(...,'Property1',Value1,'Name2',Value2,...) sets the
%    values of specified properties, including:
%      'C' - Alternate method of specifying the covariance matrix
%      'mu' - Alternate method of specifying the ellipse (-oid) center
%      'conf' - A value betwen 0 and 1 specifying the confidence interval.
%        the default is 0.5 which is the 50% error ellipse.
%      'scale' - Allow the plot the be scaled to difference units.
%      'style' - A plotting style used to format ellipses.
%      'clip' - specifies a clipping radius. Portions of the ellipse, -oid,
%        outside the radius will not be shown.
%    NOTES: C must be positive definite for this function to work properly.

default_properties = struct(...
  'C', [], ... % The covaraince matrix (required)
  'mu', [], ... % Center of ellipse (optional)
  'conf', 0.5, ... % Percent confidence/100
  'scale', 1, ... % Scale factor, e.g. 1e-3 to plot m as km
  'style', '', ...  % Plot style
  'clip', inf); % Clipping radius

if length(varargin) >= 1 & isnumeric(varargin{1})
  default_properties.C = varargin{1};
  varargin(1) = [];
end

if length(varargin) >= 1 & isnumeric(varargin{1})
  default_properties.mu = varargin{1};
  varargin(1) = [];
end

if length(varargin) >= 1 & isnumeric(varargin{1})
  default_properties.conf = varargin{1};
  varargin(1) = [];
end

if length(varargin) >= 1 & isnumeric(varargin{1})
  default_properties.scale = varargin{1};
  varargin(1) = [];
end

if length(varargin) >= 1 & ~ischar(varargin{1})
  error('Invalid parameter/value pair arguments.')
end

prop = getopt(default_properties, varargin{:});
C = prop.C;

if isempty(prop.mu)
  mu = zeros(length(C),1);
else
```

```
  mu = prop.mu;
end

conf = prop.conf;
scale = prop.scale;
style = prop.style;

if conf <= 0 | conf >= 1
  error('conf parameter must be in range 0 to 1, exclusive')
end

[r,c] = size(C);
if r ~= c | (r ~= 2 & r ~= 3)
  error(['Don''t know what to do with ',num2str(r),'x',num2str(c),' matrix'])
end

x0=mu(1);
y0=mu(2);

% Compute quantile for the desired percentile
k = sqrt(qchisq(conf,r)); % r is the number of dimensions (degrees of freedom)

hold_state = get(gca,'nextplot');

if r==3 & c==3
  z0=mu(3);

  % Make the matrix has positive eigenvalues - else it's not a valid covariance matrix!
  if any(eig(C) <=0)
    error('The covariance matrix must be positive definite (it has non-positive
eigenvalues)')
  end

  % C is 3x3; extract the 2x2 matricies, and plot the associated error
  % ellipses. They are drawn in space, around the ellipsoid; it may be
  % preferable to draw them on the axes.
  Cxy = C(1:2,1:2);
  Cyz = C(2:3,2:3);
  Czx = C([3 1],[3 1]);

  [x,y,z] = getpoints(Cxy,prop.clip);
  h1=plot3(x0+k*x,y0+k*y,z0+k*z,prop.style);hold on
  [y,z,x] = getpoints(Cyz,prop.clip);
  h2=plot3(x0+k*x,y0+k*y,z0+k*z,prop.style);hold on
  [z,x,y] = getpoints(Czx,prop.clip);
  h3=plot3(x0+k*x,y0+k*y,z0+k*z,prop.style);hold on


  [eigvec,eigval] = eig(C);

  [X,Y,Z] = ellipsoid(0,0,0,1,1,1);
  XYZ = [X(:),Y(:),Z(:)]*sqrt(eigval)*eigvec';

  X(:) = scale*(k*XYZ(:,1)+x0);
  Y(:) = scale*(k*XYZ(:,2)+y0);
  Z(:) = scale*(k*XYZ(:,3)+z0);
  h4=surf(X,Y,Z);
  colormap gray
  alpha(0.3)
  camlight
  if nargout
    h=[h1 h2 h3 h4];
  end
elseif r==2 & c==2
  % Make the matrix has positive eigenvalues - else it's not a valid covariance matrix!
  if any(eig(C) <=0)
    error('The covariance matrix must be positive definite (it has non-positive
eigenvalues)')
  end

  [x,y,z] = getpoints(C,prop.clip);
```

```
  h1=plot(scale*(x0+k*x),scale*(y0+k*y),prop.style,'color','b','LineWidth',2);
  set(h1,'zdata',z+1)
  if nargout
    h=h1;
  end
else
  error('C (covaraince matrix) must be specified as a 2x2 or 3x3 matrix)')
end
%axis equal

set(gca,'nextplot',hold_state);

%----------------------------------------------------------------
% getpoints - Generate x and y points that define an ellipse, given a 2x2
%   covariance matrix, C. z, if requested, is all zeros with same shape as
%   x and y.
function [x,y,z] = getpoints(C,clipping_radius)

n=100; % Number of points around ellipse
p=0:pi/n:2*pi; % angles around a circle

[eigvec,eigval] = eig(C); % Compute eigen-stuff
xy = [cos(p'),sin(p')] * sqrt(eigval) * eigvec'; % Transformation
x = xy(:,1);
y = xy(:,2);
z = zeros(size(x));

% Clip data to a bounding radius
if nargin >= 2
  r = sqrt(sum(xy.^2,2)); % Euclidian distance (distance from center)
  x(r > clipping_radius) = nan;
  y(r > clipping_radius) = nan;
  z(r > clipping_radius) = nan;
end

%----------------------------------------------------------------
function x=qchisq(P,n)
% QCHISQ(P,N) - quantile of the chi-square distribution.
if nargin<2
  n=1;
end

s0 = P==0;
s1 = P==1;
s = P>0 & P<1;
x = 0.5*ones(size(P));
x(s0) = -inf;
x(s1) = inf;
x(~(s0|s1|s))=nan;

for ii=1:14
  dx = -(pchisq(x(s),n)-P(s))./dchisq(x(s),n);
  x(s) = x(s)+dx;
  if all(abs(dx) < 1e-6)
    break;
  end
end

%----------------------------------------------------------------
function F=pchisq(x,n)
% PCHISQ(X,N) - Probability function of the chi-square distribution.
if nargin<2
  n=1;
end
F=zeros(size(x));

if rem(n,2) == 0
  s = x>0;
  k = 0;
  for jj = 0:n/2-1;
    k = k + (x(s)/2).^jj/factorial(jj);
```

```matlab
    end
  F(s) = 1-exp(-x(s)/2).*k;
else
  for ii=1:numel(x)
    if x(ii) > 0
      F(ii) = quadl(@dchisq,0,x(ii),1e-6,0,n);
    else
      F(ii) = 0;
    end
  end
end

%-------------------------------------------------------------
function f=dchisq(x,n)
% DCHISQ(X,N) - Density function of the chi-square distribution.
if nargin<2
  n=1;
end
f=zeros(size(x));
s = x>=0;
f(s) = x(s).^(n/2-1).*exp(-x(s)/2)./(2^(n/2)*gamma(n/2));

%-------------------------------------------------------------
function properties = getopt(properties,varargin)
%GETOPT - Process paired optional arguments as 'prop1',val1,'prop2',val2,...
%
%   getopt(properties,varargin) returns a modified properties structure,
%   given an initial properties structure, and a list of paired arguments.
%   Each argumnet pair should be of the form property_name,val where
%   property_name is the name of one of the field in properties, and val is
%   the value to be assigned to that structure field.
%
%   No validation of the values is performed.
%
% EXAMPLE:
%   properties = struct('zoom',1.0,'aspect',1.0,'gamma',1.0,'file',[],'bg',[]);
%   properties = getopt(properties,'aspect',0.76,'file','mydata.dat')
% would return:
%   properties =
%          zoom: 1
%        aspect: 0.7600
%         gamma: 1
%          file: 'mydata.dat'
%            bg: []
%
% Typical usage in a function:
%   properties = getopt(properties,varargin{:})

% Process the properties (optional input arguments)
prop_names = fieldnames(properties);
TargetField = [];
for ii=1:length(varargin)
  arg = varargin{ii};
  if isempty(TargetField)
    if ~ischar(arg)
      error('Propery names must be character strings');
    end
    f = find(strcmp(prop_names, arg));
    if length(f) == 0
      error('%s ',['invalid property ''',arg,'''; must be one of:'],prop_names{:});
    end
    TargetField = arg;
  else
    % properties.(TargetField) = arg; % Ver 6.5 and later only
    properties = setfield(properties, TargetField, arg); % Ver 6.1 friendly
    TargetField = '';
  end
end
if ~isempty(TargetField)
  error('Property names and values must be specified in pairs.');
end
```